INTERFACIAL ENGINEERING OF TRANSPARENT ELECTRODES AND NANOPARTICLES WITH PHOSPHONIC ACIDS AND METAL-ORGANIC DOPANTS FOR ORGANIC ELECTRONIC APPLICATIONS

A Thesis
Presented to
The Academic Faculty

by

Sergio Paniagua-Barrantes

In Partial Fulfillment
of the Requirements for the Degree
Doctor of Philosophy in the
School of Chemistry and Biochemistry

Georgia Institute of Technology

December 2013

INTERFACIAL ENGINEERING OF TRANSPARENT ELECTRODES AND NANOPARTICLES WITH PHOSPHONIC ACIDS AND METAL-ORGANIC DOPANTS FOR ORGANIC ELECTRONIC APPLICATIONS

Approved by:

Dr. Seth R. Marder, Advisor
School of Chemistry and Biochemistry
Georgia Institute of Technology

Dr. Joseph R. Perry
School of Chemistry and Biochemistry
Georgia Institute of Technology

Dr. Jean-Luc Brédas
School of Chemistry and Biochemistry
Georgia Institute of Technology

Dr. Laren Tolbert
School of Chemistry and Biochemistry
Georgia Institute of Technology

Dr. Bernard Kippelen
School of Electrical and Computer Engineering
Georgia Institute of Technology

Date Approved: August 9, 2013.

To my parents and my wife.

ACKNOWLEDGEMENTS

I would like to thank everyone who has supported me in one way or another during my Ph.D. studies starting with Dr. Marder for accepting me in his group and providing me with the tools needed to do proper surface science, *i.e.* critical thinking… and some machines and reagents too. I am grateful for the friendship and camaraderie with Anthony Giordano, O'Neil Smith and the rest of the surface modification subgroup, especially my mentees Ritesh Kumar, Emily Li and Katherine Henry, as well as Siyuan Zhang. I want to thank Dr. Cristina Rumi for her suggestions and example of discipline, Dr. Tim Parker for helping with several lab equipment, and Dr. Steve Barlow for useful discussions and for editing this dissertation. The Marder group has really been welcoming, friendly and nice to be a part of, and I would like to thank all of the members, past and present, for making the group as special as it is.

I want to acknowledge collaborators from different departments, including Yunsang Kim, José Baltazar, Dr. Anu Bulusu, and Dr. Hossein Sojoudi, for their technical support and useful discussions, as well as Walter Henderson who has helped me maintain the Kratos XPS for the past two years. I thank the members of my committee for their valuable time and suggestions, especially Dr. Perry and Dr. Kippelen for letting me use their instrumentation when needed, and thank the Center for Organic Photonics and Electronics (COPE) for the fellowship awarded.

I want to thank collaborators from different universities including Prof. Christine Luscombe, Dr. Natasha Doubina, Kristina Knesting, Dr. Andres Garcia, Dr. Joseph

Berry, Dr. Armstrong at Arizona and his group, where every time I visit I still feel part of it.

Finally, I am grateful for the support and encouragement of the Paniagua / Barrantes / Nock / Hughes families throughout my studies. None of this would be possible without the love of my family. My wife Jessie helped me all along, and I am eternally grateful to have her by my side in all the journeys of life.

TABLE OF CONTENTS

LIST OF TABLES

LIST OF FIGURES

LIST OF SYMBOLS

E	energy
E_{ads}	energy of adsorption
E_F	Fermi level
E_{des}	energy of desorption
E^i	incident beam
E^r	reflected beam
k_b	Boltzman's constant
T	temperature
ν	stretching mode
q_{ads}	heat of adsorption
Φ	work function
N	surface coverage
μ_z	interface dipole contribution from the modifier
ε_0	vacuum permittivity
ε_{eff}	effective dielectric constant
γ	surface energy
U_{max}	maximum energy density
ε_r	relative permittivity of the dielectric

LIST OF ABBREVIATIONS

AFM	atomic force microscopy
AP	air plasma
ATRP	atom transfer radical polymerization
BD	bond dipole
BHJ	bulk heterojunction
BTO	barium titanate
CA	contact angle
CB	conduction band
COPE	Center for Organic Photonics and Electronics
CV	cyclic voltammetry
CVD	chemical vapor deposition
DFT	density functional theory
DSC	detergent/solvent-cleaned
EIS	electrochemical impedance spectroscopy
ETL	electron transport layer
HTL	hole transport layer
IMFP	inelastic mean free path
IRRAS	infrared-reflection absorption spectroscopy
ITO	indium tin oxide
LUMO	lowest unoccupied molecular orbital
NEXAFS	near-edge X-rays absorption fine structure
NMR	nuclear magnetic resonance spectroscopy

NREL	National Renewable Energy Laboratory
OFET	organic field effect transistor
OLED	organic light emitting dipole
OPV	organic photovoltaic
PA	phosphonic acid
QCM	quartz crystal microbalance
SAM	self-assembled monolayer
SEE	secondary electron edge
T-BAG	tethering by aggregation and growth
TCO	transparent conductive oxide
TGA	thermogravimetric analysis
UPS	ultraviolet photoelectron spectroscopy
VB	valence band
VBM	valence band maximum
WF	work function
XPS	X-ray photoelectron spectroscopy

SUMMARY

This thesis focuses on understanding the chemistry involved in a variety of surface modification reactions, both on metal oxides and graphene. In the last few years the application of phosphonic acids to metal oxide films has become a popular means of modifying their surface properties, including work function and surface tension, which are important for transparent conductive electrodes in organic electronics. In this work, the rates of chemisorption of a prototypical phosphonic acid on ITO under several processing protocols are measured using XPS to determine the optimal procedure. UPS is used to track the dependence of the electronic structure of the system, specifically of the work function and position of the valence band maximum on coverage.

Phosphonic acid monolayers with appropriate tail groups can also be used to initiate chemistry from surfaces, which has potential for building layers of organic-electronic devices, including organic solar cells and capacitors. The growth of non-conjugated polymers from $BaTiO_3$ nanoparticles using a facile ATRP technique is studied via solution-phase and solid-state techniques to determine its applicability to make matrix-free composites for hybrid dielectrics. In addition, the surface chemistry involved in Kumada Catalyst-Transfer to grow polythiophene derivatives from ITO is examined via XPS.

Finally, the newly emerged alternative for replacement of ITO as transparent electrode, graphene, is n- and p-doped using redox-active, solution-processable metal-organics, which increased its conductivity and allowed the work function to be tuned over a range of 1.8 eV. The systems are characterized in a systematic study, and the results are promising for future applications of graphene.

CHAPTER 1 INTRODUCTION AND BACKGROUND

1.1 The importance of surfaces and surface chemistry

Surface science deals with the physics and chemistry at interfaces, be it solid-liquid, solid-gas, solid-vacuum, liquid-gas, or liquid-liquid. Surfactants, substances that adsorb onto surfaces and interfaces, have been tremendously important for industry for dispersion and floculation applications;[1] they are used daily, as in the case of detergents, to make "dirt" dispersable in water and be able to wash it away, through the formation of micelles.

Regardless of surface area to volume ratio, several properties of a material in the final analysis depend partially or even completely on the surface. For instance, heterogeneous catalytic activity,[2] adhesion,[3] and contact resistance[4] are critically dependent on the nature of the surface; hence the importance of surface engineering, which we can define as manipulation of the surface properties through physical processes and chemistry. The roughness of a surface can affect the hydrophobicity of a material, and is a major contributor to the lotus flower ultrahydrophobicity.[5] The chemical modification of a surface can be used to create anti-corrosion films for metals,[6] self-cleaning glass,[7] antifog[8] and antifouling[9] coatings, among other applications.

1.2 Organic monolayers on oxides

Within surface science, the deposition of ultrathin layers of atoms and compounds (submonolayer, monolayer and few-layer coverage) has been extensively researched. Monolayers consist of one-layer thick coatings on a surface, be it flat, spherical or irregular. Given that the surface affects the interfacial properties, one monolayer can induce remarkable changes on the interfacial behavior of the surface. Using organic molecules as building blocks for monolayers offers the possibility of choosing the

functionalities needed for a particular surface in a particular application through rational design and synthesis.

The molecules used as monolayer-forming modifiers can typically be broken down into the anchoring (head) group, spacer, and tail group (Figure 1.1). The choice of head group will determine the affinity for the surface and the possibility or absence of homo-condensation with other molecules during deposition. The spacer group will (in part) determine the intermolecular interaction between neighboring molecules on the surface, as well as define the separation between anchoring group and any functionality that is placed at the end of the molecule. It can include alkane chains or conjugated moieties, such as rings, as the backbone. The tail group can consist of merely an inert capping group, or include a chemically reactive moiety. Tail groups will largely determine the wettability of the modified substrate for subsequent layer depositions.[10]

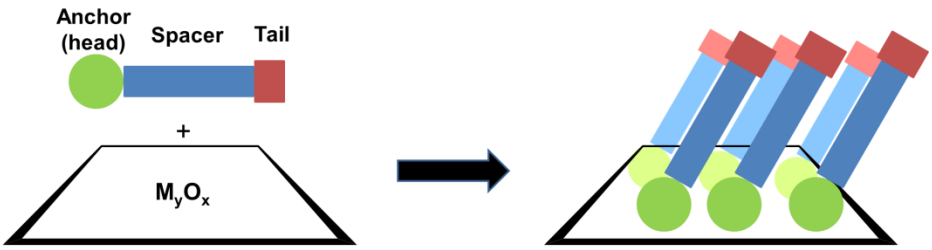

Figure 1.1 Monolayer coating of a metal oxide with an organic modifier.

Self-assembly and Langmuir-Blodgett film transfer have been the main methods for monolayer deposition from solution.[11] In self-assembly, a grafting group positions the molecules on the surface, and the molecular interactions from the spacer group organizes the monolayer. In the Langmuir-Blodgett technique, an ambiphilic monolayer forms on the air liquid interface. This can be transferred to a solid substrate by immersing (or removing) the solid into (from) the liquid due to distinct affinity of the monolayer for each of the phases involved.[12] Surface functionalization of gold surfaces with thiols and

their derivatives has been extensively researched from the 1980's, and has served as the iconic system to examine many basic science questions related to self-assembly.[13] In addition, self-assembly of thiols on gold has enabled a variety of applications in biomedicine, dispersion of nanoclusters in polymer matrices and solvents, blocking of sites for anisotropic crystal growth, electrochemical methods, etc.[13]

The work presented in Chapters 2, 3 and 4 of this dissertation focuses on the less extensively studied surface modification of oxides, geared towards organic electronics, using phosphonic acids as anchoring moiety. The next sections provide a short overview on why this thesis focuses on this particular grafting group, and a brief summary of analytical techniques that have been used by the surface science community to characterize interfaces.

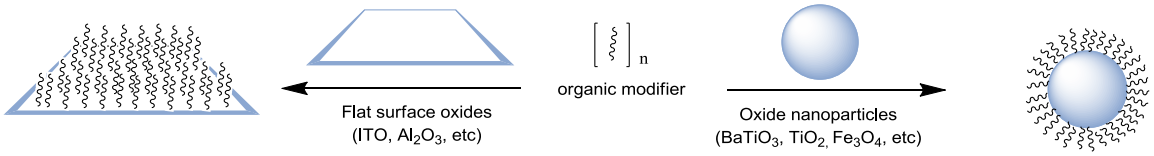

Figure 1.2 Monolayer coating of oxide flat surfaces and nanoparticles.

1.3 Physisorption and chemisorption

The attachment of small molecules to oxides can occur through physisorption or chemisorption. In physisorption, the interaction is relatively weak, such as van der Waals forces, weak coordinate bonds, or hydrogen bonds. There are typically small activation barriers for physisorption, and the dissociation energy of the modifier from the surface is low. In chemisorption, new covalent bonds are formed, with dissociation energies that can be orders-of-magnitude higher than physisorption. Chemisorption is characterized by chemical specificity, with changes in electronic states detectable by suitable physical means, and an elementary step involving an activation energy. In Figure 1.2, a one-

dimensional potential for a system consisting of an atom **A** approaching a surface **σ** is shown. The interaction is favorable at the physisorption well, and even more so in the chemisorption well, but **A** must come with a certain kinetic energy to overcome the energy barrier E_{ads}. Typical chemisorption energies are 15-100 kcal/mol, while physisorption energies are 2-10 kcal/mol.[14]

When the attachment is due to physisorption, the coating may be easily removed via heat, solvents, or sonication. Reversal of the behavior back to the initial untreated surface properties upon exposure to any of these removal techniques can indicate if the attachment is only through physical adsorption. The same anchoring group that leads to physisorption in a given oxide can lead to chemisorption in a different one (for example, a carboxylic acid on indium-tin oxide *vs.* on titania); also, the modification protocol can be changed to favor chemisorption over physisorption, through heating for example.[15]

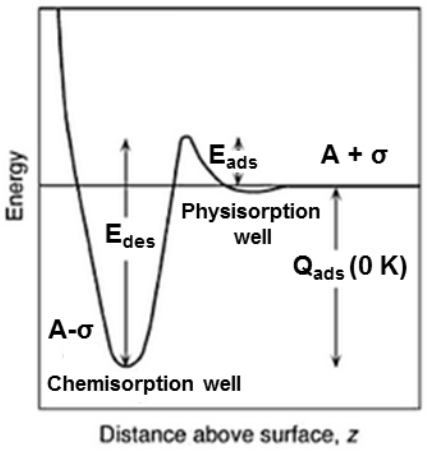

Figure 1.3 Energetics of chemisorption vs. physisorption. A one-dimension representation of the potential energy of a system consisting of a surface σ and an approaching atom A. No energy barrier is presented for physisorption. Modified from Kolasinski.[14]

Most of the reports on oxide modification, particularly from the 1990's and early 2000's, used carboxylic acids and alkoxy/halosilanes as anchor groups. Other

functionalities that can be found in the literature include acyls, thionyls and phosphoryls,[16] amines,[17] hydroxamic acid,[18,19] sulfonates,[18] and recently there has been a surge in the R&D community of a variety of phosphorus based moieties, including phosphonates[20] and phosphates.[21] Chapters 2 and 3 of this thesis concentrate on phosphonic acids as anchoring groups for modification of metal oxide surfaces with applications in organic electronics.

1.4 Analytical techniques for characterization of monolayers

The signal-to-noise ratio of many typical analytical techniques is not sufficiently good for analysis of surfaces, especially when considering flat surfaces given the ultrathin path lengths and small amount of material on top. Nonetheless, there are a number of analytical tools that can help determine if a monolayer is formed and probe the nature of attachment present. An analysis of observations from a combination of techniques provides more information to enable one to paint a self-consistent picture of the detailed structure of the modified surface. Some techniques that are helpful in determining coverage include thermogravimetric analysis (TGA), quartz-crystal microbalance (QCM), X-ray photoelectron spectroscopy (XPS), near-edge X-ray absorption fine structure (NEXAFS), contact angle (CA), cyclic voltammetry (CV), scanning probe microscopies (such as atomic force, AFM), electron microscopies, and for very small, dispersable nanoparticles, nuclear magnetic resonance (NMR) and ultraviolet/visible spectroscopy (UV/Vis). There are also techniques that can help elucidate binding modes; in the case of chemisorption, multiple bonds might be formed between the organic and the oxide. For instance, infrared spectroscopy (in transmission or dispersion mode for nanoparticles, and in reflection mode for flat surfaces) is one of the most powerful tools, along with Raman spectroscopy. Solid state (SS) NMR and XPS can sometimes be helpful as well. A brief explanation of some of these techniques -those that

were used for this thesis, or are part of someone else's work relevant to this thesis- is presented below, and more detailed explanations are offered throughout the text as needed.

In XPS, X-ray radiation ionizes the atoms at the surface (and a few microns in) of the sample. Electrons from atoms that originate within 0-10 nm from the surface are able to escape, with a probability of escape proportional to a negative exponential on the distance from the surface. These are collected by the spectrometer detector, which separates the electrons as a function of their kinetic energies. These kinetic energies in turn relate back to the orbital energies from which they originated. The intensities of the peaks allow one to determine the relative atomic concentrations at the interface, and given that the chemical environment changes the orbital energies slightly, information on the functionalities present can be also be extracted in some cases. Detection limits as low as 0.1% atom concentrations can be achieved.[22]

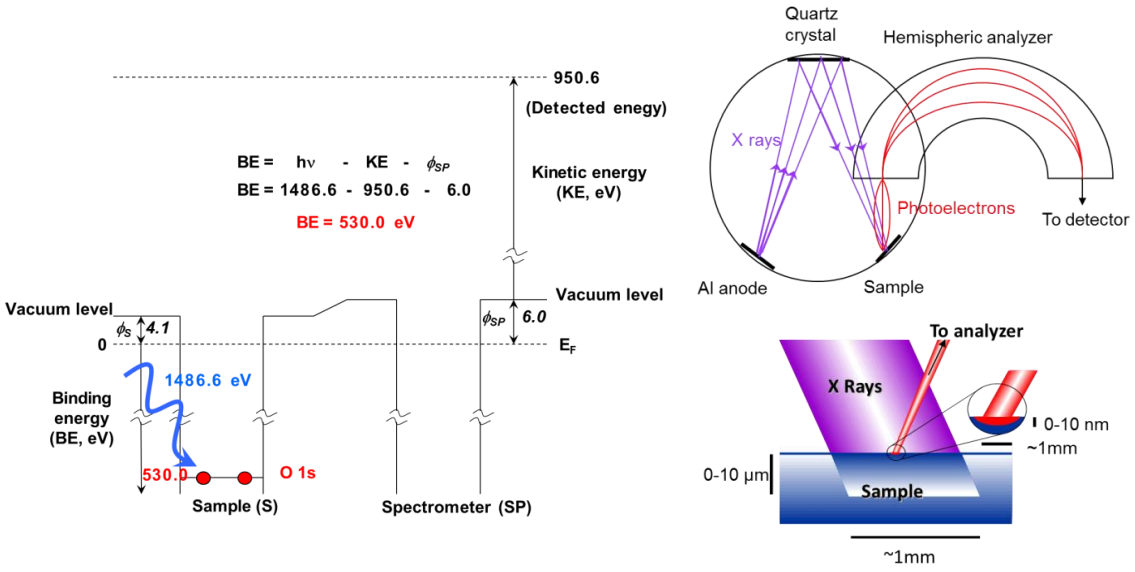

(a) (b)

Figure 1.4 XPS fundamental processes: (a) Energetics of the process of photoemission and detection of associated kinetic energies from which the binding energies can be deduced. (b) Schematic of the instrumentation (top) and zoom into the analysis area (bottom). The X-rays are generated by electron impingement on an Al anode and

monochromatized using a quartz crystal. The photoelectrons are detected using a hemispheric analyzer. The X-rays penetrate a few microns into the sample, but only electrons emerging from the top 10 nm are released into vacuum and detected. (b) was modified from Haasch.[23]

AFM is one of many scanning probe microscopies. In intermittent-contact mode, traditionally used to probe monolayers on oxides, a cantilever is stimulated through a piezoelectric crystal to oscillate at its resonance frequency at a given amplitude such that the tip enters for short periods of time the short-range force field of the surface being probed. Normally, a digital feedback mechanism is in place to adjust the amplitude of the cantilever oscillation so that it is constant, and an image suggestive of the topography is drawn based on the adjustment of the cantilever height needed to keep constant amplitude. Given the short interactions with the surface in intermittent contact tapping mode, damage to the sample is usually avoided. A phase image can also be obtained, which consists of the phase difference between the commanded oscillations of the piezoelectric and the oscillations detected by the feedback loop, dictated by the compositional differences of the sample. On atomically smooth oxides, the coverage by modifiers can be observed as height differences or phase differences, but for polycrystalline substrates it is hard to discern molecules from the substrate and is used instead only to determine roughness or check for morphological changes.

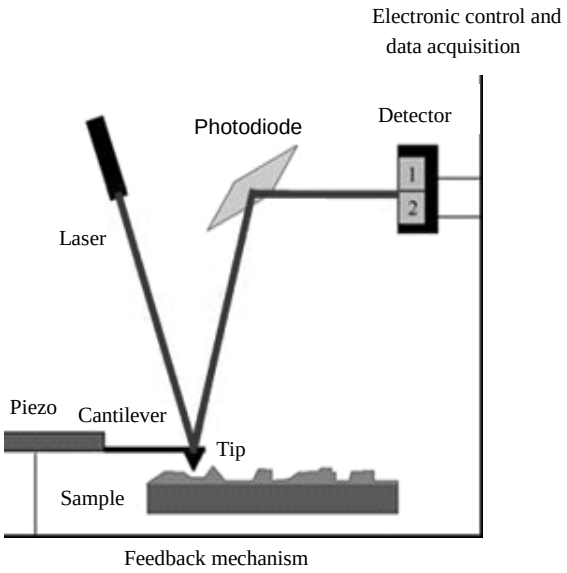

Figure 1.5 Schematic of intermittent-contact mode AFM system.

In infrared-reflection absorption spectroscopy (IRRAS), a grazing angle geometry is used to collect information on surface vibrational modes on an IR-reflective substrate. A stationary wave perpendicular to the surface results from the incidence of an IR ray on the surface, where the incident and reflected beams interfere constructively (Figure 1.6a). In Figure 1.6b the amplitude of the electric field on the surface is plotted for this perpendicular wave. The electric field is remarkably enhanced at high grazing angles. Only vibrations with a dipole moments aligned perpendicular to the surface can interact with p-polarized light. By comparison with the infrared spectrum of the modifier itself, binding modes can be identified, and orientation can be determined via careful modeling of the vibrational modes of the attached molecules. Polarization Modulation (PM)-IRRAS can additionally increase sensitivity by acquiring the p- and s-polarized light (quasi)simultaneously and then doing a ratio of the two. Fractions of a monolayer can be detected depending on the system being probed.[24]

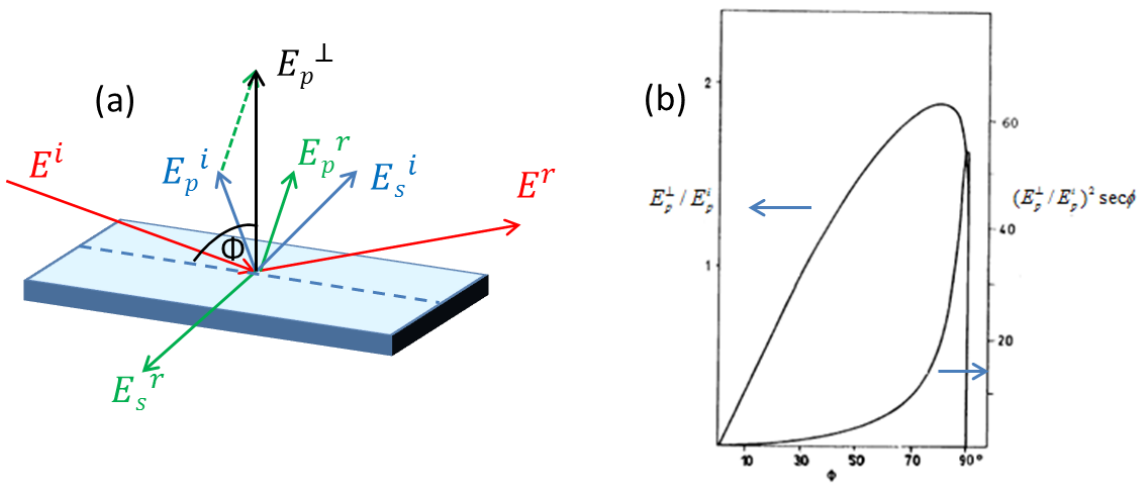

Figure 1.6 (a) IRRAS experiment: incident beam (E^i) on a surface in a grazing angle geometry. s- and p-components of the incident beam are shown in blue, and s- and p-components of the reflected beam Er are in green. Constructive interference of $E_p^{\,i}+E_p^{\,r}$ give rise to $E_p^{\perp}$, which will have a relative amplitude with respect to the incident p-polarized field dependent on the incident angle Φ of $(E_p^{\perp}/ E_p^{\,i})^2$, as shown in (b). (b) Modified from Hayden.[25]

In cyclic voltammetry (CV) for analysis of monolayers, a conventional three-electrode electrochemical cell is used wherein the surface-modified electrode serves as the working electrode. The potential across the cell is ramped linearly with time until a redox process of a given species in solution (or at the tail group of the monolayer) is observed as a change in current; then the potential ramp is reverted to observe the reversible redox reaction (if possible). The properties of the working electrode determine in part the shape of the curve observed, and hence information on monolayer quality and thickness can be inferred from peak (potential) separations and the currents registered. These values can be used to determine charge transfer rates through the monolayers, compared with different monolayers and against the bare (unmodified) electrode.

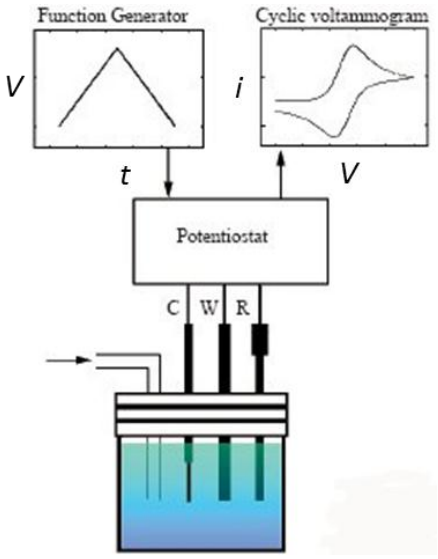

Figure 1.7 Schematic of a CV measurement. The working electrode (W) will have the surface being probed. A counter electrode (C) completes the circuit and a reference electrode (R) serves to calibrate the potential. From ALS©.[26]

Near-edge X-ray absorption fine structure spectroscopy (NEXAFS) can be used to evaluate the order and quantify the molecular tilt angle of monolayers on oxides. It is a form of X-ray spectroscopy that uses high intensity, monochromatic, linearly polarized light from a synchrotron source to measure electronic transitions near the absorption edge of an atom present in the near surface (few nm).[27] Linearly polarized X-rays from a synchrotron source are absorbed through excitations of core electrons to antibonding orbitals above the vacuum or Fermi level. The created holes are then filled by Auger decay (see figure below). The intensity of the emitted primary Auger electrons and the photoelectrons are a direct measure of the x-ray absorption. Analyses of the electronic transitions near the carbon K-edge are commonly used to characterize order in monolayers with long-chain alkyl groups.[28] The cross section for these excitations is a function of the linearly polarized light's alignment with the antibonding orbital. Thus, by collecting spectra at multiple angles of incidence the amount of alkyl chain alignment can be assessed.

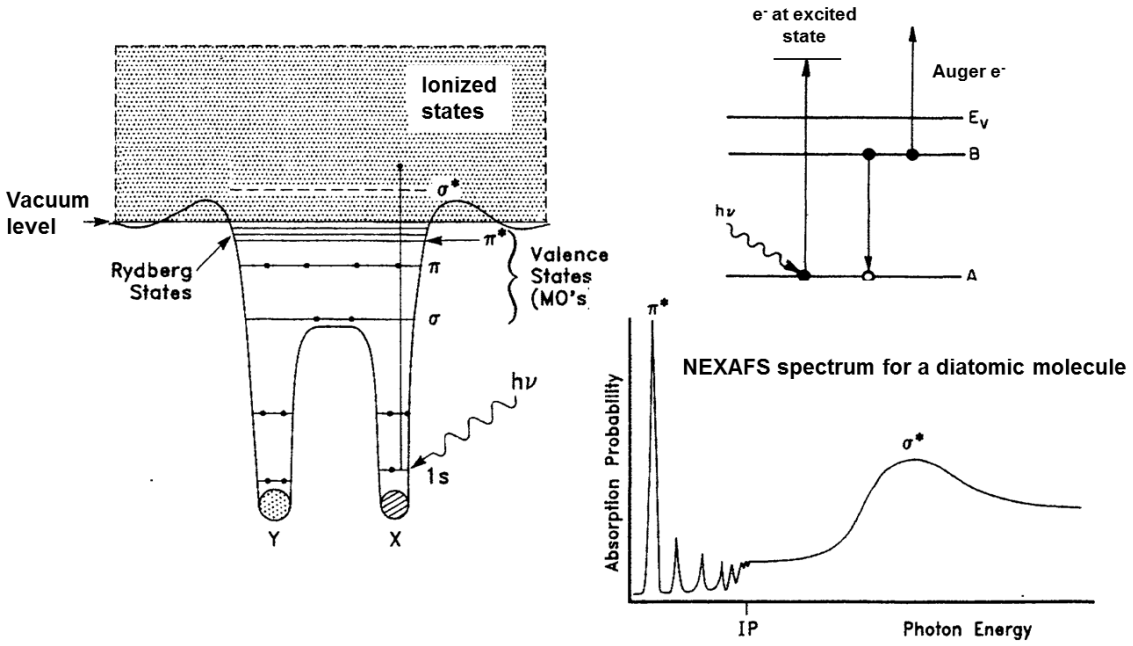

Figure 1.8 NEXAFS for a diatomic molecule: the X-ray radiation takes a core level electron to an antibonding orbital; an electron from another level fills the hole, releasing energy in the process that will ionize another (Auger) electron. Reproduced from Stohr.[27]

1.5 Phosphonic acids as monolayers

1.5.1 Attachment modes to oxides

The general structure of a phosphonic acid (PA) is shown on the left in Figure 1.9. PAs display three geminal bonding sites: the acidic hydroxyls (pK_{a1} 1-4, pK_{a2} 5-9) and the phosphoryl moiety.[29] The phosphonate group has great affinity for metal oxides, which explains the abundance of natural clays that consist in part of metal phosphates. Phosphonic acids offer the possibility of self-limiting monolayers given that the strongest interaction is between the metal oxide and the anchor group; homocondensation to form P-O-P bonds is not favored except under strictly anhydrous conditions at high temperatures,[30] and unless another anchor group is in the tail, there should be a very limited driving force to make multilayers other than the weak physisorption of unreacted

molecules lying on top of the monolayer, which can be removed through rinsing and sonication.[31] Given that there are three oxygen atoms available for reaction with a metal oxide, multiple binding modes to the metal oxides are possible (Figure 1.9).

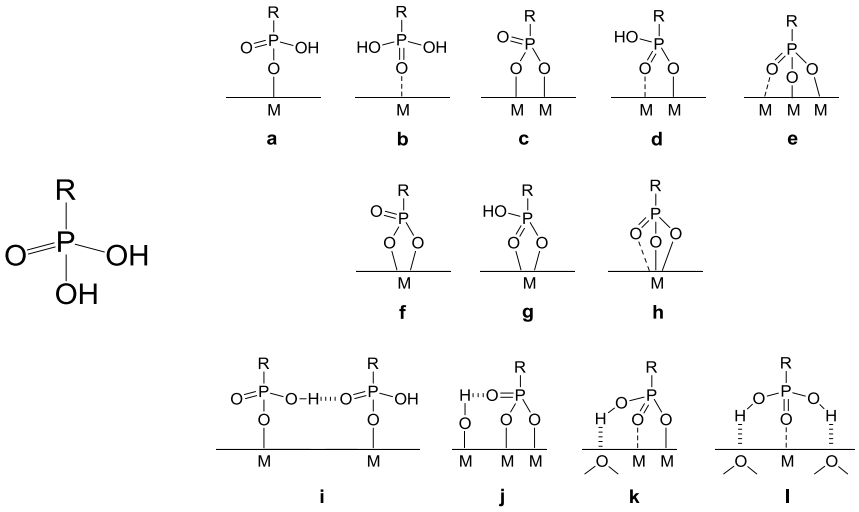

Figure 1.9 (Left) The phosphonic acid functionality connected to a given R spacer/tail. (Right) Some possible binding modes of phosphonic acids to a metal oxide surface. M = metal: Monodentate (a and b), bridging bidentate (c and d), bridging tridentate (e), chelating bidentate (f and g), chelating tridentate (h), and some possible additional hydrogen bonding interactions (i – l). Modified from Mutin, *et al*.[32]

Figure 1.10 shows some plausible mechanisms for attachment of a phosphonic acid to a metal oxide surface. The P center can act as electrophile for nucleophilic surface hydroxide groups with cleavage of P-OH and formation of P-OM (route 1) and/or a Lewis acid/base interaction between the phosphoryl and the metal center can initiate the heterocondensation (route 2).

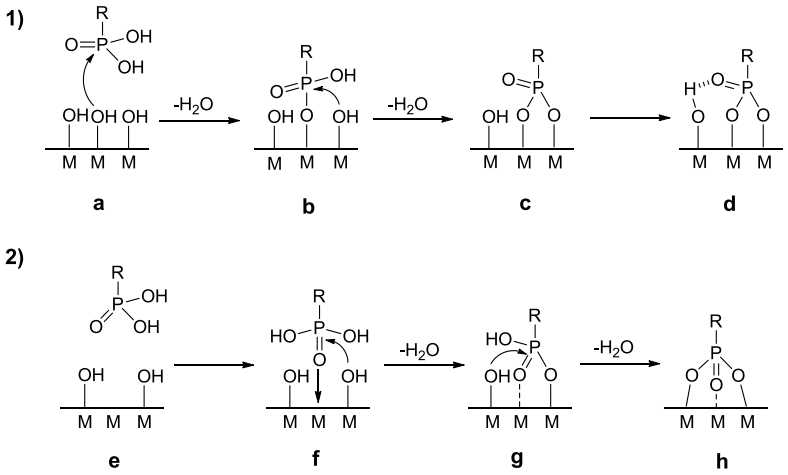

Figure 1.10 1) Mechanism of phosphonic acid attachment to poorly Lewis-acidic metal oxides: a) heterocondensation with a surface hydroxyl group, b) second heterocondensation with the surface, c) bidentate bound state, d) hydrogen bonding of phosphoryl group with surface hydroxyl. 2) Mechanism of phosphonic acid attachment to Lewis acidic metal oxides: e) initial conditions, f) coordination of the phosphoryl oxygen to a Lewis acidic site on the surface followed by heterocondensation with the now more electrophilic phosphorus, g) additional heterocondensation, h) final tridentate binding state. Reproduced from Hotchkiss, *et al*.[33]

Binding modes have been determined using multiple techniques. Figure 1.11 shows vibrational characterization through PM-IRRAS of octadecylphosphonic acid modified indium-tin oxide (ITO) in the region where the stretching νP-O absorptions occur, and comparison with the free acid in powder form. It is clear that the νP=O stretching mode is still present on the modified substrate, while the P-O-H absorptions appear to have faded. This is consistent with structure 1d in Figure 1.9. Figure 1.12 shows that XPS can also be helpful to gain insight into the bonding mode of the phosphonic acid; here a comparison between the O 1s XP spectra of the powder of octylphosphonic acid (OPA) and OPA modified ITO is made. DFT calculations predict that there will not be any protons attached to any of the P-O bonds, which is consistent with the XPS data, which shows no overlap between the modified ITO and the P-O-H component of the O 1s spectrum of the powder.

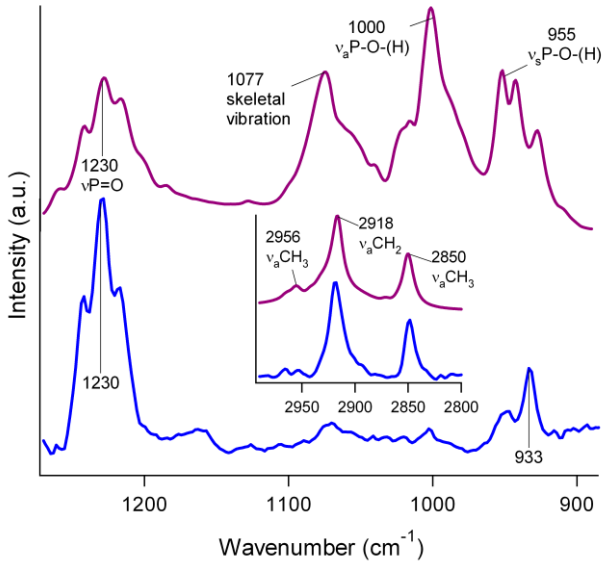

Figure 1.11 Comparison of the ODPA transmission FTIR spectrum (top spectrum) and the PM–IRRAS spectrum for an ODPA modified DSC/OP–treated ITO surface (bottom spectrum) in the ν(P–O) region. Inset: Spectral comparisons for the ν(C–H) region.[34]

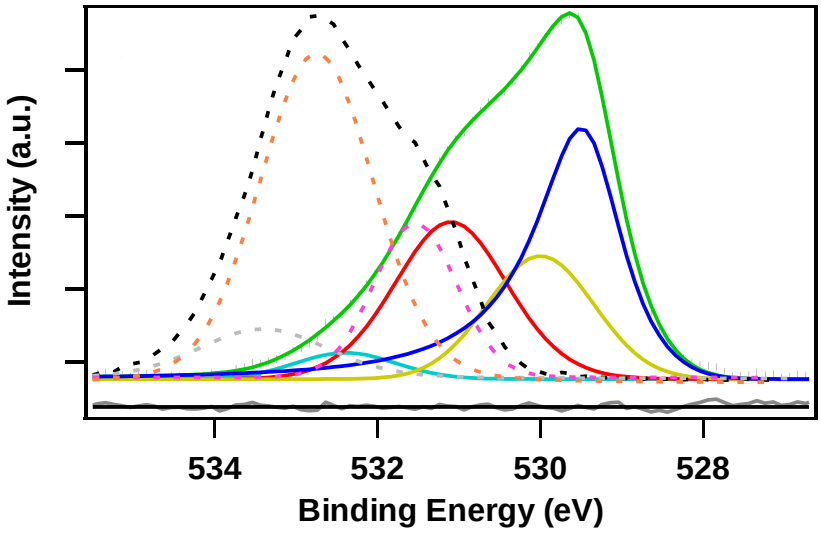

Figure 1.12 Experimental O 1s core level XPS spectrum for OPA adsorbed on the ITO surface (dots), fitted with components calculated at the DFT level (yellow, blue, red lines); gray baseline corresponds to fit error. The three main components of the DFT fit are at 529.5 eV (bulk O); 530.0 eV (surface In–O–In and Sn–O species); and 531.1 eV (P–O–In, P=O...In, and surface In–OH). An additional peak at 532.6 eV was used to complete the fit (light blue). XPS spectrum of isolated OPA powder (dashed line) is shown for comparison, along with synthetic peaks for P=O (pink) and P-O-H (orange) and an extra component (likely contamination, in gray). Modified from Paramonov, *et al*.[35]

1.5.2 Comparison with other anchoring groups

Silanes have been extensively used for silica/glass modification[36-38] as well as for indium-tin oxide (ITO),[39,40] and are readily available for commercial applications. A variety of terminations (R-Si-X_3, X=Cl, alkoxy and other hydrolyzable groups) may be used that affect the reactivity with the oxide;[41] for instance, trichlorosilanes are very reactive. It has been well established that high quality self-assembled monolayers (SAMs) are difficult to produce using trichlorosilanes given the strict control of water content and concentration needed to avoid homocondensation reactions leading to multilayers (Figure 1.13).[30] It is common to prepare alkoxylsilanes which give better stability and reaction control. Ethoxy-terminated silanes give more controllable reactions then their methoxy analogues. Even this slower reacting moiety needs optimization of surface modification conditions to avoid multilayer formation, as shown in Figure 1.14.

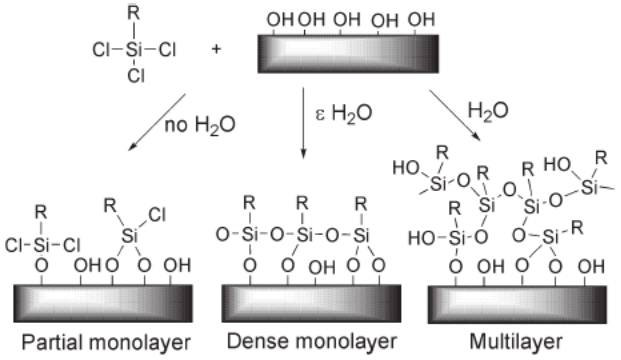

Figure 1.13 Schematic representation of possible outcomes of trichlorosilane reaction with an oxide surface as a function of water content. Reproduced from Mutin, *et al*.[30]

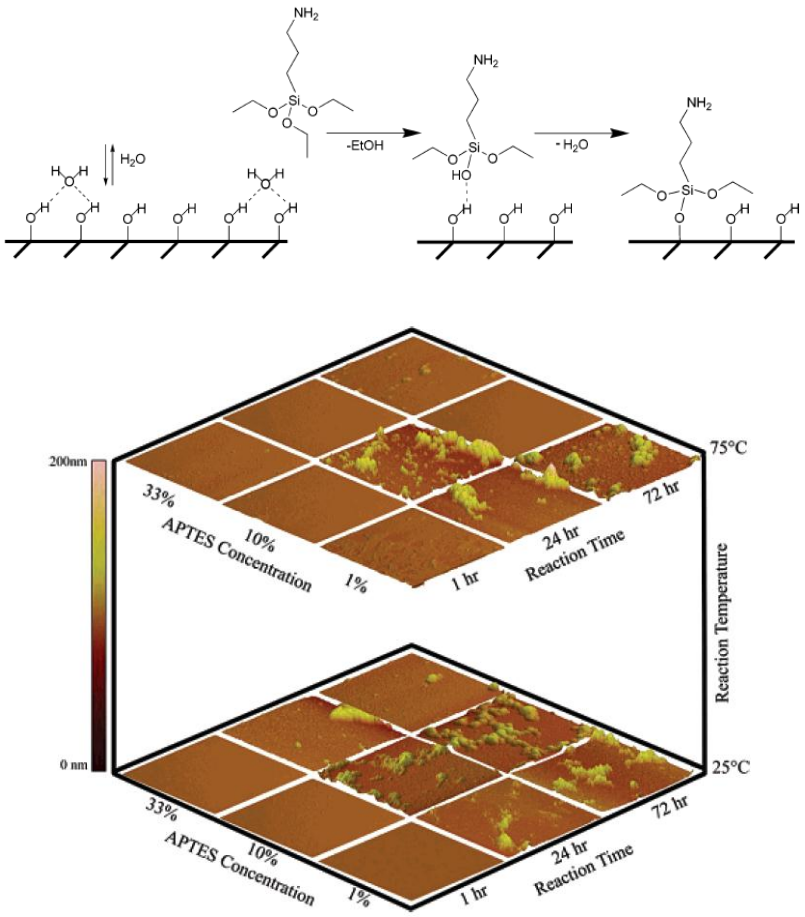

Figure 1.14 Top: Scheme on alkoxysilane anchoring on a metal oxide (the silane shown is the prototypical 3-aminopropyltriethoxysilane, APTES). Bottom: AFM characterization of films prepared under different reaction times, concentrations and temperatures. Reproduced from Howarter and Youngblood.[37]

For carboxylic (fatty) acids, the driving force for attachment to metal oxides is usually hydrogen bonding with polar groups on the surface, or formation of a surface salt between the carboxylate anion and the surface metal cation.

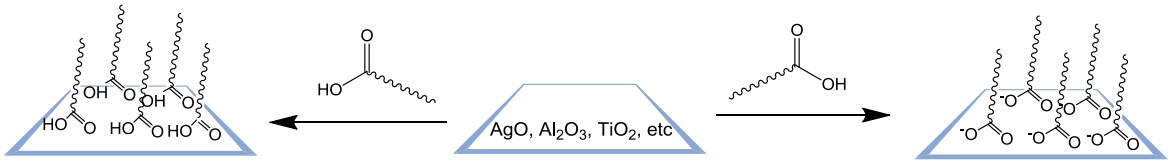

Figure 1.15 Grafting of carboxylic acid to metal oxides via H-bonding (left) and salt formation (right).

Carboxylic acids have been deposited on various substrates for organic electronic applications, for improving charge collection through work function tuning or surface energy engineering[42,43] and are anchoring group of choice for dyes in dye-sensitized solar cells.[44] Nonetheless, in the last decade, the use of phosphonic acids to a variety of metal oxides has propagated, challenging the dominant role of carboxylic acids, especially on alumina,[45-47] and on indium tin oxide (for organic electronic applications),[33,48-53] A study by Vercelli and coworkers points out the differences between using carboxylic acids (CA) *vs.* phosphonic acids (PA); they compared the coverage of 6-ferrocenylhexyl tail group with a CA or a PA anchor group on ITO by CV.[49] They found that under the same modification protocols, the PA gave a coverage of 4.2×10^{-10} mol/cm^2, while the CA gave 1×10^{-10} mol/cm^2 (ideal monolayer coverage was estimated at 4.5×10^{-10} mol/cm^2). As Figure 1.16 shows, the voltammogram in the case of the PA is very symmetric, indicative of fast and reversible electron transfer from/to the electrode. The film was also robust (survived multiple cycles).

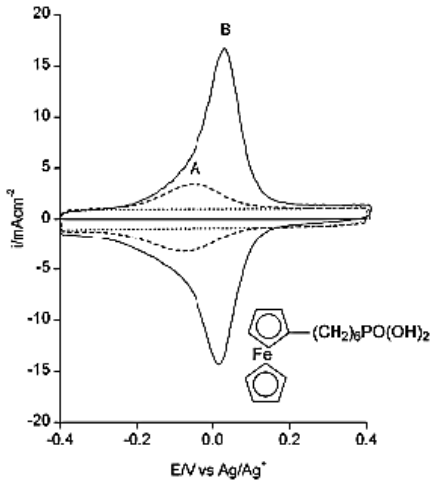

Figure 1.16 Cyclic voltammetry of hexylferrocene phosphonic acid in 0.1 M Bu_4NClO_4 adsorbed onto ITO from EtOH solutions at A)10^{-5} M and B) 10^{-3} M concentrations. Reproduced from Vercelli, *et al.*[49]

1.5.3 Synthesis of phosphonic acids

There are multiple approaches to making phosphonic acids. In the Michaelis-Arbuzov reaction an alkyl halide reacts with a trialkylphosphite to form a phosphonate precursor (Figure 1.17). It typically provides good yields and is performed by refluxing of the alkyl halide in neat triethylphosphite. If the purity of the starting material is high, after removal of excess triethylphosphite under vacuum, no additional purification will typically be required for the phosphonate. Another approach is the Michaelis-Becker reaction, using diethylphosphite in the presence of a base.[54] The conversion to the acid can be done in a variety of ways; the indirect methodology consisting of replacement of ethoxy groups for silyls and subsequent deprotection with water is of widespread use nowadays.[54]

The Michaelis-Arbuzov reaction is not applicable to phenyl halides, so other approaches are pursued, such as light mediated coupling, Hirao cross-coupling using dialkyl phosphites (Figure 1.18) and other related transition metal catalyzed reactions. These strategies are nicely reviewed in a recent report by Bujoli and coworkers.[54]

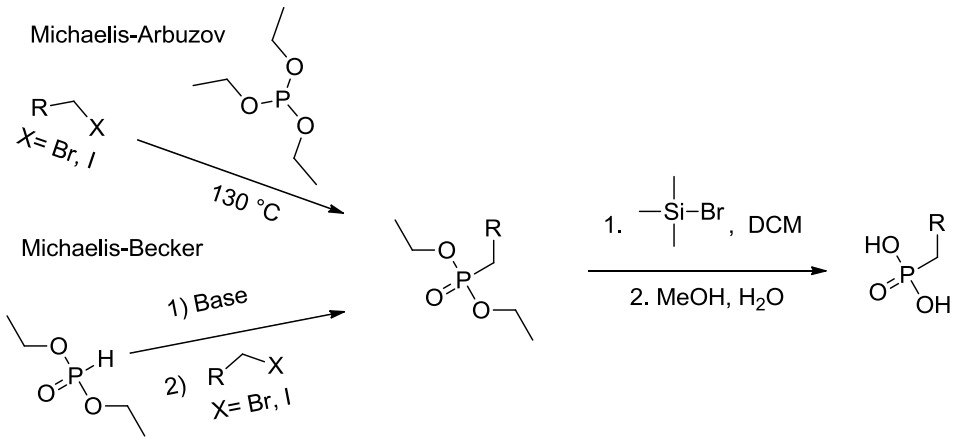

Figure 1.17 Michaelis-Arbuzov and Michaelis-Becker conversion of alkyl/benzyl halides to the phosphonate and subsequent hydrolysis.

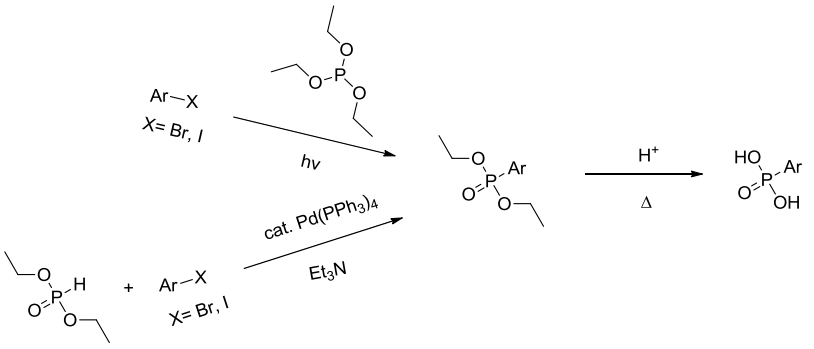

Figure 1.18 UV light mediated conversion of halide to phosphonate, Hirao cross-coupling of halide with dialkyl phosphite, and subsequent direct conversion to the acid.

1.5.4 Deposition of phosphonic acids on transparent conductive oxides

In the last 15 years, several reports have been published of phosphonic acids for modification of transparent electrodes, especially ITO, which is not surprising given that it has been the most widely used transparent conductor used in commercial applications. Reports vary in terms of surface preparation (cleaning conditions), deposition protocols, surface analysis and properties after deposition, device fabrication / characterization, and theoretical studies on binding modes and work function changes. Before reviewing what has been done, ITO itself will be briefly introduced.

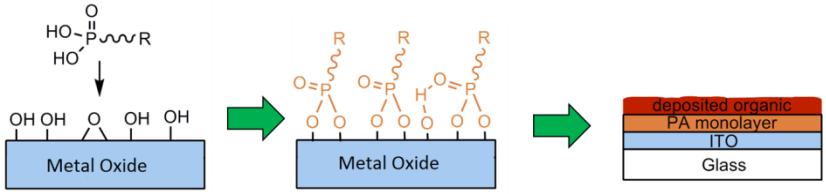

Figure 1.19 Left: surface modification with phosphonic acid to increase adhesion of deposited organic on the surface. Reproduced from Hotchkiss, *et al*.[33]

1.5.4.1 Crystal and electronic structure of indium-tin oxide (ITO)

Low resistance commercially available ITO typically consists of polycrystalline In_2O_3 with Sn substitutions for Indium in ~10-14 % of the sites sputtered deposited as films ~100 nm thick on glass or plastic. Annealing under anoxic conditions results in oxygen vacancy sites, leaving a pair of electrons behind.[55] Such dopings result in the electronic structure shown in Figure 1.20, where the additional electrons introduced result in the Fermi level shifted close to or within the conduction band minimum (see Section 1.5.5),[56] which confers it remarkable conductivity in thin films while maintain over 90% transparency in the visible range.[57] Figure 1.20 shows a cross-section schematic of a clean ITO film, where a clean, hydroxylated surface due to reaction with moisture is present.[58]

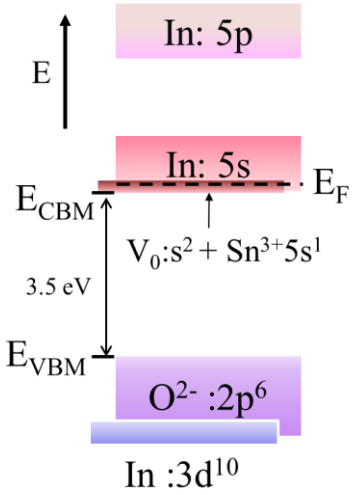

Figure 1.20 Schematic view of the frontier orbitals in ITO thin films (flat bands). High concentration of oxygen vacancies produce electron-rich bands that with energies as high as the In 5s orbitals. Doping with Sn introduce additional electron-rich sites. Significant doping results in the Fermi level lying in the conduction band. Adapted from Fan and Goodenough.[56]

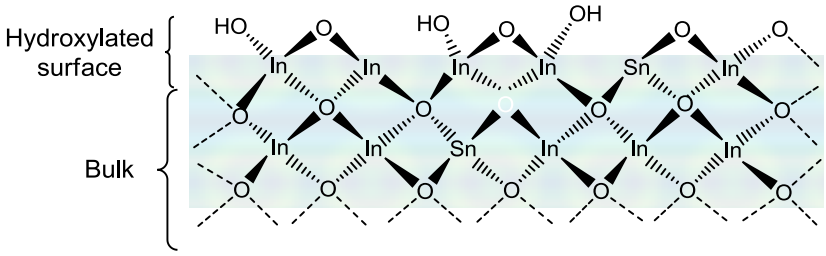

Figure 1.21 Cartoon for the cross-section of indium-tin oxide.

1.5.4.2 Literature precedents on phosphonic acid deposition on TCOs

Some of the earliest reports on the use of PAs on ITO adapted the methodologies for other anchor groups or other oxides such as SiO_2 or mica (a silicate with K, Mg and Al cations). The deposition of PA on atomically flat mica was studied in the 1990's by D. K. Schwartz and collaborators.[59,60] One of the techniques they used to track adsorption over time was atomic force microscopy (AFM). Figure 1.22 shows *ex situ* AFM images of mica that has adsorbed octadecylphosphonic acid from tetrahydrofuran. In the first couple of minutes, small islands (< 10 nm diameter) are seen, which grow as time progresses. The coverage data acquired from AFM did not fit properly to the usual adsorption and growth kinetics model where the coverage is proportional (by a constant α) with time to a fitted power ν: $\theta = \alpha t^{\nu}$; however, if the model is modified to account for interfacial transfer when the substrate is brought into/out of the solution -so that $\theta = \alpha t^{\nu} + \theta_0(1 - \alpha t^{\nu})$- where θ_0 is proportional to concentration, the data fits much better. This additional term is attributed to a quasi-Langmuir Blodgett deposition, the physisorption methodology mentioned earlier in the chapter that relies on transfer of films from different phases through application of pressure.

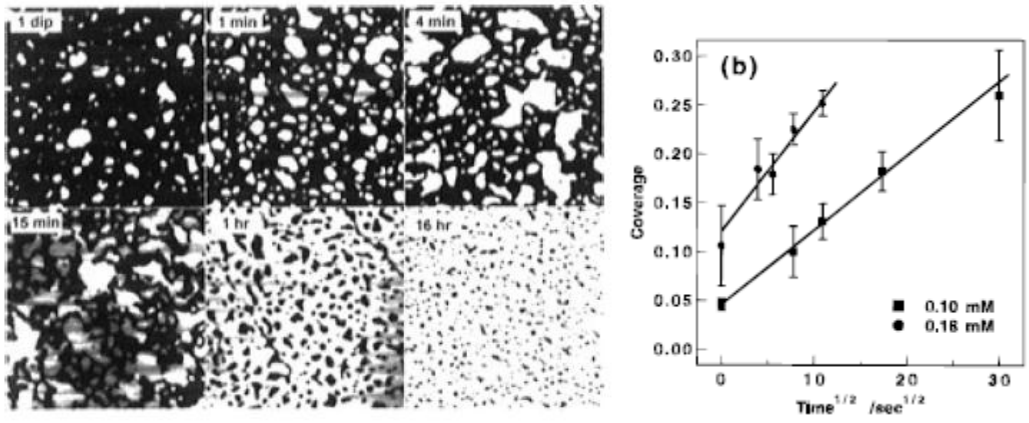

Figure 1.22 Left: AFM images (1 μm × 1 μm) of mica surface exposed to 0.2 mM ODPA solution in THF. Gray scale represents 5 nm height. Reproduced from Woodward, *et al*.[59]

Right: Coverage data for experiments at two concentrations, fitted to a $t^{1/2}$ function. Reproduced from Woodward, *et al*.[60]

The nature of the attachment was not discussed (presumably the layers are only physisorbed), but a modification of this method would be later developed by the J. Schwartz group from in the early 2000's,[15] for bonding phosphonic acids to the native oxide of silicon. In their procedure a substrate was held vertically in a solution of the phosphonic acid in THF below the critical micelle concentration, and the solvent allowed to evaporate slowly, with the purpose of taking advantage of the quasi-Langmuir deposition first described by D. K. Schwartz. They coined the protocol "tethering by aggregation and growth" (T-BAG). Washing this film in dilute base would remove most of it, so in order to make the film more robust they would heat the substrate subsequent to deposition to covert the surface-adsorbed phosphonic acid to surface-bound phosphonate. They used IRRAS to determine that the phosphonate functionality was present on the surface, quartz-crystal microbalance (QCM) to quantify packing density, and AFM to probe the thickness of the layer, all giving results consistent with a chemisorbed monolayer on the oxide of silicon.

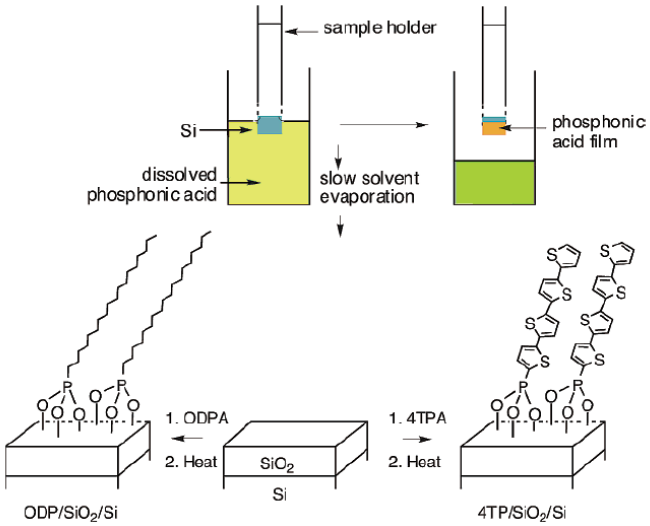

Figure 1.23 T-BAG setup and chemical reactions on the native oxide of Si. Reproduced from Hanson, *et al*.[15]

T-BAG for the native oxide of silicon would later be adapted for ITO, without any characterization other than QCM on a film prepared on ITO with 1/7000th the concentration (0.1μM) used for all other experiments (0.7 mM). [31] Some of their results from devices using the modified ITOs are presented in subsequent sections below.

Chen and coworkers examined several solvents for deposition of PAs on ITO,[61] including triethylamine, diethyl ether, tetrahydrofuran, pyridine, acetone, methanol, acetonitrile, dimethyl sulfoxide, and water. They compared the CV, contact angle, and XPS for monolayers of phenyl, 4-aminobenzyl, n-cotadecylphosphonic acids as well as 16-phosphohexadecanoic acid, created using the same modification protocol. Preparation of the monolayers consisted of immersion of solvent/base-cleaned susbtrates in 1 mM solutions for 24 h followed by rinsing in the solvent and annealing for 24 h at 200 °C to promote covalent bonding, followed by rinsing with water. P/In XPS ratios were used to assess coverage for a given phosphonic acid. The electrochemical behavior of ITO is changed when covered with the phosphonate films, as the peak separation between the oxidation and reduction peak of a redox-active species in solution is dependent on the rate of electron transfer. This could be used to assess not only the extent of defects on a monolayer, but also to track the stability of the monolayers upon electrochemical cycling. To directly observe the defects, underpotential deposition of Pb was used: lead would only deposit in bare ITO sites given that less overpotential is required to deposit the metal on the electrode than to nucleate it in the bulk solution. The lead could be quantified by scanning tunneling microscopy and XPS. The conclusion was that high quality monolayers were obtained with the lower dielectric constant solvents that did not have nitrogen groups to complex to the ITO.

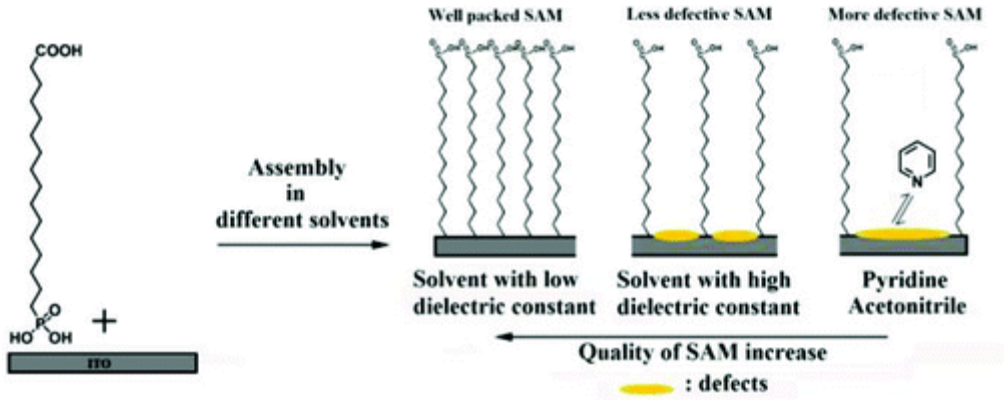

Figure 1.24 Representation of phosphonocarboxylic acid monolayer quality dependency on solvent used. From Chen, *et al*.[61]

Losego and collaborators studied the deposition of monolayers of alkanephosphonic acids with chain lengths between 8 and 18 carbons on ITO deposited on atomically flat SiO_2.[28] Near-edge X-ray absorption fine structure (NEXAFS) spectroscopy experiments were conducted to evaluate the effects of chain length. Before depositing the SAMs, organic residue was removed from the ITO surface via a 10 min UV ozonolysis treatment, after which the ITO samples were immediately immersed in 1 mM ethanolic solutions for 12 h, time after which the samples were rinsed with ethanol and tetrahydrofuran. They determined that long-chain SAMs are more highly ordered, and have a smaller tilt angle, than short-chain SAMs. They also found that only when the ITO surface roughness becomes greater than the modifier chain length (~15 Å) that these alkanephosphonate films become relatively disordered.

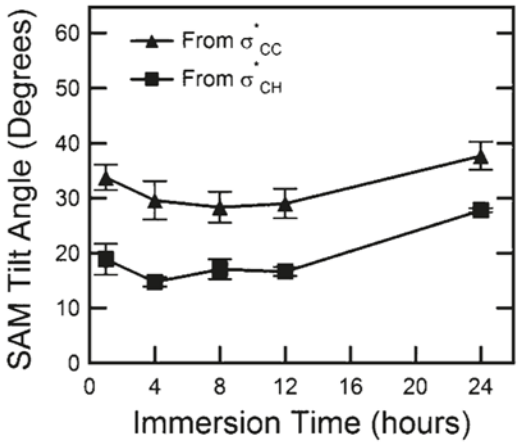

Figure 1.25 NEXAFS-derived results for high-quality ITO coated with octadecylphosphonic acid with increasing immersion times. From Losego, *et al*.[28]

Chapter 2 of this thesis examines chemisorption kinetics of PA deposition on indium-tin oxide from ethanol, and a brief review on the latest efforts of the surface science community to learn more on the deposition of PAs from polar solvents on various metal oxides is presented there.

1.5.5 Modulating the work function of indium tin oxide (ITO) other TCOs

Electrons in solids follow Fermi-Dirac statistics, as in Equation 1.1, where f(E), the probability of finding an electron at an energy (E) depends on kT and a reference energy E_F known as the Fermi level, at which the probability is 1 when T = 0 K, but ½ for any other T.

Equation 1.1 $$f(E) = \frac{1}{e^{(E-E_F)/kT}+1} \text{ for } T > 0 \text{ K}$$

A material will have a density of states dependent on its components and its crystal structure. In metals, the occupied states overlap with the unoccupied states, and hence there is no band gap. In semiconductors and insulators, there is no overlap, and a

band gap is present. In any case, the extent to which those bands are filled depends on temperature and the Fermi energy, as shown in Figure 1.26. At T = 0 K, no electron will populate bands that lie higher in energy than the Fermi level. For metals, this is the top of the valence band. For an intrinsic semiconductor or an insulator, it is in the middle of the band gap. As T increases, it becomes more feasible for electrons to fill the conduction band, and the narrower the band gap, the more likely it is to find electrons in the conduction band. The vacuum level, the energy at which electrons become unbound from the system, can be used as a reference to compare the position of the Fermi level between different materials. The energy required to remove an electron from E_F and place in vacuum is known as the work function (φ).

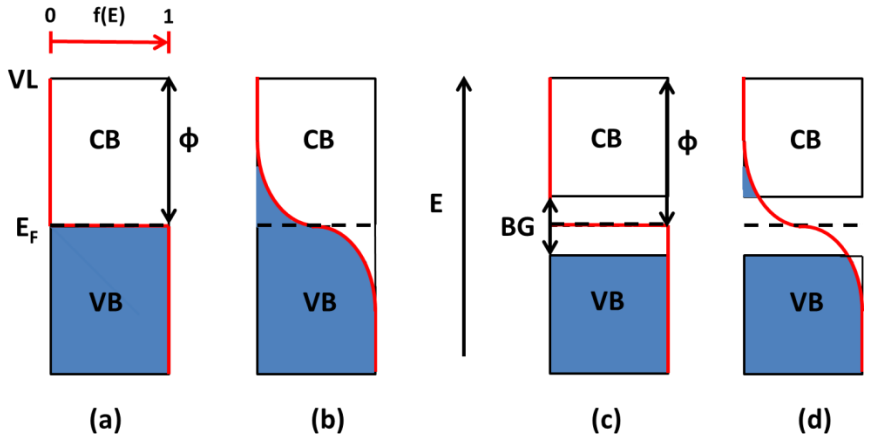

Figure 1.26 (a) Electronic structure of a metal at T = 0 K. The Fermi level E_F, vacuum level VL, conduction band (CB) and valence band (VB) are shown). The Fermi-Dirac distribution is represented by the red trace, and the work function is φ. (b) Electronic structure of the metal at T >> 0 K. (c) Electronic structure of a semiconductor at T = 0 K, with a band gap BG and work function φ. (d) Semiconductor at T >> 0 K.

Figure 1.27 shows how the Fermi level position changes in the case of intrinsic, n-doped and p-doped semiconductors. It is clear that for doped semiconductors the Fermi level tracks the density of states and carrier concentrations. Hence, the work function can serve as a reference to tell how accessible certain states can be.

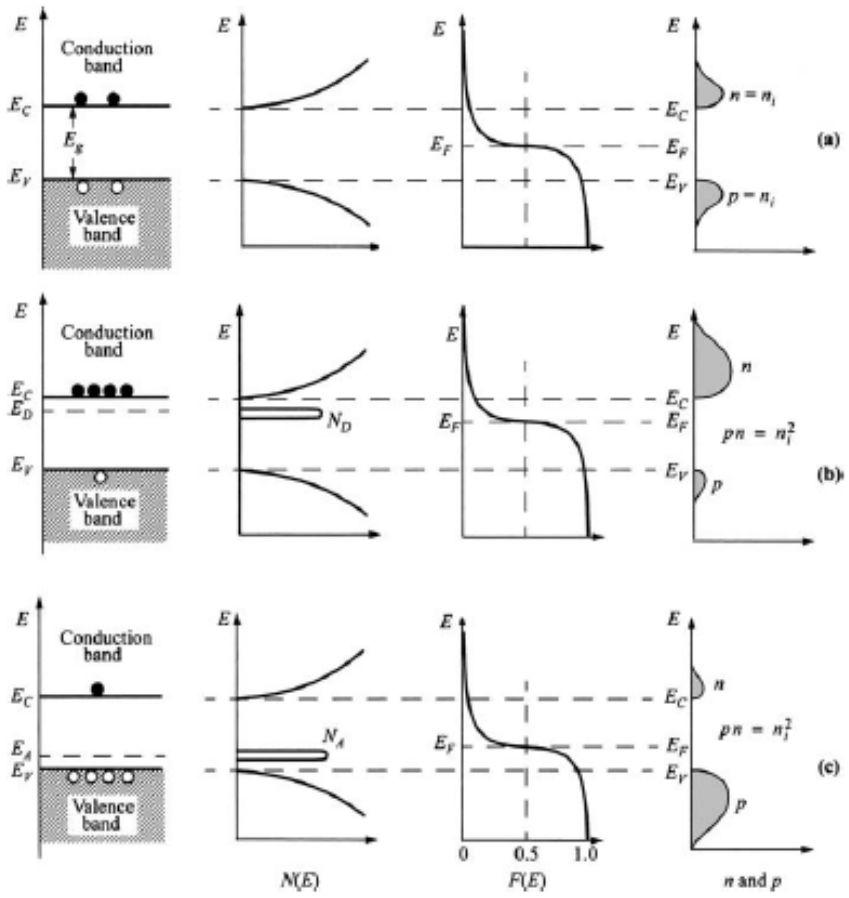

Figure 1.27 Schematic band diagram, density of states, Fermi-Dirac distribution, and carrier concentrations for (a) intrinsic, (b) n-type, and (c) p-type semiconductors at thermal equilibrium. E_C and E_V are the conduction band minimum and valence band maximum respectively; E_g is the band gap; E_D, E_A, and N_D, N_A are the energy levels and density of states associated with the donor and acceptor respectively; the relative density of carriers associated with n- and p- dopants are labeled in the last column as *n* and *p* respectively. Reproduced from Sze and Ng.[62]

There are three factors that can lead to modification of the work function when attaching interface modifiers, such as phosphonic acids:[63] bond dipole (BD) – due to the chemical bonding of the modifier; geometry rearrangement ($\Delta\phi_M$) – brought about by changes in the surface geometry after chemisorption, and molecular dipole ($\Delta\phi_{MD}$) – induced by the molecular dipole of the attached modifier, which changes only the vacuum level.

Equation 1.2 $$\Delta\phi = BD + \Delta\phi_M + \Delta\phi_{MD}$$

Figure 1.28 shows this graphically; $\Delta\Phi_M = \Phi_M - \Phi_0$ (Φ_M is the WF of a virtual surface of a bare substrate in the modified geometry after chemisorption and Φ_O is the WF of the optimized bare substrate).[64]

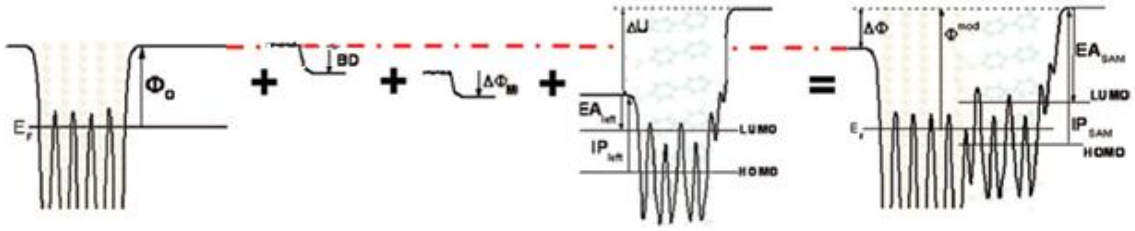

Figure 1.28. Work function change of a surface with original work function Φ_0 by surface modifier. Modified from Heimel, *et al.*[65]

While the magnitude of these factors can depend on the coverage, for the phosphonic acid/ITO system, the molecular dipole when using dipolar modifiers is the biggest contributor to the work function change,[63] and can be estimated by

Equation 1.3 $$\Delta\phi_{SD} = \frac{N\mu_z}{\varepsilon_{eff}\varepsilon_0}$$

where N is the surface coverage, μ_z is the interface dipole contribution from the modifier, projected along the normal axis, ε_0 is the vacuum permittivity and ε_{eff} is the effective dielectric constant, which accounts for the fact the $\mu_\perp$ is reduced relative to that calculated for isolated molecules as the coverage increases due to depolarization from the neighboring dipoles ($\varepsilon_{eff} = \mu_{z0}/\mu_z$).[63]

In an OLED, as seen in Figure 1.29, the ionization potential (IP) of the hole transport layer (HTL) is greater than the work function of the anode (ITO), which creates a barrier to hole injection (electron extraction from the HTL to the electrode). A dipolar modifier, such as a semifluorinated phosphonic acid, can change the energy level alignment. Further discussion is presented below, in conjunction with Figure 1.30.

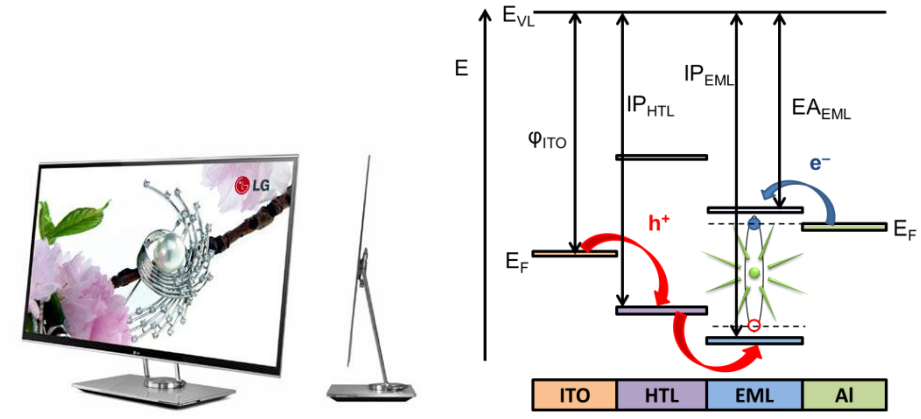

Figure 1.29 Left: LG OLED TV. Right: basic schematic for the operation of an OLED, with holes injected from the anode (ITO) into the hole transport layer (HTL), which can migrate to the emissive layer (EML) to form an exciton with the electrons injected from the cathode. The exciton may relax by emitting light corresponding to the band gap of the EML (minus the exciton binding energy).

Figure 1.30 presents a couple of different scenarios: In (A), an ITO electrode with an effective work function of *ca.* 4.5 eV, shows a difference in energy between its Fermi level and the HOMO of the HTL prior to contact; after electronic equilibrium has been achieved (B) through charge transfer between ITO and the HTL, there is a decrease in effective work function for ITO at the ITO/HTL interface, and movement of $E_{F,ITO}$ into the conduction band region, leading to an energy barrier for hole injection ΔE_{hole}. In (C), the ITO electrode has been modified with a dipolar small molecule modifier that possesses a strong dipole pointing away from the surface; this results in an increase of the vacuum level, and hence an increase in the work function of the ITO surface relative to the untreated ITO, which increases the effective work function for ITO at the ITO/HTL interface. Contact with the HTL (D) and alignment of the Fermi levels results in a decrease in the energy barrier for hole injection to $\Delta E'_{hole}$.

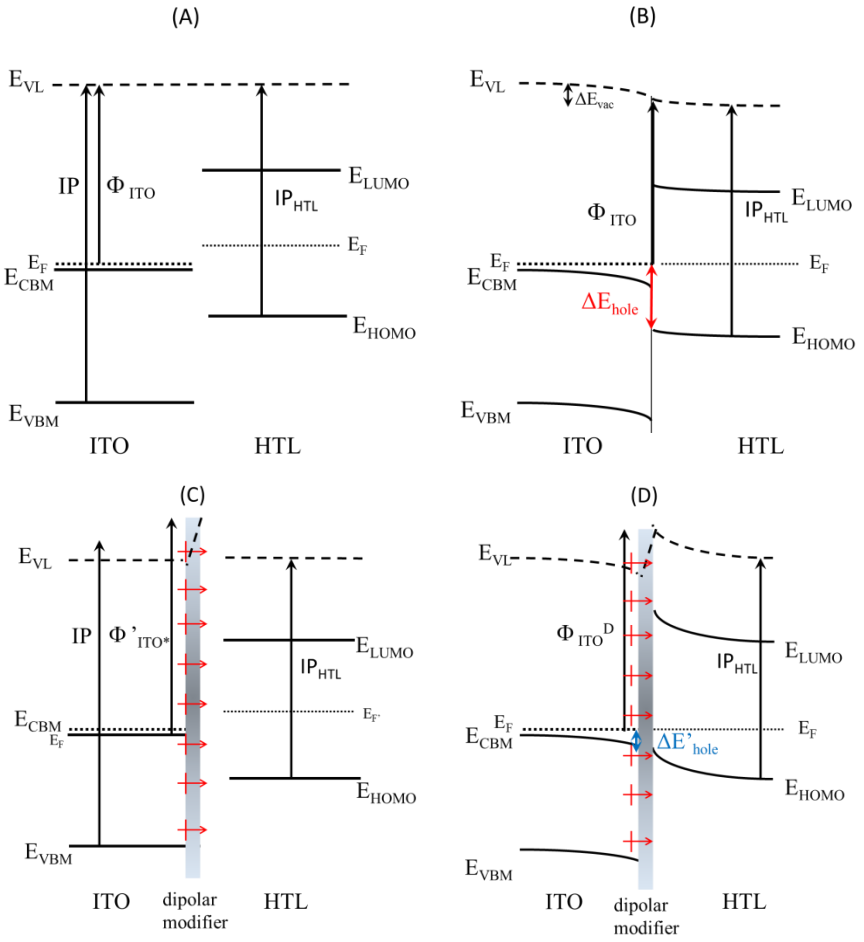

Figure 1.30 Schematic energy level diagrams for bare ITO (A) contacting a hole transport layer (B), and also the case where the ITO is modified with a dipolar modifier (C) and the effect on the energy level alignment (D). Before contact, the materials show flat bands, which bend upon contact to align Fermi levels. Reproduced from Hotchkiss, *et al.*[33]

1.6 Tuning the surface energy of TCOs: interface modification to promote adhesion and stability

Semiconducting polymers for OPVs or OLEDs are solution processed onto ink-jet printing or stamping substrates coated with a conductive film (usually ITO) through spin casting, dip coating, techniques. A homogeneous, smooth, pinhole-free film with controlled thickness is desired. Good wetting by the solvent and the polymer with the substrate is needed. Phosphonic acids have been used to modify substrates to improve

wetting and adhesion not only for good film formation but for it to be stable over time and operation.[51]

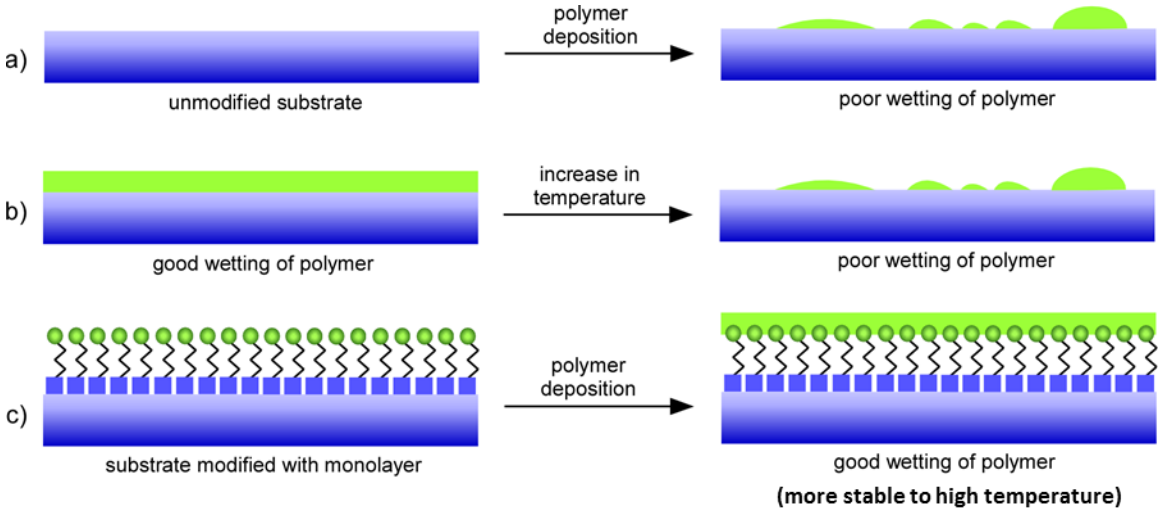

Figure 1.31 Wetting scenarios for a polymer (or other organic) deposited on a flat substrate. Reproduced from Hotchkiss, *et al*.[33]

The surface energy (γ) is a quantification of the imbalance of forces at a surface or interface. Surface energies of differently treated ITOs were previously studied by the author during his MS studies (Figure 1.32).[34] These can be obtained from contact angles with two liquids, and can be broken down into dispersive (instantaneous dipoles) and polar contributions (H bonds, dipole/dipole, induced dipole). There was a significant decrease in the surface energy upon phosphonic acids deposition with various R groups compared to that of plasma treated ITO. It was also possible to determine that the overall decrease in surface energy was mainly due to a decrease in the polar component of the surface energies, given that it is the tail groups which end up defining the wetting properties.

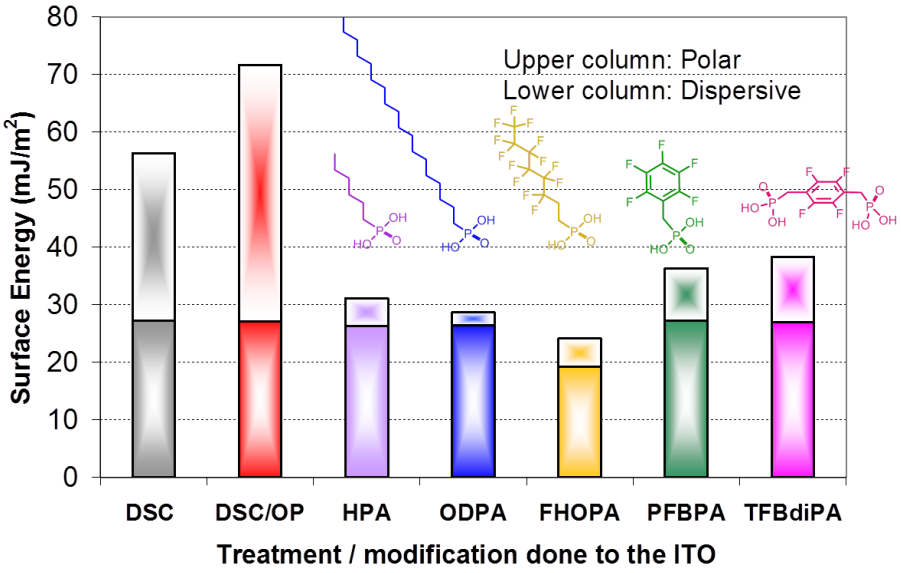

Figure 1.32 Surface energies (broken into polar and dispersive components) for ITO cleaned by scrubbing and sonication protocol (DSC), DSC followed by oxygen plasma, and different phosphonic acids after oxygen plasma pretreatment.

1.6.1 Examples of applications in organic electronics

There are numerous studies in which the principles discussed in the previous sections have been used to modify the electrodes of organic electronic devices with the goal of improving their performance. It is, however, difficult to separate the effects of work function and surface energy engineering because both are affected by monolayer deposition. In this section a small review of studies done by others is presented, where the effects from both work function and surface energy tuning are observed.

One of the earliest reports was that by Appleyard and coworkers for OLEDs,[66] where short-chain phosphonic acids with polar tail groups were used to modify ITO with the purpose of increasing the work function and, in this way, reduce the barrier for hole injection and increase built-in potential in a device consisting of *N,N'*-bis(3-methylphenyl)-*N,N*'-diphenyl-1,1'-biphenyl-4,4'-diamine (TPD) as hole transport layer and tris(quinolin-8-olato)aluminum (Alq_3) as electron transport layer. The phosphonic

acids were deposited from 0.1 mM methanol/chloroform solvent mixtures, and no characterization of the resulting film was provided other than work functions, which were measured via Kelvin probe, and were compared against that of solvent-cleaned ITO (Table 1.1). For a given voltage, the luminance and the external quantum efficiency is higher for the high work function anodes, and the turn on voltage lower than bare ITO.

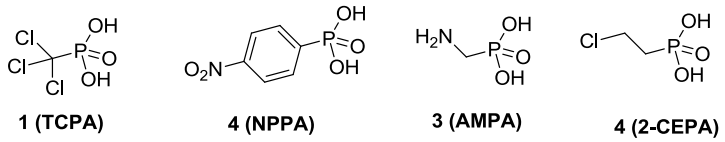

Figure 1.33 Structures and abbreviations of phosphonic acids used by Appleyard, *et al*.

Table 1.1 Calculated and measured work functions. The dipole moments were calculated using a semi-empirical Hartree-Fock geometry optimization and single point calculation at the PM3 level of approximation. From Appleyard, *et al*. [66]

Modifier	Work function change, $\Delta\phi$ /eV	Calculated dipole, $\mu_{mol\perp}$ /D	Calculated work function change, $\Delta\phi$ /eV
4-NPPA	0.303	5.73	0.720
TCPA	0.185	1.76	0.221
2-CEPA	0.179	1.69	0.212
AMPA	–0.140	–1.43	–0.179

Table 1.2 Characteristic device performance info using derivatized ITO-electrodes. Device structure: ITO|SAM|TPD|Alq_3|Al. From Appleyard, *et al*. [66]

Device	Threshold voltage/V	Max. luminance /cd m^{-2}/V	Device voltage @ 300 cd m^{-2}/V	Q.E. @ 300 cd m^{-2} (%)	L.E. @ 300 cd m^{-2}/lm W^{-1}
4-NPPA	2.0	13120@14 V	7.88	0.91	1.28
TCPA	2.0	9037@15.6 V	8.82	0.69	0.81
2-CEPA	4.0	7120@15.7 V	9.51	0.63	0.92
Bare	6.0	3640@20.5 V	13.60	0.61	0.56
AMPA	9.5	3010@20 V	15.50	0.46	0.30

Besbes and coworkers focused on the wettability of ITO after treatment with 2-chloroethylphosphonic acid (2-CEPA).[67] They characterized the resulting surface via contact angle using three probe liquids to break down contributions into dispersive, and

the acidic and basic subcomponents of the polar interaction. Treatment with 2-CEPA decreased the basic component relative to RCA-cleaned ITO. Solvent-cleaned ITO treated with 2-CEPA afforded the smallest threshold voltages in polymer light emitting diodes (PLEDs) using a PPV-derivative as emissive polymer, and displayed a space-charge limited behavior rather than injection-limited behavior without the modification.

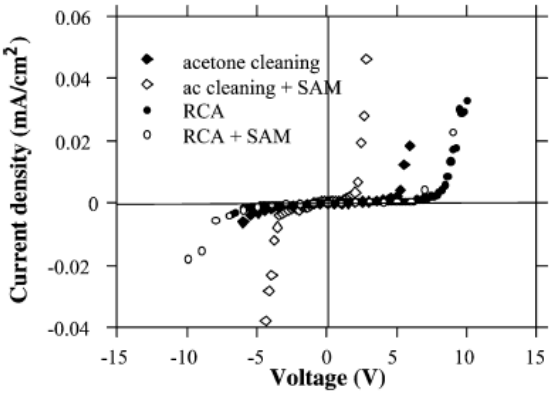

Figure 1.34 J/V characteristics of a one-layer PLED made with differently treated ITO: cleaned with acetone and RCA or modified with CEPA (labeled here as SAM). Reproduced from Besbes, *et al*.[67]

Schwartz and coworkers showed enhanced hole injection in OLEDs applying α-quarterthiophene-2-phosphonate (4TP) film on ITO via the T-BAG method mentioned above, and p-doped it with 2,3,5,6-tetrafluoro-7,7,8,8-tetracyanoquinodimethane (F_4-TCNQ). In a first publication, they applied this to *N,N'*-bis-(1-naphtyl)-*N,N'*-diphenyl-1,1-biphenyl-4,4'-diamine (α-NPD)/Alq_3 OLED.[31]

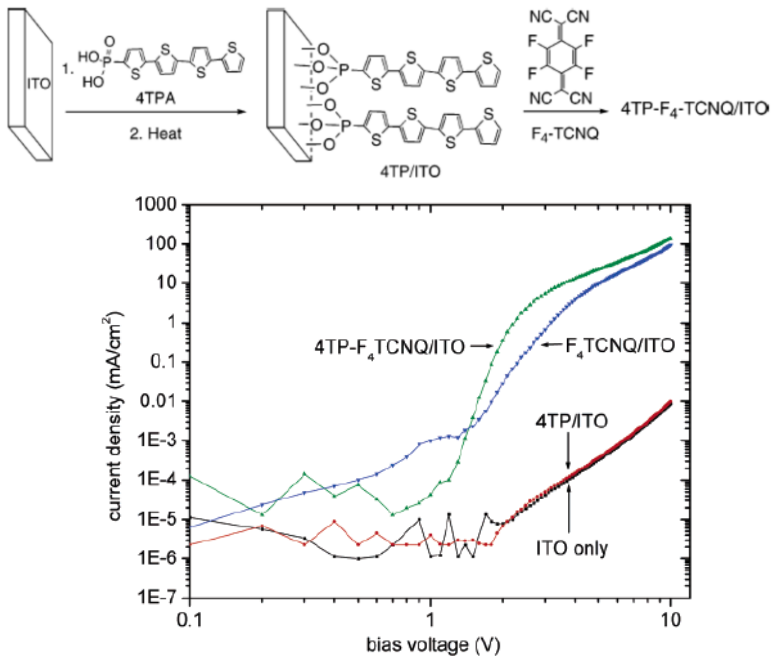

Figure 1.35 Modification of ITO with 4-TPA and subsequent doping, and comparison of the J/V characteristics of OLEDs made with the differently treated ITOs. Reproduced from Hanson, *et al*.[31]

A good comparison of the 4-TP-modified ITO used in a polymer light emitting dioded against ITO coated with the usual poly(3,4-ethylenedioxythiophene) poly(styrenesulfonate) (PEDOT:PSS) planarizing hole-transporting polymer, would be reported later.[68] They measured work functions and noticed that while the work function is higher for the PEDOT:PSS treated ITO, the current and luminance behavior were similar to that of the p-doped monolayer-treated ITO.

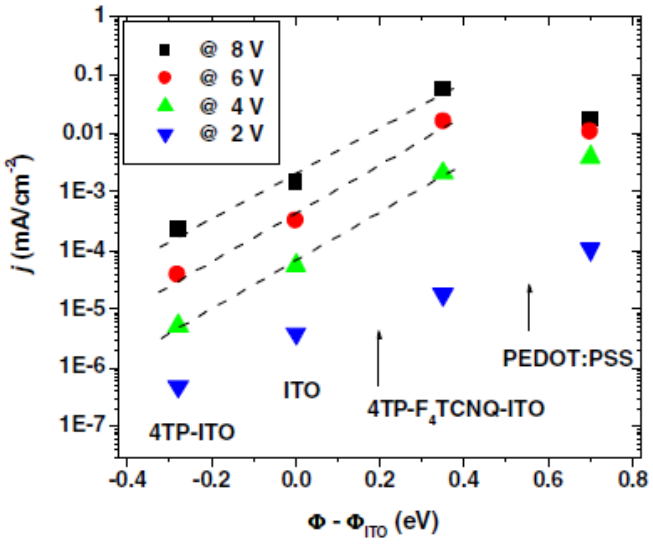

Figure 1.36 Relationship between currents for a given bias and anode used (bare ITO, phosphonic acid-coated ITO, p-doped phosphonic acid coated ITO and PEDOT:PSS coated ITO). Reproduced from Guo, *et al*.[68]

The Marder and Kippelen groups have also explored making devices using phosponic acid-modified ITO. In one study, the effect of applying a dipolar, semifluorinated phosphonic acid to increase the work function of ITO was examined.[51] While the work function was similar to that of air plasma treated ITO, it was much more stable over time in ambient conditions; this motivated lifetime studies which showed improved device stability in luminance and voltage needed to drive the device.

Table 1.3 Surface treatment on ITO and resulting work functions and contact angles with water. From Sharma, *et al*.[51]

	Surface modifier	Work function (eV)	Contact angle
	Untreated	4.6±0.02	4.6±3°
	Air plasma	5.4±0.06	<10°
OPA	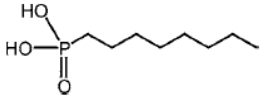	4.6±0.03	104±2°
FOPA	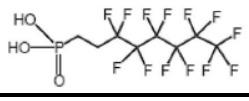	5.3±0.04	108±2°

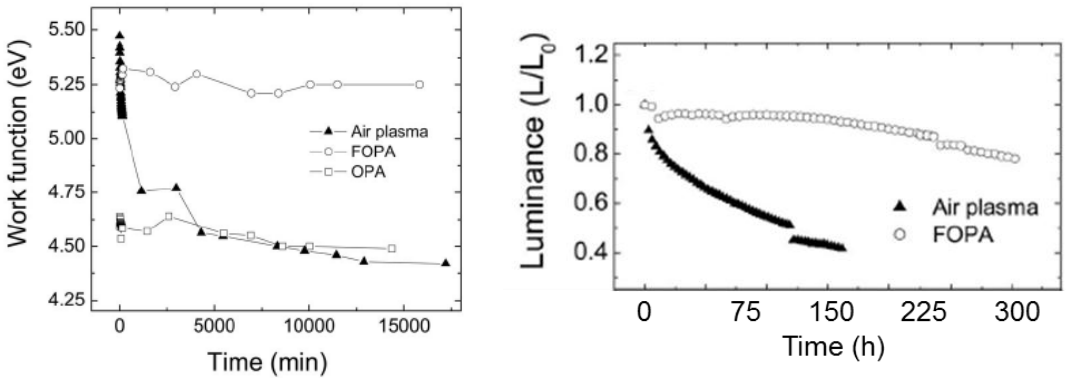

Figure 1.37 Using a semifluorinated alkyl phosphonic acid (FOPA), the work function and luminance in an OLED device are more stable than using an untreated ITO. Reproduced from Sharma, *et al*.[51]

1.7 Surface-initiated polymerization

Phosphonic acids can be used to incorporate reactive groups on a surface to serve as rectants in subsequent chemical reactions, including grafting of polymers.[69,70] In the following subsections, the general motivation for such an approach is presented, and a brief overview of the polymerization types is given, before moving in the next section to envisioned applications in organic electronics.

1.7.1 Coating substrates with polymers for organic electronics

Polymers have played a central role in the development of organic electronics. The 2000 Nobel Prize in Chemistry was awarded to Alan Heeger, Alan MacDiarmid and Hideki Shirakawa for the discovery and development of conductive polymers; their seminal work in the late 1970's has led to solution processable conductors and semiconductors,[71-73] used as electrodes and active materials in organic light emitting diodes (OLEDs), organic photovoltaics (OPVs) and organic field effect transistors (OFETs), to name a few technologies that make use of the properties of these remarkable materials. Besides processability, the ability to make ultra-thin, flexible devices with less

stringent purity requirements than traditional semiconductor technology is appealing. Non-conjugated polymers have also been of importance when insulating materials are needed, such as the case of capacitors, the dielectric in field effect transistors, encapsulants, matrices, diluents, and substrates.

With the traditional solution-processing techniques, the polymers are adsorbed only by physical interactions, with the limitations that the films can be destroyed by delamination, desorption by solvent or displacement by other molecules. In recent years, the use of *grafting to* and *grafting from* approaches has extended due to potential benefits of having a covalent attachment: it can alleviate the problems associated with having only physical interactions with the substrate, and allows for polymer deposition on non-flat surfaces and particles (Figure 1.38).[74]

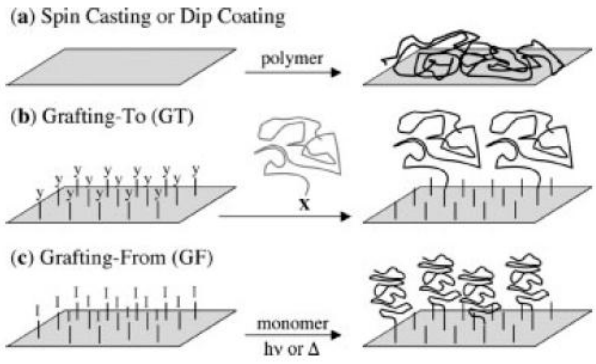

Figure 1.38 Approaches for modifying inorganic substrates with organic polymers. Reproduced from Dyer.[74]

1.7.2 Grafting polymers to the surface

Grafting of polymers *to* substrates involves having a functionality on the surface of the substrate that will react with a functionality on the polymer to which it will be exposed. Under appropriate conditions, the polymer will covalently attach to the surface through that moiety. While the grafting to approach offers the possibility of pre-building the polymer with good control of the process (in a typical homogeneous polymerization),

the steric hindrance due to the random coil conformation limits accessibility to reach the surface and react. Hence, the grafting density is low.[75] At low surface concentrations, the chains lie on the surface and form a "pancake" structure, where thicknesses will rarely be above a couple of nm. If increased graft density could be achieved so that the mean distance "*d*" between attachment sites was smaller than the average random coil diameter D_m, the conformation would assimilate a mushroom structure. Unfortunately, this is very unlikely to happen in the "grafting to" methodology.

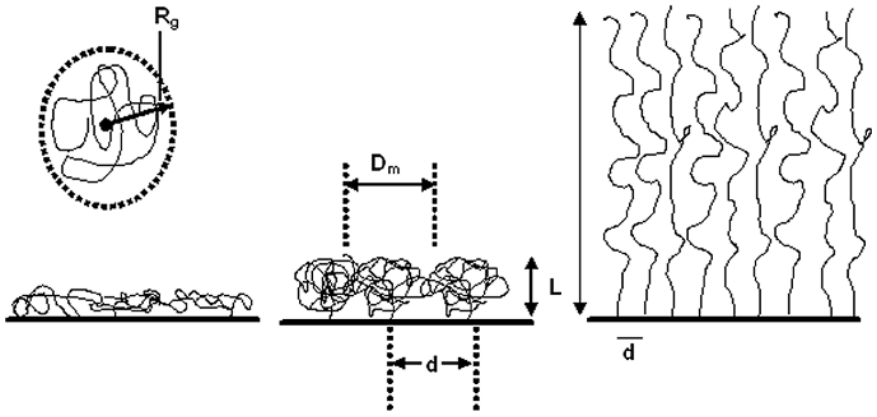

Figure 1.39 Models comparing conformation of random coil (top left) and grafted chains as a function of grafting density (d) on a surface. Conformation changes from pancake to mushroom to brush. Reproduced from LeMieux, *et al*.[76]

1.7.3 Grafting polymers from the surface (surface initiated polymerization)

To discuss the grafting *from* strategy, it is necessary to first examine how polymers are made: methods can be divided into two different approaches. In step-growth polymerizations, there is formation of dimers, followed by trimers, then longer oligomers, and finally long chain polymers in a stepped way such that the degree of polymerization is low until the reaction is close to completion (~90%). Every molecular species can react with another one, so the monomer is quickly consumed. There is only one type of reaction throughout (excluding possible side reactions). While a reactive group could be placed on the surface, there would be no kinetic or thermodynamic

preference for the monomers to react with that surface functionality over other reacting groups in solution; in fact, it would be less likely to react with the surface-bound species given the reduced degrees of freedom.

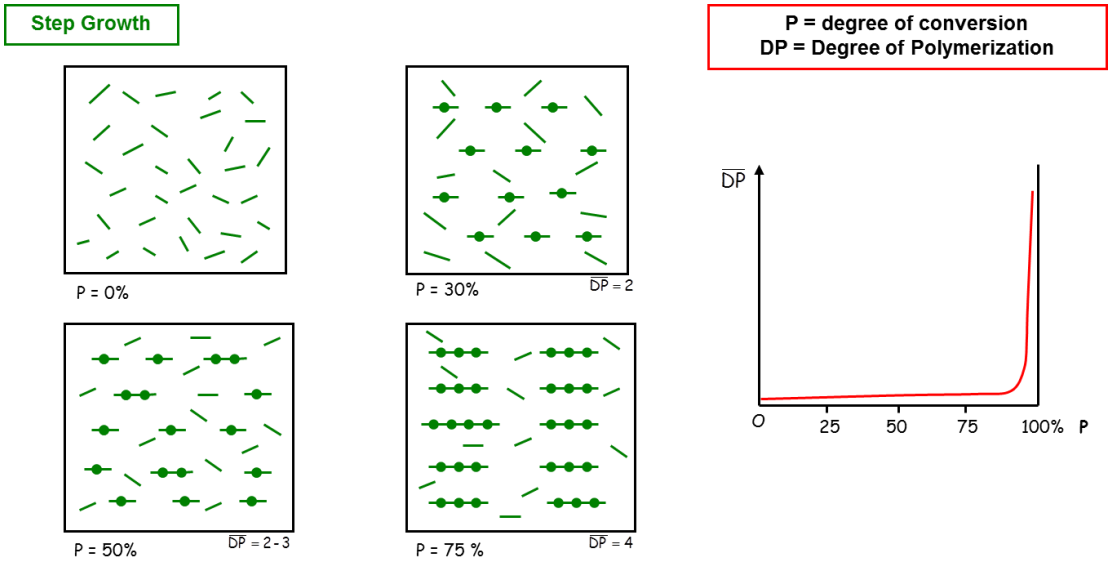

Figure 1.40 Schematic for step-growth polymerization and degree of polymerization with as a function of conversion % (P). Figure courtesy of Gäelle Deshayes.

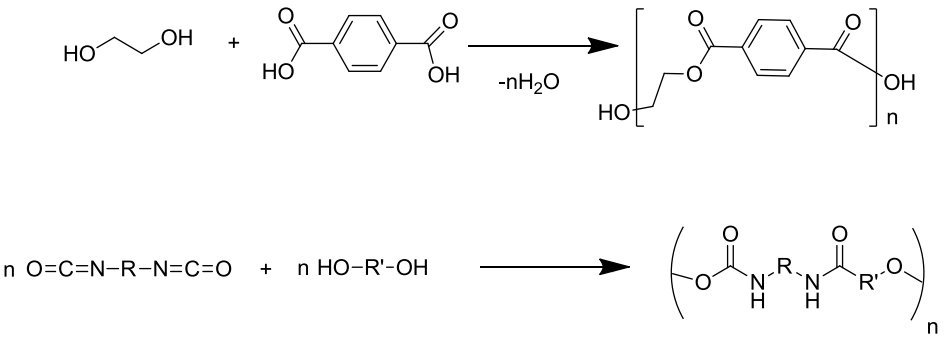

Figure 1.41 Synthesis of polyethylene terephthalate and a polyurethane through condensation and addition (step growth).

In the chain-growth mechanism, initiation of polymerization occurs through external activation of the monomers; the monomer concentration will decrease

progressively as the chains grow, and high molecular weights can be obtained even at low conversion. A general representation is:

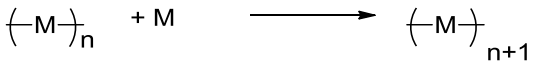

Each polymer molecule increases in size at a rapid rate once its growth has started, and the mechanisms and rates of reactions that initiate, propagate and terminate polymer growth are different.

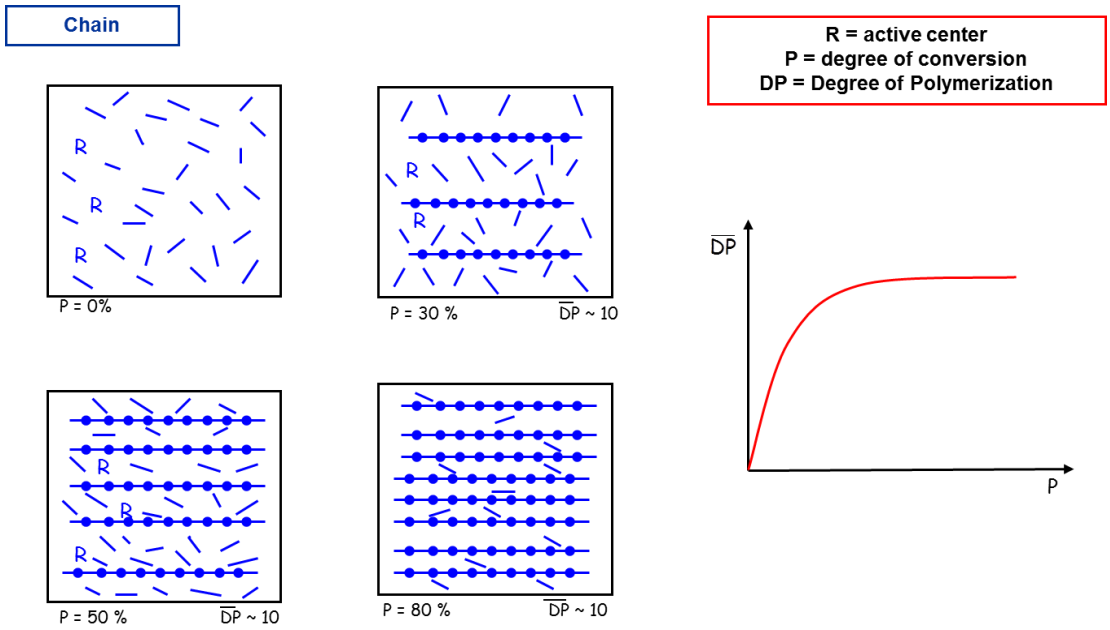

Figure 1.42 Schematic for chain growth polymerization and degree of polymerization as a function of conversion % (P). Figure courtesy of Gäelle Deshayes.

In this case, if the initiating species is only present on the surface and side reactions are eliminated through proper conditions, long chains of polymers could be grown from the surface, being able to afford high grafting densities since there would be no significant hindrance for monomers to reach the propagating site if growth occurs

simultaneously from all initiating species.[77] This could place the polymer in the mushroom conformation, or even form a polymer brush, with the chains mostly aligned perpendicular to the surface (Figure 1.43).

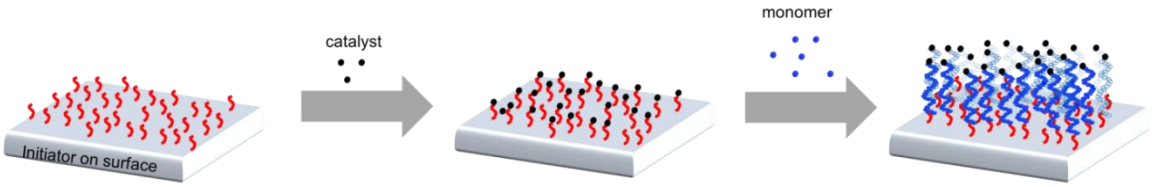

Figure 1.43 Scheme for surface initiated polymerization from a surface to produce polymer brushes.

1.8 Applications of polymer grafts to organic electronic devices

1.8.1 Surface-initiated polymerization from $BaTiO_3$ nanoparticles for composite dielectrics

In its simplest form, a capacitor is a device that stores energy in the form of separated charges across a dielectric medium that is placed between two electrodes. The dielectric is an insulator that polarizes in the presence of an electric field, and in the process it stores energy electrostatically that can be released upon connection to a load. In contrast to batteries, no chemical reaction is involved in the storage/release of energy.

In the case of linear dielectrics, the maximum energy *density* U_{max} that can be stored in a capacitor depends on the relative permittivity of the dielectric, ε_r, and the breakdown field, E_B, which is the electric field (voltage over thickness) that the device can support for charging, above which the dielectric becomes conductive.

Equation 1.4 $$\boldsymbol{U_{max} = \frac{1}{2}\varepsilon_0\varepsilon_r E_B{}^2}$$

For most applications, a compromise between weight, size and energy density has to be achieved, so research is being done to miniaturize capacitors, reduce their weight/volume and process them in new ways. Metal oxides are one commonly used class of dielectrics, often utilized for transistors and capacitors. Among these, barium titanate (BTO) thin films with dielectric constants (ε_r) of ~2500 can be obtained through a somewhat complex process involving chemical solution deposition followed by high temperature sintering (900 °C) and reoxidation.[78] Nonetheless, the breakdown field is very low, and the processing conditions are not compatible with flexible substrates. On the other hand, polymer-based dielectrics typically have good processability and high dielectric strengths, but suffer from low permittivity which limits their storage capacity.[79] For dielectrics in high capacitance OFETs and flexible capacitors, a hybrid approach combining inorganic oxides and organic materials is suitable, as it can potentially take advantage of the high permittivity of the inorganic inclusions as well as the high breakdown strength, mechanical flexibility, and solution processability of the organic polymers.[79,80]

Within the Center for Organic Photonics and Electronics (COPE) at Georgia Tech, the approach in this line of research has been to use BTO nanoparticles (which possess dielectric constants of up to ~150 when bare) that have been surface modified with phosphonic acids that show affinity for dielectric polymers, ball mill (mix via grinding) the polymer and nanoparticles for 12 days to make a dispersion, and spin coat a composite of materials on the substrate affording films with homogeneous nanoparticle dispersions.[79,81,82] Good devices have been obtained with this approach, as for instance an ε_r of 37±2 (@1 kHz) has been obtained with a perfluorinated phosphonic acid modified BTO (50%) + p(VDF-HFP) (*aka* Viton) (50%) mixture, with high energy density storage.[79] Nonetheless, there is still room for improvement in breakdown field and energy storage, which can be achieved by preventing particle-particle contact and reducing voids.

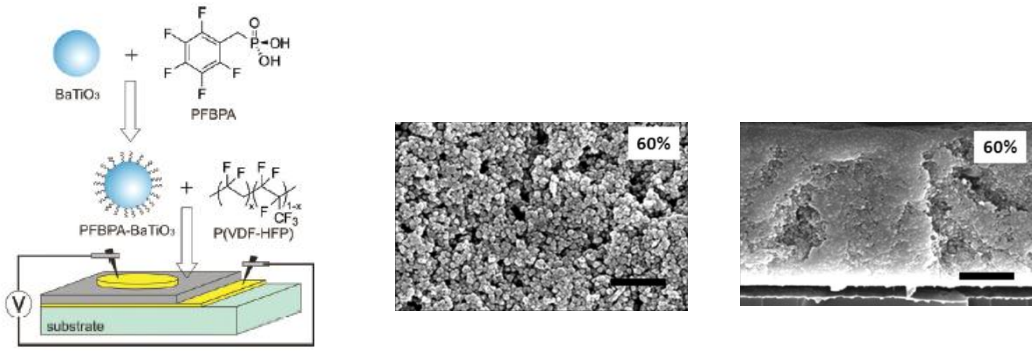

Figure 1.44 Hybrid dielectric composed of phosphonic acid modified $BaTiO_3$ nanoparticles mixed with viton polymer deposited on metallic substrate to use as a capacitor. Top view and cross section SEM images are shown for 60% v/v $BaTiO_3$ in polymer. Scale bars are 1 μm.[82]

If the polymeric component of the hybrid material were to be grown from the nanoparticles instead of mixed in, with homogeneous growth and sufficient thickness to prevent breakdown paths, it could lead to enhancements in breakdown field.[83] It could also ease the processing since there would be no compatibilization required with the polymer matrix since this would be grown from the nanoparticles: a one component system, with two constituents (the nanoparticles covalently attached to the polymer). Surface-initiated polymerization can occur by several means, including free radical, cationic, anionic, and ring opening metathesis, among others. Within this list, atom transfer radical polymerization (ATRP) is currently one of the most popular methods,[84] and there is a version of it in which the activators are regenerated by electron transfer (ARGET ATRP)[85], which offers several advantages and interesting properties:

- Provides continuous controlled polymerization
- Constant regeneration of the Cu(I) activator by reducing agent
- Catalyst levels decreased to ppm from parts per thousands in regular ATRP
- Side reactions of monomer radical with Cu(II), which affect formation of high molecular weight polymers, are limited

- Can be done in limited presence of air.

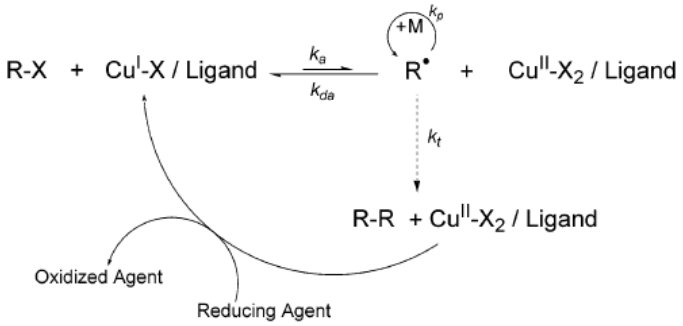

Figure 1.45 Mechanism proposed by Matyjaszewski, *et al.* for ARGET ATRP. Reproduced from Jakuboswki, *et al.*[85]

Chapter 3 of this thesis focuses on the synthesis of BTO-non conjugated polymers using ARGET ATRP in phosphonic acid monolayer initiated polymerization, as schematically summarized in Figure 1.46.

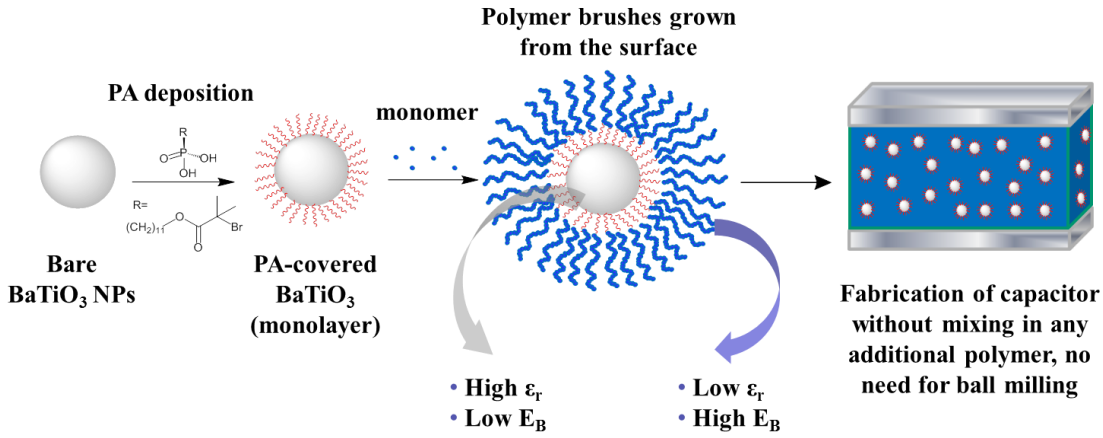

Figure 1.46 Scheme for creation of a one component, three-constituent hybrid dielectric that can be used to build capacitors.

1.8.2 Growing polythiophenes from the ITO surface

Polythiophene films are used as active layers or hole-transport layers in organic solar cells, and as semiconductors in organic field-effect transistors.[86,87] Covalent attachment of a polymer to its substrate may preclude delamination over time and provide

increased thermal stability.[88] The polymer properties can be (beneficially) different from those obtained by solution processing: polythiophene brushes grown from ITO may possess desirable optical and electrical properties for OPV applications. It has been suggested that the performance of organic solar cells employing polythiophenes may be increased through better organization of the nanoscale morphology of the donor / acceptor heterojunction,[89] and that having the molecular semiconductor covalently attached to the anode should be highly efficient at collecting charge.[90]

The Luscombe group at the University of Washington has made progress toward external initiation of homogeneous polymerization of high regioregularity poly(3-hexylthiophene), P3HT, by Kumada catalyst-transfer polymerization.[91] They noticed that a ligand exchange can be used in order to initiate the polymerization from a catalyst complex that will give a controlled polymerization. For example, using bidentate ligands optimized the rates of oxidative addition, transmetallation, and reductive elimination.[92] Their best results have been with 2-chlorotoluene as initiator, with the ligand 1,3-bis(diphenylphosphino)propane (dppp), which gave 100% initiation, 100% regioregularity, a PDI of 1.2 and an M_n (9.8 kDa, GPC) very close to the expected 10.5 kDa.[91]

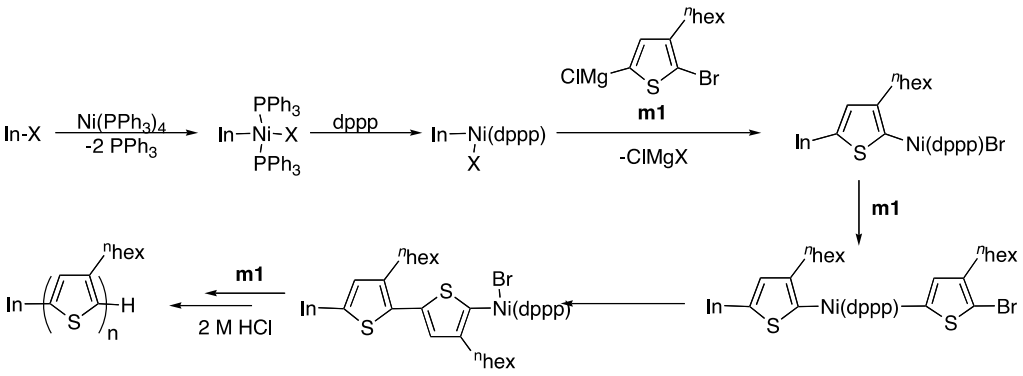

Figure 1.47 Kumada Catalyst-Transfer Polymerization from halogenated initiator (In-X).[93]

Collaborative efforts with the Luscombe group to study if external initiation could be done with tailored-made phosphonates and ITO surfaces modified with phosphonic

acids are discussed in Chaper 4, including design and synthesis of initiators, monolayer depositions, polymerization attempts, and XPS analysis of intermediates involved. If the methodology were to be perfected, one could think of building excitonic solar cells where the donor would be grown from the TCO, the acceptor material added in, and the top electrode deposited to complete a device (Figure 1.48). This could have interesting properties, including a) higher stability and highly efficient charge collection due to the all covalent attachment of the first organic layer, b) having to not to worry about orthogonal solvents for deposition of subsequent layers to avoid dissolution, and c) the possibility of new morphologies.

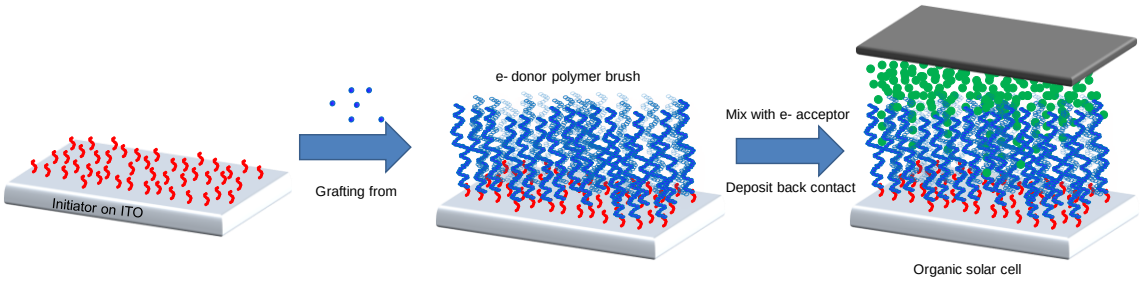

Figure 1.48. Scheme for surface initiated polymerization from a TCO, with potential applications to organic solar cells.

1.9 Doping of graphene for electrode applications

1.9.1 Background on graphene

The most common form of carbon on earth is graphite, which consists of stacked sheets of carbon in a hexagonal structure. Graphene is the name given to a single sheet: a two-dimensional, one atom-thick layer of sp^2-hybridized carbon. This recently isolated material has a number of unique properties, attracting interest of scientists and engineers, and even the general public, since the Nobel Prize in Physics 2010 was awarded to Geim and Novoselov, who succeeded in producing, isolating, identifying and characterizing the material in 2004 and 2005.[94,95] The other stable allotropes of carbon can be thought of as

derived from graphene, such as nanotubes (rolled into cylinders) and fullerenes (folded into ball-like structures).

The in-plane conductivity of high quality graphene is comparable to that of copper (~10^7 $\Omega^{-1}cm^{-1}$), while its thermal conductivity is more than 10 times higher than copper. Its tensile strength is approximately 100 times that of hypothetical monolayer steel. Since graphene is only a monolayer thick, it is almost transparent (97 % throughout the visible range),[96] and is very light, with a density of only 0.77 mg/m^2.[97] The reason behind these striking properties can be traced back to its 2D conformation and its electronic structure. Given the periodicity, the band structure of graphene is usually discussed as an energy *vs.* momentum (reciprocal space) graph (Figure 1.49b). The Fermi surface consists of six double cones, with the Fermi level right at the intersection of the cones. A density of states can be calculated by summing over the upper and lower bands in a unit cell (Figure 1.49c). Around the K points, the dispersion relation for electrons and holes is linear as shown in Equation 1.5, with a proportionality constant that includes the Fermi velocity υ_F –the speed of electrons in graphene, which is 1/300th that of light.[95] Hence, it is common to represent the band structure of graphene close to the Dirac point as in Figure 1.50.

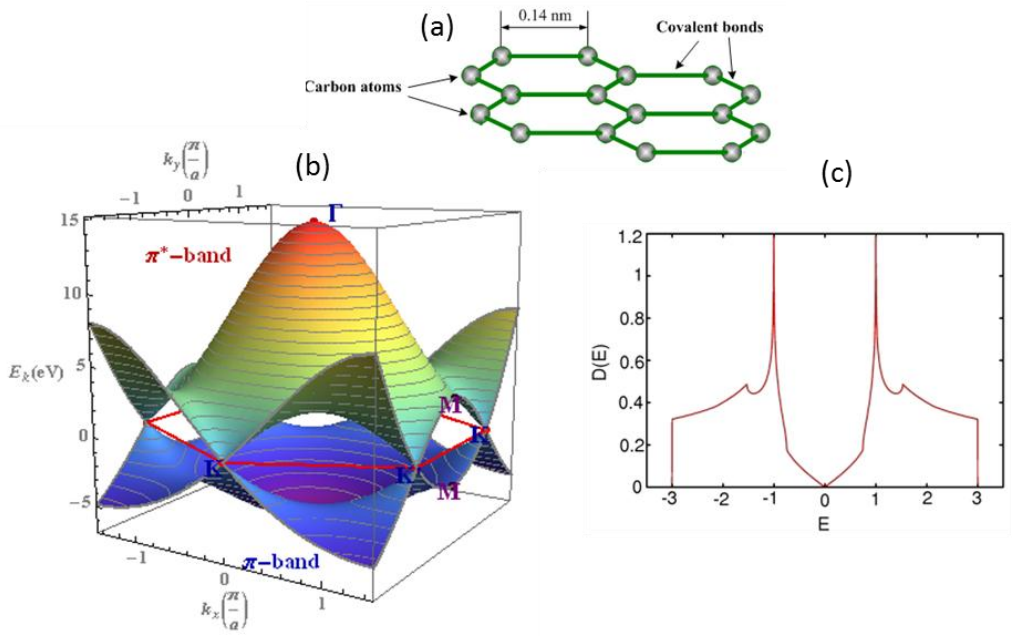

Figure 1.49 a) Schematic of a section of a graphene sheet. (b) π/ π* bands structure in graphene.[98] (c) Calculated density of states for graphene. From Laughlin.[99]

Equation 1.5 $$E_{\pm}(k) \approx \hbar v_F |k - K|$$

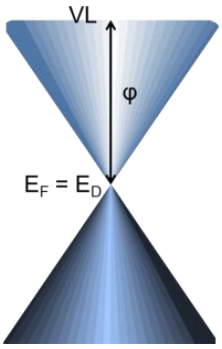

Figure 1.50 Cone representation of π/ π* bands centered at the K points (*e.g.* $k_x = 0$, $k_y = 2\pi/a$); work function φ is shown as the separation between Fermi level E_F (at the same energy as the Dirac point E_D for the undoped state) and the vacuum level VL.

The first reports from Geim and Novoselov involved graphene exfoliated from graphite using sticky tape and deposited onto an atomically flat surface for measurements.[94] Other methods for producing graphene have surfaced since, including

epitaxial growth from SiC,[100] liquid phase exfoliation,[101] reduction of graphene oxide,[102] molecular assembly from small molecules,[103] and chemical vapor deposition (CVD).[104]

1.9.2 Application as electrode

Although ITO is the dominant material used in transparent conductive films, many companies are looking to replace it for several reasons: the supply of indium is unreliable, leading to large price surges;[105] ITO is brittle, degrades over time (particularly in touchscreens), and is not as flexible as would be ideal for future applications. Graphene has recently emerged as a potential alternative to ITO, and its use as a conductive film is likely its first commercial application. Its remarkable conductivity originates in its band structure, which resembles that of a metal in that the π valence band meets the π* conduction band, with no band gap. Besides, the 97% percent transparency of a single sheet of graphene, its flexibility, low weight and cheap raw material makes it very appealing to use as a transparent electrode. [106]

Table 1.4 Comparison of emerging technologies to replace ITO. From Jo.[106]

Material	T(%)	R_S (Ω /□)	Status	Issue
ITO	>85	15–30	Standard	Cost, brittle, corrosion by salts or acids, slow vacuum process
Ag nanowire	>80	0.4–116	Commercialized, emerging	Roughness, environmental stability, haze, light scattering
CNT	90	50	Emerging	High resistance, doping stability, roughness
PEDOT:PSS	80	100	Limited use	Electrical/environmental stability, color tinge
Graphene (unoptimized)	85	400 or more	Emerging	High resistance, doping stability
Graphene (doped)	85	Less than 100	Emerging	More doping up to a few Ω /□, doping stability

As Table 1.4 points out, stable doping of graphene is needed to lower the sheet resistance to make it competitive with ITO and other emerging technologies. Table 1.5 shows that multi-layer stacks of CVD graphene can give sheet resistances as low as 300

Ω/□,[1] but commercially available ITO typically has sheet resistances as as 10 Ω/□. Just as for TCOs, the adjustment of work function for a particular device will be needed. In Chapter 5, doping of graphene using submonolayer adsorption of redox-active, solution-processable metal-organics is shown to increase its conductivity and adjust its work function while maintaining single-layer transparency. Making use of data acquired from multiple techniques, a molecular picture can be drawn, such as that in Figure 1.51.

Table 1.5 Comparison of key features for use as (transparent) electrode. Modified from Jo.[106]

Comparison	ITO	Graphene
Sheet resistance (Ω /□)[a]	As low as 10	~125 for best CVD
Transmittance (%)	90	~90
Thickness (nm)	100–200	1.3 (4 layers)
Failure strain %	2–3	>10
Manufacturing process	Sputtering	Coating, transfer, roll to roll

[a]Note that sheet resistance is the resistivity normalized by the thickness; ITO films are much thicker than graphene films.

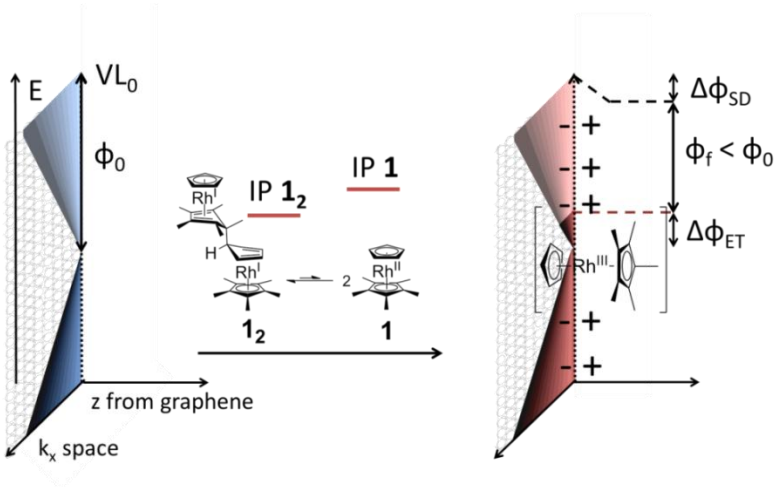

Figure 1.51 n-doping of CVD graphene through redox chemistry using a rhodocene dimer. Changes in electronic structure in reciprocal and real space are shown.

[1] Theoretically, the sheet resistance of a single graphene sheet, Rs_1, should be related to that of a multilayer film, Rs_n, via $Rs_n = Rs_1/n$ if all n layers are acting independently of each other; experimentally, while a decrease in resistance is observed when stacking layers, it is less than expected. Note that increasing the number of layers causes a concomitant decrease in transparency.

1.10 Overview and organization of the thesis

The introduction and background information put forward in this chapter served to introduce the studies presented in this thesis. While the systems probed vary through the thesis, all chapters share the multi-technique analytical characterization approach to gain a more comprehensive understanding of the interfaces involved.

In Chapter 2, entitled "Phosphonic acid adsorption on transparent conductive oxides", kinetic studies involving a prototypical phosphonic acid on ITO are presented, for which XPS, UPS and IRRAS are used to give a more complete picture of the results of different deposition protocols. Application of these protocols using the prototypical phosphonic acid as well as others to not only ITO but also solution processed NiO_x are presented. The chapter concludes with the results obtained in collaboration with the Graham group (Mechanical Engineering, Georgia Institute of Technology) on spray coating phsophonic acids.

Chapter 3 entitled "Grafting non-conjugated polymers via controlled radical polymerization from $BaTiO_3$ nanoparticles" dwells on process development of activator-regeneration by electron transfer (ARGET) atom transfer radical polymerization (ATRP) of styrene and methylmethacrylate for hybrid dielectric applications.

Chapter 4, "Surface-initiated Kumada Catalyst-Transfer Polymerization for growth of polythiophenes from ITO" incorporates the efforts towards surface initiated polymerization from ITO films, starting with the design and synthesis of initiators for growth of polythiophenes both in solution and from the surface, in conjunction with the efforts from the Luscombe group (Materials Science, University of Washington).

Chapter 5, with the self-explanatory title "Production of heavily n- and p-doped CVD graphene with solution-processed redox-active metal-organic species" not only presents the results from such treatments but also proposes plausible explanations for

them based on the characterization results from electrical measurements, photoemission and UV-Visible/IR spectroscopies.

Chapter 6, "Conclusions and outlook" summarizes the findings presented in this dissertation and brings forward some challenges for the deposition, characterization, and application of monolayers on nanoparticles, transparent conductive oxides and graphene for organic electronic applications.

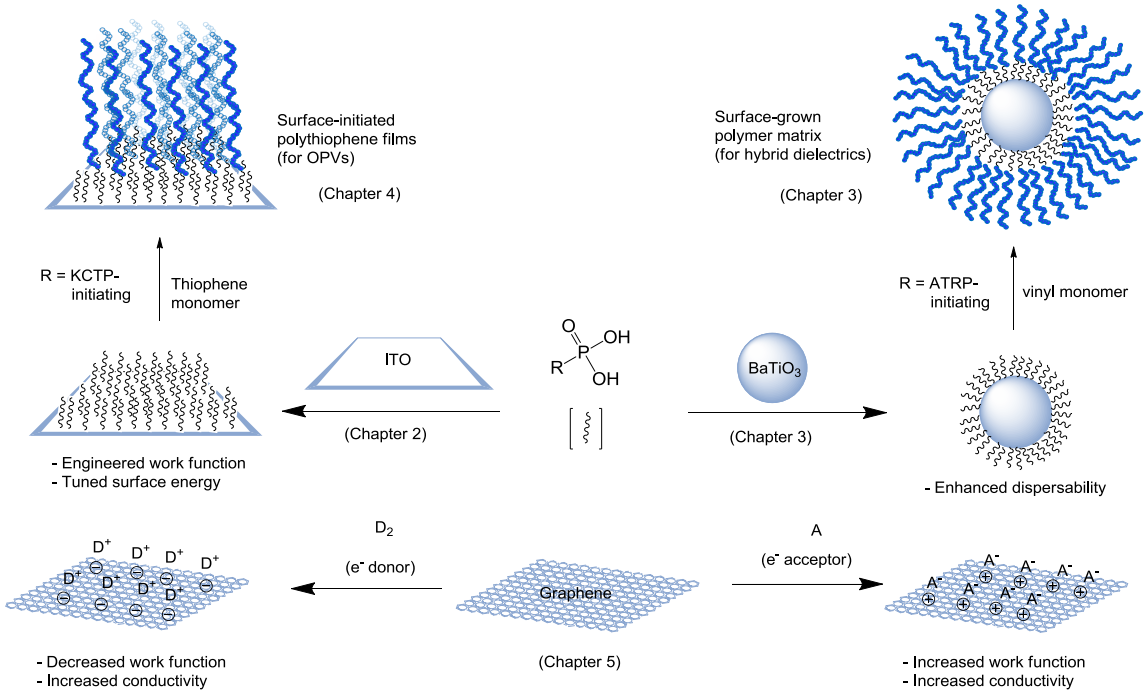

Figure 1.52 Organization of the thesis.

1.11 References

(1) Rosen, M. J.; Kunjappu, J. T. *Surfactants and Interfacial Phenomena (4th Edition)*; John Wiley & Sons: Hoboken, NJ, USA, 2012.

(2) White, J. M.; Campbell, C. T. *J. Chem. Educ.* **1980**, *57*, 471.

(3) Ebnesajjad, S. *Handbook of adhesives and surface preparation*; Elsevier: Amsterdam, 2011.

(4) Armstrong, N. R.; Veneman, P. A.; Ratcliff, E.; Placencia, D.; Brumbach, M. *Acc. Chem. Res.* **2009**, *42*, 1748.

(5) Wang, J.; Chen, H.; Sui, T.; Li, A.; Chen, D. *Plant Sci.* **2009**, *176*, 687.

(6) Sørensen, P. A.; Kiil, S.; Dam-Johansen, K.; Weinell, C. E. *J Coat Technol Res* **2009**, *6*, 135.

(7) pilkingtonselfcleaningglass.co.uk.

(8) Chevallier, P.; Turgeon, S. p.; Sarra-Bournet, C.; Turcotte, R. l.; Laroche, G. t. *ACS Appl. Mater. Interfaces* **2011**, *3*, 750.

(9) Shivapooja, P.; Wang, Q.; Orihuela, B.; Rittschof, D.; López, G. P.; Zhao, X. *Adv. Mater.* **2013**, *25*, 1430.

(10) Laibinis, P. E.; Whitesides, G. M. *J. Am. Chem. Soc.* **1992**, *114*, 1990.

(11) Ulman, A. *Chem. Rev.* **1996**, *96*, 1533.

(12) Peterson, I. R. *J. Phys. D: Appl. Phys.* **1990**, *23*, 379.

(13) Love, J. C.; Estroff, L. A.; Kriebel, J. K.; Nuzzo, R. G.; Whitesides, G. M. *Chem. Rev.* **2005**, *105*, 1103.

(14) Kolasinski, K. *Surface Science: Foundation of Catalysis and Nanoscience*; John Wiley & Sons Ltd.: Chichester, 2008.

(15) Hanson, E. L.; Schwartz, J.; Nickel, B.; Koch, N.; Danisman, M. F. *J. Am. Chem. Soc.* **2003**, *125*, 16074.

(16) Ganzorig, C.; Kwak, K. J.; Yagi, K.; Fujihira, M. *Appl. Phys. Lett.* **2001**, *79*, 272.

(17) Kim, C., O.; Hong, S. Y.; Kim, M.; Park, S. M.; Park, J. W. *J. Colloid Interface Sci.* **2004**, *277*, 499.

(18) Raman, A.; Quiñones, R.; Barriger, L.; Eastman, R.; Parsi, A.; Gawalt, E. S. *Langmuir* **2009**, *26*, 1747.

(19) Folkers, J. P.; Gorman, C. B.; Laibinis, P. E.; Buchholz, S.; Whitesides, G. M.; Nuzzo, R. G. *Langmuir* **1995**, *11*, 813.

(20) Maliakal, A.; Katz, H.; Cotts, P. M.; Subramoney, S.; Mirau, P. *J. Am. Chem. Soc.* **2005**, *127*, 14655.

(21) Textor, M.; Ruiz, L.; Hofer, R.; Rossi, A.; Feldman, K.; Hähner, G.; Spencer, N. D. *Langmuir* **2000**, *16*, 3257.

(22) *From xpsdata.com/Technique_limits_p1.pdf.*

(23) Haasch, R., mrl.illinois.edu/sites/default/files/AMC/downloads/AMC-Workshop-2012_Tutorial-3_XPS_AES.pdf.

(24) Tolstoy, V. P.; Chernyshova, I. V.; Skryshevsky, V. A. *Handbook of Infrared Spectroscopy of Ultrathin Films*; John Wiley & Sons, Inc.: New Jersey, 2003.

(25) Hayden, B. E. In *Vibrational Spectroscopy of Molecules on Surfaces*; Yates, J. T., Madey, T. E., Eds.; Plenum Press: New York, 1987, p 267.

(26) als-japan.com/we_what_is_cv.html.

(27) Stohr, J. *NEXAFS spectroscopy*; Springer: Berlin, 2003.

(28) Losego, M. D.; Guske, J. T.; Efremenko, A.; Maria, J.-P.; Franzen, S. *Langmuir* **2011**, *27*, 11883.

(29) Freedman, L. D.; Doak, G. O. *Chem. Rev.* **1957**, *57*, 479.

(30) Mutin, P. H.; Guerrero, G.; Vioux, A. *J. Mater. Chem.* **2005**, *15*, 3761.

(31) Hanson, E. L.; Guo, J.; Koch, N.; Schwartz, J.; Bernasek, S. L. *J. Am. Chem. Soc.* **2005**, *127*, 10058.

(32) Brodard-Severac, F.; Guerrero, G.; Maquet, J.; Florian, P.; Gervais, C.; Mutin, P. H. *Chem. Mater.* **2008**, *20*, 5191.

(33) Hotchkiss, P. J.; Jones, S. C.; Paniagua, S. A.; Sharma, A.; Kippelen, B.; Armstrong, N. R.; Marder, S. R. *Acc. Chem. Res.* **2011**, *45*, 337.

(34) Paniagua, S. A.; Hotchkiss, P. J.; Jones, S. C.; Marrikar, F. S.; Mudalige, A.; Pemberton, J. E.; Marder, S. R.; Armstrong, N. R. *J. Phys. Chem. C.* **2008**, *112*, 7809.

(35) Paramonov, P. B.; Paniagua, S. A.; Hotchkiss, P. J.; Jones, S. C.; Armstrong, N. R.; Marder, S. R.; Brédas, J. L. *Chem. Mater.* **2008**, *20*, 5131.

(36) Aswal, D. K.; Lenfant, S.; Guerin, D.; Yakhmi, J. V.; Vuillaume, D. *Anal. Chim. Acta* **2006**, *568*, 84.

(37) Howarter, J. A.; Youngblood, J. P. *Langmuir* **2006**, *22*, 11142.

(38) Baltazar, J.; Sojoudi, H.; Paniagua, S. A.; Kowalik, J.; Marder, S. R.; Tolbert, L. M.; Graham, S.; Henderson, C. L. *J. Phys. Chem. C* **2012**, *116*, 19095.

(39) Cui, J.; Huang, Q.; Wang, Q.; Marks, T. J. *Langmuir* **2001**, *17*, 2051.

(40) Lee, J.; Jung, B. J.; Lee, J. I.; Chu, H. Y.; Do, L. M.; Shim, H. K. *J. Mater. Chem.* **2002**, *12*, 3494.

(41) Plueddemann, E. P. *Silane coupling agents*; Plenum Press: New York, 1982.

(42) Carter, C.; Brumbach, M.; Donley, C.; Hreha, R. D.; Marder, S. R.; Domercq, B.; Yoo, S.; Kippelen, B.; Armstrong, N. R. *J. Phys. Chem. B* **2006**, *110*, 25191.

(43) Goh, C.; Scully, S. R.; McGehee, M. D. *J. Appl. Phys.* **2007**, *101*, 114503.

(44) O´Reagan, B.; Grätzel, M. *Nature* **1991**, *353*, 737.

(45) Giza, M.; Thissen, P.; Grundmeier, G. *Langmuir* **2008**, *24*, 8688.

(46) Thissen, P.; Valtiner, M.; Grundmeier, G. *Langmuir* **2009**, *26*, 156.

(47) Hauffman, T.; Blajiev, O.; Snauwaert, J.; van Haesendonck, C.; Hubin, A.; Terryn, H. *Langmuir* **2008**, *24*, 13450.

(48) Bardecker, J. A.; Ma, H.; Kim, T.; Huang, F.; Liu, M. S.; Cheng, Y.-J.; Ting, G.; Jen, A. K. Y. *Adv. Funct. Mater.* **2008**, *18*, 3964.

(49) Vercelli, B.; Zotti, G.; Schiavon, G.; Zecchin, S.; Berlin, A. *Langmuir* **2003**, *19*, 9351.

(50) Sharma, A.; Haldi, A.; Potscavage Jr, W. J.; Hotchkiss, P. J.; Marder, S. R.; Kippelen, B. *J. Mater. Chem.* **2009**, *19*, 5298.

(51) Sharma, A.; Kippelen, B.; Hotchkiss, P. J.; Marder, S. R. *Appl. Phys. Lett.* **2008**, *93*, 163308.

(52) Sharma, A.; Haldi, A.; Hotchkiss, P. J.; Marder, S. R.; Kippelen, B. *J. Appl. Phys.* **2009**, *105*, 074511.

(53) Sharma, A.; Hotchkiss, P. J.; Marder, S. R.; Kippelen, B. *J. Appl. Phys.* **2009**, *105*, 084507.

(54) Queffélec, C.; Petit, M.; Janvier, P.; Knight, D. A.; Bujoli, B. *Chem. Rev.* **2012**, *112*, 3777.

(55) Yaglioglu, B.; Huang, Y. J.; Yeom, H. Y.; Paine, D. C. *Thin Solid Films* **2006**, *496*, 89.

(56) Fan, J. C. C.; Goodenough, J. B. *J. Appl. Phys.* **1977**, *48*, 3524.

(57) Nadaud, N.; Lequeux, N.; Nanot, M.; Jové, J.; Roisnel, T. *J. Solid State Chem.* **1998**, *135*, 140.

(58) Brumbach, M.; Veneman, P. A.; Marrikar, F. S.; Schulmeyer, T.; Simmonds, A.; Xia, W.; Lee, P.; Armstrong, N. R. *Langmuir* **2007**, *23*, 11089.

(59) Woodward, J. T.; Doudevski, I.; Sikes, H. D.; Schwartz, D. K. *J. Phys. Chem. B* **1997**, *101*, 7535.

(60) Woodward, J. T.; Schwartz, D. K. *J. Am. Chem. Soc.* **1996**, *118*, 7861.

(61) Chen, X.; Luais, E.; Darwish, N.; Ciampi, S.; Thordarson, P.; Gooding, J. J. *Langmuir* **2012**, *28*, 9487.

(62) Sze, S. M.; Ng, K. K. *Physics of semiconductors*; 3rd. ed.; Wiley Interscience: New Jersey, 2006.

(63) Li, H.; Paramonov, P.; Bredas, J.-L. *J. Mater. Chem.* **2010**, *20*, 2630.

(64) Veinot, J. G. C.; Marks, T. J. *Acc. Chem. Res.* **2005**, *38*, 632.

(65) Nie, H. Y.; Walzak, M. J.; McIntyre, N. S. *Langmuir* **2002**, *18*, 2955.

(66) Appleyard, S. F. J.; Day, S. R.; Pickford, R. D.; Willis, M. R. *J. Mater. Chem.* **2000**, *10*, 169.

(67) Besbes, S.; Ltaief, A.; Reybier, K.; Ponsonnet, L.; Jaffrezic, N.; Davenas, J.; Ben Ouada, H. *Synth. Met.* **2003**, *138*, 197

(68) Guo, J.; Koch, N.; Bernasek, S. L.; Schwartz, J. *Chem. Phys. Lett.* **2006**, *426*, 370.

(69) Pahnke, J.; Rühe, J. *Macromol. Rapid Commun.* **2004**, *25*, 1396.

(70) Griep-Raming, N.; Karger, M.; Menzel, H. *Langmuir* **2004**, *20*, 11811.

(71) Shirakawa, H. *Angew. Chem. Int. Ed.* **2001**, *40*, 2574.

(72) Heeger, A. J. *Angew. Chem. Int. Ed.* **2001**, *40*, 2591.

(73) MacDiarmid, A. G. *Angew. Chem. Int. Ed.* **2001**, *40*, 2581.

(74) Dyer, D. J. *Adv. Funct. Mat.* **2003**, *13*, 667.

(75) Granville, A. M.; Brittain, W. J. In *Polymer Brushes*; Advincula, R. C., Brittain, W. J., Caster, K. C., Rühe, J., Eds.; Wiley-VCH: Weinheim, 2004.

(76) LeMieux, M. C.; Usov, D.; Minko, S.; Stamm, M.; Tsukruk, V. V. In *Polymer Brushes*; Advincula, R. C., Brittain, W. J., Caster, K. C., Rühe, J., Eds.; Wiley-VCH: Weinheim, 2004.

(77) Radhakrishnan, B.; Ranjan, R.; Brittain, W. J. *Soft Matter* **2006**, *2*, 386.

(78) Ilhefeld, J.; Laughlin, B.; Hunt-Lowery, A.; Borland, W.; Kingon, A.; Maria, J.-P. *J. Electroceram.* **2005**, *14*, 95.

(79) Kim, P.; Jones, S. C.; Hotchkiss, P. J.; Haddock, J. N.; Kippelen, B.; Marder, S. R.; Perry, J. W. *Adv. Mater.* **2007**, *19*, 1001.

(80) Ponce-Ortiz, R.; Facchetti, A.; Marks, T. J. *Chem. Rev.* **2009**, *110*, 205.

(81) Kim, P.; Zhang, X. H.; Domercq, B.; Jones, S. C.; Hotchkiss, P. J.; Marder, S. R.; Kippelen, B.; Perry, J. W. *Appl. Phys. Lett.* **2008**, *93*, 013302.

(82) Kim, P.; Doss, N. M.; Tillotson, J. P.; Hotchkiss, P. J.; Pan, M.-J.; Marder, S. R.; Li, J.; Calame, J. P.; Perry, J. W. *ACS Nano* **2009**, *3*, 2581.

(83) Guo, N.; DiBenedetto, S. A.; Kwon, D.-K.; Wang, L.; Russell, M. T.; Lanagan, M. T.; Facchetti, A.; Marks, T. J. *J. Am. Chem. Soc.* **2007**, *129*, 766.

(84) Braunecker, W. A.; Matyjaszewski, K. *Prog. Polym. Sci.* **2007**, *32*, 93.

(85) Jakubowski, W.; Min, K.; Matyjaszewski, K. *Macromolecules* **2006**, *39*, 39.

(86) Günes, S.; Neugebauer, H.; Sariciftci, N. S. *Chem. Rev.* **2007**, *107*, 1324.

(87) Arias, A. C.; MacKenzie, J. D.; McCulloch, I.; Rivnay, J.; Salleo, A. *Chem. Rev.* **2010**, *110*, 3.

(88) Kawakami, A.; Katsuki, K.; Advincula, R. C.; Tanaka, K.; Ogino, K.; Usui, H. *Jpn. J. Apply. Phys.* **2008**, *47*, 3156.

(89) Khanduyeva, N.; Senkovskyy, V.; Beryozkina, T.; Horecha, M.; Stamm, M.; Uhrich, C.; Riede, M.; Leo, K.; Kiriy, A. *J. Am. Chem. Soc.* **2008**, *131*, 153.

(90) Snaith, H. J.; Whiting, G. L.; Sun, B.; Greenham, N. C.; Huck, W. T. S.; Friend, R. H. *Nano Lett.* **2005**, *5*, 1653.

(91) Bronstein, H. A.; Luscombe, C. K. *J. Am. Chem. Soc.* **2009**, *131*, 12894.

(92) Doubina, N.; Ho, A.; Jen, A. K. Y.; Luscombe, C. K. *Macromolecules* **2009**, *42*, 7670.

(93) Doubina, N.; Paniagua, S. A.; Soldatova, A. V.; Jen, A. K. Y.; Marder, S. R.; Luscombe, C. K. *Macromolecules* **2011**, *44*, 512.

(94) Novoselov, K. S.; Geim, A. K.; Morozov, S. V.; Jiang, D.; Zhang, Y.; Dubonos, S. V.; Grigorieva, I. V.; Firsov, A. A. *Science* **2004**, *306*, 666.

(95) Novoselov, K. S.; Geim, A. K.; Morozov, S. V.; Jiang, D.; Katsnelson, M. I.; Grigorieva, I. V.; Dubonos, S. V.; Firsov, A. A. *Nature* **2005**, *438*, 197.

(96) Mak, K. F.; Ju, L.; Wang, F.; Heinz, T. F. *Solid State Commun.* **2012**, *152*, 1341.

(97) *The Nobel Prize in Chemistry 2010 Advanced Information- The Royal Swedish Academy of Sciences*.

(98) *Wolfram Demonstrations Project. demonstrations.wolfram.com/GrapheneBrillouinZoneAndElectronicEnergyDispersion/*

(99) Laughlin, R. B. *large.stanford.edu/courses/2008/ph373/laughlin2/*.

(100) Berger, C.; Song, Z.; Li, T.; Li, X.; Ogbazghi, A. Y.; Feng, R.; Dai, Z.; Marchenkov, A. N.; Conrad, E. H.; First, P. N.; de Heer, W. A. *J. Phys. Chem. B.* **2004**, *108*, 19912.

(101) Hernandez, Y.; Nicolosi, V.; Lotya, M.; Blighe, F. M.; Sun, Z.; De, S.; McGovern, I. T.; Holland, B.; Byrne, M.; Gun'Ko, Y. K.; Boland, J. J.; Niraj, P.; Duesberg, G.; Krishnamurthy, S.; Goodhue, R.; Hutchison, J.; Scardaci, V.; Ferrari, A. C.; Coleman, J. N. *Nature Nanotech.* **2008**, *3*, 563.

(102) Stankovich, S.; Dikin, D. A.; Piner, R. D.; Kohlhaas, K. A.; Kleinhammes, A.; Jia, Y.; Wu, Y.; Nguyen, S. T.; Ruoff, R. S. *Carbon* **2007**, *45*, 1558.

(103) Dössel, L.; Gherghel, L.; Feng, X.; Müllen, K. *Angew. Chem. Int. Ed.* **2011**, *50*, 2540.

(104) Li, X.; Cai, W.; An, J.; Kim, S.; Nah, J.; Yang, D.; Piner, R.; Velamakanni, A.; Jung, I.; Tutuc, E.; Banerjee, S. K.; Colombo, L.; Ruoff, R. S. *Science* **2009**, *324*, 1312.

(105) *Lux Research. Sorting hype from reality in printed, organic and flexible display technologies.* *luxresearch.web8.hubspot.com/Portals/86611/docs/research%20downloads/lux_research_sorting_hype_from_reality_printed_organic_and_display_technologies[1].pdf* **2010**.

(106) Jo, G.; Choe, M.; Lee, S.; Park, W.; Kahng, Y. H.; Lee, T. *Nanotechnology* **2012**, *23*, 112001.

CHAPTER 2 PHOSPHONIC ACID ADSORPTION ON TRANSPARENT CONDUCTIVE OXIDES

2.1 Adsorption studies of phosphonic acid on ITO: towards optimal conditions

While phosphonic acids have become popular surface modifiers for metal oxides, especially in the past decade,[1,2] there is still a lack of consensus on deposition protocols, and there are few reports on the quality of monolayers obtained. Examining the quality of the phosphonate film created is of uttermost importance for organic electronics, such as OPVs, OLEDs, and OFETs, where indium-tin oxide and other transparent conducting oxides are usually modified to a) enhance wetting by the organic layers that will be deposited on top,[3,4] b) tailor the work function of the electrode to increase built-in potential or reduce energy barriers for charge injection or collection,[5,6] or c) perform chemistry directly off the coated electrode.[7,8] Contaminants on top of the modifier film, or between the molecules assembling the monolayer, will reduce charge transfer to and from the electrode.[9] Multilayer formation may disrupt the interface dipoles intended and could act as charge traps and decrease charge transfer across the interface. Defects in the monolayer such as vacancies of modifier can hinder proper wetting or lead to subsequent delamination.

This chapter analyzes phosphonic acid deposition from ethanol from the perspective of coverage, quality of film deposited, and electronic structure changes induced. In sections 2.1.1 and 2.1.2 the physical chemistry fundamentals needed to understand the process of chemisorption are briefly reviewed, and some literature precedents are summarized in 2.2 before presenting and discussing experimental results.

2.1.1 Thermodynamics of chemisorption

A molecule adsorbing to a clean surface from solution has to replace solvent molecules, and the adsorbing molecule will have fewer interactions with the solvent. It follows that molecules not only adsorb because they are attracted to a surface, but because of rejection from the solvent (e.g. hydrophobic substances in water will easily adsorb to most surfaces).[10] The reaction can be represented as

$$\boldsymbol{A}^{L} + \nu \boldsymbol{L}^{\sigma} \leftrightharpoons \boldsymbol{A}^{\sigma} + \nu \boldsymbol{L}^{L}$$

showing how the molecule **A**, dissolved in a liquid **L**, displaces ν number of **L** molecules from the surface, $\boldsymbol{\sigma}$; in an ideal case the molecules displaced are only solvent molecules, but in high surface energy samples prepared *ex-situ*, could also include adsorbates from the environment.

An attraction-repulsion potential can be considered for the approach of a phosphonic acid to a metal oxide surface such as that in Figure 2.1. The attractive interaction due to hydrogen bonding and polar interaction gives a well in energy at a distance z_{phys}, but in order to reach z_{chem}, the chemical bond length, a barrier E_{ads} must be overcome. It can also be assumed that after covalent monodentation, if the thermodynamics are appropriate for chelation to form multidentate bonding, it will happen on a fast time scale.

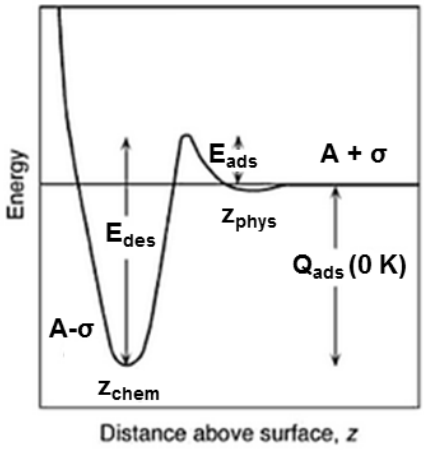

Figure 2.1 A one-dimensional potential for molecular chemisorption with energy barrier. Eads and Edes are the adsorption and desorption activation energies; Qads the heat released by chemisorption, and zchem and zphys the equilibrium adsorbate-surface bond length for chemisorption and physisorption respectively. Modified from Kolasinski.[11]

The following relation approximates the case in question:

Equation 2.1 $$E_{des} = E_{ads} + Q_{ads}(0\ K)$$

where $Q_{ads}(0\ K)$ is the temperature independent bond strength enthalpy between the acid **A** and the surface **σ**. Recall from thermodynamics that the Gibbs free energy difference is a function of the enthalpy change and the entropy change (times the temperature):

Equation 2.2 $$\Delta G = \Delta H - T\Delta S$$

Since any system will relax to the minimum Gibbs energy possible as long as no kinetic constraints prevent it, $\Delta G < 0$ for all spontaneous processes. Given that adsorption confines the solute to a surface, in most cases $\Delta S < 0$, which leaves that ΔH must be negative for spontaneous adsorption. It is known that phosphonic acids do attach spontaneously to metal oxides such as ITO.[12]

2.1.2 Kinetics of chemisorption

For physisorption, residence times at the solid/liquid interface are often short, and the rate of adsorption is often determined solely by the supply rate.[13] In such diffusion-controlled adsorption models, no activation energy barrier is assumed to transfer solute molecules to the surface; hence, diffusion is the only mechanism needed in establishing adsorption equlibrium. In this case, initial coverage Γ_i depends on the concentration and the square roots of time *t*, and diffusion coefficient *D*:[13]

Equation 2.3 $$\Gamma_i(t) = \frac{2D^{1/2}ct^{1/2}}{\pi^{1/2}}$$

Nonetheless, if chemisorption takes place, the rate may be diffusion-controlled or adsorption-controlled. The former is expected if the reaction is fast, the diffusion coefficient is small, or the solution concentration is sub-micromolar.[14] Adsorption-controlled kinetics are followed if there is a significant activation energy and, therefore, an Arrhenius type of temperature dependence. The rate of adsorption will be first order in the adsorbing species, and first order in the concentration of free sites at the surface, to give a Langmuir-like behavior. Given the the virtually irreversible nature of chemisorption, k_{des} is assumed to be negligible compared to k_{ads}.[15]

Equation 2.4 $$\frac{\delta\Gamma}{\delta t} = k_{ads}c(\Gamma_{max} - \Gamma)$$

This equation can be integrated to give coverage as a function of time if the E_{des} and E_{ads} from Equation 2.1 are assumed independent of coverage; then, at a given temperature:

Equation 2.5 $$\Gamma = \Gamma_{max}(1 - \exp(-k_{ads}ct))$$

Note that from transition state theory,[16]

Equation 2.6 $$k_{ads} = \frac{k_b T}{h} \exp\left(\frac{\Delta S^{\ddagger}}{R} - \frac{\Delta H^{\ddagger}}{RT}\right)$$

so that an increase in temperature must lead to an increase in adsorption rate.

2.2 Adsorption kinetics reported in literature for phosphonic acids

After the work of Schwartz in the 1990's referenced in Section 1.5.4.2, [60,61] other groups have undertaken kinetic studies on metal oxide surfaces for a variety of applications. There are several publications on the treatment of native aluminum oxides with phosphonic acids, usually motivated by corrosion protection. For instance, Giza and coworkers briefly examined the adsorption kinetics of octadecylphosphonic acid on various plasma treated aluminum films, characterizing the starting surfaces by IRRAS and XPS and the PA treated surfaces by quartz crystal microbalance (QCM) and IRRAS Figure 2.2.[17] Regardless of plasma treatment, uptake was very fast during the first few minutes. Water-plasma gave the fastest kinetics due to increase in surface hydroxide concentration, although no fits to kinetic models were reported.

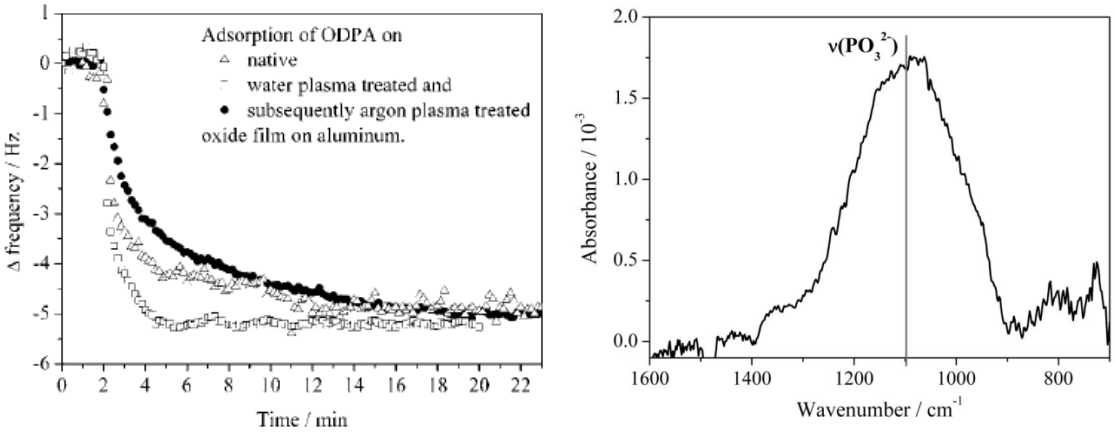

Figure 2.2 (left) Frequency changes on differently treated aluminum-coated QCM due to reaction with 0.1 mM ODPA solution. (right) IRRAS spectrum showing region of

phosphonate vibration for 2 h ODPA-treated water plasma cleaned Al film. Reproduced from Giza, et al.[17]

Pellerite and coworkers studied the deposition of straight chain alkanephosphonic acids ($CH_3(CH_2)_nPO_3H_2$, n = 14-20, abbreviated as H15-H21PA), as well as a partially fluorinated straight chain PA, $CF_3(CF_2)_7(CH_2)_{11}PO_3H_2$ (abbreviated as F8H11PA) onto UV/O_3-treated aluminum from 0.1% EtOH or THF solutions.[18] Ellipsometry showed a very rapid increase in thickness in the first 5 s, followed by a much slower increase over a matter of minutes for F18H11PA until it reached a plateau; similar behavior was observed for H16PA and H22PA, but the plateau was not reached until ~10^4 s (a few hours, see Figure 2.3). IRRAS was used to probe the orientation and binding modes of the molecules in the phosphonate film. At short immersion times, multidentate bonding with an average molecular tilt close to 35° is suggested, but this changes to more vertical orientation at longer exposure times; however, given the broad P-O stretch signal, no conclusive assignment to binding modes could be done.

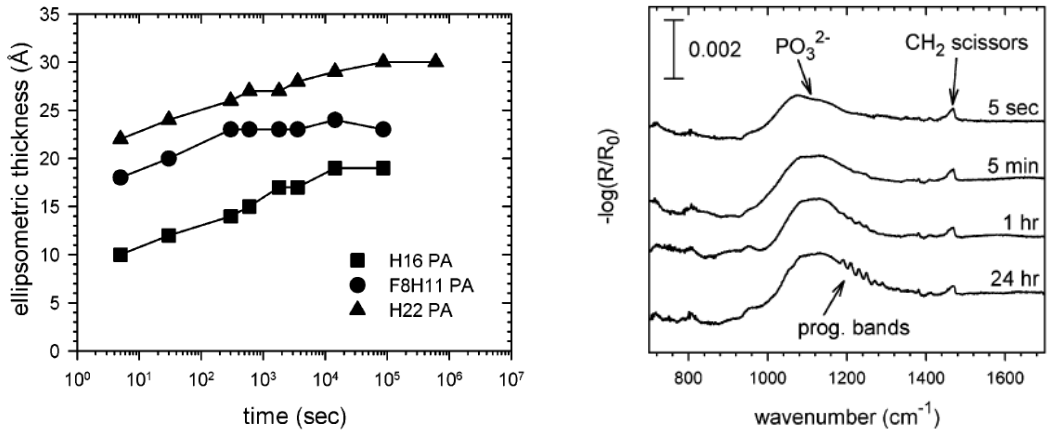

Figure 2.3 (left) Ellipsometric film thickness vs. immersion time for PA treatments on oxidized Al. (right) PM-IRRAS in the phosphonate region for hexadecylphosphonic acid on Al. Reproduced from Pellerite, *et al*.[18]

To the best of the author's knowledge, there are only two kinetic studies on deposition of phosphonic acids to ITO (and related oxides). Chockalingam *et al.* looked

at the importance of the ITO substrate on the quality of the PA monolayers.[19] They observed the expected correlation between surface hydroxide concentration (determined by XPS) and PA coverage as judged by contact angle. They found that the higher the surface roughness, the more defects were found in the monolayer as judged by electrochemical deposition of lead, which can only occur on bare ITO and is measured by XPS.

Perhaps the closest study to the goal of this Chapter is that by Jo *et al*,[20] in which the adsorption kinetics of straight chain phosphonic acids with a carboxylic acid terminal group to a peroxide pretreated ITO was examined via cyclic voltammetry (CV) and electrochemical impedance spectroscopy (EIS). EIS is similar to CV in that it measures the charge transfer resistance from a redox active species in solution to the electrode, but does it with the application of a periodic small amplitude alternating current signal instead of linear potential ramps. Figure 2.4 shows how the reduction/oxidation peak separation for $Fe(CN)_6^{3-/4-}$ increases while the area under the curves decrease as the ITO used is immersed for longer time in 10 mM aqueous solution of 3-phosphonopropanoic acid (PPA), suggesting a decrease in charge transfer due to increasing coating coverage. Similarly, the diameter of the resistance semicircles for the EIS plot increases, pointing to increased resistance R_{CT}, which can be correlated with coverage via Equation 2.7.[20]

Equation 2.7
$$\frac{\Gamma}{\Gamma_{max}} = \theta = 1 - \frac{R_{CT}^{bare}}{R_{CT}^{PA}}$$

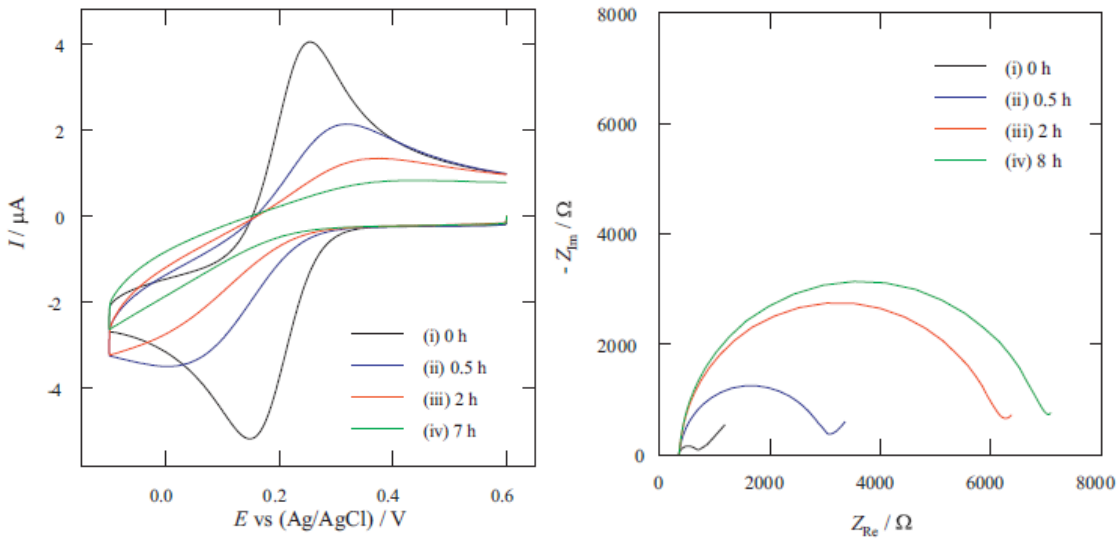

Figure 2.4 CV traces (left) and EIS plots (right) for $Fe(CN)_6^{3-}$ (0.10 mM) in a phosphate buffer using ITO electrodes modified for different amount of times with 3-phosphonopropanoic acid (PPA). Reproduced from Jo, *et al.*[20]

The relative coverage was plotted as function of immersion time for different concentrations (Figure 2.5) and fitted nicely to the Langmuirian model as in Equation 2.5. The observed rate constants $k_{obs} = k_{ads}c$ for three concentrations are shown to the right.

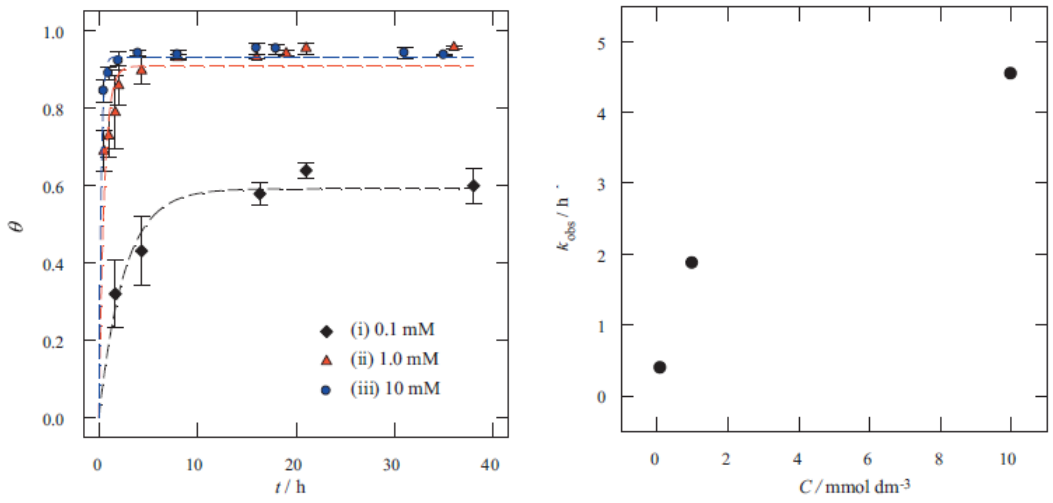

Figure 2.5 Left: Langmuir adsorption-fit of coverage data obtained from EIS for immersion in different concentrations of PPA. Right: Increase in observed rate constant with increasing concentration of PPA. Reproduced from Jo, *et al.*[20]

2.3 Characterizing the adsorption of a phosphonic acid on ITO

It is clear that there is a need for studies addressing quality and coverage of PA layers on TCOs. There are multiple reports of PA monolayers without any evidence that the protocol lead to an actual monolayer other than the presence of phosphorus as detected by XPS, or a change in contact angle or work function. If the deposition process were properly understood, ways to achieve fast deposition of a high quality monolayer could be devised. It would be desirable for both industrial applications and R&D if high coverage were obtained in a matter of seconds. In this section, studies varying some deposition conditions that can have an influence on the chemisorption rate, such as concentration, temperature, and surface pretreatment, are presented. X-ray photoelectron spectroscopy (XPS) is used to follow kinetics and extent of adsorption of 2,3,4,5,6-pentafluorobenzyl phosphonic acid (PFBPA) onto ITO from ethanol solution at concentrations of 1, 10 and 100 mM at room temperature (r.t.) for immersion times increasing from seconds to days (Figure 2.6). As shown in Section 2.3.1, 10 mM solution shows the fastest kinetics, so a comparison of 10 mM adsorption at r.t. vs 75 °C is undertaken, which points to much higher adsorption rate at the high temperature. Atomic force microscopy is used to examine the roughness after PFBPA treatments. In a second study (2.3.2), not only XPS is used to compare using plasma vs detergent/solvent cleaned-only pretreatments, but Ultraviolet Photoelectron Spectroscopy (UPS) is used to track changes in work function and explain those changes as originating in molecular dipoles, or valence band maxima shifts; infrared reflection-absorption spectroscopy (IRRAS) supplements with information on binding modes.

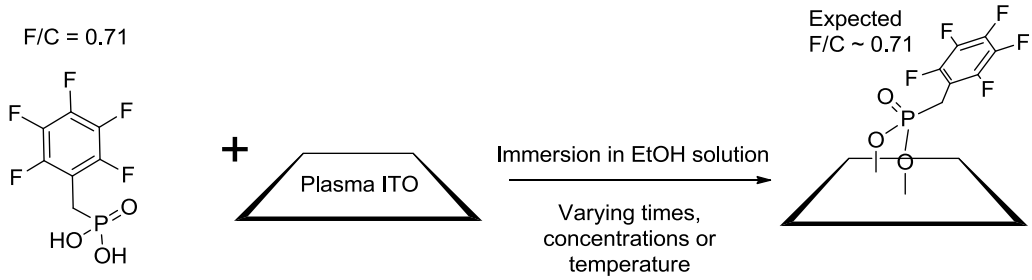

Figure 2.6 PFBPA modification of plasma treated ITO with PFBPA to track chemisorption.

PFBPA was chosen as a representative modifier, since attention in the organic electronics community is now shifting to aryl R groups.[2,5,6,21,22] This PA has been used in published studies regarding modification of electrodes for OPVs and OLEDs,[5,23-25] and has five fluorine atoms which give a strong signal in XPS, enabling easy detection even at submonolayer coverages obtained at short reaction times. Since the difference in attenuation in the range of 0-1 monolayer is so small compared to three times the inelastic mean free path (IMFP) for electrons originating from In $3p_{3/2}$ or In $3d_{5/2}$ (~8 nm, see below), it is possible to follow the adsorption kinetics using direct comparison of F/In ratios.

Quantification using XPS involves detemining the area under the peaks for each core level (A_{CL}) and relating them to the area of peaks from other elements. In this case, the the ratio of the number of F atoms (N_F) over the number of In atoms (N_{IN}) probed can be stated as Equation 2.8:

Equation 2.8
$$\frac{N_F}{N_{In}} = \frac{(A_{F1s}/SF_{F1s})}{(A_{In3p_{3/2}}/SF_{In3p_{3/2}})}$$

where sensitivity factors *SF* are accounted for each orbital. These correct for instrumental factors, attenuation due to different in kinetic energies, and the quantum-mechanical probabilities of photoionizations for each core level. When quantifying from only one of the multiplicities of a core level that shows spin-orbit coupling (due to interaction of the

electron spin with the orbital angular momentum), the sensitivity factor needs to be corrected accordingly.

The F/In ratios from XPS can be compared to theoretical values for a close-packed monolayer of PFBPA on ITO. Figure 2.7 shows a model for the ITO surface made by Brédas group; the ITO 222 crystalline face has been used as the model given its abundance in polycrystalline ITO obtained using a variery of fabrication techniques.[26] Its unit cell area is composed of 28 In and 4 Sn atoms (per layer). Each layer is separared from the next by 3.32 Å.

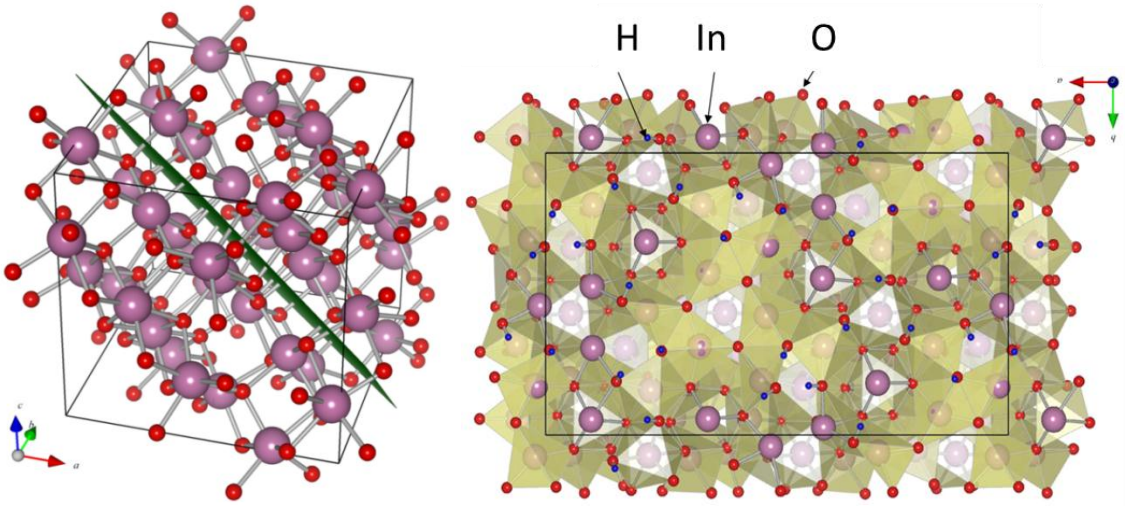

Figure 2.7 Left: Bulk In_2O_3 unit cell (cubic) with the (222) lattice plane highlighted in green. Right: Top view of a rectangular, OH-terminated ITO (222) surface slab, optimized at the DFT level. The periodic rectangular supercell is indicated. Sn-substitutions are randomly distributed over the cationic positions throughout the slab. Reproduced from Paramonov, *et al*.[26]

For Al Kα radiation, electrons emerging from the In $3p_{3/2}$ orbitals (*ca.* 666 eV binding energy) will have a kinetic energy of *ca.* 816 eV. This energy determines the inelastic mean free path (λ) for the photoelectrons being scattered as they emerge. One λ_M^{CL} is, by definition, the average distance electrons ejected from a given core level (*CL*) can travel through a material *M* before 1-1/e (63%) are inelastically scattered: hence, only

a 1/e fraction of all the electrons at a depth of λ from the surface will be detected without energy loss.

Equation 2.9 describes the decay in signal from electrons originating at a distance *t* from the surface.[27]

Equation 2.9 $$I = I_S \exp\left(-\frac{t}{\lambda cos\theta}\right)$$

where I_S is the unscattered intensity and θ the detection angle relative to the surface normal. Since all data discussed here was acquired at normal angle detection, $cos\theta$ is 1. Figure 2.8 shows the decrease in intensity for a given distance from a surface.

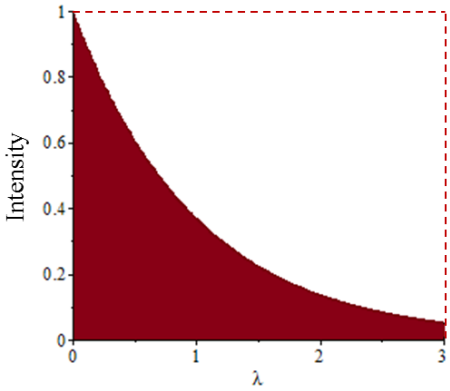

Figure 2.8 Signal intensity as a function of distance from surface in units of λ for normal angle detection.

Integration of Equation 2.9 from 0 to 3λ will give the total intensity for electrons coming from right at the surface to those 3λ deep into the sample (information depth is 3λ). This evaluates to 0.95λ, which translates into 95% of the signal coming from within 3λ. It can be seen from Figure 2.8 that if there were no attenuation ($I = I_S$), the integration would be merely the area of a rectangle 1 × 3λ = 3λ (shown in dashed lines). Hence, it is possible to correct for the scattering attenuation by dividing the expected F/In ratio by the factor 3.16 (= 3λ / 0.95λ), or multiplying the observed XPS F/In by 3.16. For

the In $3p_{3/2}$ line in ITO, $\lambda_{ITO}^{In3p_{3/2}}$ = 27.4 Å using the inelastic mean free path curve for inorganic materials.[27]

The value of 3λ for In $3p_{3/2}$ is 8.2 nm, which can fit 24.8 layers of ITO according to the model put forward by Paramonov.[26] Considering PFBPA on top of one of these layers, the footprint of each PA is 22.62 $Å^2$.[28] This corresponds to a maximum coverage of 4.4×10^{14} molecules cm^{-2}. Each 22.6 $Å^2$ can hold 1.78 In atoms, so in 3λ there will be a total of 44 In atoms. This gives an expected PFBPA / In ratio of 1/44 = 5 F atoms per 44 In atoms = 0.11 F/In ratio. Hence, a close-packed monolayer of PFBPA on smooth ITO would have a ratio of 0.11 F/In, considering an information depth of 3λ. If this hypothetical structure was measured by XPS, the In signal would be attenuated as discussed in the previous paragraph, so the expected measured F / In would be 0.11×3.16 = 0.36.

2.3.1 First study on chemisorption kinetics

In the first study, three set of experiments were performed; in each set, seven slides of ITO were detergent-solvent cleaned and then oxygen plasma etched simultaneously, followed by immersion for varying amounts of time in separate vials with the same volume of solution with a given concentration of phosphonic acid. Figure 2.9, as an example, shows the XPS F 1s and In $3p_{3/2}$ signals for substrates immersed in 10 mM PFBPA ethanolic solution, after extensive rinsing and sonication in fresh ethanol. The trend clearly shows that the longer the immersion time, the higher the fluorine signal. The F 1s / In $3p_{3/2}$ is converted to F/In after correcting for instrumental factors and sensitivity factors.

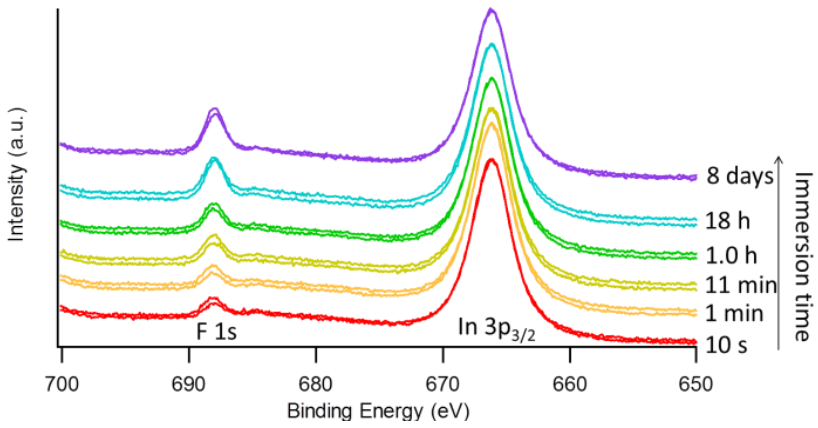

Figure 2.9 F 1s / In $3p_{3/2}$ XPS signal comparisons for ITOs immersed in PFBPA 10 mM solution for increasing times. Two spectra for each sample are shown; traces offset for clarity.

Common concentrations reported in literature for assembly of monolayers are 1-10 mM, and hence those were used here. Since it was of interest to see if increasing the concentration would lead to faster rates of adsorption, a concentration of 100 mM was also used. Figure 2.10a shows the F/In for samples prepared in parallel after oxygen plasma cleaning and immersion for varying times at room temperature in PFBPA at these concentrations. The trend for all is quick adsorption, followed by a decrease in adsorption rate as the number of available sites decrease, agreeing at least qualitatively with the Langmuirian adsorption model discussed in the introduction.

Examination of the trends shows that for 10 mM the observed deposition rate is faster than 1 mM or 100 mM: for instance, after 1 h the coverage at 10 mM is that attained by 1 mM and 100 mM only after 18 h. Nonetheless, after 8 days of immersion they all achieve similar F/In ratio. Fits to Equation 2.5 were attempted for all, and the results are shown in Figure 2.10b and Table 2.1. The correlation coefficients R^2 are barely acceptable for all cases, so the quantitative information is not very reliable, but the numerical trends follow what is observed by eye: 10 mM gives the highest observed rate

constant k_{obs}, but the adsorption constant k_{ads}, calculated by dividing k_{obs} by the concentration used, is similar to that of the 1 mM batch. In this sense, 100 mM concentration gives an observed rate constant that is slightly larger than that of 1 mM, but the value of k_{ads} is much lower, and 100 times more material has been employed. This might be due to the low pH associated with such a concentrated solution, a factor not taken into account in the simple Equation 2.5. The apparent pHs of the solutions were measured to be 3.7 (1 mM), 2.9 (10 mM) and 1.8 (100 mM).

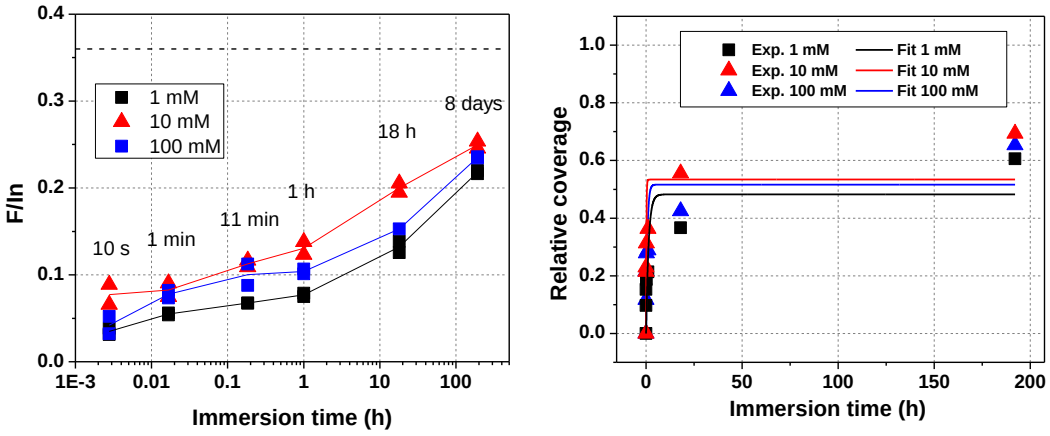

(a) (b)

Figure 2.10 (a) XPS F/In for samples prepared at different PFBPA concentrations. Trend lines are shown as a guide for the eye. The black dash line represents expected F/In for close-packed monolayer. (b) Fit to Equation 2.5 of the relative coverage to F/In=0.36.

Table 2.1 Results from Langmuirian fit $\boldsymbol{\Gamma/\Gamma_{max} = A(1 - \exp(-k_{ads}ct))}$ to adsorption kinetics for PFBPA depositions at different concentrations (all at room temperature)

Concentration c_b	1 mM	10 mM	100 mM
Max. coverage A	0.48 ± 0.09	0.53 ± 0.09	0.52 ± 0.11
$k_{obs} = k_{ads} \times c$ (h^{-1})	0.8 ± 0.6	6 ± 5	2 ± 1
k_{ads} (10^2 $M^{-1}h^{-1}$)	8 ± 6	6 ± 5	0.2 ± 0.1
R^2	0.61	0.50	0.47

As mentioned in the introduction to this chapter, k_{ads} should increase with temperature. This was put to the test. It must be noted that at 75 °C, close to the boiling point of ethanol, samples tend to dry out quickly when removed from the solution. As Figure 2.11 shows, a sample that has been immersed in 10 mM PFBPA at 75 °C and then

simply left to dry after removing from the hot solution leads to multilayers of varying thicknesses, with large spot-to-spot variation in the F/In ratio. After ethanol rinse, the value is closer to what is expected of a close-packed monolayer based on the analysis performed above, but still higher than expected. A base rinse with triethylamine 5% in EtOH has been reported in literature to remove multilayers, and was applied to ensure removal of any multilayer films. After 10 min subsequent sonication in triethylamine, the F/In falls into the range expected for a monolayer, and its value will depend on the extent of chemisorption, which is time dependent. This work-up was used for all subsequent experiments.

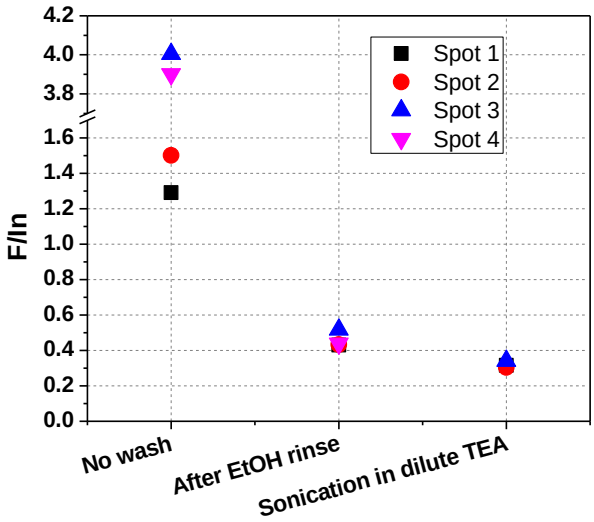

Figure 2.11 F/In XPS ratios for several spots in (a) ITO sample left to dry after removal from PFBPA solution, (b) after ethanol rinse, (c) after successive sonication in 5% v/v triethylamine in ethanol.

Figure 2.12a shows comparison of the adsorption kinetics at 75 °C and room temperature (r.t.). Note that a different oxygen plasma system from that use for the concentration studies above was used here. Some interesting observations from these results are summarized as follows: first, at 75 °C the rates were not only faster (the F/In ratio at 10 min was the same as that after 1 week at r.t.), but a plateau was reached within 1 hour, while for the r.t. after 1 week the F/In ratio had not saturated. The last four F/In

ratios for the 75 °C runs were within 15% of the expected F/In = 0.36. Second, after 1 week at r.t. the F/In ratio was not as high as that of the plateau at 75 °C, indicating that room temperature deposition cannot achieve full coverage in a reasonable time scale.

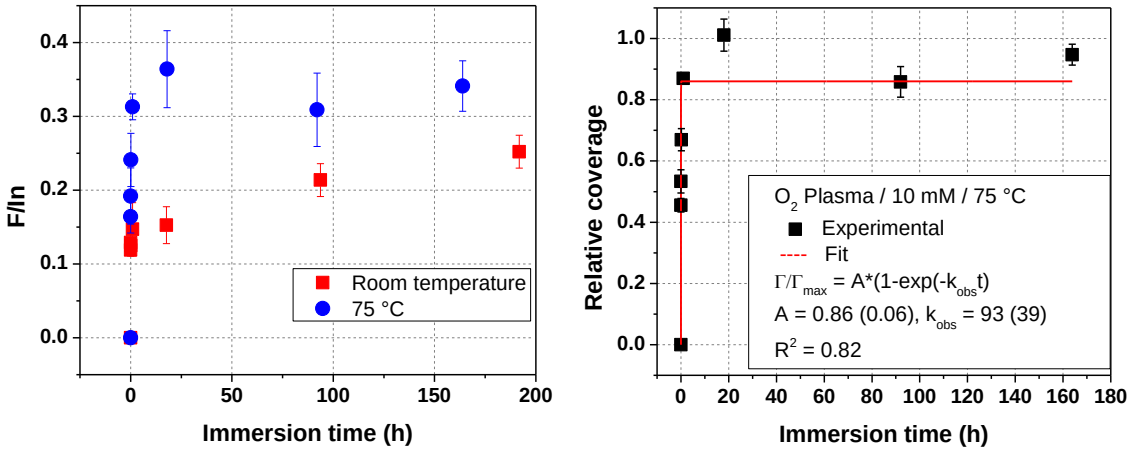

(a) (b)

Figure 2.12 (a) F/In XPS ratios after ITO immersion in PFBPA 10 mM ethanol solutions at 75 °C. (b) Fit to Langmuirian kinetics behavior for (F/In)/0.36 for O_2 plasma, 10 mM PFPBA / 75 °C batch.

A fit to Equation 2.5 was attempted for (F/In)/0.36 (the expected ratio for close-packed monolayer); the result is shown in Figure 2.12b. The fit is better than what resulted from the room temperature depositions; R^2 = 0.82 and the fitted maximum coverage is 86% that of the predicted value for close-packed monolayer; also, the observed rate constant is 93 h^{-1}, which results in $k_{ads} = 93\times10^2$ $M^{-1}h^{-1}$, an order of magnitude larger than for the room temperature cases.

Selected samples from the batches discussed were observed by atomic force microscopy to check for etching or roughness changes. Representative images are compared in Figure 2.13. The topography features are the same, even for the harsher treatments. As Table 2.2 shows, for samples treated in 10 mM PFBPA for 15 s at r.t. or several days at 75 °C, a roughness close to 3.2 nm was determined. Even in the case of 0.1 mM treated samples, the roughness was still 3.3 nm. It is concluded that the acidities

and temperatures used during these treatments are not appreciatively affecting the surface roughness, nor etching the ITO.

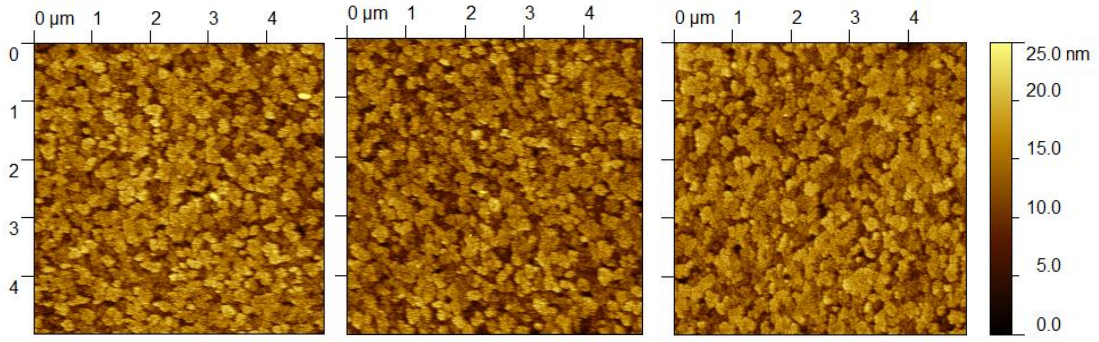

(a) (b) (c)

Figure 2.13 Typical AFM micrographs: (a) 75 °C 10 mM treatment for 4 days, (b) 18 h in 100 mM at r.t. and (c) 15 s in 10 mM r.t.

Table 2.2 Roughness determined from 5 × 5 micron AFM images.

Sample	RMS / nm
Plasma	3.2
15 s / 10 mM rt	3.2
10 in / 10 mM rt	3.4
1 h / 10 mM rt	3.4
18 / 100 mM rt	3.3
4-7 days / 10 mM 75°C (average)	3.2

2.3.2 Second study of adsorption kinetics: tracking work function changes with coverage

This work was undertaken with the aid of Ms. Emily Li (a Georgia Tech undergraduate student in Mechanical Engineering) to expand upon the experiments from the previous section. The effect of not using plasma was studied both at room temperature and 75 °C, as well as the use of buffered solutions. The coverage is examined and the quality of the overlayers is assessed via quantification of the F/C ratios from F 1s and C 1s. The work function and valence band maxima were tracked by Ultraviolet Photoelectron Spectroscopy (UPS) as the coverage varied. It must be noted

that a different plasma etcher was used for this section (air plasma instead of pure oxygen), as well as a different photoelectron spectroscopy system. Since UPS is introduced in this section, and will be used throughout the rest of this chapter as well as Chapter 5, a brief explanation of its use for tracking work function and the valence band region is presented below before discussing the results.

In UPS, the ultraviolet radiation is generated using helium gas. The He I line (21.22 eV) is produced by arc-excitation of He, which will excite an electron to a 2p orbital and the atoms will fluoresce as it relaxes back to its ground state with a 2p→1s orbital transition.[29] The radiation is directed to the sample to photo-excite electrons that are no more than 21.22 eV below vacuum level (Figure 2.14). The electrons are detected and analyzed by their kinetic energies. The spectrum acquired depends not only on the density of states in the valence band region but also the cross-sections (quantum-mechanical probabilities) for a given ionization, as well as the inelastic mean free path associated with the material and kinetic energy involved. Electrons scattered inelastically contribute to a background that increases exponentially with kinetic energy.

As mentioned in Section 1.5.4.1, ITO is a heavily doped semiconductor such that in the bulk, the Fermi level resides in the conduction band. Given the imbalance in charge neutrality close to the surface, there is an upward band bending so that for the top layers, the Fermi level lies in the band gap (Figure 2.14). UPS is a surface-sensitive technique (λ = 2-10 nm depending on kinetic energy[27]), so the electronic structure measured is that at the surface. While the independent variable in the raw UPS data is kinetic energy, it can easily be converted into binding energy by measurement of a clean metal with a visible Fermi edge ($E_F = 0$). The UPS spectrum shows an abrupt cutoff, the secondary electron edge (SEE), determined by the radiation used and the work function of the material. Subtracting the width of the spectrum (the difference between the SEE binding energy and the Fermi edge) from the radiation used affords the local work function of the film in question ($\Phi = h\nu - SEE$).

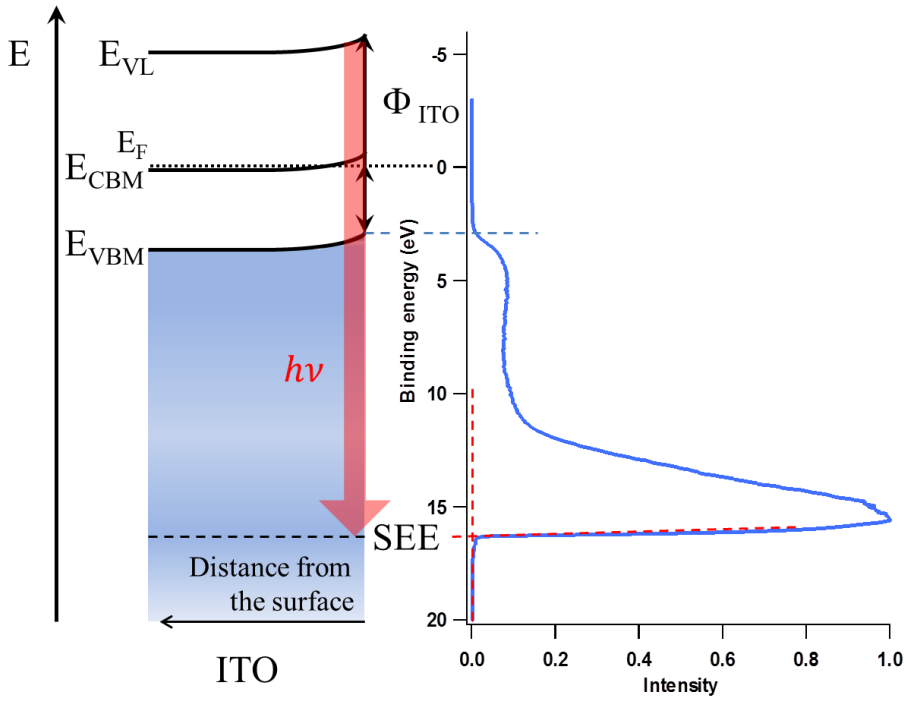

Figure 2.14 Tracking work function and valence band maximum by UPS: on the left, the electronic structure of ITO, with its corresponding energy levels onsets (VBM = valence band maximum, CBM = conduction band minimum) and their bending in the depletion layer near the surface. The work function (Φ) and UV radiation energy (hν) are also marked. No electrons deeper in energy from the vacuum level (E_{VL}) than hν will be released from the material; those slightly above will be detected with the minimum kinetic energy, and along with scattered electrons that have lost energy on the way to vacuum will make up the secondary electron edge (SEE, abrupt end at high binding energy of the UP spectrum to the right).

2.3.2.1 Modification of ITO with 10 mM PFBPA at room temperature without plasma pretreatment

Detergent-solvent cleaning offers limited removal of adventitious carbon on the ITO surface.[3] Typically there will be around four times greater amount of carbon on the surface then when using some etching procedure such as plasma cleaning. The contamination is composed of hydrocarbons and oxidized organic species that are in the atmosphere, in the solvents employed, and on the tweezers and containers used that come into contact with the sample over time. They may affect the adsorption of modifiers since

they are occupying adsorption sites. One of the goals of the following subsection is to investigate the extent to which this affects the adsorption rate.

The F/C and C/In ratios were followed carefully in this study, besides the usual F/In. In Figure 2.15 the C 1s XPS spectrum for a 7-day treated sample is shown, displaying the expected fluorinated carbons from the phosphonic acid. The non-fluorinated components come from both non-fluorinated carbons of the acid plus the contamination. Hence, the F/C ratio serves as an indication of the overlayer quality: since each molecule has seven carbons per five fluorine atoms, and that stoichiometry (F/C~0.71) should remain in a clean overlayer, that ratio can be used to assess the quality of the monolayer. If there are unreacted spots that are dirty, or the overlayer has material deposited on top, the ratio will decrease.

Figure 2.15 shows the F/In and F/C comparison after increasing modification times when no plasma activation is used. The F/In and F/C track each other well, pointing to an increase in quality of the monolayer as the coverage increases. The F/In ratio is far from that expected for a close-packed monolayer (0.36) even after a week of treatment, similar to what was observed in the previous section: 61% of a monolayer is determined from the highest F/In ratio measured (at 0.22). In this case the quality of the PA film as judged by the F/C ratio only comes close to the expected 0.71 after one week of treatment (F/C=0.52).

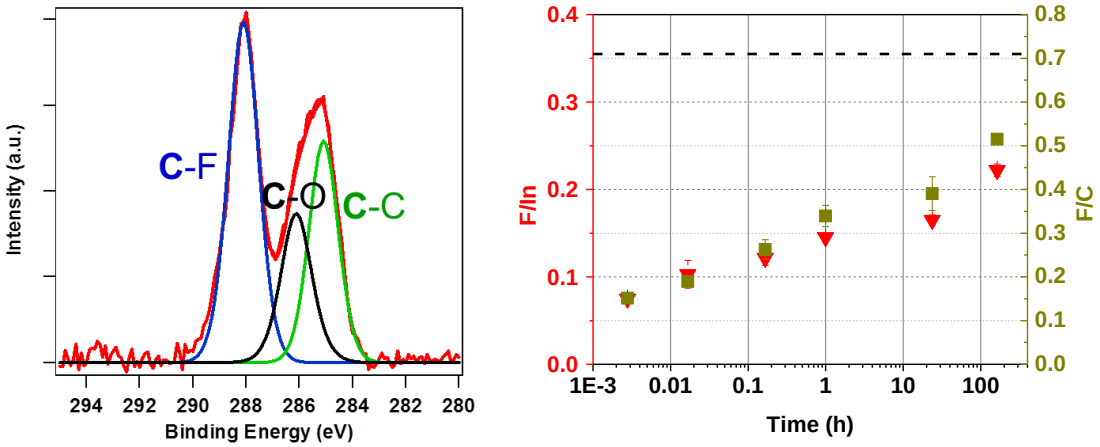

Figure 2.15 Results from treatment with PFBPA 10 mM at r.t. Left: C 1s XP spectrum after 7 day treatment, showing fits for different carbon species. Right: F/In and F/C XPS ratio variation with immersion time (of replicate samples). Dashed line shows expected F/In for close-packed monolayer and ideal F/C ratio.

Figure 2.16 shows the surface electronic structure changes as probed by UPS. The work function suffers a slight dip after initial immersion in the PA solution, reaching a minimum of 4.64 eV at 1 min immersion; the valence band maximum stays constant while the work function has decreased slightly. As the phosphonic acid starts reacting there is no order to the orientation of the molecules attaching given the low coverage, and hence no significant molecular dipole pointing away from the surface is generated. Nonetheless, any adsorption of material will cause a *pillow effect*, the pushback of the intrinsic spilling electron cloud out of the surface, thereby reducing the work function (Figure 2.17).[30]

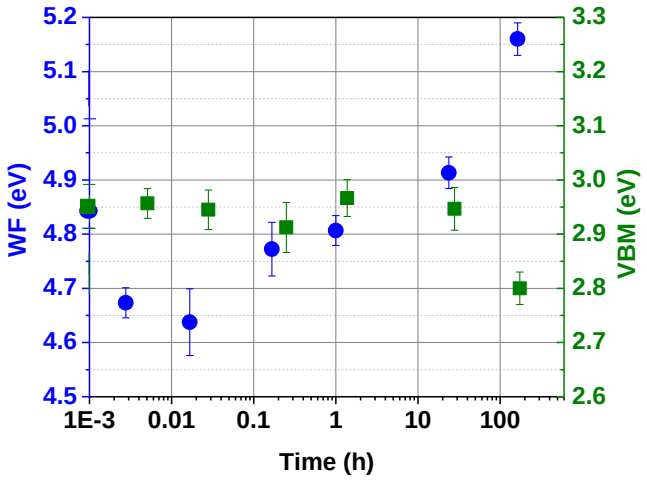

Figure 2.16 Room temperature, 10 mM PFBPA modification. Work function (WF, left axis) and valence band maximum (VBM, right axis) as a function of immersion time. The values for bare ITO are on the leftmost side of the graph.

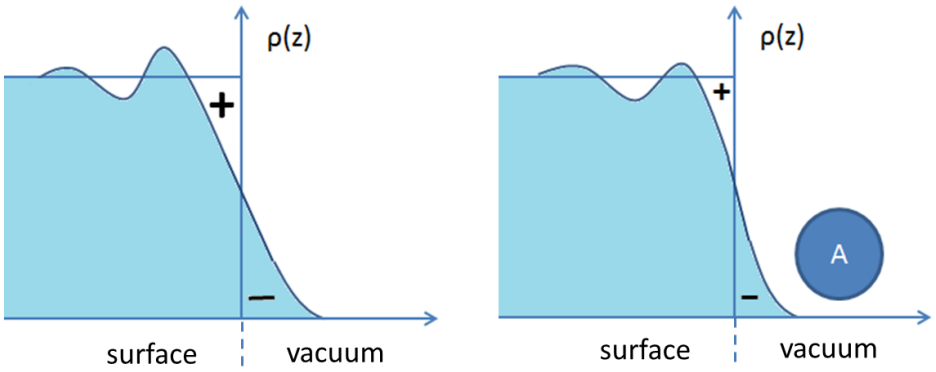

Figure 2.17 Spillover of the electron cloud at the surface and pillow effect from adsorbates.

As the coverage increases, the work function approaches its initial value after 1 h immersion and increases beyond the starting value at longer immersion times, while the VBM stays constant (within 0.1 eV) for all examined immersion times, from which it can be inferred that there is no significant net effect on the work function from bond dipole or geometry rearrangement. The observed molecular dipole contributions can be plotted against the absolute adsorbate concentration to examine if the linear trend from Equation 1.3 holds.

Equation 1.3 $$\Delta\phi_{MD} = \frac{N\mu_z}{\varepsilon_{eff}\varepsilon_0}$$

The relative coverages are multiplied by the close-packed monolayer density discussed in Section 2.3 (4.4×10^{14} molecules/cm^2). The resulting plot is shown in Figure 2.18. After the minimum work function is reached (attributed to the pillow effect) at ~1×10^{14} cm^{-2} coverage, the PFBPA molecular dipole has a stronger effect and raises the work function in linear fashion, in agreement with the model above. Recent calculations estimated that PFBPA on ITO contributes a molecular dipole of 1.49 D,[28] and due to depolarization effects as the coverage increases the effective dielectric constant can be in the range of 1 to 2.5 depending on the molecule.[31] An intermediate value of ε_{eff} = 2.0 results in $\Delta\phi_{SD}/N$ = 2.8×10^{-15} Vcm^2, which completely agrees with the experimentally estimated value determined from the slope of the fit (2.8×10^{-15} Vcm^2).

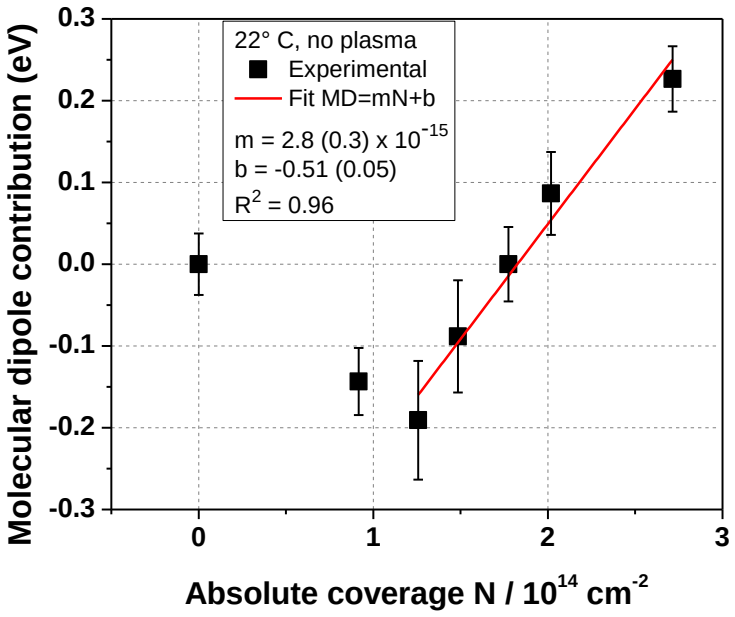

Figure 2.18 Tracking the molecular dipole as the PFBPA coverage increases.

Figure 2.19 summarizes the results observed by UPS and incorporates the XPS results in schematic fashion. It can be concluded that treatment at room temperature only offers a high quality phosphonic acid overlayer after days of treatment, with a molecular dipole induced by the modifier which gradually increases the work function. The effect of plasma cleaning to achieve higher coverages and probe the electronic structure changes is studied in the next section.

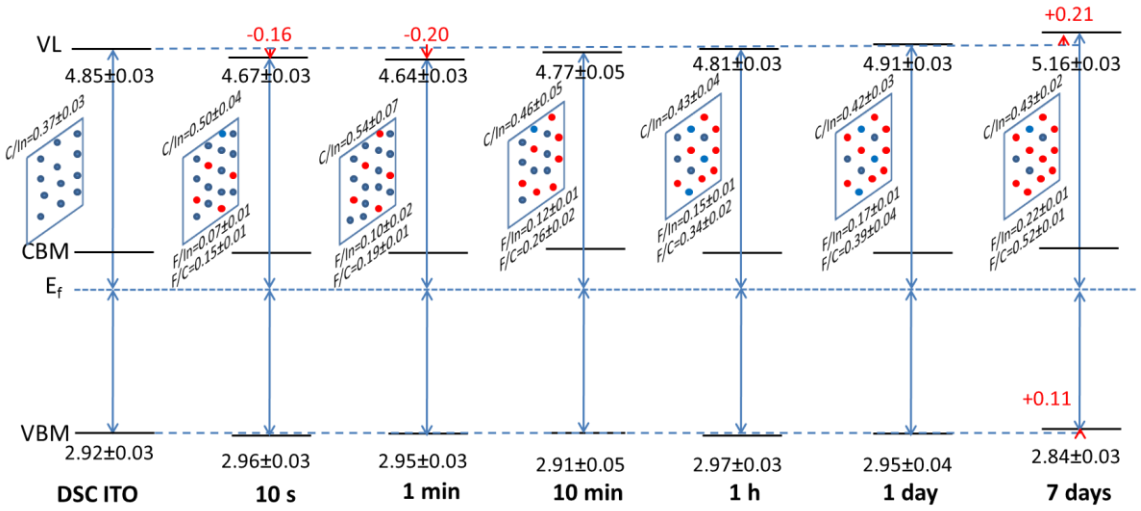

Figure 2.19 Energy level diagrams (constructed from UPS data) and schematic representation of the changes on the surface according to XPS for DSC ITO treated with PFBPA 10 mM at room temperature. Significant changes in molecular dipole or valence band maximum relative to starting DSC ITO are represented by the small red arrows at the vacuum level. Band gap assumed as 3.6 eV and maintained constant throughout. Blue circles represent adventitious carbon and red circles phosphonic acid.

2.3.2.2 Modification of ITO with 10 mM PFBPA at room temperature after plasma pretreatment

Figure 2.20 summarizes the changes induced on ITO after air plasma treatment, as probed by XPS, UPS and infrared reflection-absorption spectroscopy (IRRAS): the C/In ratio decreases substantially, from 0.37 to 0.08. This adventitious carbon adhered to the ITO also induces a pillow effect, suppressing the intrinsic spill-over of the electron cloud from the surface. Plasma treatment returns ITO with a high work function due in part to

removal of most of this carbon (and the pillow effect it induces), as well as generation of hydroxyl groups on the surface.[32] This is verified by IRRAS: the spectrum of air plasma-treated ITO using the spectrum of detergent/solvent cleaned ITO as background shows an absorption in the O-H region around 3300 cm^{-1}. UPS shows a valence band maximum shift towards the Fermi level of 0.3 eV due to either geometry rearrangement or the bond dipole from the hydroxyl species.

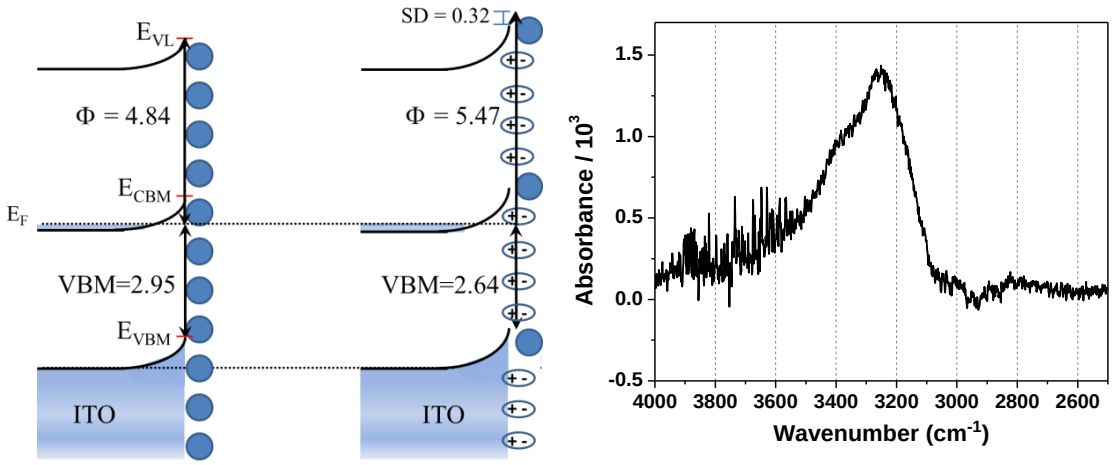

Figure 2.20 (Left) Comparison of electronic structure for detergent/solvent cleaned ITO and after plasma treatment. Blue circles represent adventitious carbon. All energies in eV. Right: IRRAS spectrum of air plasma treated ITO using DSC ITO as background.

The same systematic XPS/UPS study was employed on plasma-activated ITO on immersion in 10 mM PFBPA solution. Figure 2.21 shows some of the XPS results for this batch; the F/In ratio follows what was observed with the oxygen plasma pretreatment from the previous section. In this case, the F/C ratio tracks well the F/In evolution: in general, the quality of the monolayer increases with immersion time.

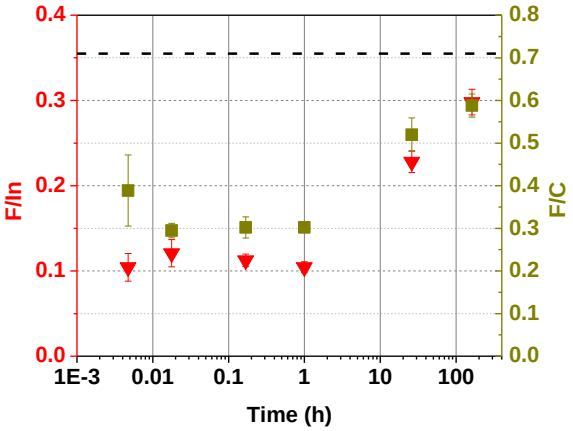

Figure 2.21 Room temperature, 10 mM PFBPA modification. F/In and F/C ratio variation with immersion time (of replicate samples). Dashed line shows expected F/In for close-packed monolayer and ideal F/C ratio.

Figure 2.22 shows the result of the treatments on the electronic structure of plasma cleaned ITO; the work function decreases with immersion on the phosphonic acid solution and only after 7 days recovers slightly. This incremental decrease of the work function can be traced back to a decrease in the molecular dipole contribution, as shown in Figure 2.23: the surface dipole gained from the plasma treatment is lost upon immersion in the phosphonic acid solution in the early stages of phosphonate deposition. When the plasma sample is immersed in the PFBPA solution, after only 10 seconds the C/In ratio increases to 0.27 and the F/In goes from 0 to 0.10. However, as observed in Figure 2.21 the F/C deviates from the expected stoichiometry (0.39 vs 0.71), which suggests that there is a mixture of phosphonic acid and adventitious carbon. There is a significant valence band shift (+0.20 eV) relative to the bare plasma sample. This implies band bending or geometry rearrangement. This shift would normally cause an increase in the work function, but the surface dipole obtained through plasma treatment is lost after 10 s immersion. This is likely due to the pillow effect from the adsorbed, disordered phosphonic acid and additional contaminants not present on the air plasma sample before immersion. A control experiment where the plasma ITO is immersed in pure ethanol for

10 s leaves the work function intact but shifts the valence band maximum closer to E_F, in the same range as the 10 s immersion in 10 mM PFBPA solution does; hence, both the phosphonic acid and the ethanol, or whatever contaminants adhere to the ITO in this period, are responsible for the decrease in the intrinsic surface dipole of ITO. After 7 days the molecular dipole contribution from the phosphonate film is comparable with that of the bare plasma-cleaned ITO. The work function after such an immersion time is lower due to a shift in the valence band further from the Fermi level than that of plasma-clean ITO; again this can be due to geometry rearrangement or decrease of the band bending to its pre-plasma configuration.

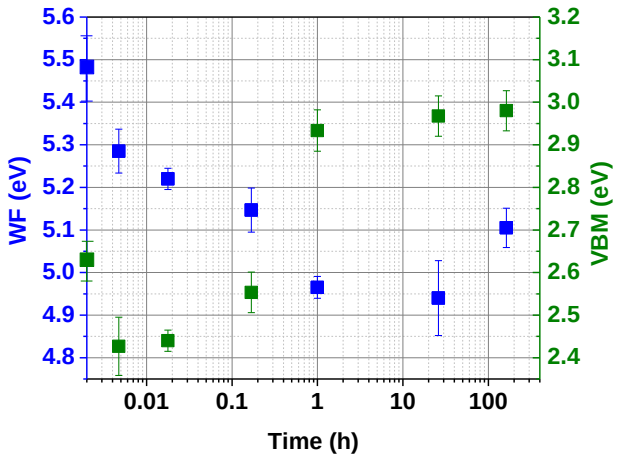

Figure 2.22 Room temperature, 10 mM PFBPA modification with air plasma pretreatment. Work function (WF, left axis) and valence band maximum (VBM, right axis) as a function of immersion time. The values for bare ITO are on the leftmost side of the plot.

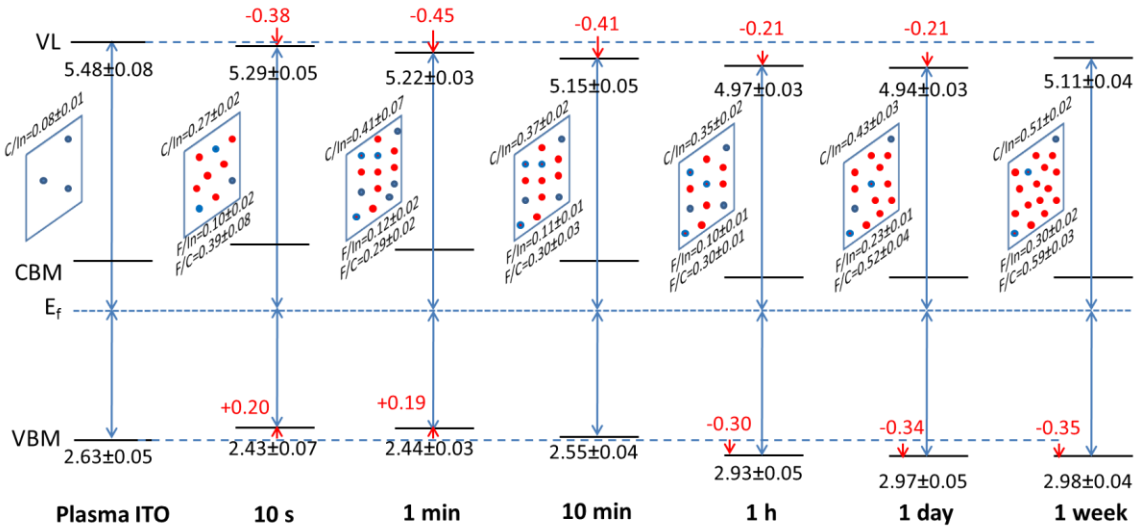

Figure 2.23 Energy level diagrams constructed from UPS data for plasma treated ITO, and different immersion times in 10 mM PFBPA solution at room temperature. Significant changes in vacuum potential or valence band maximum relative to starting DSC ITO are represented by the small red arrows at the vacuum level. Band gap assumed as 3.6 eV and maintained constant throughout. Blue circles represent adventitious carbon and red circles phosphonic acid.

By allowing the plasma cleaned sample to react for 7 days, the F/In ratio increases substantially (from 0.10±0.01 to 0.30±0.02) and the F/C approaches the expected ratio of 0.71 (reaching 0.59±0.03). Interestingly neither the F/In nor F/C seem to reach a plateau yet, which leads to the next set of experiments at high temperature. In comparison with the non-plasma set, the coverage and quality obtained for this plasma set in one day is similar to that of DSC-only ITO modified for a week (Figure 2.24).

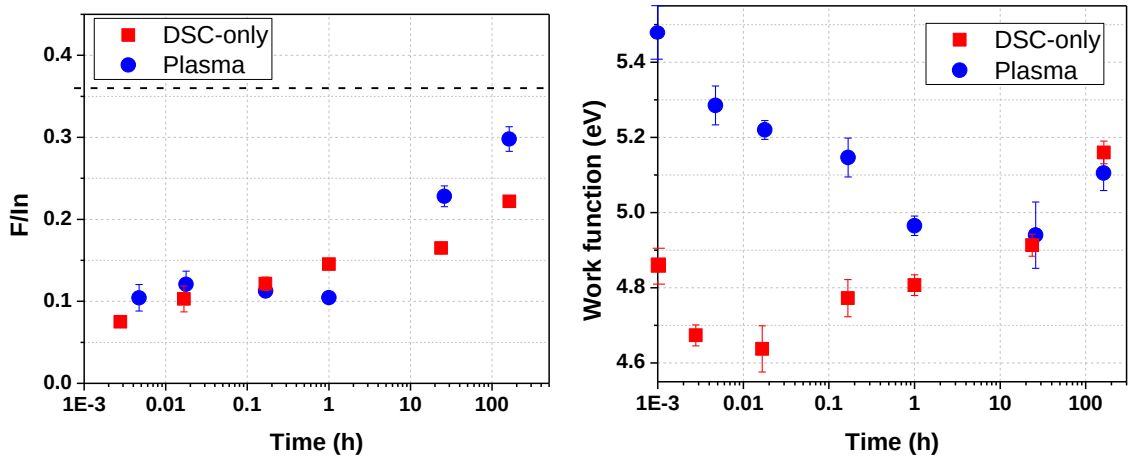

Figure 2.24 F/In and work function variation with time for modifications at room temperature for DSC ITO and plasma-cleaned ITO.

As mentioned in Chapter 1, infrared reflection-absorption spectroscopy (IRRAS) can be used to examine the binding modes of phosphonic acids on oxides. PFBPA has many peaks in the region where the phosphonate vibrations are observed. Figure 2.25a shows the transmission IR (on KBr pellet) of PFBPA. The assignment of the νP=O and νP-O(H) vibrations is difficult since νC-F and ring vibrations also appear in this region, so a comparison with benzyl phosphonic acid was done to aid in the signal assignment, as well as reports from literature.[33,34] Comparison of the IRRAS spectrum in the P-O vibrations region of one-week treated samples that underwent detergent/solvent cleaning *vs.* plasma cleaning (Figure 2.25b) shows that both samples display (very clearly) the C-F stretches, while all other signals have diminished (δC-C=C) or disappeared (ν_sP-O-H). There is a peak from the ITO itself that appears in this reflective geometry only for p-polarized light around 1260 cm^{-1}, consistent with the wavenumber expected for δO-H on the surface of a metal oxide;[35] given that the O-H groups are diminished after modification, when the spectral ratio of the modified sample over the bare sample is done, the peak appears negative and information on the phosphoryl group is masked by this negative absorption. Nonetheless, the disappearance of the symmetric (P-O)-H

stretch and what seems to be a small new peak around 1020 cm^{-1} consistent with mono/dibasic salt of PFBPA,[36] points to similar bidentate or tridentate chemisorption regardless of cleaning procedure.

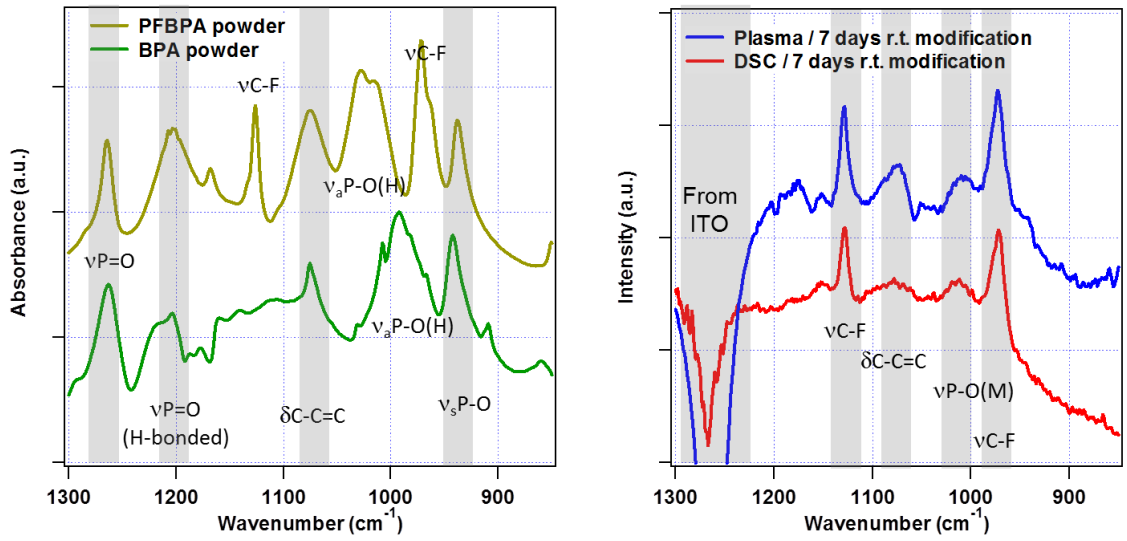

Figure 2.25 a) Transmission IR of PFBPA and BPA powders. b) IRRAS comparison of the phosphonic acid fingerprint region for room temperature treated samples.

2.3.2.3 High temperature modification on detergent/solvent-cleaned ITO

Given that using higher temperature during the immersion is expected to increase the rate constant (Equation 2.6), a new batch of samples was prepared, this time with immersions in PFBPA 10 mM EtOH solution at 75 °C (without plasma pretreatment) . As Figure 2.26 shows, using this protocol afforded the expected F/In ratio for a close-packed monolayer (0.36) after overnight deposition (F/In=0.34±0.01), with the monolayer quality tracking the coverage well as judged by the F/C ratios. This set fits the proposed model from Equation 2.5 with an $R^2 = 0.77$. An observed rate constant $k_{obs} = 4.3 \pm 2.7\ h^{-1}$ is obtained.

Given that k' = $k_{ads}c$, it translates into a k_{ads} of 4×10^2 $M^{-1}h^{-1}$ (Table 2.3).

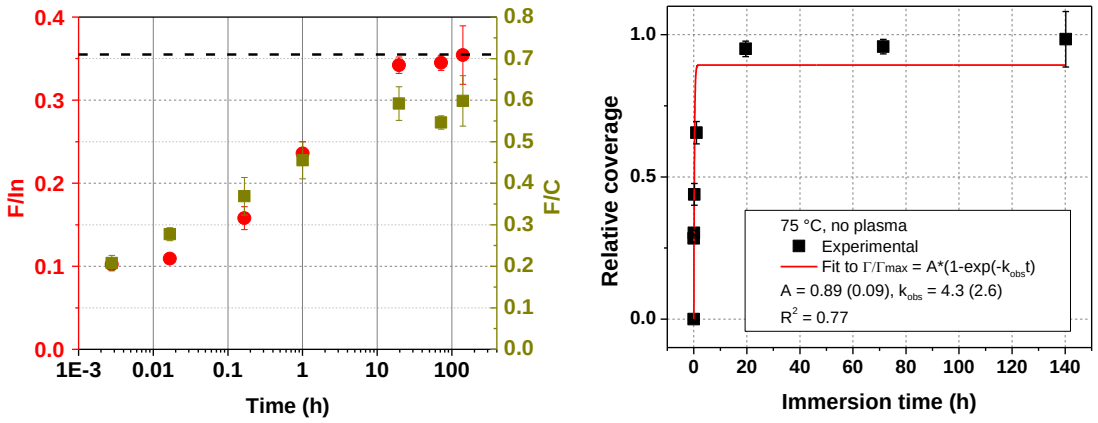

Figure 2.26 Left: F/In and F/C for modifications of DSC-only ITO at 75 °C. Right: Fit to first order rate law on available sites.

Table 2.3 Results from Langmuirian fit $\boldsymbol{\Gamma/\Gamma_{max} = A(1-\exp(-k_{ads}ct))}$ to adsorption kinetics for 10 mM PFBPA depositions at 75 °C.

Treatment	DSC-only / 75 °C	Plasma / 75 °C
Max. coverage *A*	0.89±0.09	0.93±0.06
k_{ads} /10^2 $M^{-1}h^{-1}$)	4±3	81±27
R^2	0.77	0.90

A summary of the findings for the electronic structure of samples modified using this protocol is shown in Figure 2.27. Short immersion times (10 s, 1 min) do not change the electronic structure of ITO; it is only after 10 min or more of immersion that significant molecular dipole contributions arise, and the valence band maximum is constant throughout, which means no net contribution from bond dipoles or geometry rearrangements.

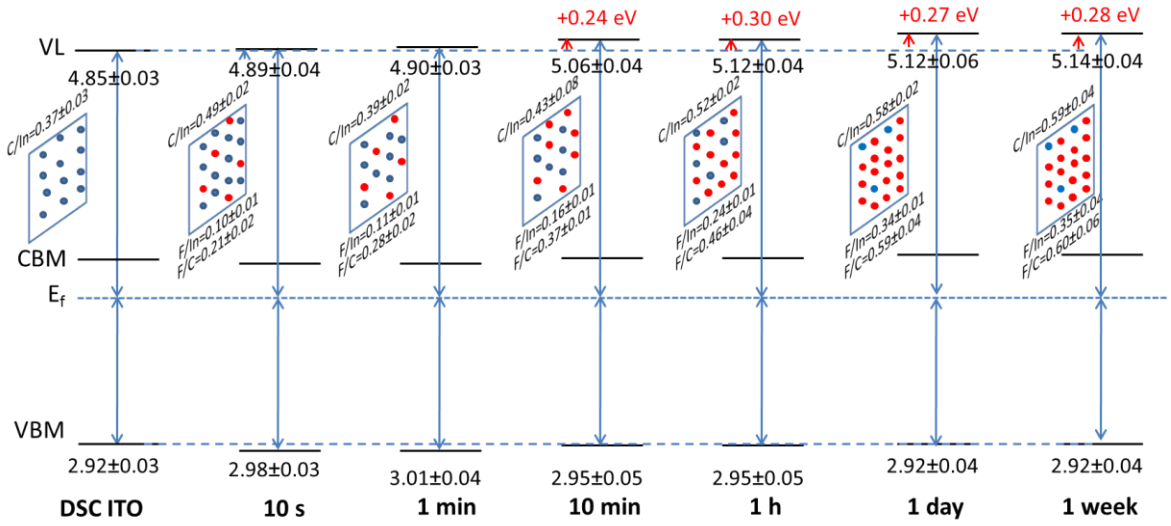

Figure 2.27 Summary of XPS and UPS results for DSC-only ITO modified with PFBPA 10 mM @ 75 °C. Significant changes in vacuum potential or valence band maximum relative to starting DSC ITO are represented by the small red arrows at the vacuum level. Band gap assumed as 3.6 eV and maintained constant throughout. Blue circles represent adventitious carbon and red circles phosphonic acid.

In Figure 2.28 the F/In ratio has been converted to absolute coverage as explained in Section 2.3, and the molecular dipole contributions deduced from UPS have been plotted as a function of coverage. A linear trend is observed for coverages up to 65% that of a close-packed monolayer, after which the dipole seems to saturate. This behavior is in line with strong depolarization at high coverages:[37] the molecular dipole contribution might no longer increase due to the counterbalancing effect of the electric field generated by the dipole moments of neighboring molecules. In the case in question, it appears that the depolarization offsets any increase in the sum of molecular dipoles, thereby leaving the vacuum potential unchanged.

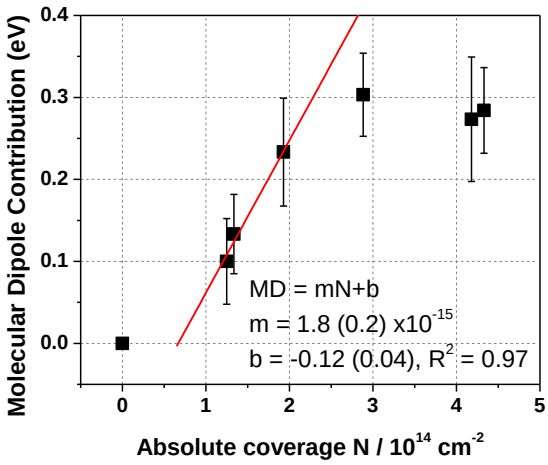

Figure 2.28 Molecular dipole contribution dependence on phosphonic acid coverage. A fit is shown for data in the range of the room temperature data from subsection 2.3.1.

A comparison of the relative coverage of the phosphonate film and work function changes for modifications on DSC-only ITO is shown in Figure 2.29. It can be seen that the high temperature deposition affords a high work function much faster than does the room temperature deposition, and this is due to the much faster adsorption kinetics.

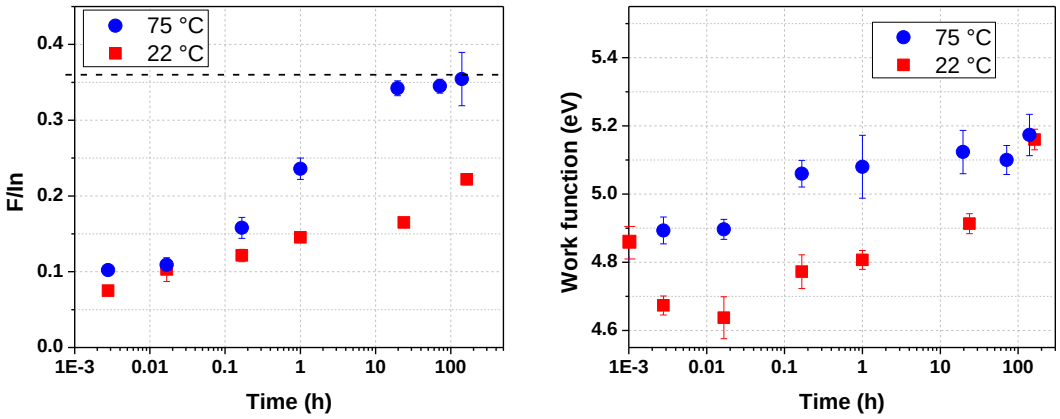

Figure 2.29 Comparison of F/In and work function for set of DSC-only samples modified at 75 °C and room temperature (22 °C).

2.3.3 High temperature modification after plasma pretreatment

To compare the results of DSC-only *vs.* plasma cleaning with 75 °C modification, a new batch of samples that underwent air plasma etching were prepared. To the left in Figure 2.30, the F/In and F/C are shown to increase in the first few minutes, and after just 10 min both the coverage and quality of the coating is in agreement with what is expected for a close-packed monolayer. The Langmuirian model fits very well (R^2 = 0.90), and results in k_{obs} and maximum coverage similar to those found with the oxygen plasma pretreatment at 75 °C from Section 2.3.1.

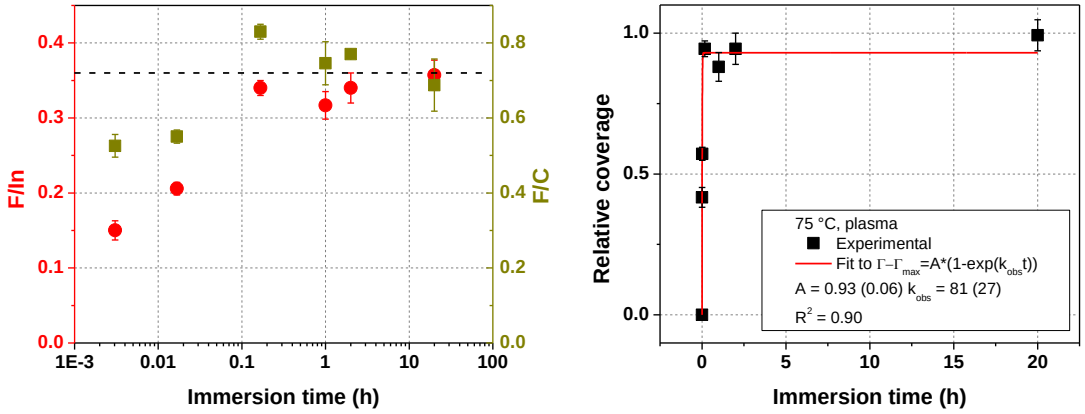

Figure 2.30 Left: F/In and F/C ratios for 75 °C immersion after plasma pretreatment. Right: fit of coverage to Langmuirian model.

As observed for the room temperature plasma-activated set, there is a decrease in the work function after the 10 s immersion attributed in part to the pillow effect, but in the 75 °C set the work function recovers after 1 min immersion and the ionization potential, defined for this system as the sum of the work function plus the valence band maximum, saturates (Figure 2.31): while there are changes in the work function, they are all explained by changes in the valence band maximum.

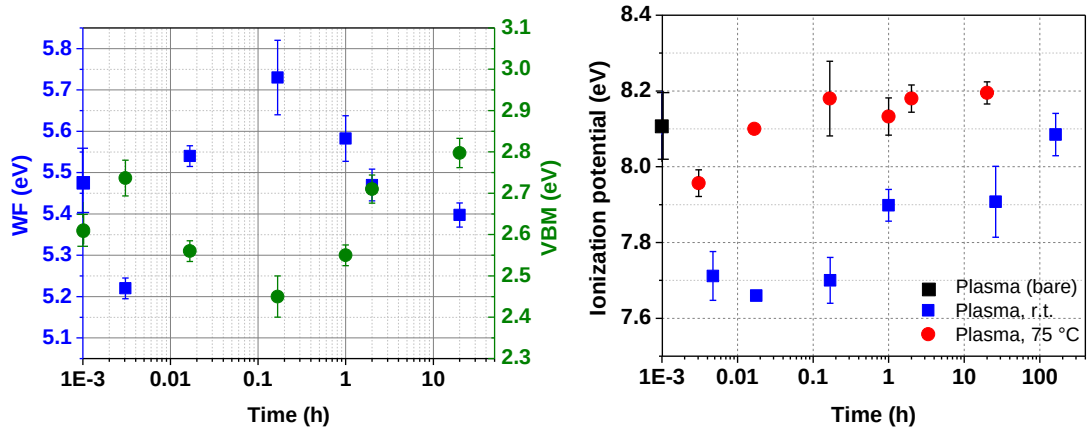

Figure 2.31 Left: work function (WF) and valence band maximum (VBM) progression immersion time for 75 °C treatment with plasma activation. Right: comparison of ionization potential for sets prepared with plasma pretreatment.

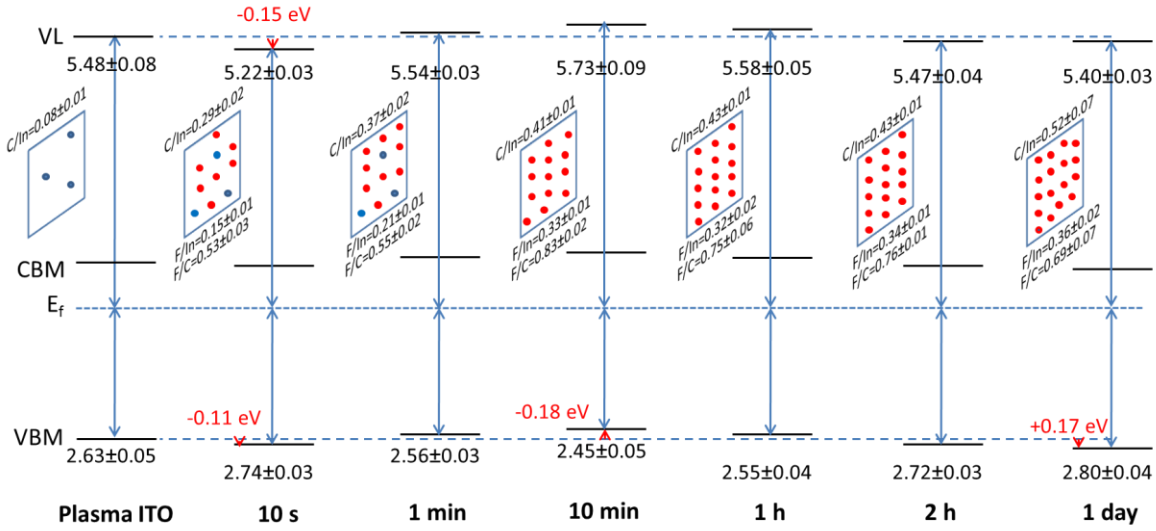

Figure 2.32 Summary of XPS and UPS results for plasma-cleaned ITO modified with PFBPA 10 mM @ 75 °C. Significant changes in molecular dipole or valence band maximum relative to starting DSC ITO are represented by the small red arrows at the vacuum level. Band gap assumed as 3.6 eV and maintained constant throughout. Blue circles represent adventitious carbon and red circles phosphonic acid.

Comparison of IRRAS for modifications done at 75 °C for one day with detergent/solvent-cleaned ITO *vs.* plasma cleaned ITO in the phosphonate region (Figure 2.33) shows only the C-F stretching modes, with no presence of the P-O(H) stretches.

Given the background signal present around 1260 cm^{-1}, where the P=O stretch would appear, no further assessment can be done other than say that in both cases the P-O (H) stretches have disappeared, which is consistent with at least bidentate attachment, just as in the case of the room temperature depositions.

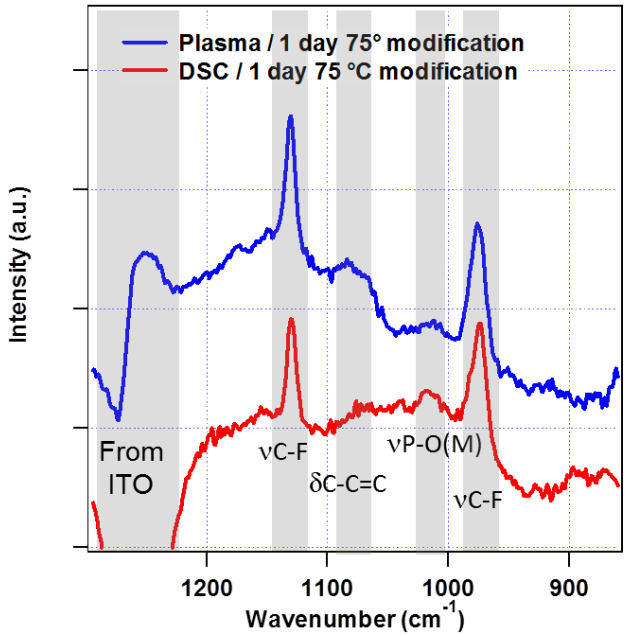

Figure 2.33 Comparison of IRRAS spectra for ITO modified with PFBPA for 1 day at 75 °C

Figure 2.34 shows a comparison of coverage, monolayer quality and ionization potential for all treatments studied in this section. It is clear that with plasma activation, after 10 min of immersion at 75 °C, close-packing in high quality is obtained, with saturation of the molecular dipole contribution. 75 °C without plasma achieves similar properties but needs several hours to do so; room temperature with or without plasma activation requires days to get to that state. It can be concluded that the order of adsorption kinetics and monolayer quality follows the trend AP 75 °C > DSC 75 °C > AP r.t. > DSC r.t.

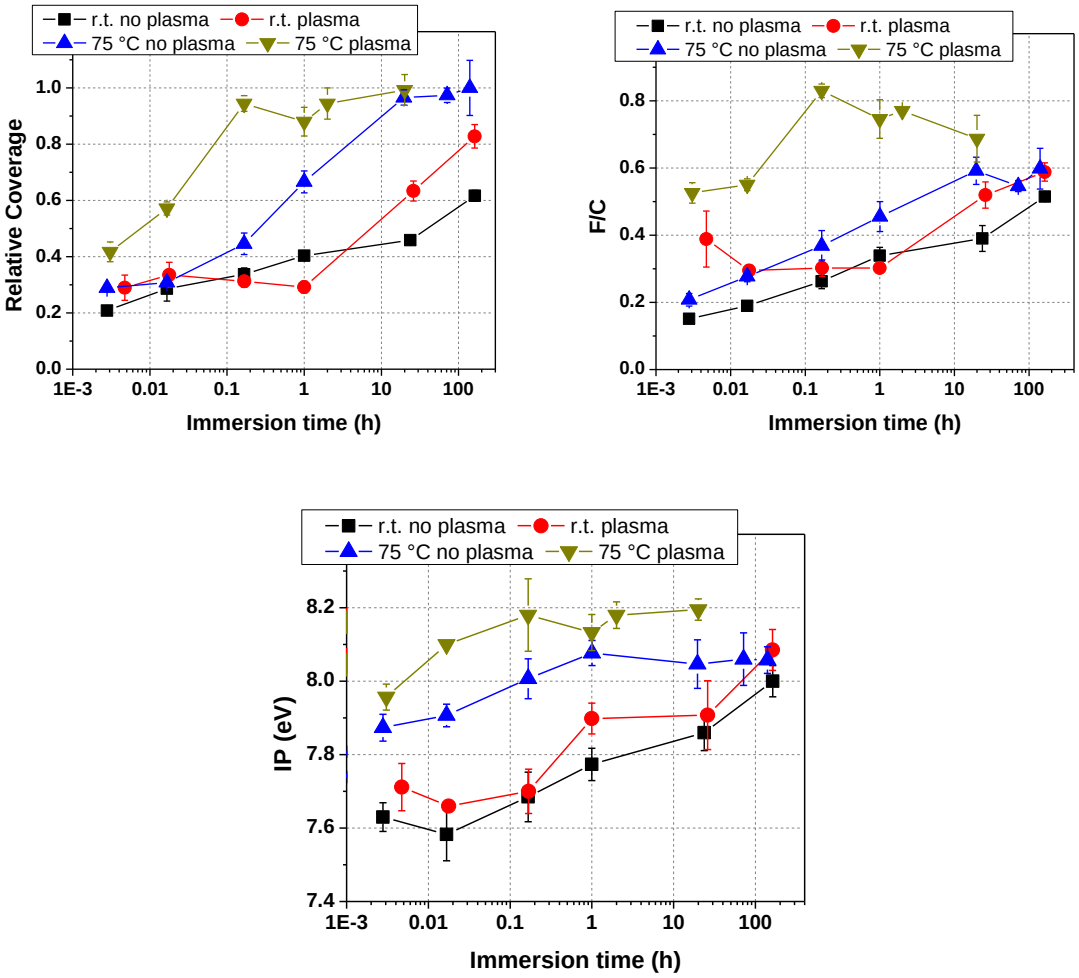

Figure 2.34 Coverage, monolayer quality and ionization potential of the phosphonate-modified ITOs for all treatments studied in Section 2.3.2.

2.4 XPS/UPS studies on modified ITO electrodes for bulk heterojunction solar cells

Using the knowledge acquired in Section 2.3, an analysis of how well the high temperature deposition performs for other phosphonic acids in the transparent conductive oxides used in BHJ solar cells follows. 4-Trifluoromethyl benzyl phosphonic acid (pCF_3BPA) and 2,6-difluorobenzyl phosphonic acid (oF_2BPA) were prepared by Anthony Giordano using published procedures.[4] ITO was detergent-solvent cleaned, and no plasma treatment was done. Reaction in 10 mM phosphonic acid solutions at 75 °C for 2 h followed. UPS results are summarized in Figure 2.35. For PFBPA

modification, no significant change in valence band maximum was found versus the starting bare ITO, but the work function increased significantly, which can be attributed to the molecular dipole. For pCF_3BPA, a somewhat large valence band maximum shift towards E_F was seen, which explains in part the higher increase in work function; oF_2BPA showed no significant molecular dipole or bond dipole, which left the work function unchanged.

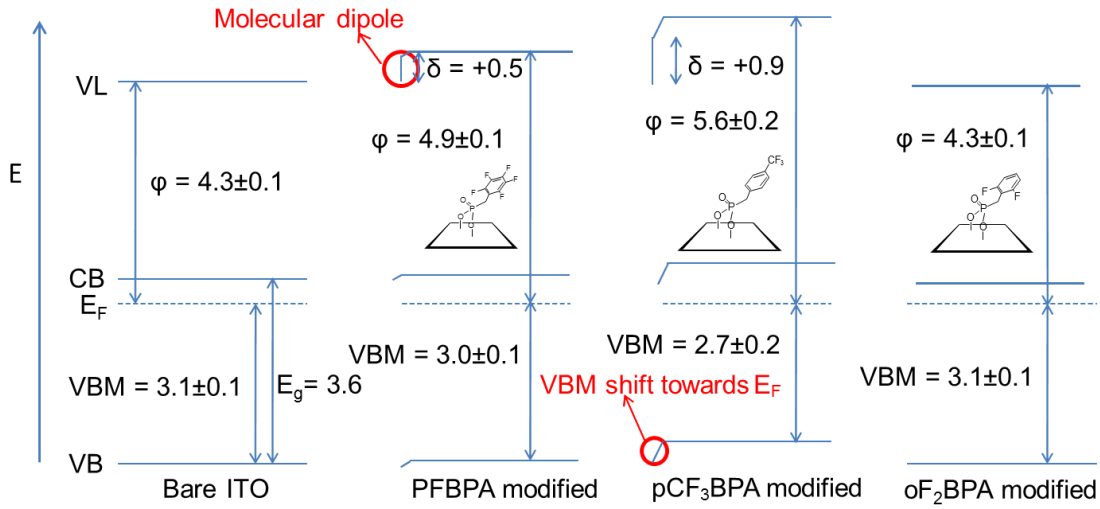

Figure 2.35 Energy level diagrams for solvent cleaned ITO and its modifications. All energies in eV.

In terms of the XPS data for the monolayers on ITO (Table 2.4), the coverage was very homogeneous, with F/In similar for PFBPA and oF_2BPA, and higher for pCF_3BPA which may be explained recalling that the CF_3 group is closer to the detector (hence increasing the F/In ratio). Likewise, the F/C for PFBPA and oF_2BPA are very close to the molecular stoichiometry, while for pCF_3BPA it was higher than the molecular stoichiometry, again attributable to the CF_3 group being closer to the detector then the other ring carbons.

Table 2.4 XPS data for monolayers on solvent cleaned ITO. Standard deviation (SD) for at least three spots.

Atomic ratios	Bare	SD	PFBPA -mod	SD	pCF3BPA -mod	SD	oF2BPA -mod	SD
C/In	0.39	0.02	0.69	0.03	0.85	0.03	0.53	0.01
F/In (adjusted for # of F atoms)			0.45 (0.09)	0.02	0.40 (0.13)	0.02	0.16 (0.08)	0.01
F/C (in a molecule)			0.66 (0.71)	0.01	0.47 (0.38)	0.03	0.31 (0.29)	0.02

It is concluded that using the same modification protocol (without plasma cleaning) for these phosphonic acids, high quality PA layers on ITO are obtained that induce large changes in work function, which is mostly attributed to molecular dipoles.

These phosphonic acids have been used by researchers at the National Renewable Energy Laboratory (NREL) and the University of Arizona to modify ITO for bulk heterojunction (BHJ) organic solar cells using PCDTBT and $PC_{71}BM$ as donor and acceptor, respectively (Figure 2.36).[21] In such a device, the difference betweenthe ionization potential of the donor (IP_D) and the electron affinity of the acceptor (EA_A) determines the maximum open circuit voltage (V_{OC}) under light (Figure 2.37), and the thermodynamic drive for photo-induced charge separation, which affects J_{SC}, is given by $\Delta G = EA_D - EA_A + EBE$, where EBE is the exciton binding energy.

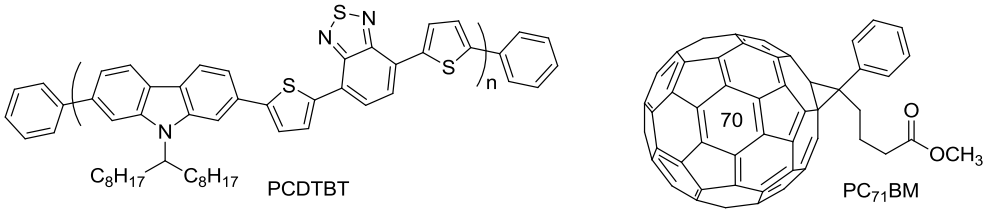

Figure 2.36 Molecular structures of PCDTBT and $PC_{71}BM$.

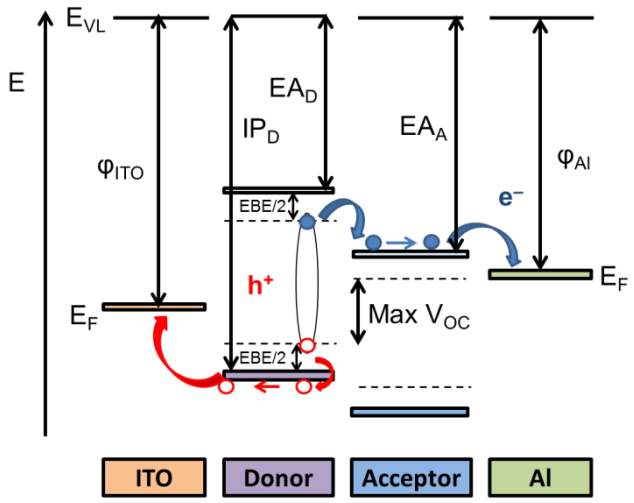

Figure 2.37 Scheme for excitonic solar cell operation, showing the organic heterojunction energy level diagram under illumination. An exciton (with an exciton binding energy EBE) is formed after absorption of photons with energy larger than the optical band gap (shown here at the donor layer), which may diffuse and reach the heterojunction, where it will dissociate transferring an electron into the acceptor. The charges can then be collected at appropriate electrodes.

However, that maximum open circuit voltage will also depend on relative position of the holes and electrons quasi-Fermi level (E_F,p and E_F,n respectively) that appear as the sample is no longer under equilibrium when illuminated. The extent of the separation between the two limits how much of the intrinsic max V_{OC} can be observed (Figure 2.38). Since the quasi-Fermi levels align with the Fermi levels of the corresponding collecting electrodes, a large difference in work function between the two electrodes can increase the V_{OC} extracted.[38] With these modifiers, the work function of the ITO can be modulated within 1.4 eV.

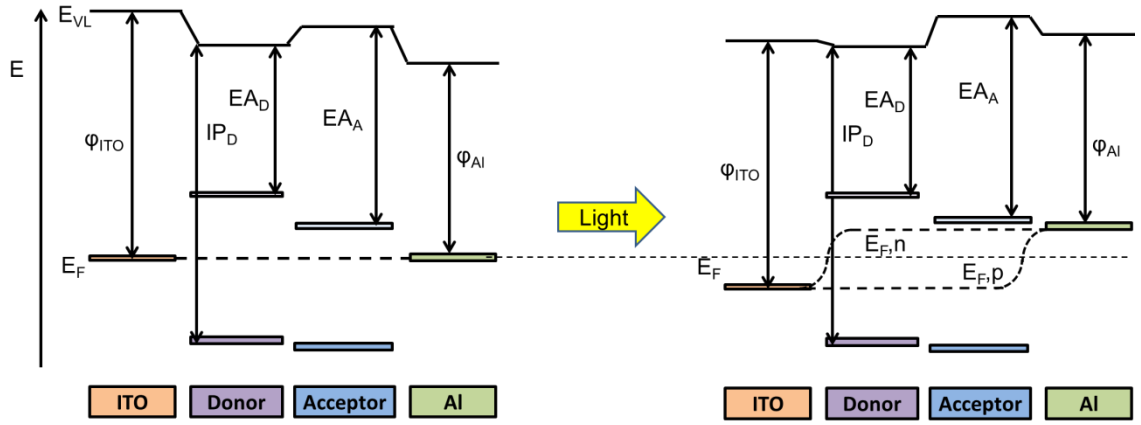

Figure 2.38 Energy level alignment in an OPV before and after illumination, with quasi-Fermi levels shown for the photo-generated electrons and holes shown. The maximum V_{OC} can be limited if the separation of quasi-Fermi levels is too small.

In this case, all ITOs were oxygen-plasma cleaned before modification or direct use as control as the anode, and all samples were prepared at NREL. The results are summarized in Table 2.5 and Figure 2.39. The figure shows that qualitatively the trend expected for V_{OC} was present, and from the table it can be observed that the current did not change significantly, so that the large variation in efficiency could be mostly explained from the increase in V_{OC} as the ITO work function increased, as has also been observed by others.[6]

Table 2.5 Work function (UPS) for the PA-modified ITO substrates and corresponding OPV device parameters from NREL-built PCDTBT/$PC_{71}BM$ BHJ solar cells.[21] IP of the donor is 5.4 eV. R_{SH} is the shunt resistance, PCE the photon-to-electron efficiency.

	oF_2BPA	ITO	PFBPA	pCF_3BPA
Φ, $E_{F,p}$ [eV]	4.1	5.0	4.9	5.5
μ_z [Debye]	0.11[a]	N/A	-1.75	-2.24
V_{oc} [mV]	516±6	631±21	785±10	828±0
J_{sc}[a] [mA cm^{-2}]	10.3	10.1	10.4	10.7
R_{SH} [Ohms]	$2.3(\pm1.1)\times10^2$	$6.1(\pm8.2)\times10^2$	$4.8(\pm5.6)\times10^2$	$3.4(\pm3.3)\times10^2$
FF [%]	51.9±0.7	56.6±0.5	57.4±1.0	61.5±0.0
PCE[a] [%]	2.7	3.6	4.5	5.4

[a)] Uncertainty in $J_{SC} \leq 0.3$ mA cm^{-2} and *for PCE* ≤ 0.2 %.

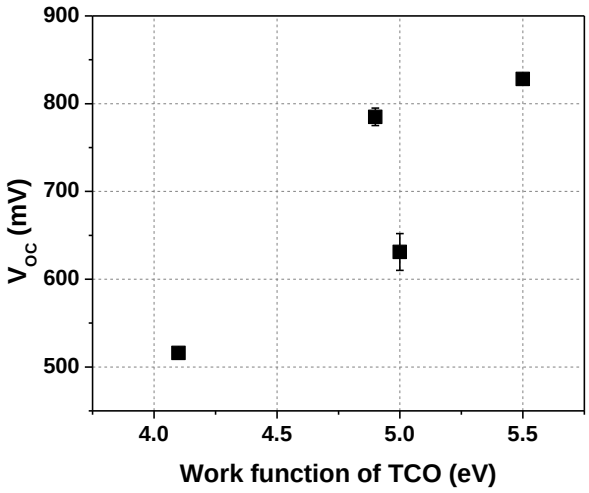

Figure 2.39 Dependency of the open circuit voltage in PCDTBT/PC71BM solar cells with the work function of the anode.

2.5 Phosphonic acid modification of NiO_x

In excitonic solar cells, a mixture of poly(3,4-ethylenedioxythiophene) and poly(styrenesulfonate), PEDOT:PSS, is usually used between the active layer and the hole collecting electrodes. This hole transport layer (HTL) aids in charge extraction, blocks electrons from getting to the transparent conductive oxide, and enhances the electric field across the active layer. However, PEDOT:PSS has issues in uniformity, stability, and is very acidic.[23] NiO_x thin films, consisting of oxygen-deficient (p-doped) nickel oxide, are being considered as replacement for PEDOT:PSS in OPVs as hole transport layers given their appropriate energy levels, tunable electric properties, non-acidity and solution processability.[39,40]

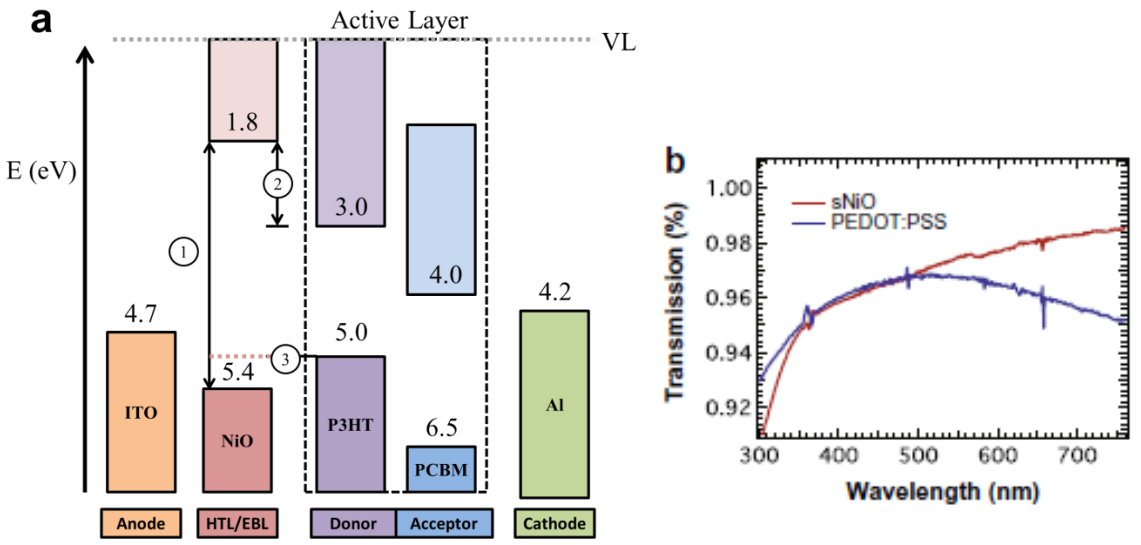

Figure 2.40 (a) Energy levels of a typical P3HT/PCBM OPV with NiO_x hole-transport layer between the active layer and ITO. Notice 1) wide band gap for transparency 2) small electron affinity to block electrons and 3) Fermi-level lineup with HOMO from donor for hole collection. (b) Transmission comparison for solution processed NiO_x and PEDOT:PSS. (a) adapted and (b) reproduced from Steirer, *et al*.[39]

The Ginley group from NREL has produced solution deposited NiO_x (5-10 nm thick) on ITO from a patented precursor Ni ink developed in-house, nickel ethylene diamine in formate medium,[41] that allows direct processing via ink jet or continuous flow printing, resulting in a film that rivals those produced with vacuum deposition in its conductivity and work function as applied in OPVs.[42] However, the wetting properties are still that of a highly polar oxide, and the work function after plasma treatment sees a decrease over time, even in inert atmosphere, which indicates that the surface chemistry is changing. It would be desirable if a high work function could be achieved without plasma treatment, and if the surface energy could be tuned. The use of phosphonic acids with the appropriate end groups were hypothesized to solve these issues, as had been accomplished on ITO, and the next section summarizes the efforts toward this goal.

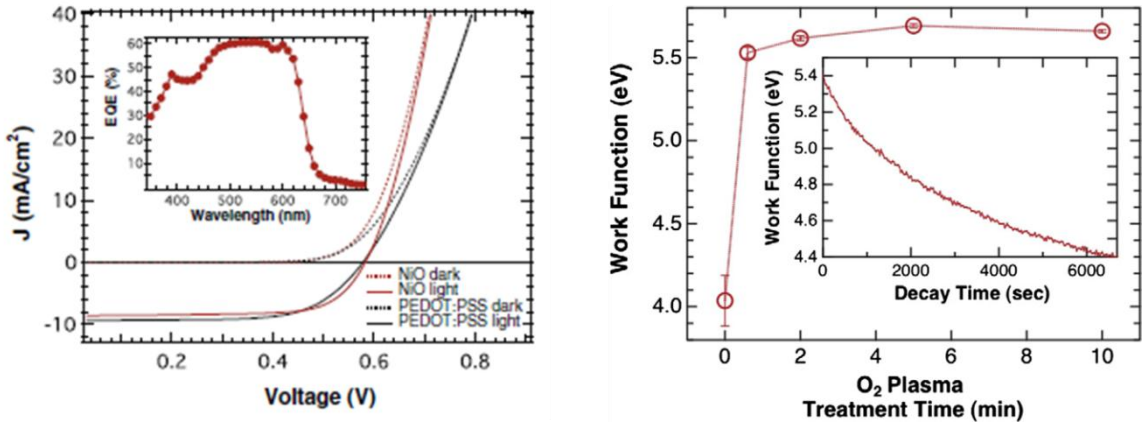

Figure 2.41 Left: Comparison of P3HT:PCBM device behavior with NiOx and PEDOT:PSS as HTL. Right: Work function adjustment of NiOx/ITO electrode with O_2 plasma treatment time, and its decay under N_2 atmosphere. Modified from Steirer, *et al.*[39]

2.5.1 Optimizing conditions for PA modification of NiO_x

Solution processed NiO_x on ITO films were received from the Ginley group at NREL. All samples underwent sonication in ethanol for cleaning, and then two of them were treated with PFBPA at room temperature (r.t.) and 75 °C, and two with 2,6-difluorobenzylphosphonic acid (OF_2BPA) (also at r.t. and 75 °C). Another four underwent the same PA treatments after additional activation with short-time oxygen plasma etching to see if there was a difference in PA overlayer quantity and quality with and without activation (Figure 2.42). All immersions were for ~20 h.

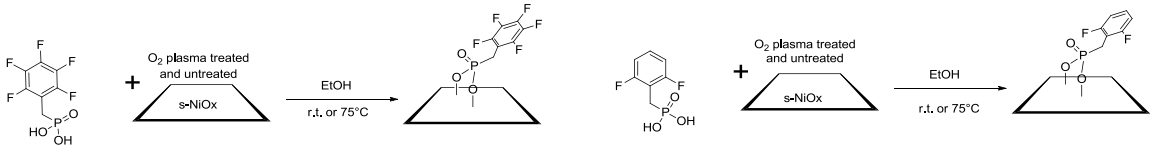

Figure 2.42 s-NiO_x modification with PFBPA and oF_2BPA for XPS studies.

Figure 2.43 summarizes the XPS results. Most samples showed significant variation in Ni/In ratios, even the control samples that were cleaned but not treated with PAs. This is not surprising since the films were so thin that film inhomogeneities could be even observed by eye. Oxygen plasma treatment resulted in cleaner surfaces (as evidenced by C/Ni for non-PA treated control samples) but no significant difference in

coverage (judged through F/Ni). Looking at this F/Ni ratio, it is clear that deposition at 75 °C gave better coverage than at room temperature for the same acid. The PFBPA treatment typically resulted in 2-3 times more F than with oF_2BPA (expected 2.5×) under the same conditions.

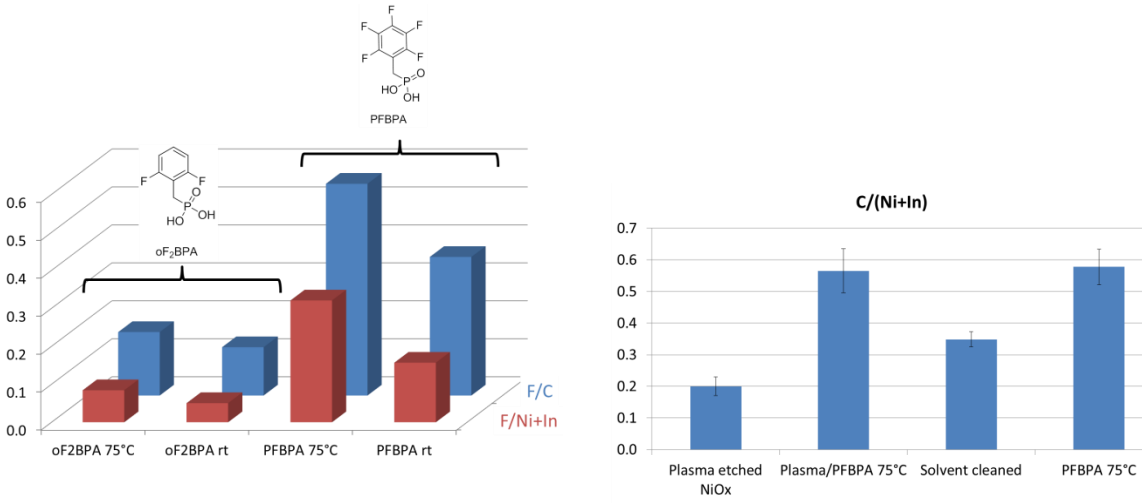

Figure 2.43 Left: XPS results for NiOx on ITO modified with PFBPA and OF_2BPA without plasma pretreatment. Right: C/metals ratios comparing plasma *vs.* no plasma bare and PFBPA treated samples.

2.5.2 Origin of the work function changes in PA modified NiO_x

UPS allowed studying the energetics of the surfaces in question, which would help to fully characterize the system in case of use in devices. pCF_3BPA from the previous section was incorporated into the study, as it was expected to increase the work function of NiO_x further, given the ITO results. The immersion time was shortened given what was learned from the ITO experiments in Section 2.3. After a brief sonication in EtOH (no plasma etching), the samples were put to react as stated with 10 mM solutions for a couple of hours and the results characterized by XPS and UPS.

2.6 shows some of the XPS results; the Ni/In ratios varied substantially from sample to sample, but the C/Ni, F/Ni and F/C seem to be consistent with each other given the number of carbon and fluorine atoms present in each monolayer. Figure 2.45

compares F/C ratios with those obtained on ITO. AFM images showed RMS roughness of 2.4-3.0 nm for a PFBPA modified sample as well as for an unmodified sample (Figure 2.46), so it seems that no major change on the surface in induced by the phosphonic acid treatment.

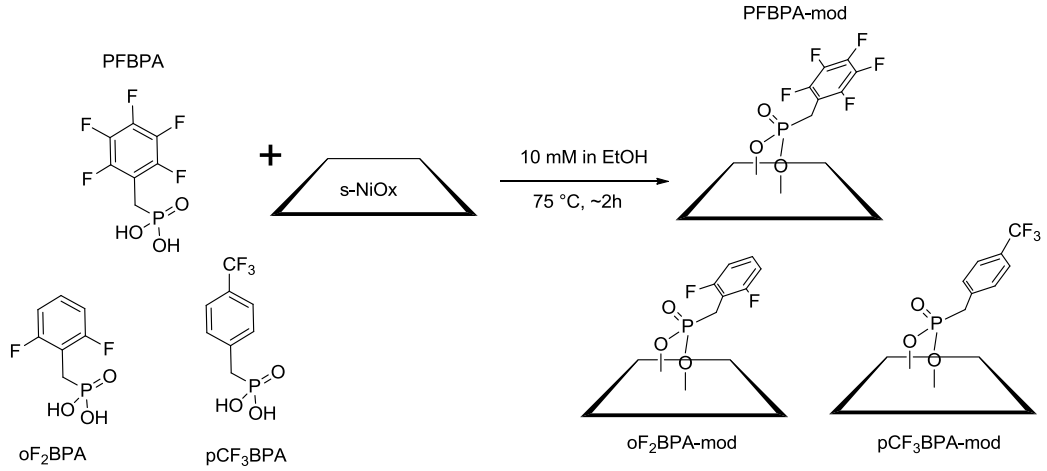

Figure 2.44 Modification of NiO_x with dipolar PAs for XPS/UPS/AFM studies.

Table 2.6 XPS data for monolayers on solvent cleaned NiO_x on ITO. Standard deviation (SD) from at least three spots.

Atomic ratios	Bare	SD	PFBPA -mod	SD	pCF_3BPA-mod	SD	oF_2BPA -mod	SD
Ni/In	13	1	8.9	0.5	0.85	0.03	0.53	0.01
C/Ni	0.73	0.05	0.45	0.03	0.40	0.02	0.16	0.01
F/Ni			0.23	0.01	0.17	0.03	0.09	0.01
F/C (in a molecule)			0.52 (0.71)	0.04	0.42 (0.38)	0.09	0.20 (0.29)	0.01

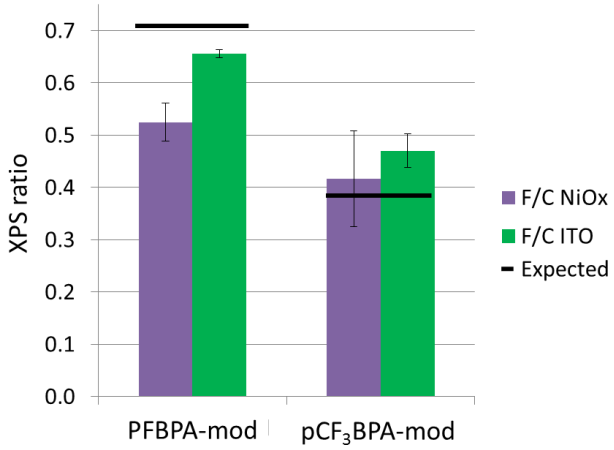

Figure 2.45 XPS ratios obtained for NiOx on ITO and ITO itself for comparison. Black lines state expected stoichiometric value.

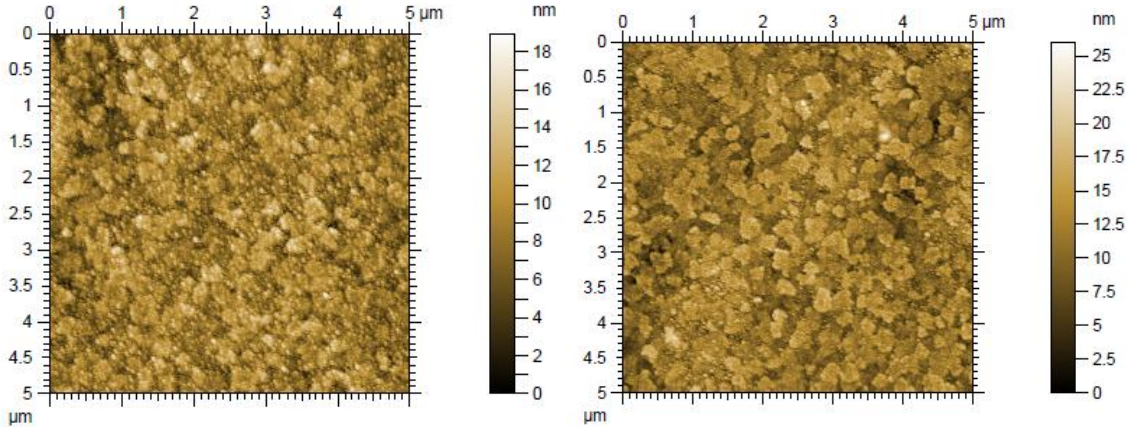

Figure 2.46 AFM topography images for PFBPA modified NiO_x/ITO (left) and bare NiO_x/ITO (right).

The induced molecular dipole and band bendings could be followed by UPS, and the results are summarized in Figure 2.47. As observed in the previous section for ITO, oF_2BPA did not induce a significant molecular dipole, but the valence band maximum shifted slightly towards the Fermi level, and hence the slight increase in work function. PFBPA and pCF_3BPA did contributed significant molecular dipoles, as observed for ITO. Hence, it can be concluded that using the same modification protocol as for ITO, similar quality phosphonic acid layers are obtained on NiO_x, and the electronic properties follow similar changes.

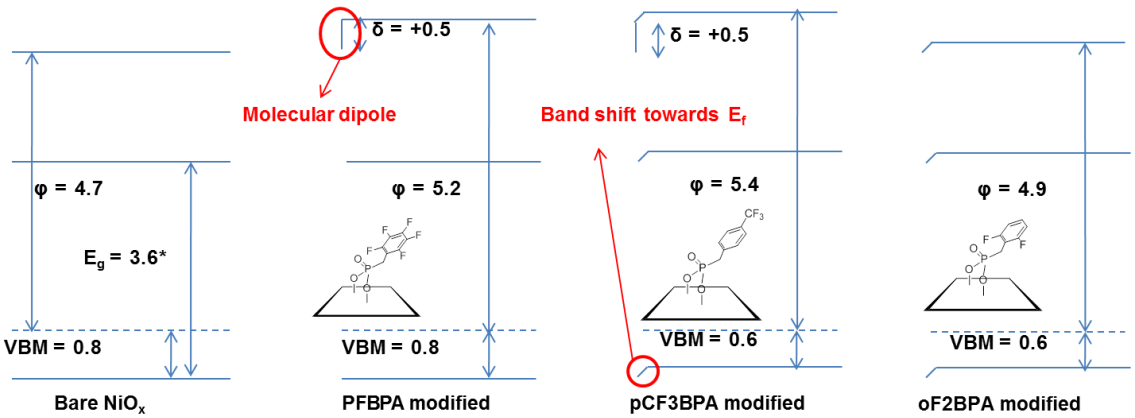

Figure 2.47 Energy level diagram from UP spectra for each modification of thin NiO_x films on ITO. All values are in eV, and had standard deviations within 0.1 eV.

Collaborators at NREL used PFBPA to modify s-NiO_x and used it in P3HT:PCBM and PCDTBT:$PC_{70}BM$ OPV devices; the treatments lead to an increase in V_{OC} while the J_{SC} stayed constant relative to bare NiO_x, similar to what is observed with plasma treated substrates.

Table 2.7 Characterization of P3HT:PCBM and PCDTBT:$PC_{70}BM$ OPV devices. Data from Dr. Andres Garcia, NREL.

P3HT:PCBM	V_{OC} (mV)	J_{SC} ($mAcm^{-2}$)	Fill Factor (%)	PCE (%)
NiO_x	444	10.3	54	2.3
NiO_x-OP	550	10.3	61	3.3
NiO_x-PFBPA	550	10.2	64	3.4
PEDOT:PSS	556	10.1	64	3.4
PCDTBT:$PC_{70}BM$	V_{OC} (mV)	J_{SC} ($mAcm^{-2}$)	Fill Factor (%)	PCE (%)
NiO_x	720	10.3	55	4.0
NiO_x-OP	848	10.8	65	5.9
NiO_x-PFBPA	848	10.7	65	5.7
PEDOT:PSS	839	11.1	61	5.4

2.6 Spray coating as an alternative to dip coating phosphonic acids

The optimization efforts for dip coating TCOs with phosphonic acids throughout this chapter have been promising, but it would be desirable to take a step further and be

able to deposit high quality monolayers in a matter of seconds. Dr. Bulusu in the Graham group (Mechanical Engineering, Georgia Tech) examined deposition of PFBPA on ITO, indium-zinc oxide (IZO), NiO_x, and ZnO using a spray coating technique, with our collaboration.[43] The approach (Figure 2.48) consists of spraying a 5-10 mM ethanolic PA solution onto heated oxide substrates: the process relies on the creation of small liquid droplets at room temperature that impinge on the heated substrate, undergoing evaporation. Given that ethanol has a relatively low boiling point, this limits the application of simple immersion to reflux temperatures, but with this alternate approach, the droplets will simply evaporate faster on the heated substrate. Once the solvent has evaporated, the substrate is left to rest on the hot plate for 2 min, time during which additional heterocondensation reactions between the phosphonate and metal oxide can occur. To ensure removal of multilayers, the same base-rinse sonication applied for dip coating is used.

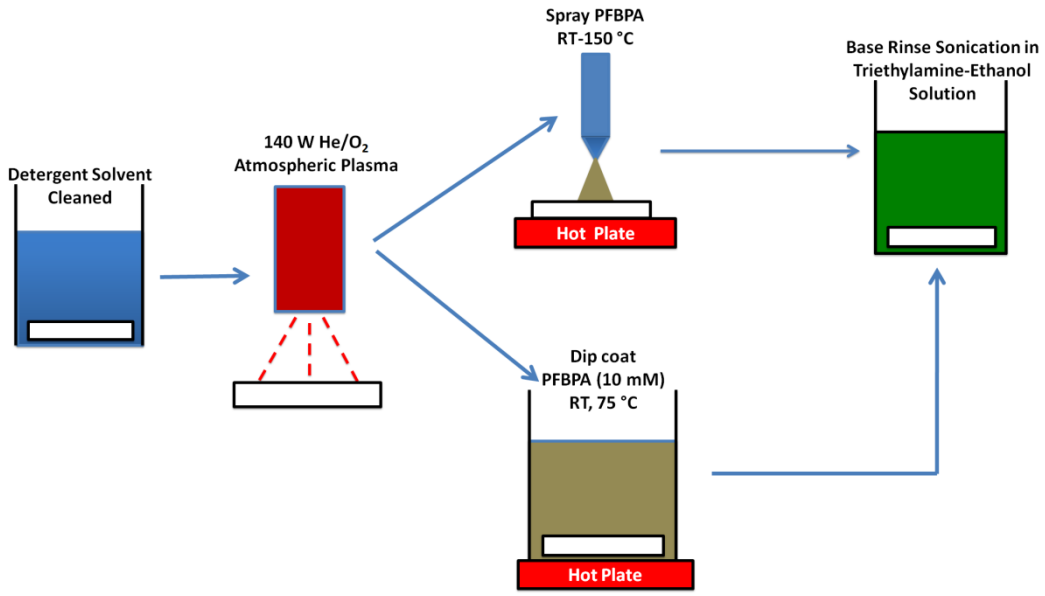

Figure 2.48 Schematic of the surface modification process through dip and spray coating methods. Reproduced from Bulusu, *et al.*[43]

Figure 2.49 shows results from spray coating of PFBPA on ITO and IZO, comparing the XPS F/In ratio (as a means to follow the chemisorption) at different

temperatures, and contrasts it with immersion deposition at the same temperature (room temperature and 75 °C, for 1 h as reported by Dr. Bulusu). For ITO, it is observed that spray coating seems to give slightly higher coverage than dipping for 1 h at the same temperature, even though it only takes 1 minute for the spray coating plus 2 min resting time on the hot plate. It is possible the evaporation of the solvent leads to a quasi-Langmuir deposition as described by D.K. Schwartz and J. Schwartz in their papers that were summarized in Chapter 1.[44,45] Deposition at temperatures over 100 °C led to significantly higher adsorption in the same amount of time. In fact, spray coating at 150 °C gives a F/In ratio of 0.38, close to the expected value of 0.36 for a close-packed monolayer, as explained in Section 2.2. Given that IZO consists of 70% In, 30% Zn, the indium content is lower and hence the F/In ratios are higher at all deposition temperatures, but a similar trend to that on ITO is observed. AFM showed no significant differences in roughness or morphology between the spray-treated samples at different temperatures, which is noteworthy given that Zn-containing oxides may suffer etching in acidic medium.[46] Indeed the author of this thesis verified that high temperature dip coated IZO exhibited some morphological changes (Figure 2.50). It seems the short times of contact with the phosphonic acid solution when spray coating do not etch.

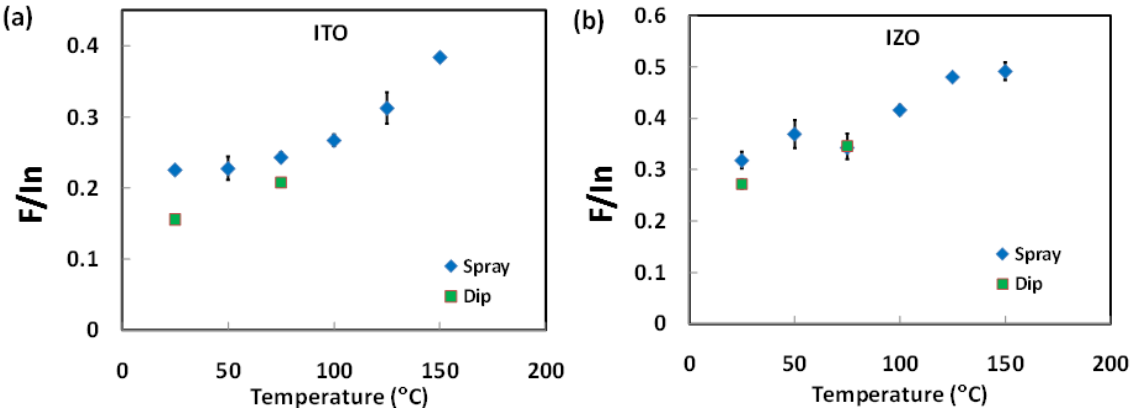

Figure 2.49 XPS-determined F/In as a function of substrate temperature in the case of spray coating and solution temperature in the case of dip coating for (a) ITO substrates and (b) IZO substrates. Data acquired by Dr. Anu Bulusu.

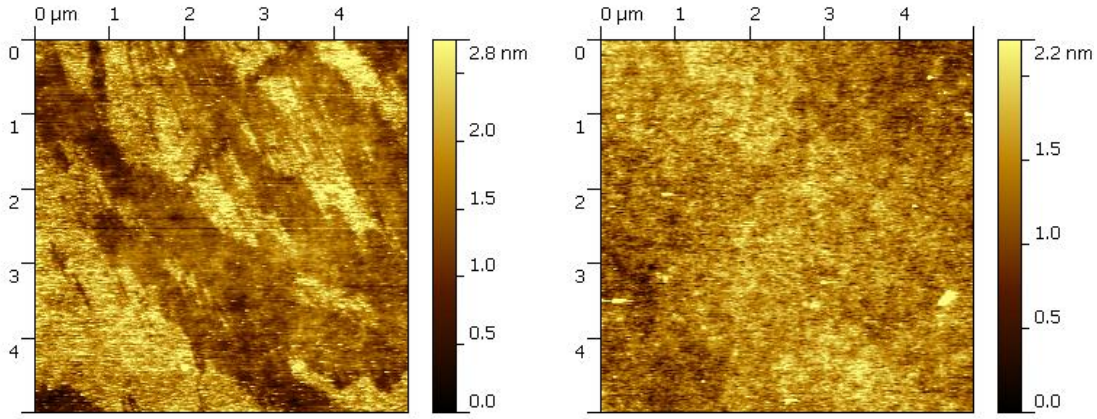

Figure 2.50 Atomic force micrographs for 1 h 75°C dip-coated IZO (left) and 1 min 75°C spray coated / 2 min heated IZO (right).

To compare the effectiveness of spray coating vs. dip coating when using the TCOs in real devices, P3HT/ICBA (bis-indene C_{60}) solar cells were built and tested using ITO coated with PEDOT:PSS vs. PFBPA deposited by spray coating and dip coating. The results (Figure 2.51 and Table 2.8) show comparable performance for all anodes.

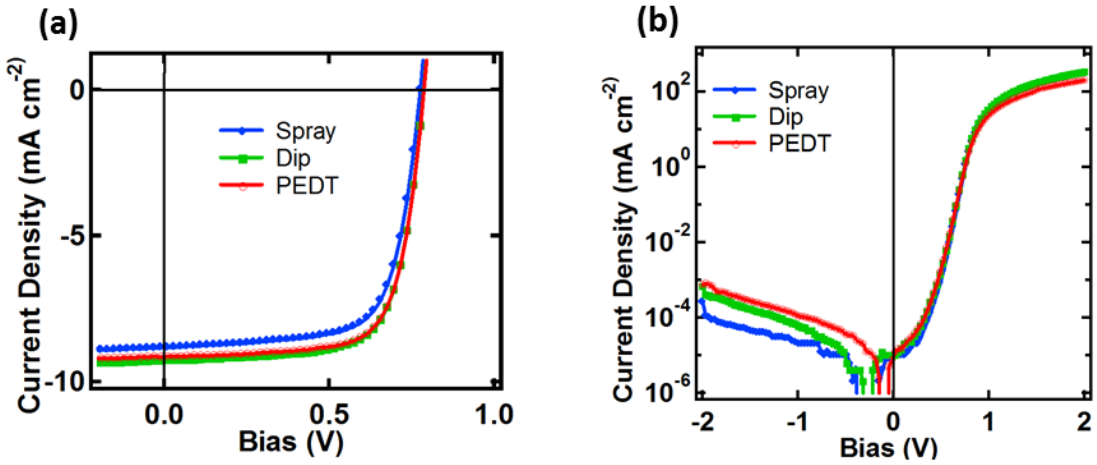

Figure 2.51 Organic solar cell current density response to applied bias, averaged for 5 device measurements under solar simulated illumination (a) and in the dark (b), for devices with PEDOT-modified ITO (red), PFBPA dip-coated ITO (green), and PFBPA spray-coated ITO (blue). Data acquired by Dr. Brad McLeod and Ajaya Sigdel (NREL).

Table 2.8 Average device characteristics of organic solar cells prepared with different surface treatments. Data from NREL.

Surface Treatment	V_{OC} [mV]	J_{SC} [mA cm^{-2}]	FF [%]	PCE [%]
PEDT	791 ± 0.004	9.1 ± 0.1	71.4 ± 0.3	5.2 ± 0.1
Dip Coat 75 °C	794 ± 0.009	9.3 ± 0.1	70.8 ± 0.4	5.2 ± 0.1
Spray Coat 75 °C	780 ± 0.012	8.8 ± 0.2	69.9 ± 0.5	4.8 ± 0.2

Spray coating is a promising approach, but some process optimization is required for reproducible results. In addition to substrate temperature, variation in surface coverage through spray coating can be achieved by changing the spray pressure, flow rate, and the distance of the nozzle from the substrate that in turn will change the impingement velocity and the deformation and breakup of the droplets striking the surface. Figure 2.52 shows the result of a study of the influence that the pressure of the N_2 line has on the deposition. The surface coverage decreased at 40 psi, leading to a decrease in work function. Impact and spreading dynamics on a solid surface for free falling droplets have been studied by other researchers who found that numerous factors affect the droplet spreading such as surface wettability, roughness and temperature, viscosity of the droplet and impact velocity;[47,48] keeping all other parameters constant, increasing the droplet impact velocity could cause the droplet to partially rebound from the surface leading to improper depositions. It is expected that in the case of spray depositions performed under pressure, additional factors such as droplet breakup, deformation at the nozzle, as well as residence time on the surface could also have an impact on surface coverage and would require additional investigations.

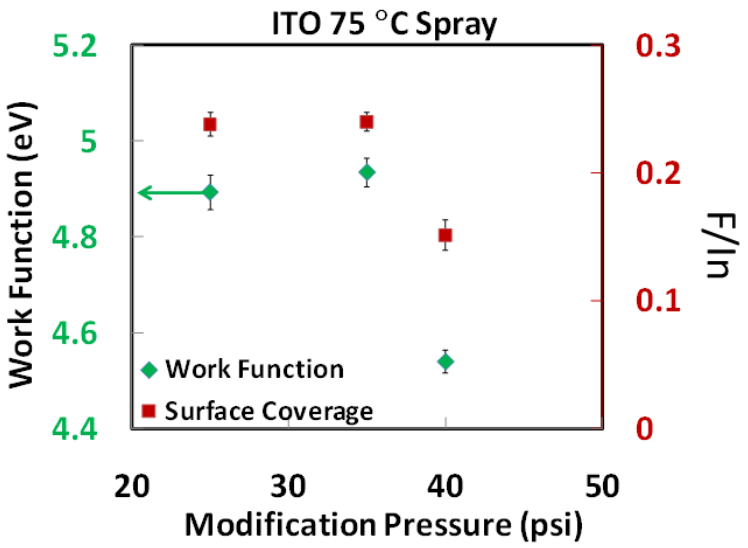

Figure 2.52 Work function of ITO modified with PFBPA using various spray pressures, plotted as a function of XPS F/In. Data acquired by Dr. A. Bulusu.

2.7 Conclusions

The main goal of this chapter was to present an analytical study on the deposition of a phosphonic acid on ITO from the perspective of coverage, quality of monolayer, and induced electronic structure changes. In a first study to settle on a concentration for further experiments, XPS was used to track the F/In ratio (proportional to the phosphonic acid coverage) for varying non-sequential deposition times, probing 1 mM, 10 mM and 100 mM in times from 10 s to 1 week. Since the fastest observed kinetics, were for 10 mM, that concentration was used for the second study. For the next set of experiments, XPS, UPS, and IRRAS were used to track not only the adsorption kinetics but also the quality of the deposited phosphonate film and the work function and valence band changes brought upon by the modifier, using room temperature and 75 °C deposition, and cleaning with just detergent/solvent (DSC) and using air plasma (AP). It was concluded that the order of adsorption kinetics and monolayer quality follows the trend AP 75 °C > DSC 75 °C > AP r.t. > DSC r.t. A very good monolayer quality and coverage can be obtained with air plasma activation and 75 °C deposition using a 10 mM solution in 10 min. The ionization potential increase by the plasma activation decreases upon immersion

in the acid solution, and is only recovered with sufficient coverage of the phosphonic acid, whose molecular dipole contribution saturates at a coverage *ca.* 65% that of a close-packed monolayer, likely due to depolarization effects. The binding modes in all cases seem similar, at least for long immersion times.

The second part of the chapter showed the application of PFBPA and related phosphonic acids for modification of transparent conductive oxides (TCOs) used as anodes in OPVs; these were also characterized by XPS and UPS, and devices built and tested by our collaborators, which showed that the main effect of the monolayer coatings in on modulating the open circuit voltage of the device. Finally, the technique of spray coating, developed by Bulusu for chemisorption of phosphonic acids on TCOs (with assistance from the author of this thesis) is a promising approach for the industrial-scale use of these nano-scale coatings for organic electronics.

2.8 Experimental

PFBPA, oF_2BPA, and pCF_3BPA were prepared as previously reported.[4] ITO substrates (Colorado Concepts, 9-15 Ω/□, RMS ~ 3 nm –for Section 2.3- and TFD Films, 20 Ω/□, RMS ~ 0.8 nm –for Section 2.4) were detergent / solvent cleaned by scrubbing with cloth soaked with Triton X-100 in water, followed by 10 min successive sonications in diluted Triton X-100, deionized water and ethanol. AFM scans for surface roughness measurements were obtained using an Agilent 5600ls in AC mode with a 100 μm scanner head using Tip B from MikroMasch NCS35/No Al (typical resonant frequency 315 kHz, spring constant 14 N/m) at 0.5 lines/s.

For Section 2.3.1, concentration comparison, O_2 plasma treatment was done in a Plasma Preen II at 100% power for 3 min. For deposition temperature comparison, a PE-50 etcher (Plasma Etch, Inc., Carson City, NV) at 50% power fed with O_2 was used for 3 min. For phosphonic acid depositions, 10 mM ethanolic solutions were placed in round bottom flasks, or vials and the slides immersed and removed according to the scheduled

immersion times, then immediately rinsed with fresh EtOH, dipped in EtOH and finally placed in 5% triethylamine solution in EtOH to sonicate for 30 min, time after which they were rinsed with EtOH and blown dried. The samples were kept under N_2 and the time between preparation and XPS analysis minimized as much as possible, never exceeding more than a day. XPS was performed in a Thermo K-Alpha with monochromated X-rays (12 kV, 6 mA) with a spot size of 400 μm and a take off angle of 90° relative to the surface.

For Section 2.3.2, the plasma cleaning was done in a Harrick plasma cleaner PDC-001 at high power for 3 min, typically at a pressure of 200 mTorr. PA modifications were done as above but sonication in 5% triethylamine was for 10 min. Loosely-capped amber bottles were used for high temperature deposition. A Kratos Axis Ultra^{DLD} XPS/UPS system was used for analysis of samples. All samples were in electronic equilibrium with the spectrometer via a metallic clip on the sample and characterizations were performed at normal take-off angle. XPS using monochromatic Al Kα line was run at a base pressure of 10^{-9} Torr with the Fermi level calibrated using atomically clean silver. Spot size was *ca.* 700 μm. Survey XPS scans were run at 160 eV pass energy and high resolution scans typically at 20 eV pass energy and 100 meV steps, while UPS was acquired at 5 eV pass energy and 0.05 eV step size with the aperture and iris set to 55 μm. XPS peak fits were done with Vision Processing Software 2.2.8 using mixed Gaussian/Lorentzian distributions to minimize χ^2.

A dry air-purged Digilab FTS-600 FT-IR instrument equipped with an MCT detector was used for measuring IR absorption spectra of powders in pressed KBr. 32 scans were collected for each spectrum with 2 cm^{-1} resolution. Each transmission spectrum was referenced to the transmission spectrum of pure KBr. A grazing-angle accessory (80° angle of incidence, from Pike) was employed in the IRRAS studies. The light was p-polarized with a gold grid polarizer from Perkin-Elmer. The resolution was 2

cm–1 and the mirror speed used was 1.28 cm/s. 4000-6000 scans were collected for each sample. DSC-only and air plasma cleaned ITO were used as references accordingly.

For Section 2.5, the bare NiO_x was used as is or plasma cleaned in the PE-50 as reported above; 1 min of sonication in EtOH was used to remove unreacted PAs. XPS was performed in a Thermo K-Alpha as reported above for initial studies, and for the later studies the Kratos Axis was used, as reported above.

2.9 References

(1) Queffélec, C.; Petit, M.; Janvier, P.; Knight, D. A.; Bujoli, B. *Chem. Rev.* **2012**, *112*, 3777.

(2) Hotchkiss, P. J.; Jones, S. C.; Paniagua, S. A.; Sharma, A.; Kippelen, B.; Armstrong, N. R.; Marder, S. R. *Acc. Chem. Res.* **2011**, *45*, 337.

(3) Paniagua, S. A.; Hotchkiss, P. J.; Jones, S. C.; Marrikar, F. S.; Mudalige, A.; Pemberton, J. E.; Marder, S. R.; Armstrong, N. R. *J. Phys. Chem. C.* **2008**, *112*, 7809.

(4) Hotchkiss, P. J.; Li, H.; Paramonov, P. B.; Paniagua, S. A.; Jones, S. C.; Armstrong, N. R.; Brédas, J.-L.; Marder, S. R. *Adv. Mater.* **2009**, *21*, 4496.

(5) Knesting, K. M.; Hotchkiss, P. J.; MacLeod, B. A.; Marder, S. R.; Ginger, D. S. *Adv. Mater.* **2012**, *24*, 570.

(6) MacLeod, B. A.; Horwitz, N. E.; Ratcliff, E. L.; Jenkins, J. L.; Armstrong, N. R.; Giordano, A. J.; Hotchkiss, P. J.; Marder, S. R.; Campbell, C. T.; Ginger, D. S. *J. Phys. Chem. Lett.* **2012**, *3*, 1202.

(7) Doubina, N.; Jenkins, J. L.; Paniagua, S. A.; Mazzio, K. A.; MacDonald, G. A.; Jen, A. K.-Y.; Armstrong, N. R.; Marder, S. R.; K., L. C. *Langmuir* **2012**, *28*, 1900.

(8) Sontag, S. K.; Sheppard, G. R.; Usselman, N. M.; Marshall, N.; Locklin, J. *Langmuir* **2011**, *27*, 12033.

(9) Love, J. C.; Estroff, L. A.; Kriebel, J. K.; Nuzzo, R. G.; Whitesides, G. M. *Chem. Rev.* **2005**, *105*, 1103.

(10) Butt, H.-J.; Graf, K.; Kappl, M. *Physics and Chemistry of Interfaces*; Wiley-VCH: Weinheim, 2003.

(11) Kolasinski, K. *Surface Science: Foundation of Catalysis and Nanoscience*; John Wiley & Sons Ltd.: Chichester, 2008.

(12) Vercelli, B.; Zotti, G.; Schiavon, G.; Zecchin, S.; Berlin, A. *Langmuir* **2003**, *19*, 9351.

(13) Lyklema, J. *Fundamentals of Interface and Colloid Science Vol II: Solid-Liquid Interfaces*; Academic Press: London, 1995.

(14) Chang, C.-H.; Franses, E. I. *Colloid Surface A* **1995**, *100*, 1.

(15) Hibbert, D. B.; Gooding, J. J.; Erokhin, P. *Langmuir* **2002**, *18*, 1770.

(16) Noggle, J. *Physical Chemistry*; 3rd ed.; HarperCollins: New York, 1996.

(17) Giza, M.; Thissen, P.; Grundmeier, G. *Langmuir* **2008**, *24*, 8688.

(18) Pellerite, M. J.; Dunbar, T. D.; Boardman, L. D.; Wood, E. J. *J. Phys. Chem. B* **2003**, *107*, 11726.

(19) Chockalingam, M.; Darwish, N.; Le Saux, G.; Gooding, J. J. *Langmuir* **2011**, *27*, 2545.

(20) Jo, K.; Yu, H.-Z.; Yang, H. *Electrochim. Acta* **2011**, *56*, 4828.

(21) Ratcliff, E. L.; Garcia, A.; Paniagua, S. A.; Cowan, S. R.; Giordano, A. J.; Ginley, D. S.; Marder, S. R.; Berry, J. J.; Olson, D. C. *Adv. Energy Mat.* **2013**, *3*, 647.

(22) Ma, H.; Yip, H. L.; Huang, F.; Jen, A. K. Y. *Adv. Funct. Mater.* **2010**, *20*, 1371.

(23) Sharma, A.; Haldi, A.; Potscavage Jr, W. J.; Hotchkiss, P. J.; Marder, S. R.; Kippelen, B. *J. Mater. Chem.* **2009**, *19*, 5298.

(24) Sharma, A.; Haldi, A.; Hotchkiss, P. J.; Marder, S. R.; Kippelen, B. *J. Appl. Phys.* **2009**, *105*, 074511.

(25) Zhou, Y.; Shim, J. W.; Fuentes-Hernandez, C.; Sharma, A.; Knauer, K. A.; Giordano, A. J.; Marder, S. R.; Kippelen, B. *PCCP* **2012**, *14*, 12014.

(26) Paramonov, P. B.; Paniagua, S. A.; Hotchkiss, P. J.; Jones, S. C.; Armstrong, N. R.; Marder, S. R.; Brédas, J. L. *Chem. Mater.* **2008**, *20*, 5131.

(27) Seah, M. P.; Dench, W. A. *Surf. Interface Anal.* **1979**, *1*, 2.

(28) Giordano, A. J.; Gliboff, M.; Hyla, A.; Li, H.; Knesting, K. M.; Nordlund, D.; Brédas, J. L.; Ginger, D. S.; Marder, S. R. *Manuscript in preparation*.

(29) Woodruff, D. P.; Delchar, T. A. *Modern Techniques of Surface Science*; 2nd ed.; Cambridge University Press: Cambridge, 1994.

(30) Witte, G.; Lukas, S.; Bagus, P. S.; Woll, C. *Appl. Phys. Lett.* **2005**, *87*, 263502.

(31) Li, H.; Paramonov, P.; Bredas, J.-L. *J. Mater. Chem.* **2010**, *20*, 2630.

(32) Kim, J. S.; Ho, P. K. H.; Thomas, D. S.; Friend, R. H.; Cacialli, F.; Bao, G.-W.; Li, S. F. Y. *Chem. Phys. Lett.* **1999**, *315*, 307.

(33) Thomas, L. C. *Interpretation of the Infrared Spectra of Organophosphorous Compounds*; Heyden & Son, Ltd.: London, 1974.

(34) Danilich, M. J.; Burton, D. J.; Marchant, R. E. *Vib. Spectrosc* **1995**, *9*, 229.

(35) Shinoda, K.; Aikawa, N. *Phys. Chem. Miner.* **1997**, *24*, 551.

(36) Smith, O. N.; Li, E.; Nwachokor, P.; Marder, S. R. *Manuscript in preparation*.

(37) Romaner, L.; Heimel, G.; Ambrosch-Draxl, C.; Zojer, E. *Adv. Funct. Mater.* **2008**, *18*, 3999.

(38) Ratcliff, E. L.; Zacher, B.; Armstrong, N. R. *J. Phys. Chem. Lett.* **2011**, *2*, 1337.

(39) Steirer, K. X.; Chesin, J. P.; Widjonarko, N. E.; Berry, J. J.; Miedaner, A.; Ginley, D. S.; Olson, D. C. *Org. Electron.* **2010**, *11*, 1414.

(40) Ratcliff, E. L.; Meyer, J.; Steirer, K. X.; Armstrong, N. R.; Olson, D.; Kahn, A. *Org. Electron.* **2012**, *13*, 744.

(41) Ginley, D. S.; Curtis, C. J.; Miedaner, A.; van Hest, M. F. A. M.; Kaydanova, T. 2008; Vol. US Patent 0003364 A1.

(42) Berry, J. J.; Widjonarko, N. E.; Bailey, B. A.; Sigdel, A. K.; Ginley, D. S.; Olson, D. C. *IEEE J. Quantum Electron.* **2010**, *16*, 1649.

(43) Bulusu, A.; Paniagua, S. A.; MacLeod, B. A.; Sigdel, A. K.; Berry, J. J.; Olson, D. C.; Marder, S. R.; Graham, S. *Langmuir* **2013**, *29*, 3935.

(44) Woodward, J. T.; Ulman, A.; Schwartz, D. K. *Langmuir* **1996**, *12*, 3626.

(45) Hanson, E. L.; Schwartz, J.; Nickel, B.; Koch, N.; Danisman, M. F. *J. Am. Chem. Soc.* **2003**, *125*, 16074.

(46) Hau, S. K.; Cheng, Y.-J.; Yip, H.-L.; Zhang, Y.; Ma, H.; Jen, A. K. Y. *ACS Appl. Mater. Interfaces* **2010**, *2*, 1892.

(47) Mao, T.; Kuhn, D. C. S.; Tran, H. *AIChE J.* **1997**, *43*, 2169.

(48) Rioboo, R.; Tropea, C.; Marengo, M. *Atomization Spray* **2001**, *11*, 12.

CHAPTER 3 GRAFTING NON-CONJUGATED POLYMERS VIA CONTROLLED RADICAL POLYMERIZATION FROM $BATIO_3$ NANOPARTICLES

Modification of surfaces using densely grafted polymers have attracted attention as a novel approach with applications in lithography,[1] corrosion resistance,[2] bio-compatibility,[3] and to generate materials responsive to solvent, pH, ion, or temperature,[4] as well as fabrication of electronic materials.[5] In this chapter, a phosphonic acid with an initiating moiety for atom transfer radical polymerization (ATRP) is used to synthesize polystyrene and polymethylmethacrylate composites from $BaTiO_3$ nanoparticles, which can have application in hybrid dielectrics. Section 3.1 offers an introduction for modification of barium titanate with phosphonic acids and explains some of the physics behind capacitors and the use of hybrid dielectrics. Section 3.2 introduced the polymerization chemistry used in this chapter, and the subsequent sections focus on the several approaches pursued, the development of the ATRP protocol for the $BaTiO_3$/polystyrene system. The chapter concludes with device results and comparison with other reports.

3.1 Phosphonic acid functionalization of $BaTiO_3$ and use in hybrid capacitors

Phosphonic acids form good monolayers on $BaTiO_3$ (BTO) nanoparticles and thin films. As part of this author's Master's research while at the Armstrong group in Arizona, the modification of BTO films 2 nm-thick on Ag-coated glass slides was done with octadecylphosphonic acid (ODPA) and a tridecafluorooctylphosphonic acid (FHOPA) to model the surface composition of similarly modified BTO nanoparticles.[6] The resulting surfaces were characterized by XPS, UPS, contact angle, and IRRAS. The expected XPS

peaks for P, F and C were present, and the IR data were consistent with bidentate attachment (Figures 3.1 and 3.2).

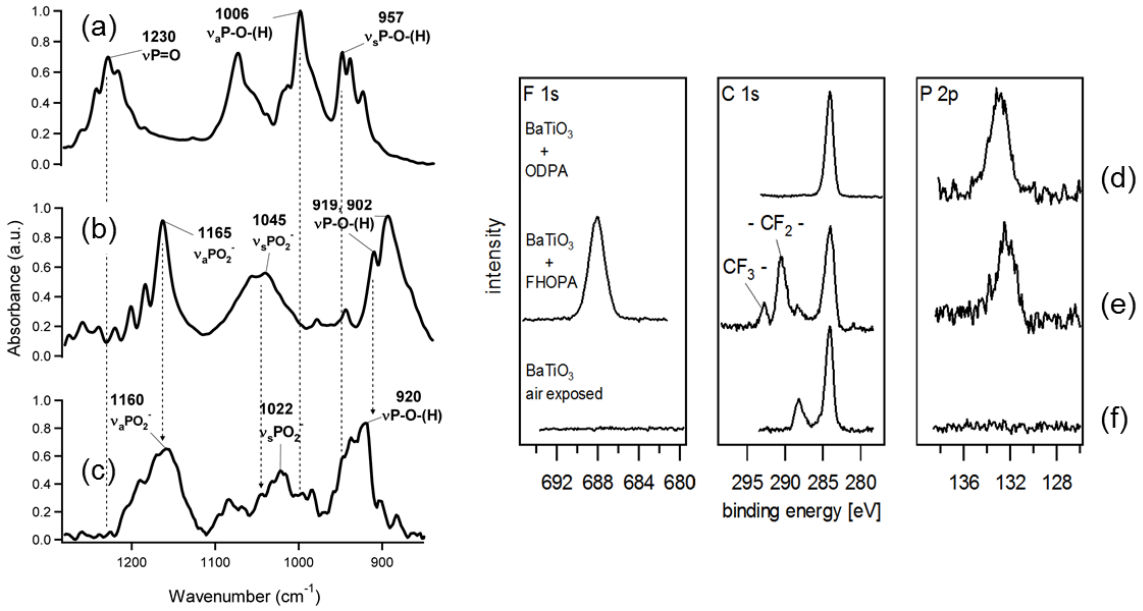

Figure 3.1 Left: comparison of IR spectra in the phosphonate stretch region: (a) Transmission IR of ODPA, (b) transmission IR of monobasic potassium salt of ODPA (K^+PA^-), and (c) PM-IRRAS of ODPA attached to ITO. Right: Comparison of XPS core level spectra before and after modification with ODPA and FHOPA. Reproduced from Schulmeyer, *et al*.[6]

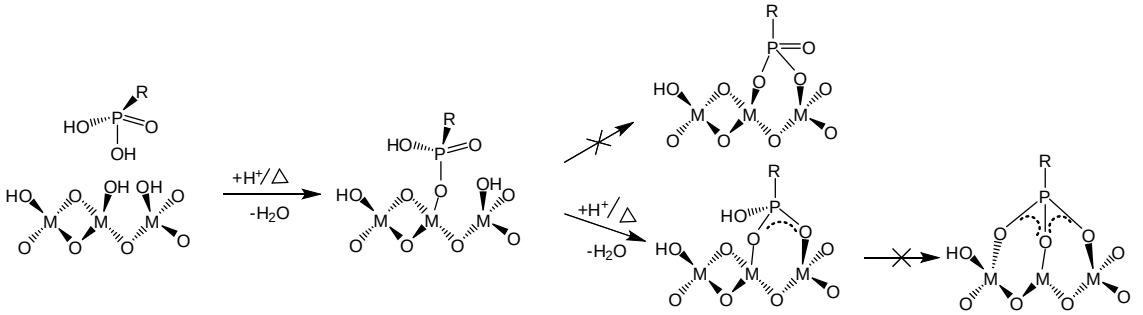

Figure 3.2 Proposed reactions of ODPA with BTO based on the characterization results for BTO thin films.

Parallel to this work, the Perry, Marder, and Kippelen groups at Georgia Tech examined the modification of BTO nanoparticles (50 nm) with various anchoring groups bearing a n-octyl tail.[7] Comparison of the FT-IR and TGA of the particles subjected to

the same modification conditions with a phosphonic acid (OPA), a sulfonic acid (OSA), a triethoxysilane (OTMOS) and a carboxylic acid (OCA) with the same tail group showed that only the OPA yielded significant attachment, while the others gave low or negligible coverage (Figure 3.3).

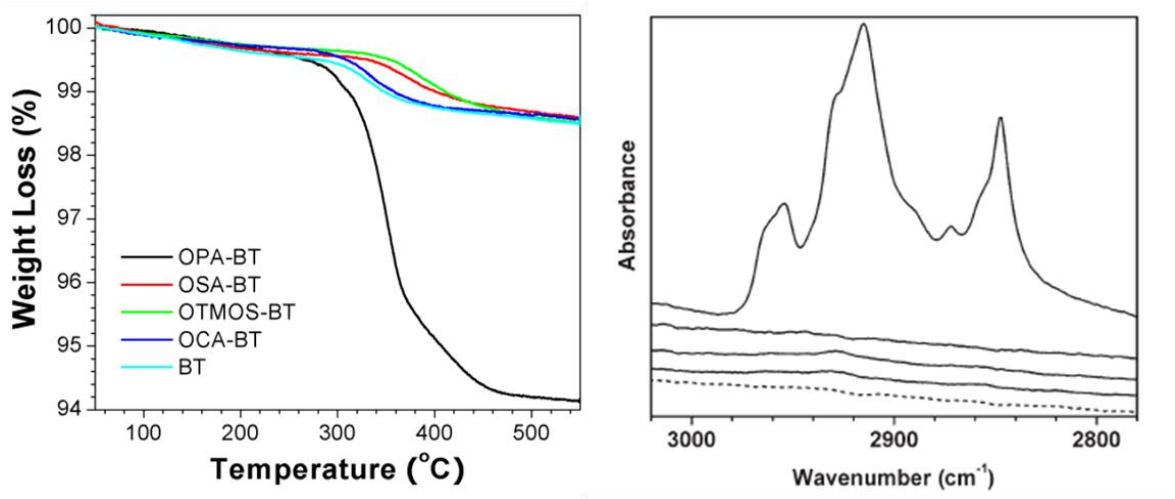

Figure 3.3 Thermogravimetric analysis and C-H stretch comparison for the result of the modification attempts. Only OPA shows weight loss consistent with a monolayer, and is the only modifier that gave significant absorption in IR. Reproduced from Kim, *et al.*[7]

The goal in this study and others published subsequently[8,9] was to control interfacial interactions between BTO nanoparticles and the dielectric host polymer that would be mixed in a suitable solvent and processed into composite films for capacitors or insulators, as mentioned in Section 1.8.1. Modification with pentafluorobenzyl phosphonic acid (PFBPA) and tri(ethylene glycol) phosphonic acid (PEGPA) afforded functionalized nanoparticles with surface energies favorable towards their interaction with the solvent needed to process the BTO, as well as compatibility with the fluorinated copolymer Viton and polycarbonate (PC), respectively, thereby producing high permittivity/high breakdown field composites. A more stable dispersion in the solvents and better film quality after ball milling was observed (Figure 3.4).

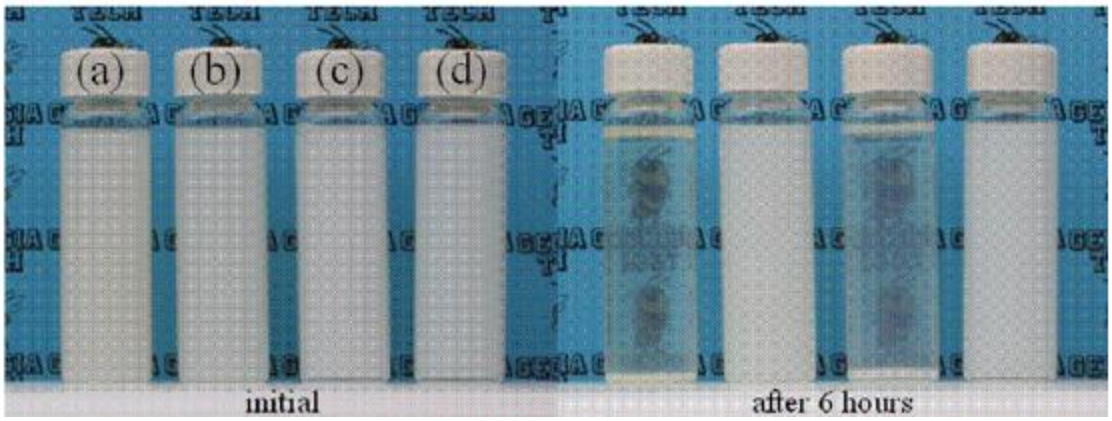

Figure 3.4 Suspension of PA-modified and unmodified BTO in host polymer solutions: (a) BTO in polycarbonate/pyridine, (b) PEGPA-BTO in polycarbonate/pyridine, (c) BTO in Viton / *N*,*N*-dimethylformamide, and (d) PFBPA-BTO in Viton / *N*,*N*-dimethylformamide. Reproduced from Kim, *et al*.[7]

3.1.1 Polarization, permittivities, capacitance, and loss tangent

Dielectric materials in an alternating field will show changes in permittivity following the polarization mechanisms that activate at different frequencies, as shown in Figure 3.5 and expressed in Equation 3.1, where ε_r' is the real component of the permittivity and ε_r'' the imaginary component.

Equation 3.1 $$\boldsymbol{\varepsilon_r^*(\omega) = \varepsilon_r'(\omega) - j\varepsilon_r''(\omega)}$$

At low frequencies (below ~10^2 Hz), only translational (interfacial) polarization will occur; this involves migration of charged species over macroscopic distances during the application of the electric field. These will be accumulated at traps, defects, and interfaces, distorting the local electric field, giving rise to large changes in permittivity. Under the influence of an electric field below 10^9 Hz, *rotational polarization* will dominate: this is associated with species that intrinsically have permanent dipoles that will orient along the direction of the field. *Vibrational polarization*, in the IR frequencies,

takes places due to displacement of atoms, giving rise to separation of charges. Finally e*lectronic polarization* is achieved when the electron cloud of neutral atoms is displaced by an electric field. This polarization is not permanent, and will dissipate once the electric field is removed. It occurs in all dielectrics up to very high frequencies (~10^{15} Hz). At very high frequencies the dielectric constant is the lowest because the other modes cannot keep up with the alternating field and do not contribute to polarization.

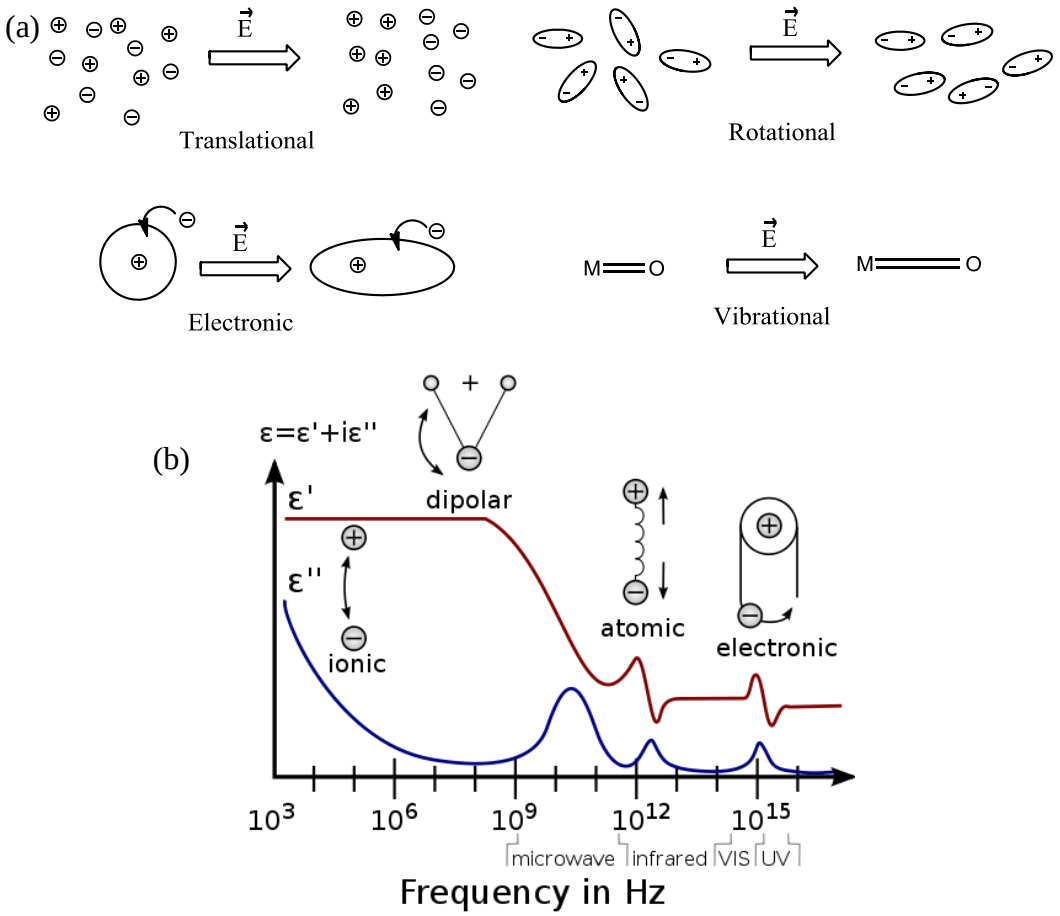

Figure 3.5 (a) Microscopic origins of polarization and (b) dielectric response with frequence. (a) Adapted from MDITR Wiki[10] and (b) reproduced from Mauritz.[11]

The ratio of the imaginary over the real component of the permittivity is known as loss tangent or dissipation factor DF; it is a measure of the ability of the capacitor to dissipate heat. High loss reduces the performance of the device.

Equation 3.2 $$\boldsymbol{DF = tan\delta = \frac{\varepsilon_r''}{\varepsilon_r'}}$$

In an ideal parallel plate capacitor, the capacitance is determined by the area of the device *A*, the thickness *t* and the relative permittivity of the dielectric ε_r, as in Equation 3.3

.

Equation 3.3 $$\boldsymbol{C = \varepsilon_0 \varepsilon_r \frac{A}{t}}$$

where ε_0 is the vacuum permittivity (ε_0 = 8.85×10^{-12} F/m). Hence, scaling factors such as the area and thickness influence the capacity to store charge. Integration of Equation 3.3 gives the total energy *E* stored in the device:

Equation 3.4 $$\boldsymbol{E = \frac{1}{2} CV^2}$$

However, the actual maximum energy that can be stored E_{max} is limited to a breakdown voltage V_B, above which the device becomes electrically conductive. Devices are measured by dielectric spectroscopy using an adjustable AC field and measuring the capacitance, from which the permittivity can be determined using Equation 3.4; hence, Equation 3.5 is equivalent to Equation 1.4.

Equation 3.5 $$E_{max} = \frac{1}{2} C {V_B}^2$$

Polymer-BTO nanoparticles composites can be considered as nanoparticle fillers distributed in a continuous dielectric polymer matrix. The Kerner model[12] treats the dielectric filler particles as polarizable spheres, in which the reduction in electric field

within the high permittivity filler particles is accounted for. The effective permittivity of the composite ε_{eff} (Equation 3.6) can be predicted by a volume fraction-weighted average of the permittivities of the filler ε_f (with volume fraction f_f) and that of the host ε_h (with volume fraction f_h).

Equation 3.6 $$\boldsymbol{\varepsilon_{eff}} = \frac{\varepsilon_h f_h + \varepsilon_f f_f \left(\frac{E_{fz}}{E_{hz}}\right)}{f_h + f_f \left(\frac{E_{fz}}{E_{hz}}\right)}$$

where $\boldsymbol{E}_{fz}$ and $\boldsymbol{E}_{hz}$ are the electric field components perpendicular to the electrodes. Note that the effect of the particles on the field of the host medium is not considered in this model. In a modified Kerner model, as proposed by Jayasundere and Smith,[13] dipolar interactions between pairs of neighboring spherical filler particles are considered, and the effective dielectric constants can be estimated from:

Equation 3.7 $$\boldsymbol{\varepsilon_{eff}} = \frac{\varepsilon_h f_h + \varepsilon_f f_f AB}{f_h + f_f AB},\ \boldsymbol{A} = \frac{3\varepsilon_h}{\varepsilon_f + 2\varepsilon_h},\ \boldsymbol{B} = \frac{3f_f(\varepsilon_f - \varepsilon_h)}{\varepsilon_f + 2\varepsilon_h}$$

This model has been compared with experimental permittivities of nanocomposites containing volume fractions up to of 50% v/v BTO in Viton.[9] At high BTO loadings, the effective permittivity will be closer to that intrinsic of the nanoparticles. The reason for adding the polymer is not only for ease of processing, but also because they possess much larger breakdown strengths than the inorganic cores.[14] Dielectric breakdown mechanisms are usually classified as *intrinsic*, *thermal* and *avalanche*.[15] Intrinsic breakdown occurs due to the nature of the material: there is a certain electric field at which it will become conductive at low temperature that is independent of the geometry and size of the system. Thermal breakdown is temperature triggered; at a slow ramping rate of the applied voltage, steady-state thermal breakdown

can occur, while impulse thermal breakdown occurs at pulsed voltages; they both depend on the geometry and size, as well as the electrode material. Finally, an electron avalanche can be generated in an insulating system due to electric current multiplication from ionization events in the presence of an electric field. The presence of air pockets, with a low breakdown strength, can severely lower the overall breakdown strength.[9]

In their most recent study on PFBPA-modified BTO, Kim *et al.* examined the morphology of spin-coated composite films made with the mixture of modified nanoparticles with Viton.[9] Scanning electron microscopy (SEM) examination of the films evidenced homogenous films up to 50% v/v BTO; higher BTO loadings gave voids and aggregation of nanoparticles (Figure 3.6).

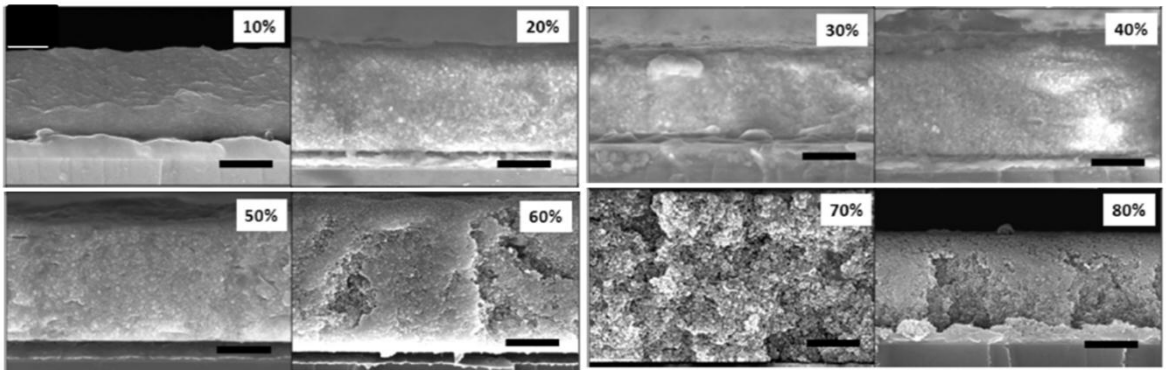

Figure 3.6 SEM images of freeze-fractured cross sections of PFBPA-BTO:Viton composite films with increasing BTO volume fractions. Scale bars are 1 micron. Reproduced from Kim, *et al*.[9]

Their characterization of devices (Figure 3.7) lead to the conclusion that initially the breakdown field decreased as the BTO loading increased but leveled at around 20% v/v BTO, while the permittivity kept increasing up to 50% v/v BTO loadings, which translated into higher maximum and measured energy densities up to 50% v/v BTO loadings (higher loadings gave decreased permittivities due to the porosity problems mentioned above).

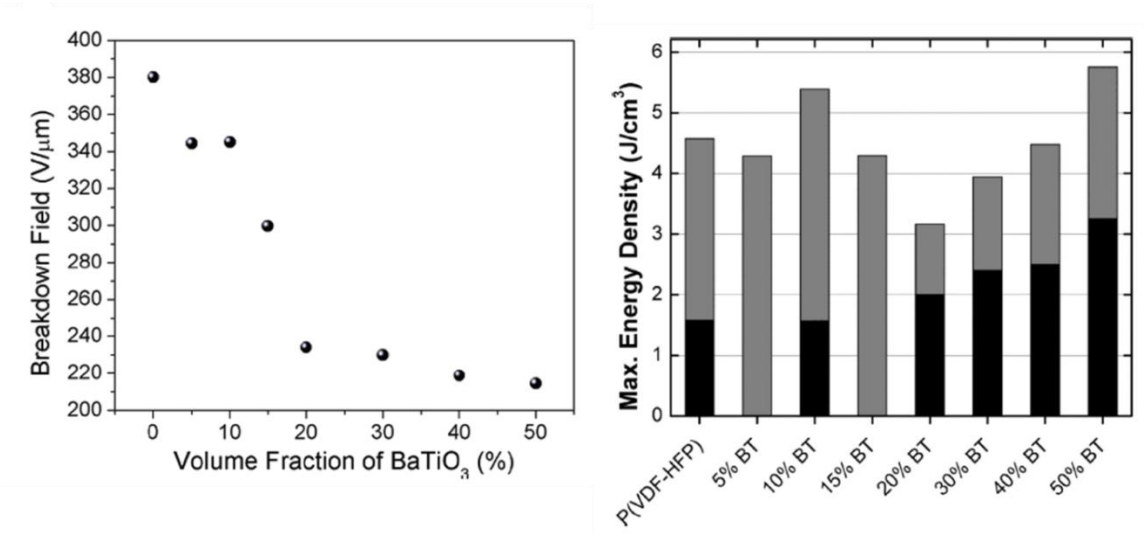

Figure 3.7 Breakdown field, calculated maximum energy density and measure energy density (by charge-discharge method) as a function of volume fraction of BTO. Reproduced from Kim, *et al*.[9]

There are several scientific and engineering challenges to improve upon the results presented above; the materials are processed by ball-milling for at least 10 days; in addition, further process optimization for film formation through either blade casting or spin coating is needed. Finding a simple way to process these materials into hybrid dielectrics that requires less time would be desirable. Another scientific question of interest is if it is possible to make composites that avoid particle-particle contacts that lead to early breakdown at high BTO volume fractions. Surface-initiated polymerization can be applied to make insulating polymers in a rapid and controllable manner that could lead to favorable morphologies where the particles are not in direct contact with each other since polymer brushes have grown in between that avoid such agglomeration. In the first part of this chapter, a form of atom-transfer radical polymerization (ATRP) is developed using a tailor-made, ATRP-initiating phosphonic acid to grow the polymer matrix from the BTO nanoparticles so that there is potentially no need to mix with additional polymer and the processing would be simplified. The electrical behavior of capacitors built with this approach is studied and the morphology of the dielectric films

probed, and as will be discussed later on, this approach results in composites with relatively high permittivity due to the inorganic inclusions and can display high breakdown strengths, which in conjunction with the ease in processability, is desirable for capacitor applications.

3.2 Atom-transfer radical polymerization (ATRP) and ATRP with Activators Regenerated by Electron Transfer (ARGET)

ATRP is a type of externally-initiated controlled radical polymerization based on the atom-transfer addition equilibrium (Figure 3.8):[16] in the activation step, a halogen atom is homolytically abstracted from a C-halogen bond by a transition metal complex that can expand its coordination sphere, increasing its oxidation state by one (and producing a radical on the terminal carbon of the initiator). The radical can react with vinylic groups making a new C-C bond, translating the radical center by two carbons. The thermodynamics of the system favor the metal complex in its reduced oxidation state: back-transfer of the halogen to cap the radical keeps the equilibrium to the left side, minimizing the concentration of free radicals in the medium, thereby minimizing possible radical-radical termination reactions. Hence, the molecular weight of the polymer chains grown can be precisely controlled. The polydispersity, the ratio of the number average molecular weight M_n and the weight average molecular weight M_w (a measure of the width in molecular weight distribution) is generally low.[16]

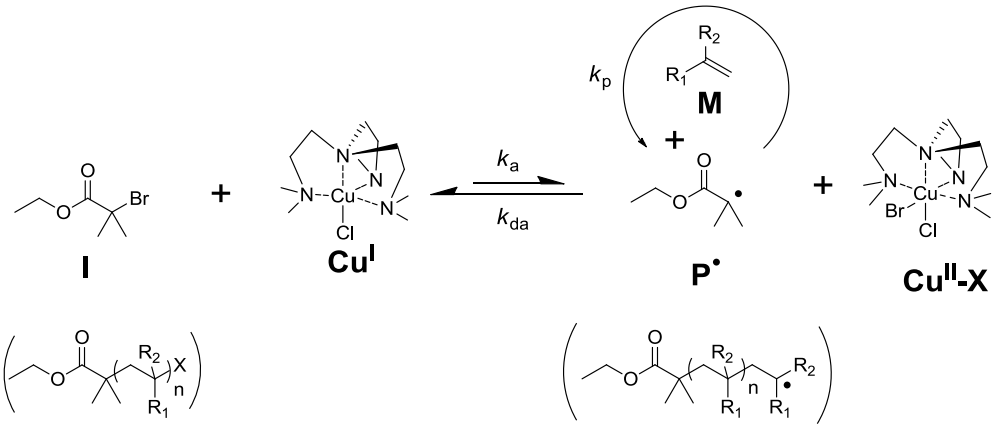

Figure 3.8 A typical ATRP using an isobutyrate as initiator **I** and a copper (I) catalyst **Cu^{I}** with Me_6TREN as chelating ligand. Atom transfer radical addition generates the propagating radical ***P*** · and deactivator **Cu^{II}-X**.

Given the vinylic reactive groups needed as monomers, only non-conjugated polymers can be prepared with this methodology, which is compatible with the need for insulating properties sought for capacitors. Typical concentrations for the species involved are [initiator] ~ [reduced catalyst] ~ [oxidized catalyst] ~ parts per thousand; the monomer is typically in the molar concentration range. Oxygen must be removed from the medium to avoid termination reactions with the propagating species, and the reduced oxidation state metal complex usually has to be purified since its surface will easily oxide in air.[17]

One of the disadvantages that limits widespread industrialization of ATRP is the removal of the transition metal catalyst (typically copper) from the reaction mixture and its recycling for further use.[18] It would be desirable to reduce its use altogether. Inspection of the ATRP rate law indicates that the propagation rate depends only on the ratio of concentrations of the Cu^{I} complex [**Cu^{I}**] to the Cu^{II}-Halogen complex [**Cu^{II}-X**], not on the absolute concentrations.[18]

Equation 3.8 $$\boldsymbol{R_p = k_p[M][P\cdot] = k_p[M]K_{eq}[I]_0\frac{[Cu^I]}{[Cu^{II}-X]}}$$

In Equation 3.8, k_p is the propagation rate constant, $[\boldsymbol{M}]$, $[\boldsymbol{P}\cdot]$, $[\boldsymbol{I}]_0$ are the monomer, propagating species and initiator concentrations respectively; K_{eq} is the ATRP equilibrium constant.Nonetheless, the absolute concentration of deactivator [$\mathbf{Cu^{II}}$-**X**] does influence the molecular weight distribution, according to Equation 3.9.[18]

Equation 3.9 $$\boldsymbol{PDI} = \frac{\boldsymbol{M_n}}{\boldsymbol{M_w}} = \mathbf{1} + \frac{\mathbf{1}}{\boldsymbol{DP}} + \left(\frac{[I]_0 k_p}{k_{da}[Cu^{II}-X]}\right)\left(\frac{\mathbf{2}}{\boldsymbol{p}} - \mathbf{1}\right)$$

where *p* is the conversion, *DP* the degree of polymerization and k_{da} the deactivation rate constant.

As an example, to obtain polystyrene with a PDI of 1.2 (typical of ATRP) at a DP of 200 with 90% conversion at 100 °C requires ~2 ppm of $\mathbf{Cu^{II}}$-**X**. In practice, a thousand times this amount is added to make up for termination reactions that will keep the equilibrium from generating sufficient Cu^I to keep the polymerization running under control.[18]

A recent attractive approach developed by the Matyjaszewski group that enables control polymerization with only parts per million levels of $\mathbf{Cu^I}$/$\mathbf{Cu^{II}}$ is to add ppm levels of $\mathbf{Cu^{II}}$-**X** and create/regenerate the $\mathbf{Cu^I}$ species *in situ* with the use of a reducing agent such as tin (II) ethylhexanoate,[18] which does not form radicals that will initiate new chains (Figure 3.9). This way there is no need to purify $\mathbf{Cu^I}$ species since they will be created in the reaction mixture, and the regenerator also takes care of residual oxygen that might be present in the reaction mixture, saving on degassing steps.

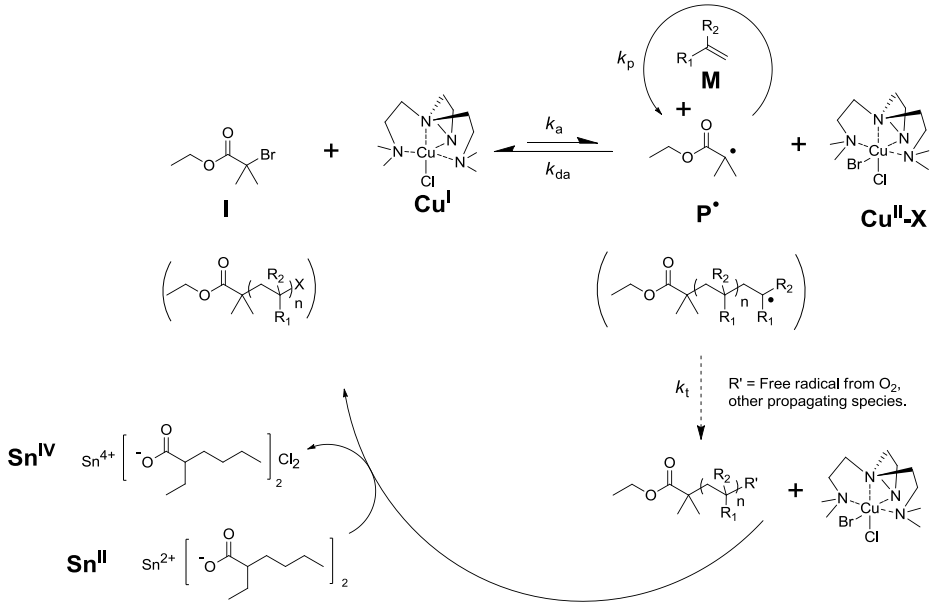

Figure 3.9 A typical ARGET ATRP using an isobutyrate as initiator **I** and a copper (I) catalyst $\mathbf{Cu^{I}}$ with $\mathbf{Me_6TREN}$ as chelating ligand. $\mathbf{Cu^{II}\text{-}X}$ is reduced to $\mathbf{Cu^{I}}$ with the added reducing agent tin (II) ethylhexanoate ($\mathbf{Sn^{II}}$) to start the equilibrium. Atom transfer radical addition generates the propagating radical $\boldsymbol{P}\cdot$ and again the deactivator $\mathbf{Cu^{II}\text{-}X}$. Any termination reaction is compensated by the reducing agent to keep the Cu complex active.

3.3 Synthesis of initiators and solution phase ATRP and ARGET ATRP

In this section, homogeneous polymerization using the ATRP methodologies discussed in Section 3.2 is shown to work with a phosphonate-terminated initiator equally well as with the commercially-available ethyl 2-bromoisobutyrate. Figure 3.10 shows the synthesis of the ATRP-initiating phosphonate **1B** and the acid derivative **1** used in the next section, following the procedure by Maliakal, *et al.*[19] A silica plug is used after the Arbuzov reaction to purify **1B** given that some **1A** is left unreacted; conversion to the phosphonic acid **1** proceeds smoothly through the typical protection/deprotection route.

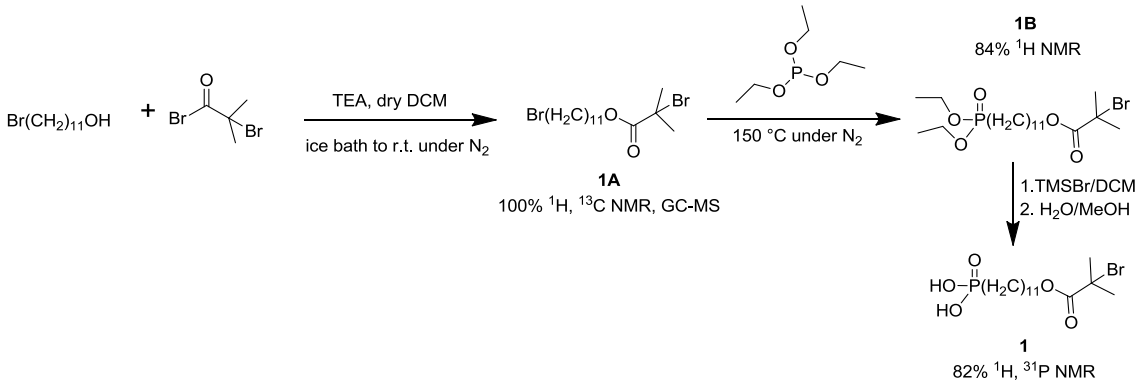

Figure 3.10 Synthesis of ATRP-initiating phosphonic acid **1** ((11-((2-bromo-2-methylpropanoyl)oxy)undecyl) phosphonic acid). **1A** is 11-bromoundecyl 2-bromo-2-methylpropanoate and **1B** is 11-(diethoxyphosphoryl) undecyl 2-bromo-2-methylpropanoate.

Figure 3.11 shows the conventional ATRP protocol, based on work from the Matyjaszweski[20] and Patten[17] groups, applied to the synthesis of a prototypical polymer such as polystyrene using home-made phosphonate **1B** as initiator. In terms of preparation, a couple of challenges are, the purification of CuBr (since its surface is usually oxidized), and the care that must be taken to avoid the presence of air in the reaction mixture since there are no means for regenerating activators after termination reactions (which could occur with oxygen). Hence, freeze-pump-thaw cycles of the mixture were done after the initiator was added, and no anisole was used to dilute the mixture. Table 3.1 summarizes the result for a homogeneous ATRP polymerization of styrene. The M_n is slightly higher than expected, but the polydispersity index (PDI = M_n/M_w) was 1.3, a low value, as expected out of a living polymerization. The work-up included filtration of the large amount of copper salts present.

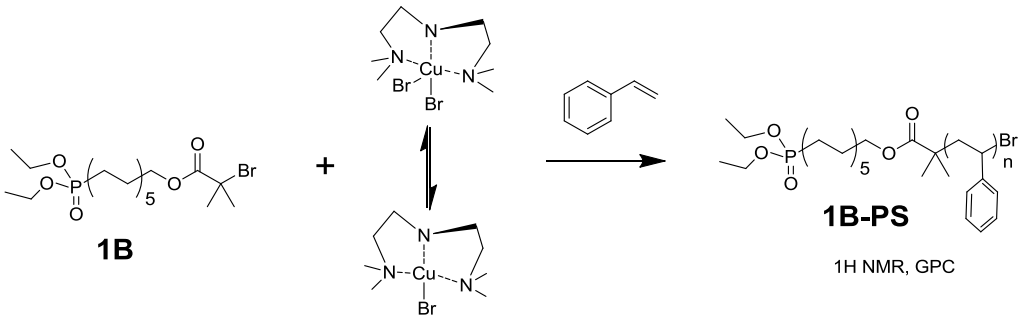

Figure 3.11 ATRP polymerization from phosphonate **1B** to synthesize polystyrene **1B-PS**. *N,N,N',N'',N''*-pentamethyldiethylenetriamine (PMDETA) was used as ligand for the copper complexes.

Table 3.1 Solution results in ATRP polymerizations of styrene

Entry	*II-25*
Initiator	**1B**
St : Initiator : Cu^{I} : Cu^{II}-X : PMDETA	400: 1 : 0.9 : 0.1 : 2.6
Time (h)	20
$M_{n\ theoretical}$ (kDa)	41.4
$M_{n,\ GPC}$ (kDa)	56.6
M_n/M_w	1.32
Notes	Solidified overnight

The polymerization kinetics in this and all cases are followed indirectly, as large polymeric peaks are prone to disturb the phasing of the ^{1}H NMR spectra. Integration of the styrene (S) and anisole (A) peaks (Figure 3.12) was used instead (Equation 3.10).

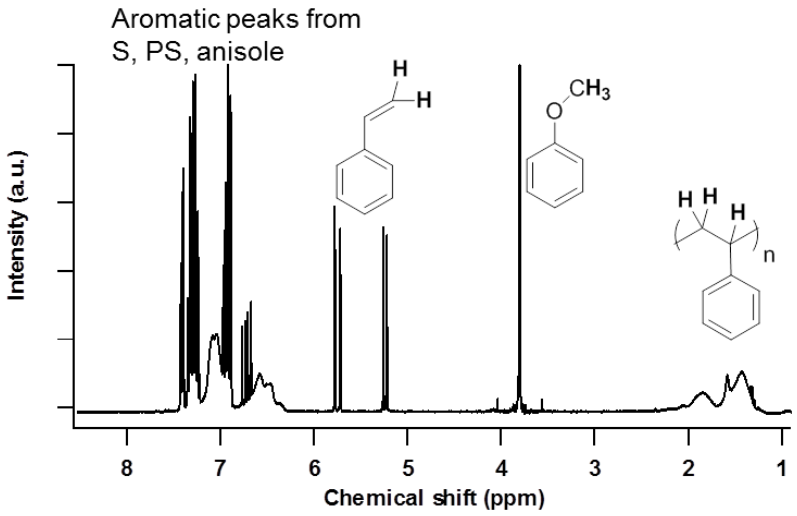

Figure 3.12 Typical ^{1}H NMR of a partially polymerized reaction mixture, emphasizing the styrene vinylic protons and the internal standard (and solvent) anisole.

Equation 3.10

$$\frac{\left(\frac{[S]_0}{[A]_0}\right)-\left(\frac{[S]}{[A]}\right)}{\left(\frac{[S]_0}{[A]_0}\right)-\left(\frac{[S]_\infty}{[A]_\infty}\right)} * 100 = conversion \quad \%$$

ARGET ATRP with the phosphonate (**1B**) and the commercially available **I** was performed multiple times following the scheme in Figure 3.13 to synthesize polystyrene, with results increasingly more successful as the experimental conditions were varied slightly (Table 3.2). The last entry in the table is a control experiment with no initiator, which shows its necessity for successful polymerization under these conditions.

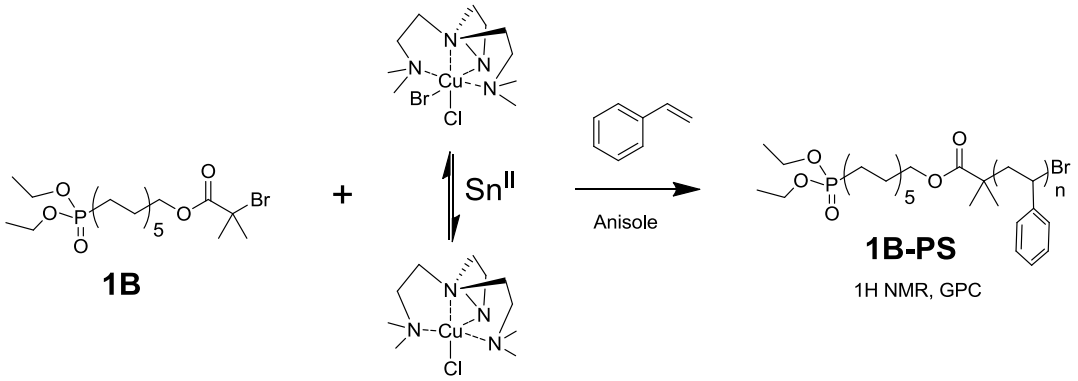

Figure 3.12. ARGET ATRP from phosphonate **1B**.

Table 3.2 Solution results in ARGET ATRP polymerizations of styrene (St)

Entry	Initiator	St : Initiator : Cu(I) : $Sn(EH)_2$. : Me_6TREN	[Sty] (M)	t (h)	Conv %	$M_{n\ theo}$ (kDa)	$M_{n,\ GPC}$ (kDa)	M_n/M_w
I-269	**1B**	200 : 1 : 0.01 : 0.1 : 0.1	3.8	23	31	6.9	5.1	1.7
I-270	**1B**	200 : 1 : 0.01 : 0.1 : 0.1	3.8	80	49	10.6	5.2	1.6
I-306B2	**1B**	30 : 1 : 0.01 : 0.1 : 0.1	6.5	38	94	3.0	3.6	1.4
II-13B	**I**	200 : 1 : 0.015 : 0.13 : 0.1	5.8	13	75	15.8	14.4	1.2
II-17D	**1B**	200 : 1 : 0.01 : 0.14 : 0.1	5.8	15	67	14.2	13.2	1.2
II-17E	**none**	200: 0 : 0.01 : 0.14 : 0.1	5.8	15	6	-	NA	NA

3.4 Modification of $BaTiO_3$ with ATRP active PA

Phosphonic acid **1** was used in the procedure optimized by Kim[14] to modify commercially available barium titanate nanoparticles of average size 50 nm (BTO-50) with phosphonic acids. Geometrical consideration of the particles' surface area and footprint of the phosphonic acid (0.24 nm^2 per molecule from a geometrical consideration of the structure of a PO_3 group and the van der Waals radii of the atoms) allow determination of the amount of phosphonic acid needed to coat a monolayer; typically a 3× excess is used to ensure maximum coverage. The protocol consists of dispersing the nanoparticles through tip sonication in ethanol in a 0.4 g BTO / 10 mL solvent, adding the phosphonic acid, and refluxing the mixture at 80 °C overnight. The SEMs shown in Figure 3.14 indicate no significant change in the particle morphology or size (spheroids of ~50 nm diameter) after the reaction. The thermogravimetric analysis (TGA) traces show that the bare $BaTiO_3$ has a small mass loss from contaminants on the surface (also seen by IR). While there is some batch-to-batch variation in phosphonic acid coverage, it is usually 60-130% of the expected monolayer, as the particles may have small variations in surface area that will affect the available surface area for reaction. IR spectra show the absorptions seen in the free phosphonic acid with some differences in the 1300-900 cm^{-1} range: a new peak appears around 1050 cm (attributed to P-OM stretching), while the

broad peaks attributed to P-OH disappear, and the P=O absorption is still observed. This is consistent with bidentate attachment.

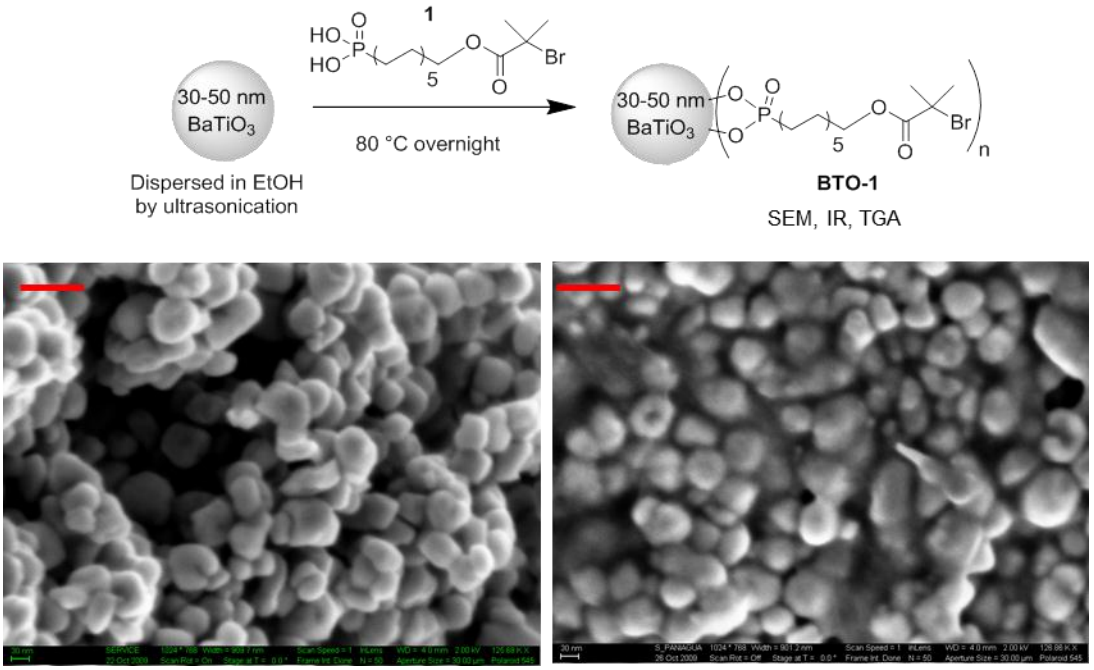

Figure 3.14 Surface modification of $BaTiO_3$ nanoparticles with **1**. SEMs of starting particles (left) and modified particles (right). Scale bar is 100 nm.

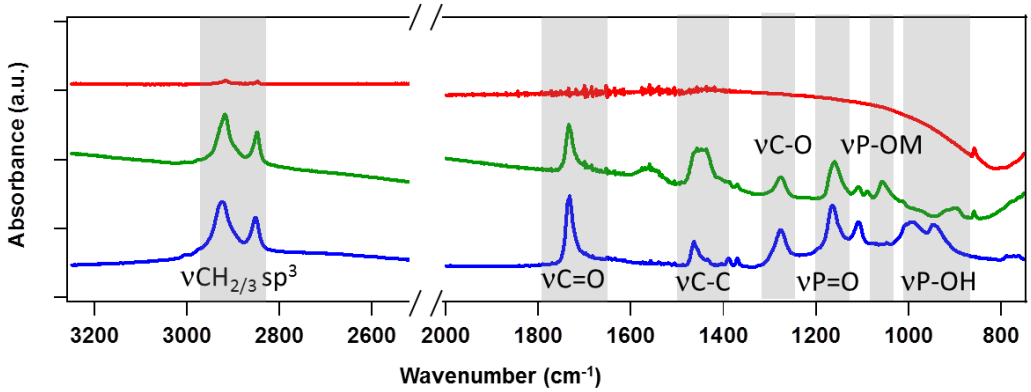

Figure 3.15 Comparison of IR spectra of the bare BTO (red), **1**-modified BTO (green) and phosphonic acid **1** (blue) in KBr pellet.

3.5 Surface initiated polymerization using ATRP protocols

3.5.1 Initial attempts at ARGET ATRP surface initiated polymerizations

As mentioned above, for a good degree of control, sufficient amount of deactivator is needed in the reaction medium to maintain a low stationary concentration of free radicals. This of course also applies as well in the case in heterogeneous polymerizations. To do this in surface-initiated polymerizations, one approach has been to add free sacrificial initiator, leading to the formation of deactivator in solution.[21] The molecular weight of the free polymer generated from free initiator has been used as a measure of the molecular weight of the grafted polymer chains.[22,23]

For the first attempts at grafting from BTO, and since there were no reports of ARGET ATRP applied to nanoparticles, a procedure was adapted from the first report from the Matjyjaszewski group on ARGET ATRP[18] and its application to growth of polybutylacrylate from silicon wafers.[24] A mixture of BTO-grafted initiator **BTO-1** and soluble **1B** as sacrificial initiator in anisole was used. **BTO-1** was dispersed in anisole through tip sonication for 4 h, and then added to the rest of the reaction mixture, which is then degassed briefly through N_2-bubbling. All reactions were carried at 110 °C, and left to react (typically overnight or longer) keeping track of conversion percent through ^{1}H NMR spectroscopy. After a significant conversion percent was reached, the mixture was removed from the heat, opened to air, and precipitated onto hexane to remove monomer. The precipitate was then washed multiple times (at least three) with chloroform to remove any free polymer, reprecipitated, and dried under vacuum.

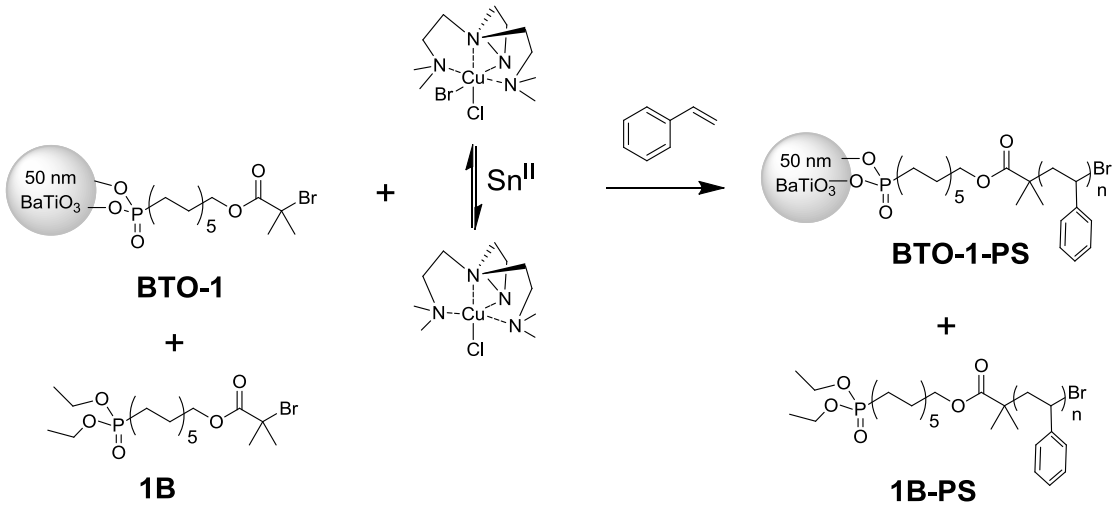

Figure 3.16 ARGET ATRP applied to surface-initiated polymerization of styrene.

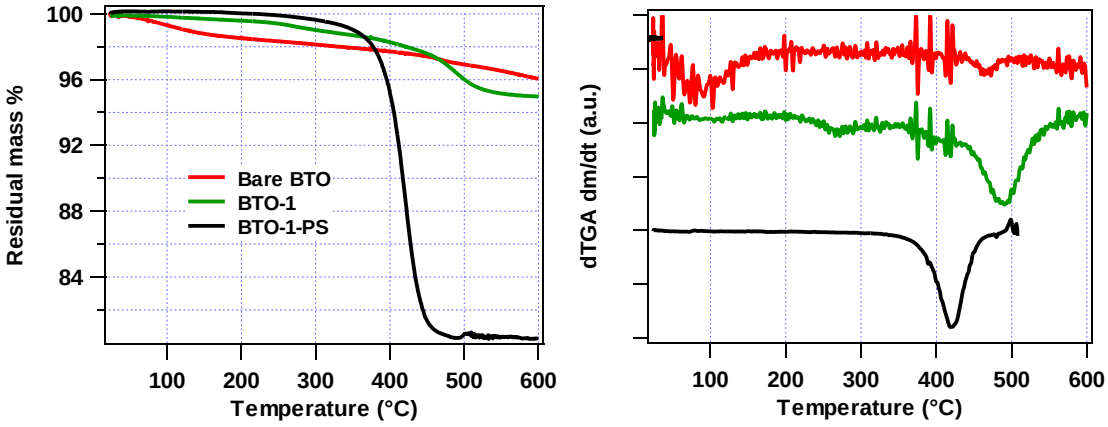

Figure 3.17 TGA characterizations of bare BTO, BTO modified with phosphonic acid **1**, and composite **BTO-I-PS** (SPB-I-237) made via surface initiated ARGET ATRP of styrene.

The composites synthesized here were all characterized by using TGA: the mass loss was used to calculate the amount of organic attached, and the derivative TGA (dTGA) indicated the temperature of maximum mass losses, which can be used to determine the identity of the organics. The dTGA (Figure 3.17) suggests that the phosphonic acid attached to BTO burns in three stages, at 260 °C, 410 °C and mostly at 480 °C, while the polystyrene attached to BTO has a maximum loss at 418 °C. An

initiation efficiency % can be calculated by assuming the polymer formed in solution is representative of that formed off the surface: the equivalents of initiator attached to the surface are used to estimate the amount of polymer grown with the GPC-determined number molecular weight, and this is compared with the TGA polymer mass fraction. The volume fraction (f) of a composite can be calculated by means of Equation 3.11, from the mass attributed to each species determined from TGA and the reported densities. Subscripts B, P, and PS refer to $BaTiO_3$, phosphonate, and polystyrene respectively.

Equation 3.11

$$f = \frac{V_B}{V_B + V_P + V_{PS}} = \frac{\frac{m_B}{\rho_B}}{\frac{m_B}{\rho_B} + \frac{m_P}{\rho_P} + \frac{m_{PS}}{\rho_{PS}}}$$

Table 3.3 summarizes results from several experimentals, with different conditions attempted, such as changing the **BTO-1** to **1B** ratio, varying reaction times and changing monomer concentration. The (total) initiator to styrene ratio was selected to give an expected 18 kDa < M_n < 34 kDa for all the cases shown in the table. An initiation efficiency was calculated for the cases where GPC of free polymer was acquired, under the assumption that 100% of initiating sites on the surface grew polymer with the same M_n; the actual polymer amount determined from TGA is compared against the total mass expected.

Table 3.3 Some initial attempts at ARGET ATRP with **BTO-1**, using **1B** as sacrificial initiator. In all cases reaction temperature was 110 °C.

Entry	**St**:**BTO-1**:**1B**:**Cu^{I}**:**Sn^{II}**	[St] (M)	Conversion %	Initiation efficiency %	Supernatant Mn (kDa) / PDI	Polymer m/m % (TGA)*	f BTO v/v %
I-127C	260 : 1 : 0.6 : 0.01 : 0.12	5.9	87	11	25 / 2.9	10.1 (8.0)	45
I-205A	820 : 1 : 3.0 : 0.04 : 0.41	4.4	32	NA	NA	7.9 (9.8)	46
I-205B	205 : 1 : 0.0 : 0.01 : 0.10	2.0	30	NA	NA	2.5 (9.8)	58
I-221B	490 : 1 : 0.5 : 0.02 : 0:25	1.6	43	NA	NA	9.2 (10.8)	42
I-237	370 : 1 : 0.9 : 0:02 : 0:19	2.4	74	33	23 / 1.9	15.8 (3.9)	42
I-260B	200 : 1 : 0.3 : 0:02 : 0:16	4.6	41	4	33 / 4.3	3 (7.0)	63
I-289	500 : 1 : 1.0 : 0.02 : 0.80	3.8	49	5	9.1 / 2.7	2.9 (6.8)	64
I-293[†]	400 : 1 : 1.0 : 0:02 : 0:80	3.3	70	NA	NA	2.7 (6.8)	64

*Polymer mass content was determined by subtraction of the organic loss in the modified nanoparticles; values in parenthesis are the mass loss attributed to phosphonic acid. [†]Microwave irradiated to heat to 180 °C for 2 h.

The table shows that the best results both in terms of efficiency and absolute polymer weight in the composite were obtained when the percent of conversion was the highest. The best result was for entry I-237, which was also characterized by transmission electron microscopy (TEM). RuO_4 staining was used to better visualize the polymer brushes. Figure 3.18 shows images with different magnification. The core shell morphology is not readily observed; instead a gray matrix is observed on the edges of some of the clumps; indeed some particles seem to have polymer brushes while others don't (perhaps because the polymers on some particles have "pancake" conformations due to low initiation efficiency).

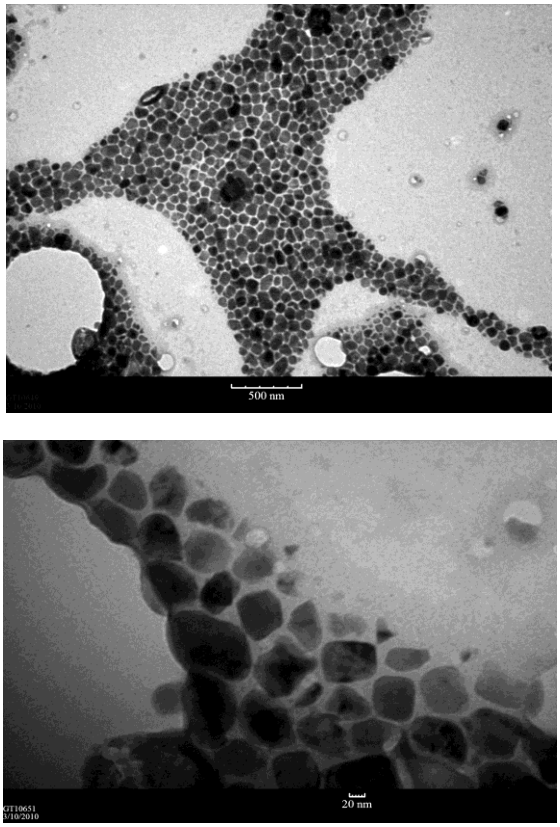

Figure 3.18 TEM images of composites from composite **BTO-1-PS** SPB-I-237. Images acquired by A. Nantalaksakul.

Other polymerizations were carried out varying the reagents ratios and reaction times, but did not afford higher polymer loadings. It seemed that the surface-initiated polymerization was not ocurring to as high an extent on the surface as in solution: conversion was high, while organic material content was low in the purified composites. Some hypotheses can be developed based on previous literature reports. Von Werne and Patten discuss in a review how termination can occur in a heterogeneous ATRP-type polymerization,[17] including how chains in the same particle can terminate forming a "loop" (Figure 3.19). If this was indeed a problem, having the initiating groups spread further apart might help diminish the occurrence of such an event. A mixed monolayer where the active group density is decreased by "dilution" with an inert phosphonic acid is one way to afford that, and the way to construct such a structure is shown in Figure 3.20.

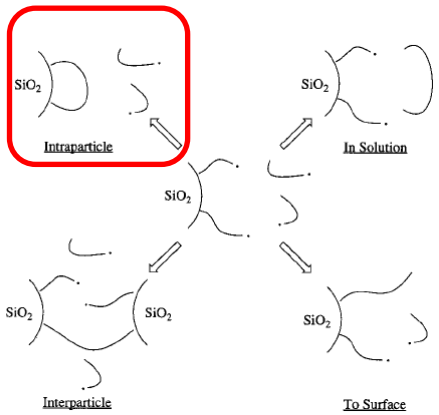

Figure 3.19 Possible termination modes in ATRP-type polymerizations from NPs. Reproduced from von Werne and Patten.[17]

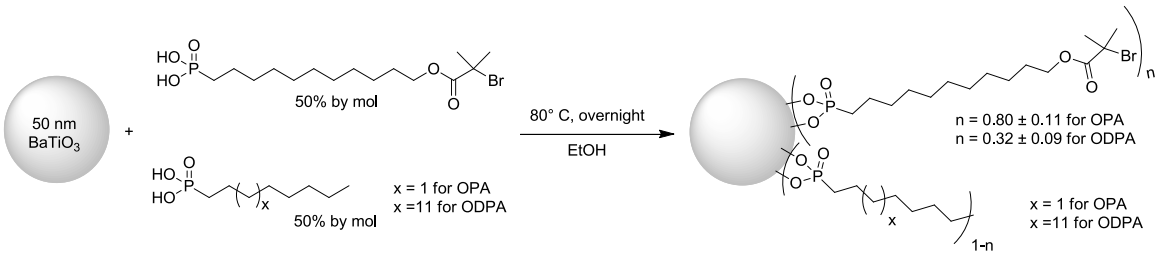

Figure 3.20 Mixed-monolayer through simultaneous reaction with alkylphosphonic acids and ATRP PA.

A first attempt at the mixed-monolayer approach was made using octadecylphosphonic acid (ODPA), which has a similar molecular weight and length to the active ATRP PA **1**, employing 2.0 equivalents of each. XPS was used to determine how much of the overlayer was the active phosphonic acid; the degree of coverage of the ATRP PA in the mixed overlayer was estimated to be 33 ± 9% by comparing the Br 3d / Ba $3d_{5/2}$ ratio *vs.* that of the simple (full) monolayer. This information was then used to estimate an average molecular weight for the overlayer to determine the quantity of modified nanoparticles to be used for polymerization for a particular monomer/initiator ratio.

Figure 3.21 shows the heterogeneous polymerization attempt. Both microwave (180 °C, 2 h) and conventional heating (110 °C, 40 h) were used in duplicate samples, and although in both cases high conversion of monomer was observed by NMR (65% and 61% respectively), there was no evidence that polymer grew (less mass loss than the starting material was observed, Table 3.4). A possible explanation for the failure to observed grafts is that the ODPA chain is longer than **1** by about three carbon atoms, leaving the bromine and/or the tertiary radical hindered from reaction with the catalyst and monomers.

Hence, a new attempt was made in which octylphosphonic acid (OPA) was used as diluent instead. Br/Ba atomic ratios were used again to calculate the percentage of active monolayer in the mixed monolayer, which in the case of mixture with OPA came to be around 80%. This could be an indicative that the longer the chain length, the faster the kinetics of absorption, given the previous data acquired with ODPA. The hydrodynamic radius of the nanoparticles determined by DLS was 125 ± 46 nm before starting the heterogeneous polymerization. The reaction was stopped after 41 h (estimated 78% conversion by NMR). While there was polymer present in the product, the mass loss is far from the best result using 100% active monolayer at similar monomer and initiator concentrations. This result seems to be consistent with some reports in the literature stating that diluents would decrease thickness of surface-initiated polymer films in ATRP type polymerizations.[25-27] It can be concluded that intra-particle chain termination is not a significant problem.

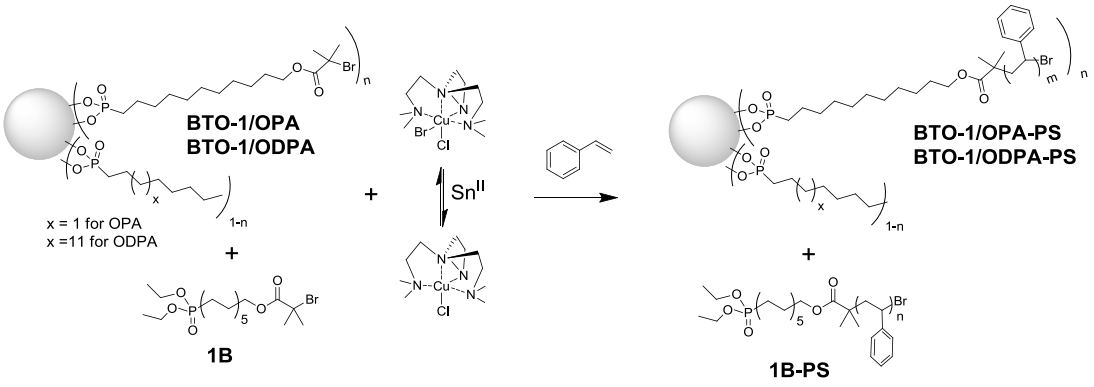

Figure 3.21 Polymerization attempt using the shown mixed monolayers.

Table 3.4 Results from mixed monolayer approach to making BTO-PS composites.

Entry	**BTO-1/ODPA**	**BTO-1/ODPA microwave**	**BTO-1/OPA**
Initiator % on BTO	32	32	80
PA m/m% of NPs*	8.0 (6.1)	8.0 (7.8)	6.7 (6.7)
St:**BTO-1** :**1B**:**Cu^{I}**:**Sn^{II}**	500:1:1.4:0.02:0.8	500:1:1.4:0.02:0.8	200:1:0.5:0.02:0.4
[St] (M)	2.4	2.4	2.8
Conv %	61	65	78
Polymer m/m %	0	0	3.2
f BTO v/v %	75	70	63

*In parenthesis the mass loss after the polymerization attributed to the PAs.

Given that the amount of polymer that could be grown seemed to be limited by concentration, a step was taken back to verify the effect of doing neat reactions, using only the styrene itself as solvent. Neat conventional ATRP and ARGET ATRP are discussed in the sections that follow.

3.5.2 Conventional ATRP surface initiated polymerization

In conventional ATRP for surface initiated polymerization, the thickness of the polymer grafts when using sacrificial initiator is limited since most monomer is consumed in solution polymerization.[28] To avoid this, the alternative has been to add excess deactivator at the beginning.[21] Following the work by Matyjaszweski,[20] no solvent and no sacrificial initiator was used for the surface-initiated polymerization attempts. Freeze-pump-thaw cycles were used to degas the reaction mixtures. A few minutes of vortex shaking sufficed to disperse the particles in the styrene, whose concentration was 8.7 M. The reaction was carried at typical temperatures for styrene polymerization (90-110 °C). After the reaction time, the mixture was removed from the heat, opened to air, and dissolved in chloroform to filter it through neutral alumina. Precipitation onto methanol is done to remove monomer, and the precipitate is washed multiple times with chloroform to remove any physisorbed polymer, reprecipitated, and dried under vacuum.

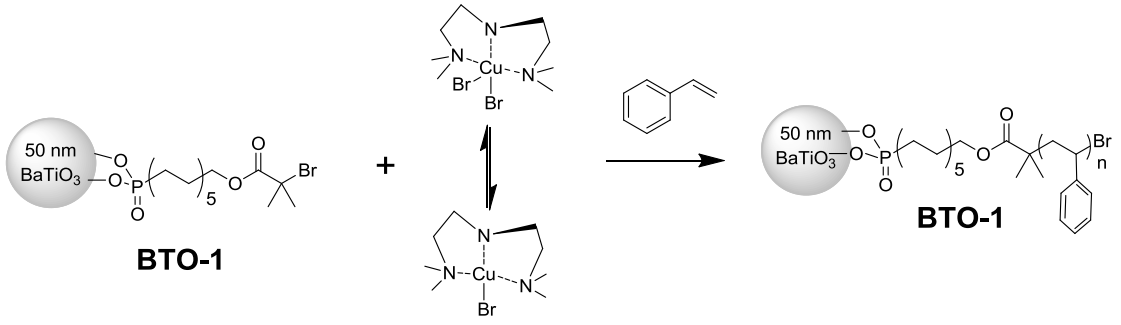

Figure 3.22 Conventional ATRP applied for surface-initiated polymerization of styrene.

The results are summarized on Table 3.5. It must be noted that for entry II-27 only 0.18 g of composite was recovered after the filtration used to remove the color in the composite (due to the copper salts), despite starting with 0.64 g of ATRP-PA modified BTO (**BTO-1**). Also, the reaction mixture was solid after overnight reaction and its dissolution in chloroform or tetrahydrofuran was difficult likely due to high molecular weight from the long reaction time. Another experiment was run at 90 °C, but very low

quantity of composite was recovered (0.07 g) and the polymer content was very low (~2% by mass) after 20 h of reaction.

Table 3.5 Surface initiated polymerization results on styrene using conventional ATRP

Entry	Initiator	St : Initiator : Cu(I) : Cu(II) : PMDETA	Time (h)	T (°C)	M_n theoretical (kDa)	Polymer m/m % (TGA)	f BTO v/v %
II-27	**BTO-1**	400: 1 : 1 : 0.1 : 2.7	16	110	41.9 k	32.6	21
II-32	**BTO-1**	400: 1 : 1 : 0.1 : 2.7	20	90	41.9 k	2.2	68

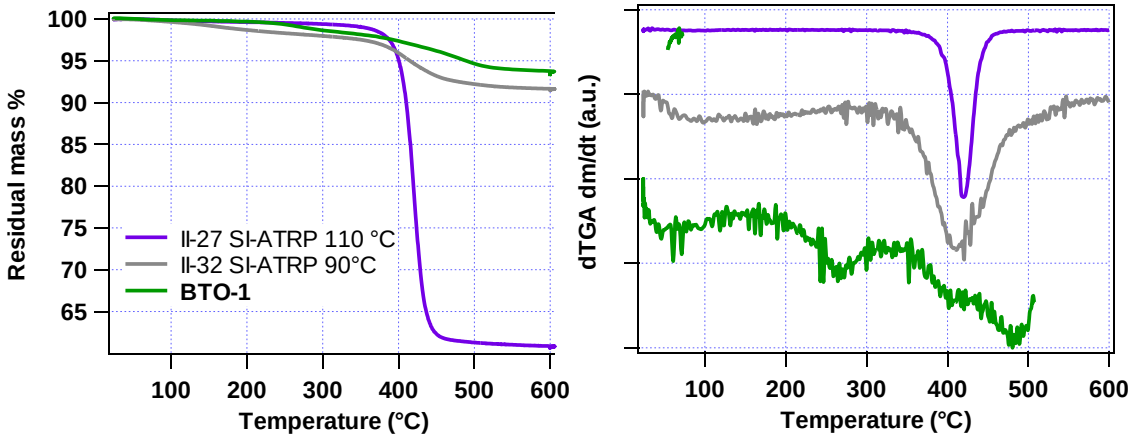

Figure 3.23 Left: TGA comparison for the modified $BaTiO_3$ **BTO-1** and composites II-27 / II-32 from the scheme in Figure 3.22 made through conventional surface initiated-ATRP. Right: Derivative TGA (normalized traces of residual mass difference over time), offset for clarity.

3.5.3 Neat ARGET ATRP surface initiated polymerizations

Given the results from the last section, ARGET ATRP was attempted again, neat, with and without sacrificial initiator, to compare with conventional ATRP, as in Figure 3.24. In all cases, the polymerization took place in a pressure vessel, and degassing was limited to a minute. The work up consisted on dissolution and precipitation onto hexane or methanol, and redispersion in chloroform to wash multiple times, followed by reprecipitation and drying; without filtration, the appearance of the composites was a

white powder, with no discernible green or blue color for Cu salts, as would be observed in conventional ATRP.

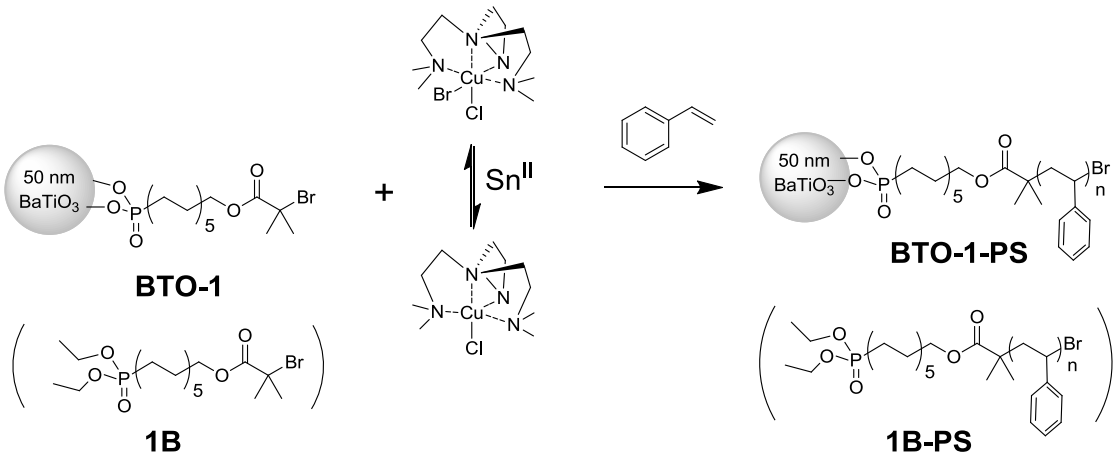

Figure 3.24 ARGET ATRP applied to surface initiated polymerization of styrene.

The amount of polymer growth was very satisfactory; a high organic content, up to 57% residual mass was observed by TGA (which translated into 37% polymer mass, Figure 3.25). The recovery was also very good in all cases (close to 0.5 g, having started with slightly under 0.5 g of ATRP-PA modified BTO) since there was no filtration involved, which is when most of the loss occurred for conventional ATRP-produced composites. Table 3.6 summarizes some of the results. It is noticeable that increasing the temperature leads to more grafted polymer, as does increasing the reaction time; using sacrificitial initiator on the other hand slightly decreases the amount grafted. The TEM image of a composite with intermediate polymer loading is shown in Figure 3.26.

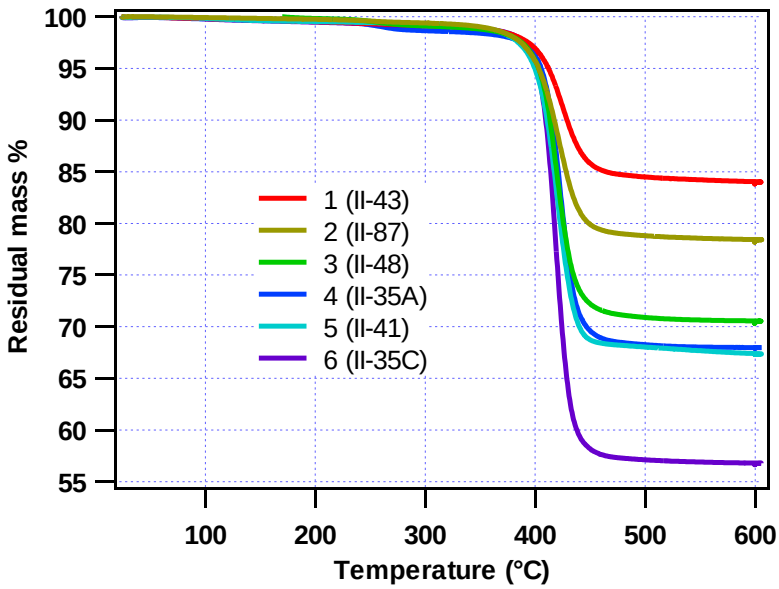

Figure 3.25 TGA comparison of $BaTiO_3$ / polystyrene composites made via ATRP and ARGET ATRP surface initiated polymerization.

Table 3.6 Polymerization conditions for the synthesis of polystyrene composites

Entry	Initiator	**St** : Initiator : **Cu^I** : **Sn^{II}** : Me_6TREN	Time (h)	T (°C)	Mass of polymer in composite %	BTO v/v %
1 (II-43)	**BTO-1**	400: 1 : 0.04 : 0.2 : 0.2	7.5	90	7.6	49
2 (II-87)	**BTO-1**	400: 1 : 0.02 : 0.2 : 0.2	3	110	13	39
3 (II-48)	**BTO-1**	340: 1 : 0.02 : 0.2 : 0.2	6	110	22	29
4 (II-41)	**BTO-1**	400 : 1 : 0.03 : 0.2 : 0.2	16*	105	25	27
5 (II-35C)	**BTO-1**	600 : 1 : 0.06 : 0.3 : 0.3	20*	110	37	19
6 (II-35A)	**1B** / **BTO-1** (1:1)	400 : 1 : 0.05 : 0.2 : 0.2	20*	110	25	27

*Solidified overnight.

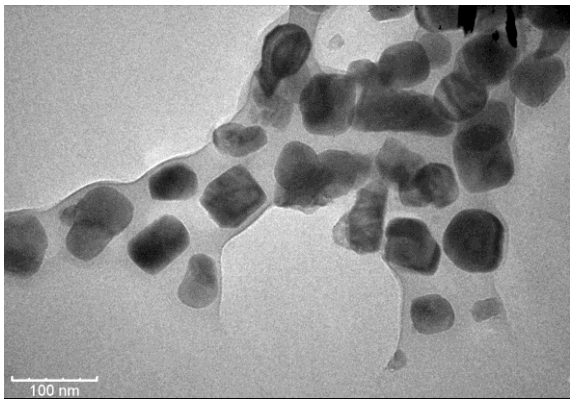

Figure 3.26 TEM micrograph of composite II-48 (29% v/v BTO). Image acquired by Dun-Yen Kang.

3.5.4 Control experiments on surface initiated ARGET ATRP of styrene

Two control experiments were performed (with the aid of Ritesh Kumar, undergraduate student from Chemical Engineering) to verify that the polymerization was occurring from the nanoparticles through ATRP chemistry: A) an inert PA such as octadecylphosphonic acid (OPA) was used to coat the BTO and attempt the polymerization in the same manner as for **BTO-1**, and B) ATRP-PA coated BTO (**BTO-1**) was used without the addition of copper salt or the reducing agent.

The modification of BTO with ODPA was performed using the same protocol as for **1** (Figure 3.27) and the TGA showed 73% monolayer coverage (based on spheres d = 50 nm). The same polymerization protocol was used as in entry 3 of Table 3.6, and as expected the TGA (Figure 3.28) showed no significant change in organic content after purification of the nanoparticles; some free (unbound) polymer was recovered and characterized by GPC. TGA confirmed that this was the case, as there was no significant increase in mass loss or difference in the shape of the trace.

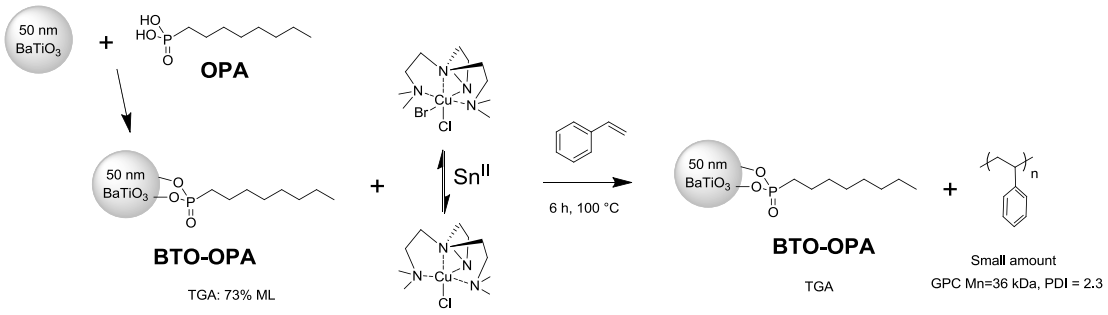

Figure 3.27 Control polymerization using ODPA modified BTO

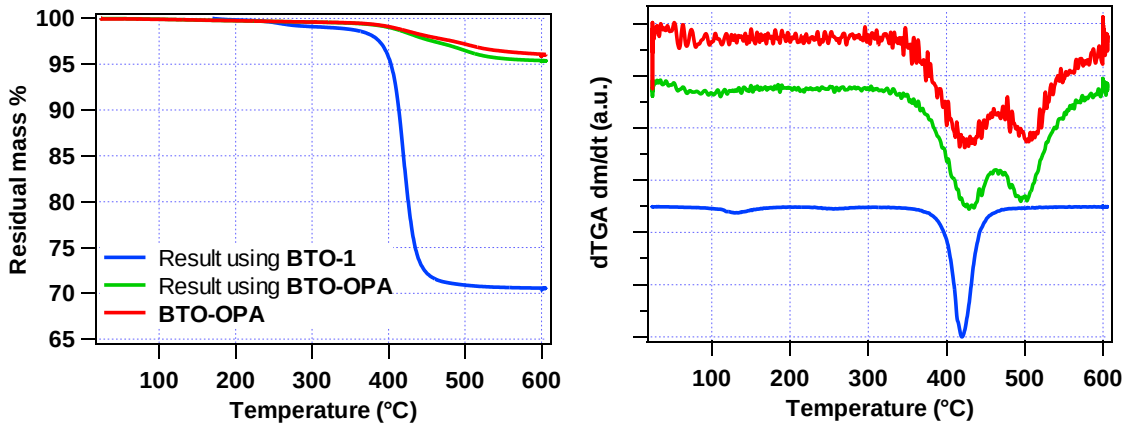

Figure 3.28 TGA comparison of particles before and after the control polymerization attempt with inert PA.

Control experiment B) was done as in Figure 3.29. TGA shows a total mass loss of only 9% (compared to 29% when using catalyst and reducing agent under the same conditions); the IR shows a small amount of aromatic C-H stretches around 3050 cm^{-1} (Figure 3.30); this is consistent with some oligostyrene incorporation into the ester group, which is possible by free radical propagation via C-Br thermolysis. The rest of the spectrum looks almost identical to the starting material, which is very different than that of a composite with large amounts of polymer grafts such as the **BTO-1-PS** shown in red in the figure, where the aromatic absorptions dominate the spectrum.

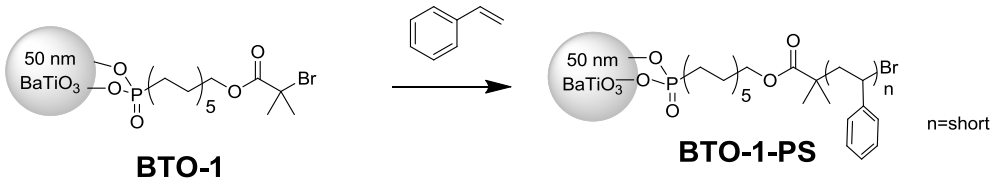

Figure 3.29 Control experiment B using ATRP PA modified BTO but no catalyst or reducing agent

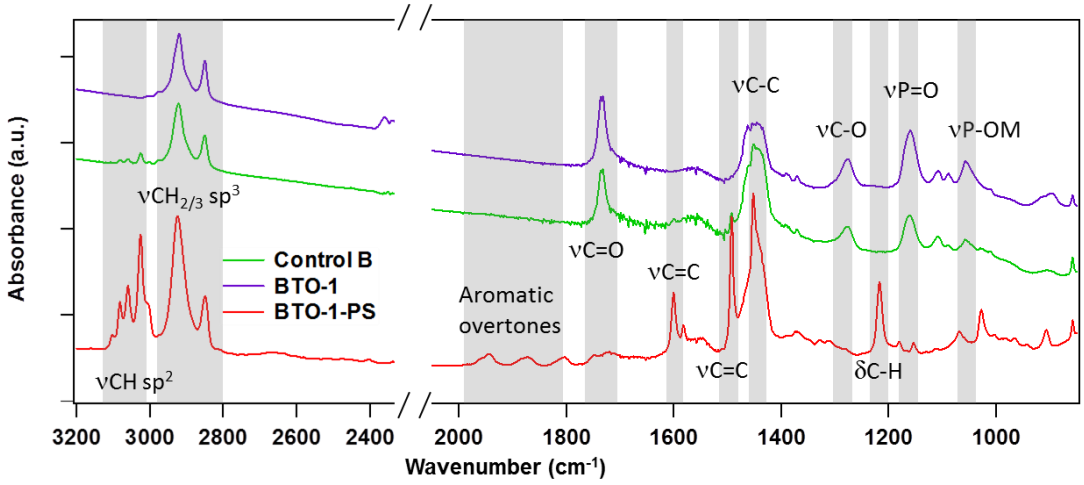

Figure 3.30 IR comparison of control B (without catalyst/reducing agent) with the starting material **BTO-1** and a composite made through ARGET ATRP using the same reaction time but with catalyst and reducing agent (entry 3 in Table 3.6)

3.6 "Grafting to" attempts

"Grafting to" has also been used to make composites of titanates with non-conjugated polymers, due to the control in molecular weight it offers and the simplicity of the approach.[19,29,30] This was also attempted here. Equation 3.11 was used to calculate how much polymer terminated in phosphonate should be added to bare BTO to achieve a composite with a given volume fraction using this approach, assuming grafting of all chains. In all cases a BTO v/v % of 10-11 was targeted (61-58% mass loss). The nanoparticles were dispersed with the tip sonicator just as they were for modifying with the ATRP-initiating phosphonic acid **1**. Dynamic light scattering was used to verify that

the nanoparticles were properly dispersed; nanoparticle sizes for all entries in Table 3.7 were 110-120 (± 40-50) nm.

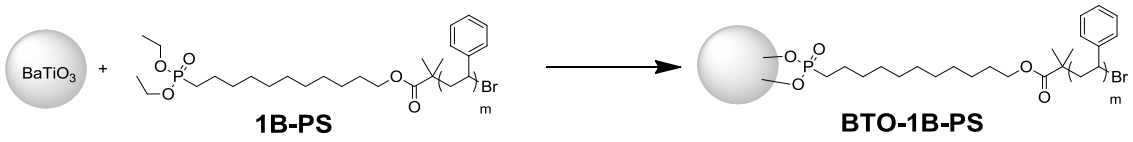

Figure 3.31 Attempts at "grafting to" $BaTiO_3$.

Table 3.7 summarizes the attempts carried out. At first (entry *1*), THF was used as solvent and the reaction left to run for 2 days at 70-80 °C. Given that the nanoparticles need a certain volume to disperse and the molecular weight of the polymer used in entry *i* was large, the polymer concentration ended up being low, less than 1 mM (a typical modification of nanoparticles makes use of 10-20 mM phosphonic acid). This may have had a negative influence on the result, since only ~3% mass loss was observed according to TGA, which gives an 85 % v/v BTO, very far from the 10% v/v targeted, and far from the results in Table 3.6. Since it was not possible to reduce the volume of the dispersion (otherwise the mixture will be too viscous due to the polymer, or the nanoparticles not fully dispersed), the solvent was changed to anisole, which allowed for higher reaction temperature (whose boiling point is 154 °C used 120 °C in case some decomposition might occur), and the reaction let run for 4 days (entry *2*); however, TGA indicated that this resulted in only slightly better results. To increase the polymer molar concentration, short polymer chains were synthesized. The hypothesis was that shorter polymer chains would have less steric hindrance in reaching reactive sites in BTO even if other chains are already anchored. As entry *3* shows, a microwave heated reaction mixture, with approximately 10 times the concentration of previous attempts, was put to stir at 180 °C (PS depolymerization has been reported to start at 200°C[25]) for 2 h. The amount of polymer grafted after work up was still low.

Table 3.7 "Grafting to" experimental conditions and results for polystyrene/$BaTiO_3$ composites.

Entry	Polymer	Mn (kDa)	[Polymer] (mM)	Solvent	Reaction time	T (°C)	TGA mass loss %	BTO v/v %
1	1B-PS	64	~0.6	THF	2 days	70-80	3.0	85
2	1B-PS	64	~0.8	Anisole	4 days	120	5.5	75
3	1B-PS	5.2	~6	Anisole	2 h	180*	4.5	79
4	1-PS	3.7[†]	~10	Anisole	2 days	120	5.2	76

*For entry *3*, microwave irradiation was used as heating source. [†]Determined from the precursor phosphonate.

Another approach at "grafting to" was to make phosphonic acid-terminated polystyrene instead of the phosphonate to see if that would induce better binding to the BTO. It was possible to convert a small molecular weight phosphonate-terminated polystyrene **1B-PS** into the phosphonic acid (Figure 3.32). Conversion to the acid was confirmed through mainly through ^{31}P NMR peak shift: the peak at 32.8 ppm for the starting material disappeared and two broad peaks at 36 and 37 ppm appeared, close to where the phosphorus signal is observed for the pure phosphonic acid **1** (Table 3.8) Also, the ester methylene groups seemed to have disappeared. The acid (0.29 g) was allowed to react with BTO NPs (0.21 g) in anisole at 120 °C for 2 days: if all the acid-polymer was consumed, TGA would have shown *ca*. 60% mass loss from organic (corresponding to approximately 10% v/v BTO) as well, but instead the mass loss found was only 6.2% (entry *4*, Table 3.7).

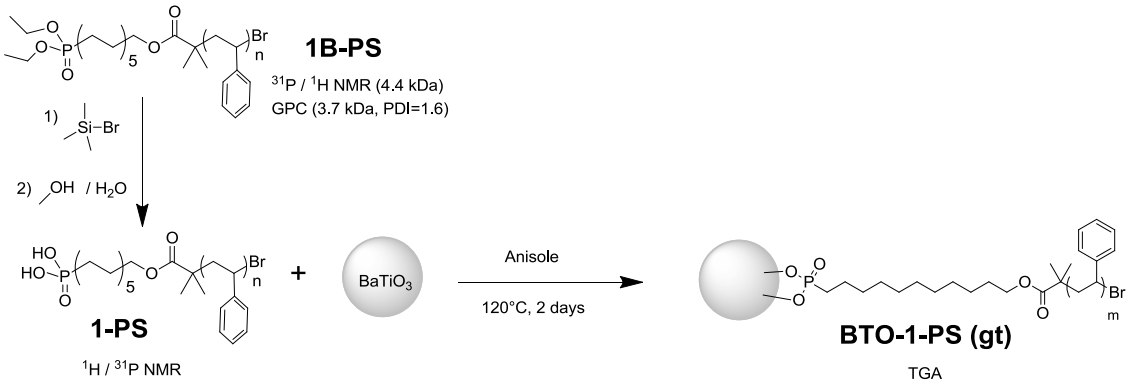

Figure 3.32 Grafting phosphonic acid-terminated PS to $BaTiO_3$ starting from phosphonate-terminated PS.

Table 3.8. ^{31}P nuclear magnetic resonance peaks found for species involved in the scheme of Figure 3.32 and comparison with unbound phosphonate and phosphonic acid.

Sample	Description	^{31}P NMR shift
1B	Phosphonate	32.8
1B-PS	Phosphonate-g-polytstyrene	32.8
1-PS	Phosphonic acid-g-polystyrene	36, 37 (broad doublets)
1	Phosphonic acid	37.5

3.7 Grafted polymers on BTO nanoparticles and application for hybrid capacitors

Most surface-initiated polymerization studies from nanoparticles are reported using SiO_2; this is attributed to the widespread availability of commercial nanoparticles and synthetic methods for specific sizes and shapes.[31] Silane monolayers are typically used as initiators. Since SiO_2 has a low dielectric constant (3.9), similar methodologies are being applied to higher dielectric constant materials, such as $BaTiO_3$ and TiO_2 nanoparticles. Given that the surface chemistry is different for the titanates than the silicates, it is possible to use phosphonic acids and other anchor groups on the titanates that do not work as effectively on silicates/silica. Both "grafting to" and surface initiated polymerization approaches are found. A mini-review is presented in this section focusing

on studies were polymers have been attached to $BaTiO_3$ or TiO_2 for capacitor applications.

Interestingly, many publications on hybrid dielectrics using grafted polymers report only permittivities, and no loss tangents or breakdown fields, and thus provide an incomplete description of the behavior of the capacitors' potential for energy storage applications. In the publications reviewed below, the values for these quantities are referenced whenever available.

Maliakal *et al.*[19] used a bromoisobutyrate terminated phosphonate to grow polystyrene and then graft it to titania nanorods (Figure 3.33). They did not report any washes after the "grafting to" reaction, which leaves open the possibility that not all the polymer measure by elemental analysis was covalently attached to the particle. The composite (with $\varepsilon = 8$) was used as gate dielectric in pentacene thin film transistors to prove that they could withstand operation in transistors, but no comparison was made in terms of mobility, on/off ratio or threshold voltage against another material used as dielectric. They report the very low breakdown strength of *ca.* 2 V/μm for films 1.25 μm thick.

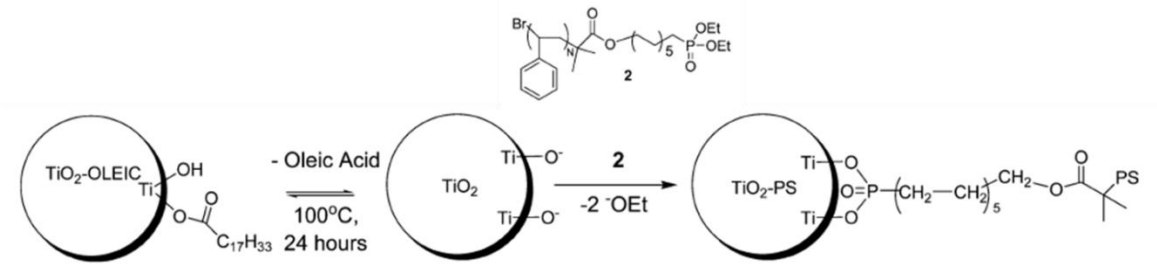

Figure 3.33 Grafting to TiO_2 using phosphonate terminated polystyrene. Reproduced from Maliakal *et al.*[19]

In the case of Tchoul *et al.*,[30] polystyrene was coupled to TiO_2 nanorods by click chemistry (Figure 3.34). The azide group needed was built on the nanoparticles as opposed to modifying the nanoparticles with the azide already coupled to the linker, which makes verification of presence of **3** in their scheme difficult (in fact no

characterization is offered in the paper). The grafting of alkyne-terminated polystyrene is said to afford composites of up to 38% m/m of polymer; nonetheless, the films gave low dielectric constant ($\varepsilon = 6.4$) and had significant amount of CuBr from the click chemistry step that could not be removed in purification steps, possibly by virtue of being strongly bound to particles by complexation to azide and triazole functionalities. Heating the films to 160 °C removed all solvent, potentially reducing mobility of Br^- ions, decreasing the loss tangent significantly.

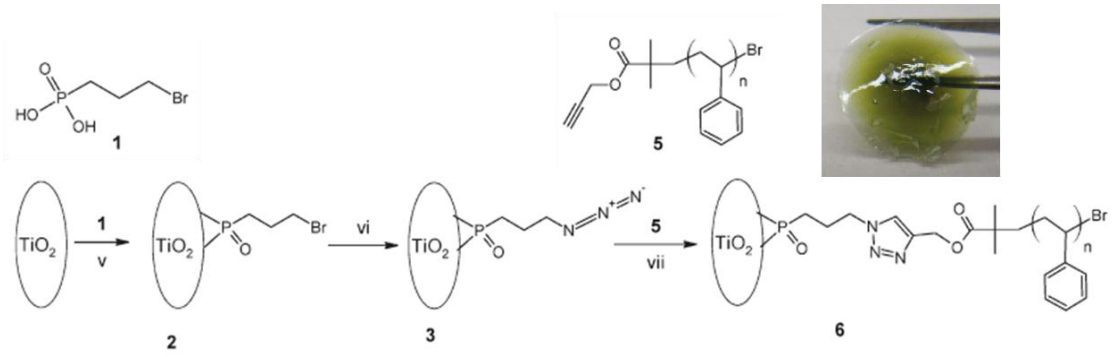

Figure 3.34 Synthesis of the azide-functionalized titanium dioxide and grafting of the alkyne terminated polystyrene. Inset: picture of a 2 mm thick assembly of the hybrid material **6**. Green color evidences high concentration of copper. From Tchoul *et al.*[30]

Jung and collaborators[32] made a composite prepared by mixing free polystyrene with a core-shell structure consisting of polystyrene-b-poly(styrene-co-vinylbenzylchloride) grafted to UV/O_3 and NaH treated 30-50 nm BT nanoparticles and reacted with triethylamine to convert residual methylene chloride groups to ammonium salts, which should strongly interact with BTO, stabilizing the polymer shell. The grafts themselves were 5-7 nm thick. With dielectric constants as high as 45 (at 10 kHz) and breakdown strength as large as 222 V/μm, they obtained energy densities close to the 10 J/cm^3 benchmark. To the best of the author's knowledge, these are the best results, in terms of maximum energy density, from covalently attached polymer-BTO hybrids.

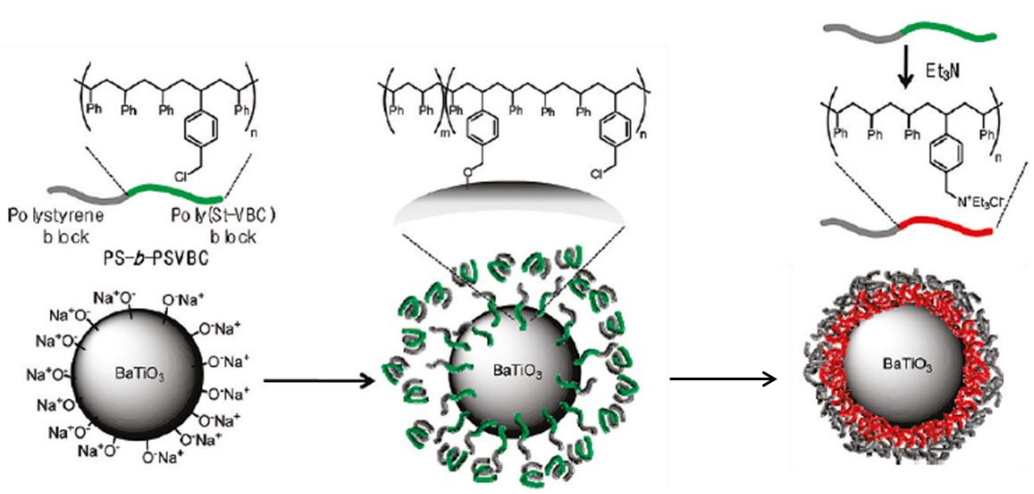

Figure 3.35 Modification of $BaTiO_3$ nanoparticles with block copolymer shell via grafting from and post-grafting treatment with base. Reproduced from Jung, *et al*.[32]

Table 3.9 Dielectric properties of BT-polymer shell nanocomposite films. From Jung, *et al*.[32]

	BT[PS-*b*-PSVBC in PS			BT[*r*-PSVBC in PS		
	75 wt %	50 wt %	25 wt %	75 wt %	50 wt %	25 wt %
Film thickness (nm)	1.84	1.30	1.28	2.41	2.16	1.79
Relative permittivity (@ 10 kHz)	44.7 ± 0.7	20.5 ± 1.2	7.5 ± 0.6	22.3 ± 1.2	12.8 ± 1.7	6.2 ± 0.6
Dialectric loss (@ 100 kHz)	0.060	0.030	0.028	0.079	0.027	0.014
Breakdown strength (V/μm)	222 ± 14	285 ± 25	394 ± 20	95 ± 9	134 ± 34	308 ± 21
Energy density (J/cm^3)	9.7	7.3	5.7	0.9	1.0	2.6

More recently Xie and coworkers[33] used a grafting-from approach where an ATRP-active silane modifier was built in two steps from H_2O_2 treated 100 nm BT particles (again complicating characterization as in the case of Tchoul *et al*. above). Surface initiated polymerization of methylmethacrylate was done through conventional ATRP, resulting in composites with up to 46% m/m of grafted polymer (Figure 3.36). It is not clear if they were able to remove the large amounts of CuBr added (12% by weight relative to nanoparticles). The highest permittivity reported, 15, was for a 20% m/m of

polymer, but they did not state breakdown fields nor maximum energy densities. Dielectric constants obtained are shown in Figure 3.37, with loss tangents *ca.* 0.04 at 1 kHz, but no breakdown strengths are reported.

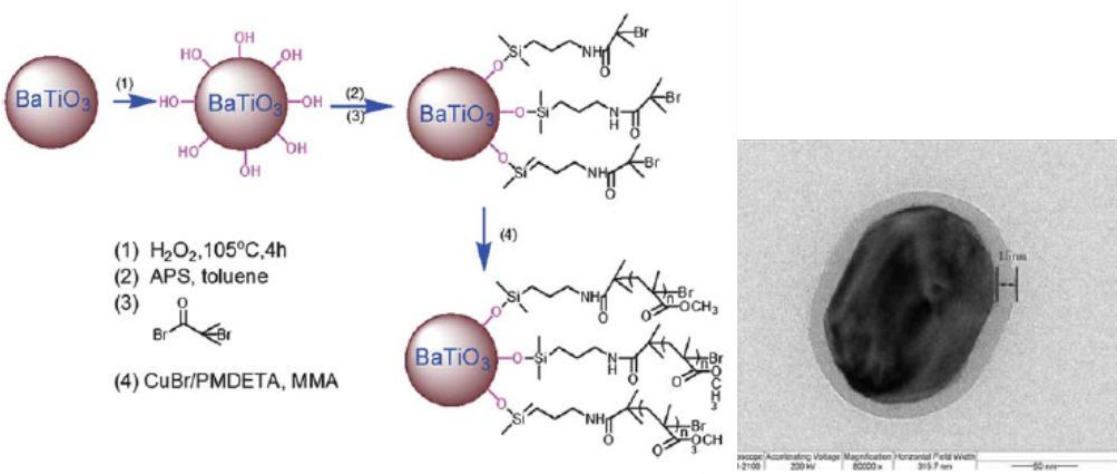

Figure 3.36 Schematic of ATRP from the surface of $BaTiO_3$ to produce PMMA shells using a silane initiator. Inset shows TEM of composite with 15 nm shell of PMMA (29% m/m PMMA). Reproduced from Xie and coworkers.[33]

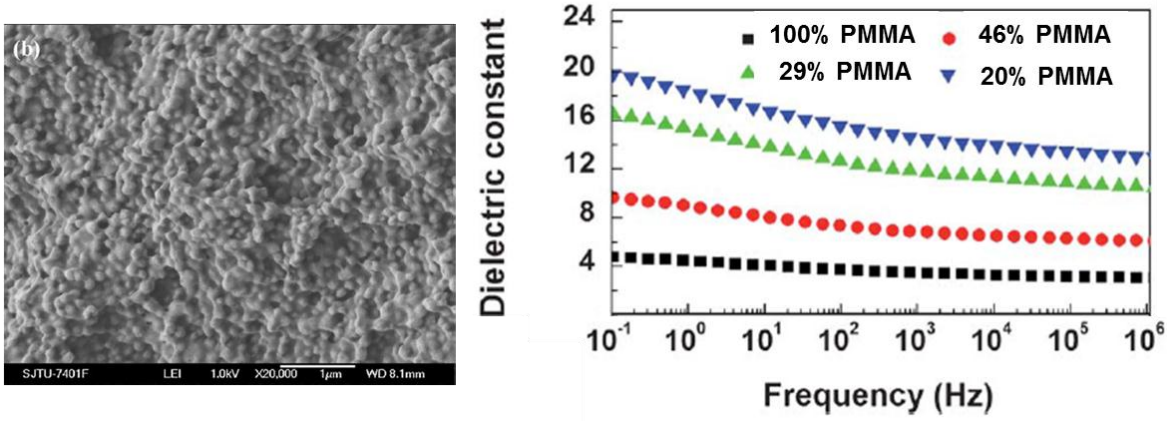

Figure 3.37 Left: SEM of film made with 29% m/m PMMA composite. Right: Dielectric constant as function of frequency for several composites. Reproduced from Xie, *et al.*[33]

3.8 Capacitors built with the BTO/PS composites

3.8.1 Early results using diluted composites

Yunsang Kim from the Perry group has collaborated in fabricating parallel plate capacitors using both pure polymer and composites with BTO-50 nm, using fabrication techniques as previously reported.[9] Early results from capacitors fabricated using a composite with very few polymer (SPB-I-260B, 3.0% polymer by mass, 63% v/v BTO - see Table 3.3) are shown in Figure 3.38. All devices were made from the composite diluted with home-made polystyrene (SPB-I-73A, M_n = 58.2 kDa, PDI = 1.51) that was stirred for one day and spin casted onto Al electrodes. Figure 3.38a shows the increase in dielectric constant as the amount of BTO increases: as qualitatively expected from effective medium models, the dielectric constant increases slightly from pure polymer (ε = 3.6) to ε = 7.7 at low, 30% v/v BTO loading; at 40% v/v and beyond, it saturates around ε = 18. Assuming the BTO nanoparticles' permittivity to be 80 (estimated from extrapolation of PFBPA-BTO in Viton[9]) gives the fit shown in Figure 3.38a for the modified Kerner model. Saturation of permittivity at high loadings was also observed by Kim *et al.* for phosphonic acid-modified BTO in Viton,[9] and is attributed to voids formed during film processing. Figure 3.38b shows that the dielectric constant is mostly independent of frequency.

Figure 3.38c shows the loss tangents for the composites made. Interestingly, the most diluted composites gave higher loss at low frequencies than the less diluted composites. This might be due to scattering of impurities from the home-made polymer that was used. At higher loading of BTO there is less polymer and hence fewer impurities, and the BTO itself may act as charge trap and preclude movement of the residual impurities.[34] It was possible to measure breakdown fields, but the thickness decreased significantly as the volume fraction increased (Figure 3.38e), hindering making a proper comparison of the composites breakdown strength, as breakdown is known to

depend on the thickness. This is attributed to the probability of finding a defect leading to a conduction path in films.[35] While adjustment of the solution concentrations or spin coating conditions could probably achieve the desired constant thickness (around 3 μm), the focus was set on making films with the pure one-component composites with low BTO loadings from section 3.5.3, as shown in the next section.

These first results were very encouraging given the latest data published by the Perry group on Viton-BTO composites (Figure 3.39). Although the dielectric constants achieved for the PS/BTO composites were around half those of Viton/BTO composites (due mostly to the high dielectric constant of Viton itself), the loss tangents were small for the high loadings of BTO in PS-BTO compared to Viton-BTO composites.

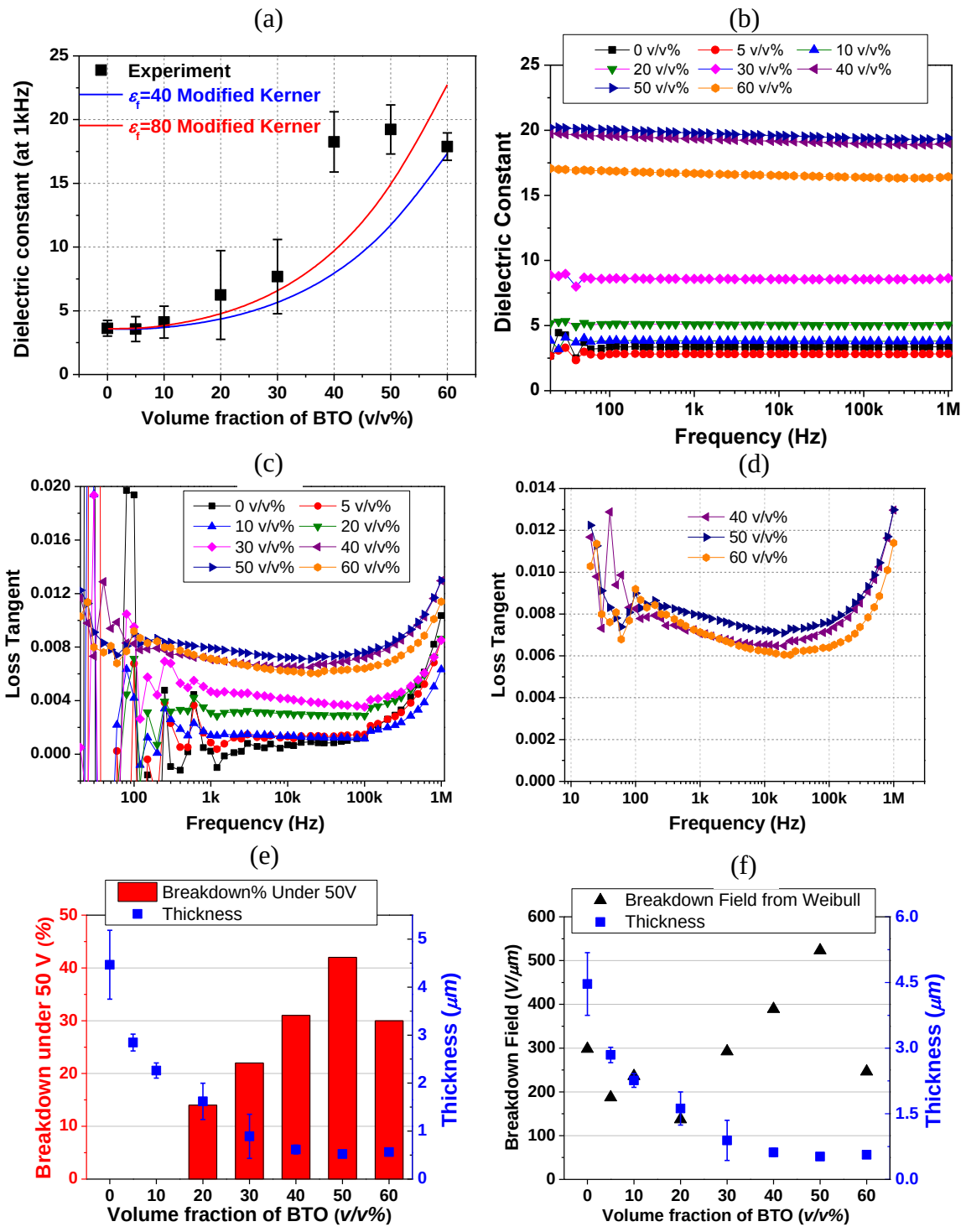

Figure 3.38 Device results from diluted **BTO-1-PS** composites: (a) dielectric constant as a function of volume fraction of BTO in the mixed composite. Calculated permittivities from modified Kerner model are shown. (b) Dielectric constant as a function of frequency applied. (c) Loss tangent over broad frequency range for all composites. (d) Loss tangent for higher loading composites. (e) Frequency of breakdown under 50 V and

film thickness for the different loadings. (f) Breakdown strengths for the different BTO loadings. Data and graphs from Yunsang Kim.

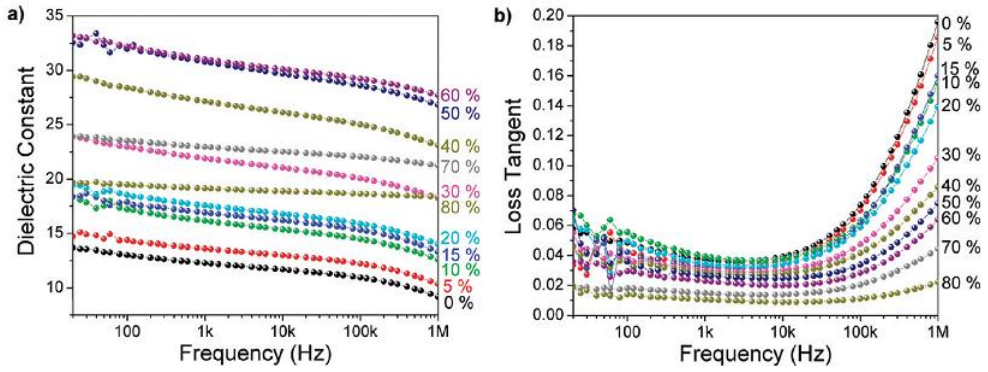

Figure 3.39 Dielectric spectroscopy results from PFBPA-modified BTO mixed with Viton. Reproduced from Kim, *et al.* [9]

3.8.2 Results from pure composites

Films from some of the undiluted composites in Table 3.6 were made by Yunsang Kim as well. Processing was very simple: the nanocomposites were dispersed in chlorobenzene by stirring overnight, and then blade-cast on ITO substrates. A pure polystyrene sample was spin-coated on ITO-glass substrate since the film prepared by blade-casting was not uniform. For these pure composites, the film thicknesses were all close to 3 μm, for fair comparison of breakdown strengths between different volume loading of nanoparticles. This was done using Weibull statistics,[36] based on the empirical failure probability distribution dependent on α, a scale parameter, β, a shape parameter that increases as the failure distribution decreases, and γ, a threshold parameter under which value of electric field no failure occurs (set to zero for these studies).

Equation 3.12 $$P_F(E) = 1 - \exp\left(-\left\{\frac{E-\gamma}{\alpha}\right\}^{\beta}\right)$$

Figure 3.40 shows the results; for this batch, the permittivity increased by twice when going from 39% to 49%v/v BTO, to reach up to $\varepsilon = 25$. Unfortunately, both 39% and 49% v/v BTO composites showed low breakdown strength (*ca.* 20 V/μm), so no Weibull analysis was done on those. Full characterization was done for 0, 20 and 29% v/v BTO loadings. While the permittivity was higher for the 20 and 29% BTO loadings than for pure PS, their breakdown strength was lower than the pure polymer (and the probability of failure higher); this compromised the maximum energy density of the composites relative to the pure polymer. Figure 3.41 show SEM images for the composites in the range of 20-50% v/v BTO. It is interesting that in the cross sections for the low volume composites (especially for 29%) the porosity is very high: observable voids in freeze-fractured nanocomposites lowered the breakdown field and effective permittivity. This suggests changing polymer system for another that would reduce porosity in nanocomposite films; in the next section, efforts to synthesize polymethylmethacrylate in solution and graft it from BTO are summarized, and devices built with such composites are discussed in Section 3.10.

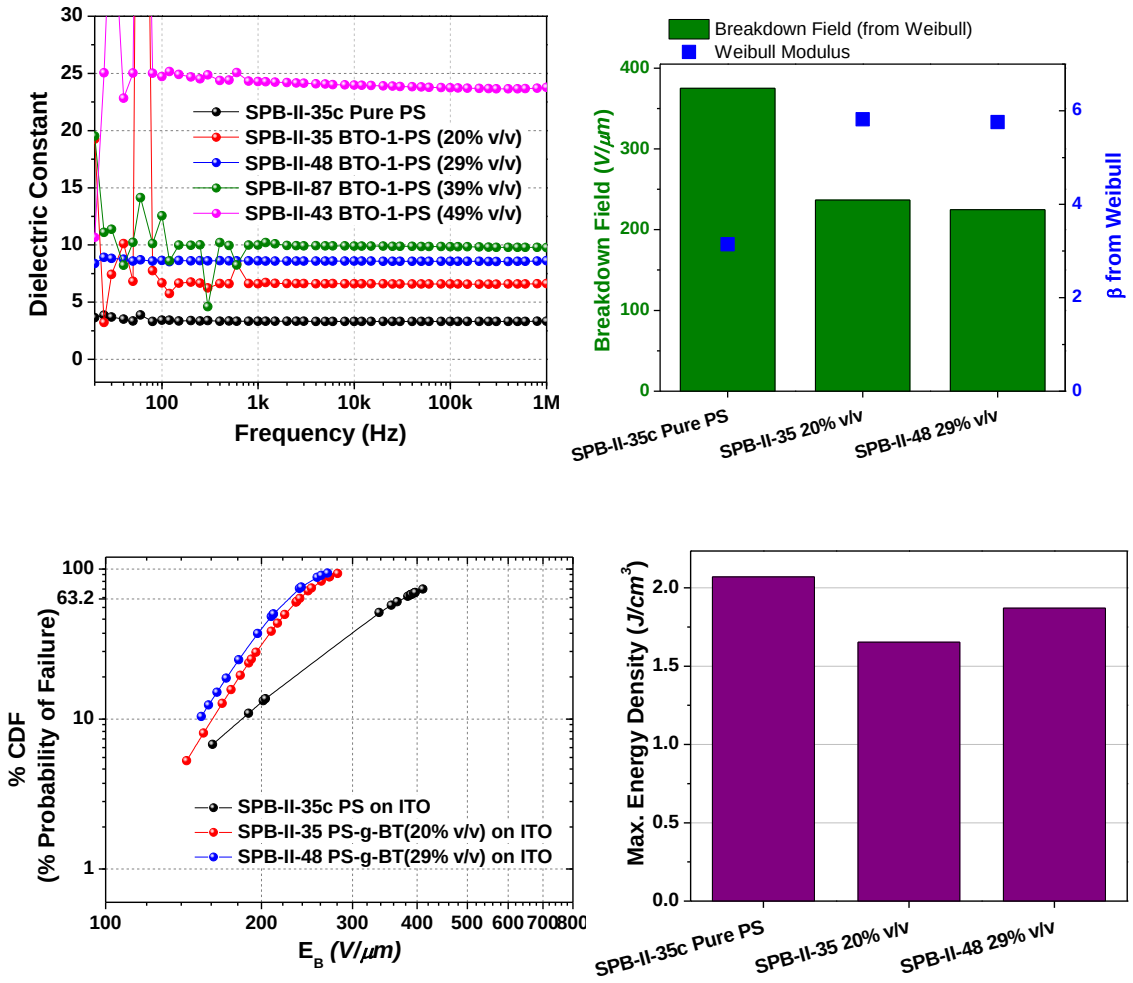

Figure 3.40 One component PS-g-BT devices characterization summary. Data and graphs from Yunsang Kim.

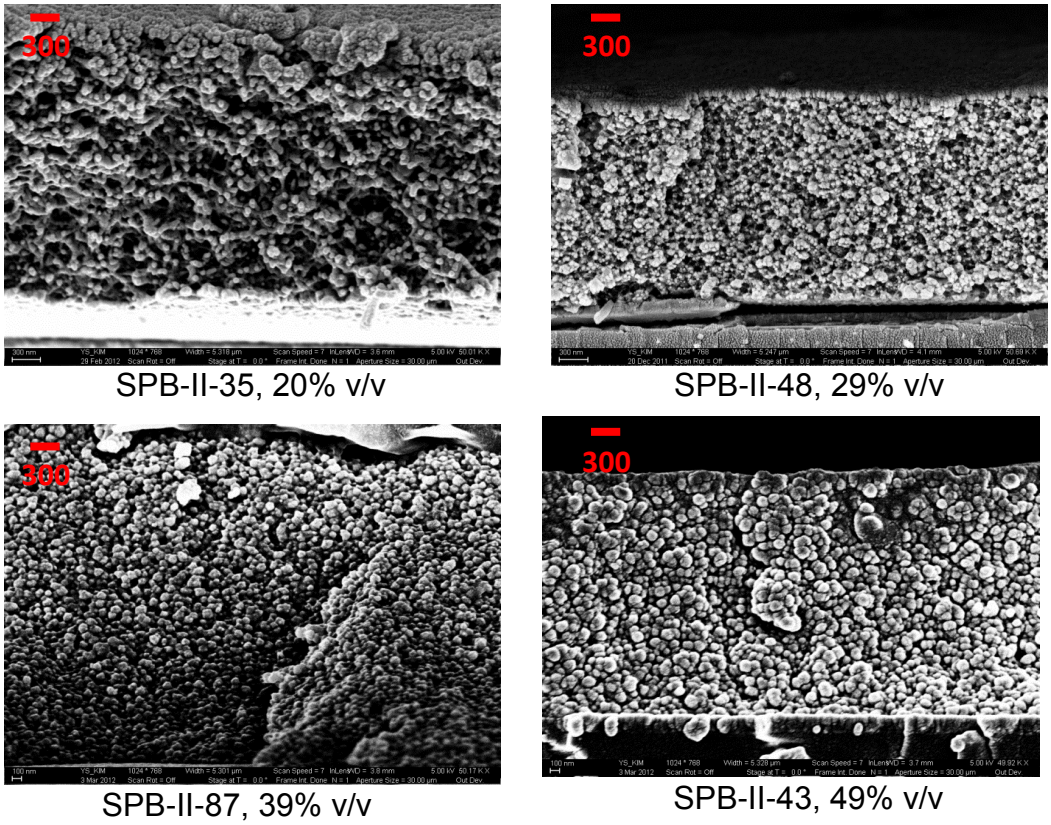

Figure 3.41 Representative SEM cross sections for BTO/PS composite films at 50 kX. Red bar is 300 nm. Images by Yunsang Kim.

3.9 Composites with polymethylmethacrylate (PMMA)

Given the device results with the one-component devices with polystyrene, we moved on to prepare composites with PMMA since it has higher permittivity and different rheological properties that could lead to better films. This work was done with the help of Ms. Katherine Henry, following the same protocols optimized for polystyrene, as shown in Figure 3.42. Methyl methacrylate has been reported to polymerize faster than styrene,[16] and this was observed in our hands as well as the polymerization was complete (~90% conversion) in just 4 h at 90 °C. Grafting from tests followed, and the conditions are summarized on Table 3.9. Higher polymer loadings are observed than in the case of PS, in much shorter reaction times. As observed for the PS composites, increasing the concentration of monomer leads to higher polymer content. To better characterize the

resulting composites, they were degrafted with acid treatments,[17,37] and the molecular weight distribution measured by GPC. In general, as the polymer content increased, so did the molecular weight and the polydispersity index. The system was also compatible with using Vitamin C as a replacement of tin (II) ethylhexanoate,[38] although the solubility was low for this reducing agent, and that led to reproducibility issues.

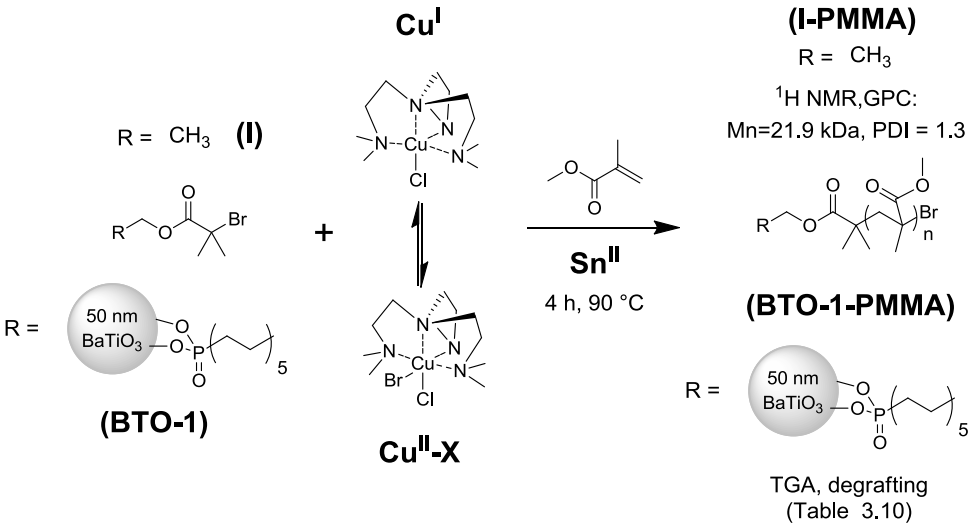

Figure 3.42 Synthesis of free and composite PMMA using ARGET ATRP with solution initiator **I** and PA modified BTO.

Table 3.10 Results for surface initiated polymerization of MMA from ATRP PA modified BTO. [M]/[A] = monomer to anisole concentration ratio.

Entry	BTO-1-PMMA22	BTO-1-PMMA10	BTO-1-PMMA16	BTO-1-PMMA28
Conditions	Neat, 15 min	[M]/[A] = 3.8, 30 min	[M]/[A] = 1.0, 30 min	[M]/[A] = 0.5, 40 min*
Conversion %	-	-	46	49
Residual mass %	59.2	34.4	50.2	66.3
BTO % v/v	22	10	16	28
Degraft M_n (kDa)	127	407	253	176
Degraft PDI	1.6	2.2	1.7	1.5

*Vitamin C used instead of **Sn^II**

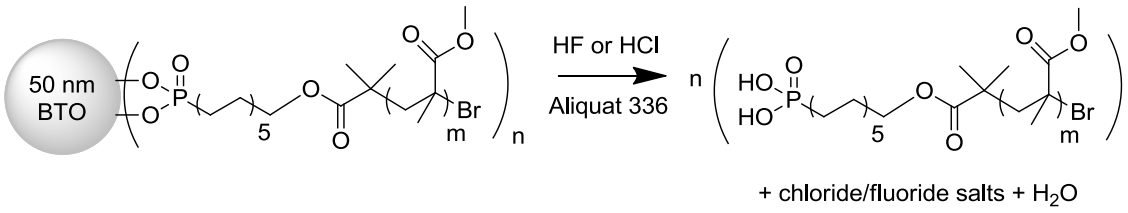

Figure 3.43 Degrafting of PMMA composite to analyze polymer by GPC and results.

3.10 Capacitors built with the BTO/PMMA composites

The composites from the previous section were transferred to Yunsang Kim in the Perry group who applied the same protocol that was used for the PS composites described in Section 3.8.2. Results are summarized in Figure 3.44. Films turned out with similar thickness, around 3 μm, which would make it possible to statistically analyze breakdown strength. Permittivity increased as expected with higher loading of BTO. The permittivity of 11 for the 59% m/m BTO loading is close to that reported by Xie *et al.*[33] for 68% m/m BTO loadings using 100 nm nanoparticles. The breakdown strength normally decreases with higher BTO loading, as observed by Kim *et al.* with mixed Viton[8] as well as in Section 3.8.2 for grafted PS composites. For these grafted PMMA composites, the highest breakdown strength was for the 10% v/v BTO composite; the pure PMMA and the 16% v/v BTO composite had similar, lower breakdown strengths, and the lowest, but still relatively high value, was for the 22% v/v BTO composite. Breakdown analyses showed similar Weibull moduli for all. To the best of the author's knowledge, this is the first report of capacitance breakdown fields using grafted PMMA. These breakdown fields were used to determine the calculated energy density. The highest loading composite (22% v/v BTO) gave the maximum energy density, attributable to the increased permittivity with little loss of breakdown strength compared to the lower loading composites. It is noteworthy that the SEM of the 22% v/v BTO shows substantially fewer pores than the PS composite with 20% v/v BTO (Figure 3.45).

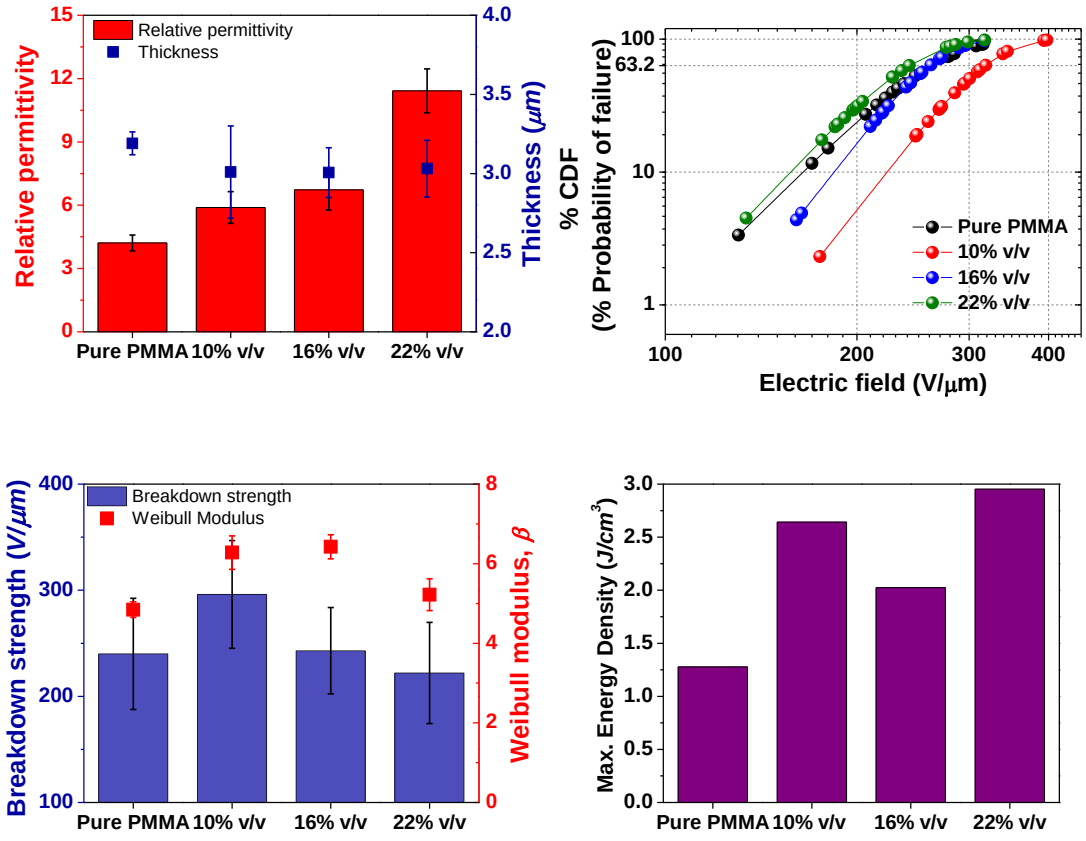

Figure 3.44 Summary of device characterization for PMMA-g-BT composites and pure PMMA. Data and graphs from Yunsang Kim.

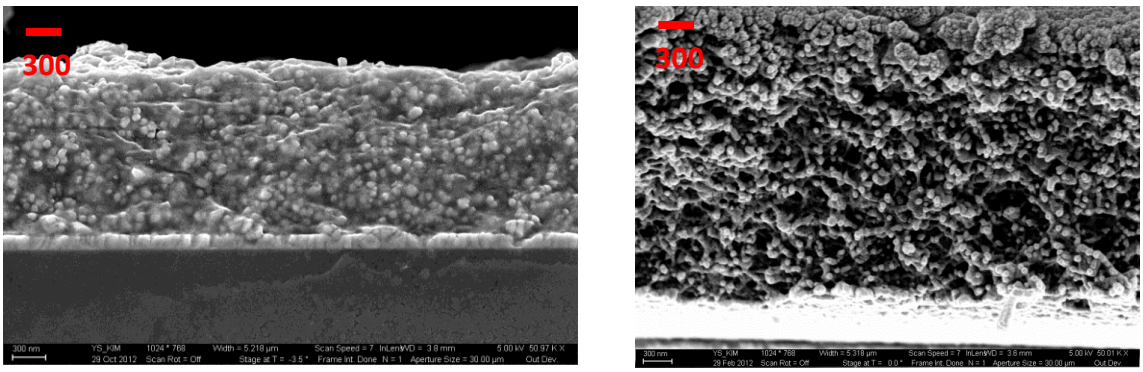

Figure 3.45 Cross section SEMs for 22% v/v **BTO-1-PMMA** composite (left) and 20% v/v **BTO-1-PS** composite (right). Scale bar is 300 nm. Images from Yunsang Kim.

3.11 Conclusions

Maliakal *et al.* had reported somewhat unsuccessful efforts on surface-initiated polymerization from initiator-coated TiO_2 due to aggregation, prompting to utilize instead the "grafting to" approach. Through some process engineering for the systems under examination in this chapter, surface initiated polymerization afforded much higher loadings than "grafting to". It has been shown throughout the chapter that changing polymerization conditions such as reaction time, temperature and concentrations can lead to vastly different results, but once conditions that were deemed optimal were chosen, varying only one (or two) of these could lead to polymer loadings in the predicted range. It has also been shown that the ARGET-ATRP methodology can be applied successfully to growth of non-conjugated polymers as an alternative to conventional ATRP surface initiated polymerization, needing less preparation procedures (no need to purify CuBr, no extensive degassing) and less stringent purification steps. For BTO-PMMA composites made with $\mathbf{Sn^{II}}$, higher polymer loadings correlated with higher molecular weight and broader weight distributions. Control experiments proved the external initiation of the ARGET ATRP polymerization.

Capacitors were made using one-component composites with PS- and PMMA-grafted BTO. High dielectric constants are reached with high BTO loading PS composites, but the breakdown strength is low. While performance of BTO-PS composites was not better than pure PS as judged by maximum storable energy density, BTO-PMMA composites did result in higher maximum energy densities than pure PMMA, especially for the highest BTO loading; this is attributable to the increased dielectric constant in the latter with breakdown strength larger than or comparable to the pure polymer. BTO-PMMA composites show lower porosity than the PS composites according to SEM.

To determine the effect that covalent attachment of the polymer has on the capacitance behavior, devices are being built to compare the one-component devices with

devices made by mixing the modified nanoparticles with commercially available PMMA (**c-PMMA**). It is expected that breakdown fields of the grafted composites will be higher and the morphologies more homogeneous than those of the composites made by mixing through ball milling.

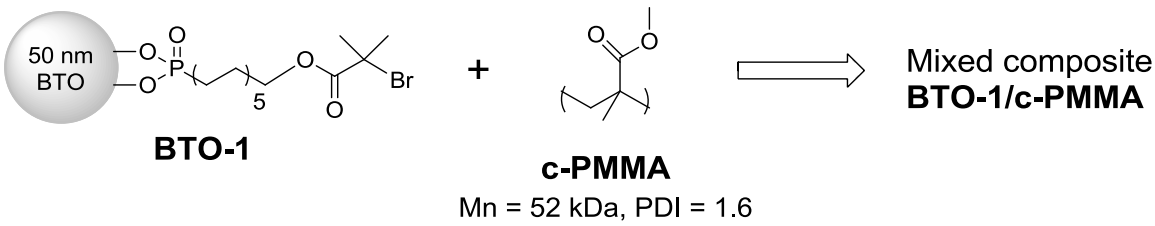

Figure 3.46. Physical mixture of ATRP-initiating phosphonic acid with commercial PMMA for device fabrication.

3.12 Experimental

3.12.1 Synthesis

All reagents were purchased from Aldrich or Alfa-Aesar and used as received unless stated otherwise. Styrene was purified by stirring overnight with CaH_2, followed by vacuum distillation, and was stored in a sealed flask under N_2. Methylmethacrylate was purified by passage through a basic alumina plug, followed by vacuum distillation, and was also stored under N_2. PMDETA was distilled in a Kugelrohr apparatus at 70 °C. CuBr was purified using published procedures, turning from green to a white color,[17] and used within the same day.

^{1}H NMR spectra were acquired using either 300 or 400 MHz Varian Mercury instruments, using deuterated chloroform as solvent and tetramethylsilane as reference (δ = 0.0 ppm). ^{31}P NMR was acquired at 162 MHz in the Varian Mercury spectrometer using 85% H_3PO_4 in a capillary tube as external reference (δ = 0.0 ppm).

FT-IR spectra of the powders and composites were acquired with the use of a Perkin Elmer Spectrum 1000 spectrometer, either by drop-casting onto NaCl plates or mixing with KBr powder. A minimum of 32 scans was acquired for each sample at 4 cm^{-1} resolution. The spectrum of a clean NaCl disk or pure KBr powder was used as a reference.

GPC was performed at 35 °C in THF to determine molecular weight(s). A combination of Waters HPLC pump 1515, UV-Vis Detector 2487, and a Refractive Index Detector 2414 were used. A Waters column (4.6 mm × 300mm; Styragel HR 5E) and polystyrene standards from Fluka were used. The polymer solution (1 mg/mL in THF) was prepared and filtered through a Mini-UniPrep PTFE vial with a 0.45 μm filter. 20 μL of each polymer solution was injected and molecular weights were calculated using Waters Breeze II software.

SEM images were acquired with a Zeiss Ultra60. High magnification images were taken using in-lens detectors at working distance of 4 mm at 5 kV (Zeiss Ultra60). For nanoparticle imaging, no surface conductive coating was needed, but for nanocomposite films, gold sputter coating was necessary to minimize charging. Freeze-fractured nanocomposite films in liquid nitrogen were sputter coated with gold before imaging. The samples were mounted vertically and observed at working distance of 6 – 8 mm at 15 – 20 kV. TGA was performed in N_2 in a Netzch STA 449 C instrument purged with N_2. A 10 °C/min heating ramp to 600 °C was followed by a plateau at 600 °C for 30 min.

A Kratos Axis Ultra^{DLD} XPS/UPS system was used for XPS analysis in Section 3.5.1. Powders were pressed on top of copper tapes. XPS using monochromatic Al Kα line was run at a base pressure of 10^{-9} Torr with charge neutralization via an electron gun calibrated using polyethylenetherephthalate. The spot size was *ca.* 700 μm. Survey XPS scans were run at 160 eV pass energy and high resolution scans typically at 20 eV pass energy and 100 meV steps.

For TEM, a chloroform or THF dispersion of the nanoparticles was drop-cast onto a copper grid coated with a carbon film. The sample was characterized in a JEOL 100CX-2 TEM operated at 100 kV. The images were acquired with a calibrated CCD camera installed in the chamber of the instrument.

DLS was performed in a TP-PCS (Protein Solutions Inc.) using appropriate dilute solutions in anisole, EtOH, or chloroform. Each value corresponds to typically the average of least 20 measurements, each having a 15 s integration time. The solution was allowed to equilibrate thermally before each set of measurements. Particle sizes were obtained by fitting the collected correlelograms to a distribution of diffusion coefficients. These values were then converted to a range of particle sizes via the Stokes-Einstein relationship. Data fitting was accomplished with a proprietary regularization algorithm that accounts for multimodal populations and non- Gaussian distributions (DYNALS, Protein Solutions).

ATRP polymerizations. For homogeneous polymerization (Section 3.2), 11-(diethoxyphosphoryl) undecyl 2-bromo-2-methylpropanoate (**1B**, 43 μL, 0.11 mmol) was added to a microwave 20 mL sealable vial. $CuBr_2$ and CuBr were added following the relative amounts shown in Table 3.1. PMDETA (61 μL, 0.29 mmol) was added to complex the copper. Styrene (5.0 mL, 44 mmol) was added, and the flask capped and deoxygenated using three cycles of freeze-pump-thaw.

After backfilling with nitrogen and sonication for 10 min to homogenize the reaction mixture, it was put to stir overnight in oil bath at 110 °C. After 19 h, it was opened to air, diluted with THF, and a sample retrieved for GPC. The mixture was precipitated onto methanol, giving a bluish solid, which was redissolved and passed through an alumina plug.

For the heterogeneous polymerizations (Section 3.5.2), proceeded the same as above but instead of adding the phosphonate, 640 mg of **BTO-1** was used, and 10 min vortex was used to disperse the particles.

ARGET ATRP polymerizations. Typically, mother solutions containing $CuCl_2$ tin(II) ethylhexanoate, and PMDETA in anhydrous anisole were prepared given the small amount (0.30 mg) of $CuCl_2$ required for each experiment. These were sonicated and heated until no solid was observed, and then an aliquot transferred to a sealable vial. Aliquots of these solutions were added to solutions of 1B in anisole or dispersions of BTO-1 in anisole. The dispersion of **BTO-1** was done in different ways for entries in Table 3.3. I-127 and I-237 used ball milling (200 rpm) in anisole with grinding media (yttria-stabilized zirconia, Inframat Advanced Materials) of three different sizes (0.5 mm diameter, spherical; 5 mm diameter and 10 mm diameter, cylindrical) for four days; I-221B used ball milling for one day. I-205, I-205B, I-260B, I-289 and I-293 were instead sonicated in anhydrous anisole, using a 1/8 stepped tip ultrasonicator (Daigger Co.) for 2 h with 30 s pulses and 5 second breaks.

Styrene was added in all cases according to the ratios in Tables 3.2, 3.3, and 3.7. N_2 was bubbled for a few seconds, and the mixtures place to stir at 600 rpm in oil bath at 110 °C. To track conversion percentages, small aliquots were retrieved before heating and at different times of reaction for ^{1}H NMR analysis. For methylmethacrylate polymerizations, ratios of catalyst and reducing agents were the same as those reported for entry 6, Table 3.6; the concentrations are reported in Table 3.9

Modification of BTO with 1 and inert phosphonic acids. The modification of BTO with **1** was done following procedures by Kim,[9,14] as described in Section 3.4, using ultrasonication to disperse the aggregated bare nanoparticles. Simultaneous reaction with ODPA and OPA was done using the same protocol but having 2 equivalents of **1** and 2 equivalents of the inert acids. Work-ups proceeded in the same way.

"Grafting to" (section 3.6). Addition of the polymer in solution was done after dispersing the bare nanoparticles using tip ultrasonication; THF or anisole were used as solvents with the concentrations presented in Table 3.7

3.12.2 Processing and characterization of nanocomposite thin films

Nanocomposites from Section 3.8.1 were prepared by ball-milling of the **BTO-1-PS** composites in chlorobenzene for two days followed by another cycle of ball-milling with the presence of **PS** for ten days. Yttria-stabilized zirconia ceramic particles of different diameter were used as grind media to prevent the aggregation of nanoparticles. The one-component composites in Sections 3.8.2 and 3.10, were simply put to stir in chlorobenzene until a homogeneous dispersion was achieved (typically a few days).

Thin films were fabricated from the resultant solutions by either spin or blade casting on an indium tin oxide (ITO) coated glass substrates (Colorado Concept Coatings, LLC) as a bottom electrode. Prior to the casting, all substrates were cleaned ultrasonically with acetone followed by with isopropyl alcohol and then treated with cold plasma at 750 W for 10 minutes. In blade casting, manual-type film applicator (Elcometer 3580) was used with a speed of ~5 cm/s. Fabricated thin films were soft-baked on a hot plate at 80 ºC for a few minutes followed by overnight drying at 120 ºC. The thickness of the films after drying was determined by using a surface profilometer (Dektak 6M, Veeco).

3.12.3 Device fabrication and characterization of dielectric properties.

Parallel-plate capacitors were fabricated by depositing circular Al top electrodes (480 nm thick and areas of 0.25 and 1.0 mm^2) on top of nanocomposite thin films using a thermal evaporator (PVD75, Kurt J. Lesker) through a shadow mask at a deposition rate of 3 Å/s. The frequency-dependent capacitance and loss tangent of capacitors were measured from 100 Hz to 1 MHz at 1 V_{rms} by using an LCR meter (Agilent 4284A). The dielectric breakdown strength was measured inside a glove box (Labmaster 130, M. Braun) by a probe station (H-100 Signatone) equipped with a micromanipulator and a microscope using a high-voltage supply (Keithley 248). Breakdown testing was

performed by ramping up a voltage from 50 V (DC) at a rate of 10 V/s until a catastrophic breakdown occurred, which was indicated by a rapid increase in leakage current to over 20 μA. The electrode area of 0.25 mm^2 was used for breakdown testing and at least 20 devices were tested to provide average and standard deviation of breakdown strength.

3.13 References

(1) Prucker, O.; Schimmel, M.; Tovar, G.; Knoll, W.; Rühe, J. *Adv. Mater.* **1998**, *10*, 1073.

(2) Frau, A. F.; Pernites, R. B.; Advincula, R. C. *Ind. Eng. Chem. Res.* **2010**, *49*, 9789.

(3) Ratner, B. D. *J. Biomed. Mater. Res.* **1993**, *27*, 837.

(4) Barbey, R.; Lavanant, L.; Paripovic, D.; Schüwer, N.; Sugnaux, C.; Tugulu, S.; Klok, H.-A. *Chem. Rev.* **2009**, *109*, 5437.

(5) Fulghum, T. M.; Taranekar, P.; Advincula, R. C. *Macromolecules* **2008**, *41*, 5681.

(6) Schulmeyer, T.; Paniagua, S. A.; Veneman, P. A.; Jones, S. C.; Hotchkiss, P. J.; Mudalige, A.; Pemberton, J. E.; Marder, S. R.; Armstrong, N. R. *J. Mater. Chem.* **2007**, *17*, 4563.

(7) Kim, P.; Jones, S. C.; Hotchkiss, P. J.; Haddock, J. N.; Kippelen, B.; Marder, S. R.; Perry, J. W. *Adv. Mater.* **2007**, *19*, 1001.

(8) Kim, P.; Zhang, X. H.; Domercq, B.; Jones, S. C.; Hotchkiss, P. J.; Marder, S. R.; Kippelen, B.; Perry, J. W. *Appl. Phys. Lett.* **2008**, *93*, 013302.

(9) Kim, P.; Doss, N. M.; Tillotson, J. P.; Hotchkiss, P. J.; Pan, M.-J.; Marder, S. R.; Li, J.; Calame, J. P.; Perry, J. W. *ACS Nano* **2009**, *3*, 2581.

(10) MDITR *MDITR Wiki. photonicswiki.org/index.php?title=Polarization_and_Polarizability* **2008**.

(11) Mauritz, K. A. *en.wikipedia.org/wiki/File:Dielectric_responses.svg* **2008**.

(12) Kerner, E. H. *Proceedings of the Physical Society. Section B* **1956**, *69*, 802.

(13) Jayasundere, N.; Smith, B. V. *J. Appl. Phys.* **1993**, *73*, 2462.

(14) Kim, P., Ph.D. Thesis, Georgia Institute of Technology, 2008.

(15) O'Dwyer, J. J. *J. Electrochem. Soc.* **1969**, *116*, 239.

(16) Braunecker, W. A.; Matyjaszewski, K. *Prog. Polym. Sci.* **2007**, *32*, 93.

(17) von Werne, T.; Patten, T. E. *J. Am. Chem. Soc.* **2001**, *123*, 7497.

(18) Jakubowski, W.; Min, K.; Matyjaszweski, K. *Macromolecules* **2006**, *39*, 39.

(19) Maliakal, A.; Katz, H.; Cotts, P. M.; Subramoney, S.; Mirau, P. *J. Am. Chem. Soc.* **2005**, *127*, 14655.

(20) Pyun, J.; Jia, S.; Kowalewski, T.; Patterson, G. D.; Matyjaszewski, K. *Macromolecules* **2003**, *36*, 5094.

(21) Jeyaprakash, J. D.; Samuel, S.; Dhamodharan, R.; Rühe, J. *Macromol. Rapid Commun.* **2002**, *23*, 277.

(22) Ejaz, M.; Yamamoto, S.; Ohno, K.; Tsujii, Y.; Fukuda, T. *Macromolecules* **1998**, *31*, 5934.

(23) Ejaz, M.; Tsujii, Y.; Fukuda, T. *Polymer* **2001**, *42*, 6811.

(24) Matyjaszewski, K.; Dong, H.; Jakubowski, W.; Pietrasik, J.; Kusumo, A. *Langmuir* **2007**, *23*, 4528.

(25) Luijk, R.; Govers, H. A. J.; Nelissen, L. *Environ. Sci.Technol.* **1992**, *26*, 2191.

(26) Ratcliff, E. L.; Jenkins, J. L.; Nebesny, K.; Armstrong, N. R. *Chem. Mater.* **2008**, *20*, 5796.

(27) Snaith, H. J.; Whiting, G. L.; Sun, B.; Greenham, N. C.; Huck, W. T. S.; Friend, R. H. *Nano Lett.* **2005**, *5*, 1653.

(28) Prucker, O.; Ruhe, J. *Macromolecules* **1998**, *31*, 602.

(29) Yang, K.; Huang, X.; Huang, Y.; Xie, L.; Jiang, P. *Chem. Mater.* **2013**.

(30) Tchoul, M. N.; Fillery, S. P.; Koerner, H.; Drummy, L. F.; Oyerokun, F. T.; Mirau, P. A.; Durstock, M. F.; Vaia, R. A. *Chem. Mater.* **2010**, *22*, 1749.

(31) Radhakrishnan, B.; Ranjan, R.; Brittain, W. J. *Soft Matter* **2006**, *2*, 386.

(32) Jung, H. M.; Kang, J.-H.; Yang, S. Y.; Won, J. C.; Kim, Y. S. *Chem. Mater.* **2009**, *22*, 450.

(33) Xie, L.; Huang, X.; Wu, C.; Jiang, P. *J. Mater. Chem.* **2011**, *21*, 5897.

(34) Kilaru, M. K.; Heikenfeld, J.; Lin, G.; Mark, J. E. *Appl. Phys. Lett.* **2007**, *90*, 212906.

(35) Kim, Y.; Kathaperumal, M.; Smith, O. N. L.; Pan, M.-J.; Cai, Y.; Sandhage, K. H.; Perry, J. W. *ACS Appl .Mater. Interfaces* **2013**, *5*, 1544.

(36) Weibull, W. *J. Appl. Mech.* **1951**, *18*, 293.

(37) Babu, K.; Dhamodharan, R. *Nanoscale Res. Lett.* **2009**, *4*, 1090

(38) Min, K.; Jakubowski, W.; Matyjaszewski, K. *Macromol. Rapid Commun.* **2006**, *27*, 594.

CHAPTER 4 SURFACE-INITIATED KUMADA CATALYST-TRANSFER POLYMERIZATION FOR GROWTH OF POLYTHIOPHENES FROM ITO

Thiophene derivatives have received much attention in the organic photovoltaic community. The prototypical poly(3-hexylthiophene) (P3HT) is a good donor in bulk heterojunction solar cells: it has a relatively small optical gap (~1.9 eV, 650 nm), is soluble in many solvents, and possesses high field-effect hole mobilities because of the semicrystalline nature of its spin-cast films.[1] Poly(alkylthiophenes) can be synthesized through controlled polymerization protocols that allow one to build chains with narrow weight distribution and high regioregularity, *i.e.* the percentage of unit pairs adopting a head to tail (HT) conformation (Figure 4.1) relative to the totality of unit pairs. Both the optical and transport properties of pristine P3HT films are known to change as a function of the molecular weight, PDI, and degree of regioregularity. It has been suggested that the performance of organic solar cells employing P3HT may be increased through better organization of the nanoscale morphology of the donor / acceptor heterojunction.[2] The possibility of growing oligomers or polymers of thiophene derivatives from a transparent electrode through a controlled polymerization is exciting given the different morphological and optical properties that could potentially be achieved compared to the typical spin coated films. As presented in this dissertation, the phosphonic acid functionality can readily be attached to ITO and related TCOs used in OPVs. In this chapter, phosphonates and phosphonic acids with tail groups that can externally initiate Kumada Catalyst Transfer Polymerization (KCTP) and Grignard Metathesis (GRIM) are designed and synthesized, and initial studies via XPS and UV-Vis are carried out for optimization of polymerization conditions with the goal of generating polyalkylthiophenes.

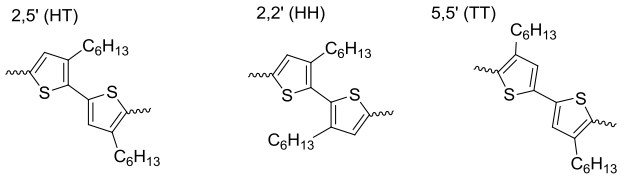

Figure 4.1 Possible couplings for P3HT.

4.1 Kumada Catalyst-Transfer and Grignard Metathesis polymerizations

In the 1990's, McCullough[3] and Rieke[4] independently developed protocols to prepare HT-regioregular polyalkylthiophenes using 1,2-bis(diphenylphosphino)ethane nickel (II) chloride, Ni(dppe)Cl_2, to catalyze organometallic condensations in which the thiophene monomers are activated with a strong Lewis base, resulting in regioregular polymers.

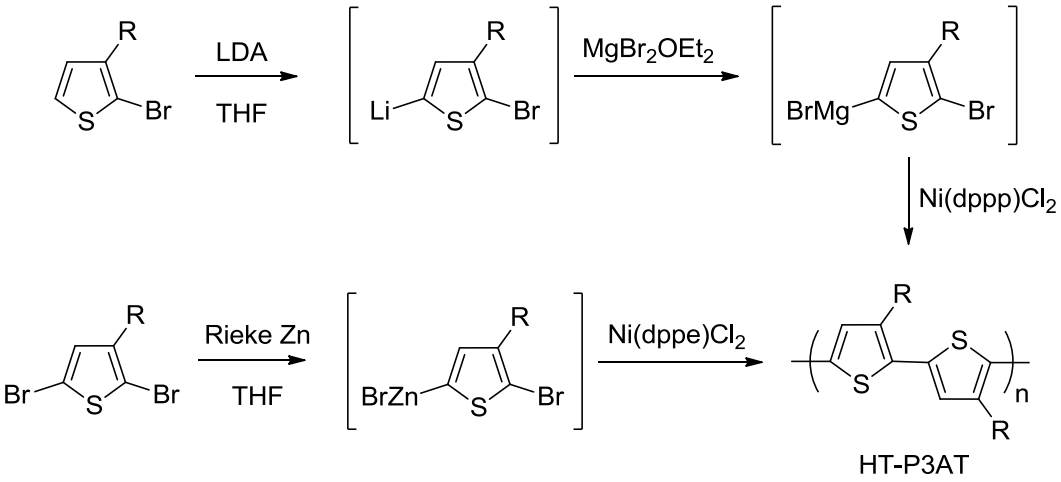

Figure 4.2 Regiocontrolled polymerization of thiophene via Mc Cullough and Rieke methods.

Yokozawa[5] and McCullough[6] improved on the molecular weight control with methodologies for which the names Kumada Catalyst Transfer (KCTP) and Grignard Metathesis (GRIM) polymerization were coined, both of which make use of 1,3-

bis(diphenylphosphino)propane nickel(II) chloride, Ni(dppp)Cl_2. In this scheme, the starting dihalothiophene is converted to a Grignard reagent, which then undergoes transmetallation with the Ni(dppp)Cl., forming a symmetric bis-organonickel species that acts as the initiator of the polymerization. Through an "arene-walking" mechanism, the metal migrates intramolecularly to insert into the C-Br at the opposite end of one of the thiophenes, forcing the two thiophene units to couple and setting up for the incorporation of another monomer unit through the same process. Since each Ni complex generates one polymer chain, the molecular weight can be controlled with the initial amount of Ni complex added. These techniques are also successful for the controlled polymerization of substituted phenylenes,[7] N-alkylpyrroles,[8] N-alkylcarbazoles and fluorenes[9] as well as thienopyrazines (Figure 4.4).[10]

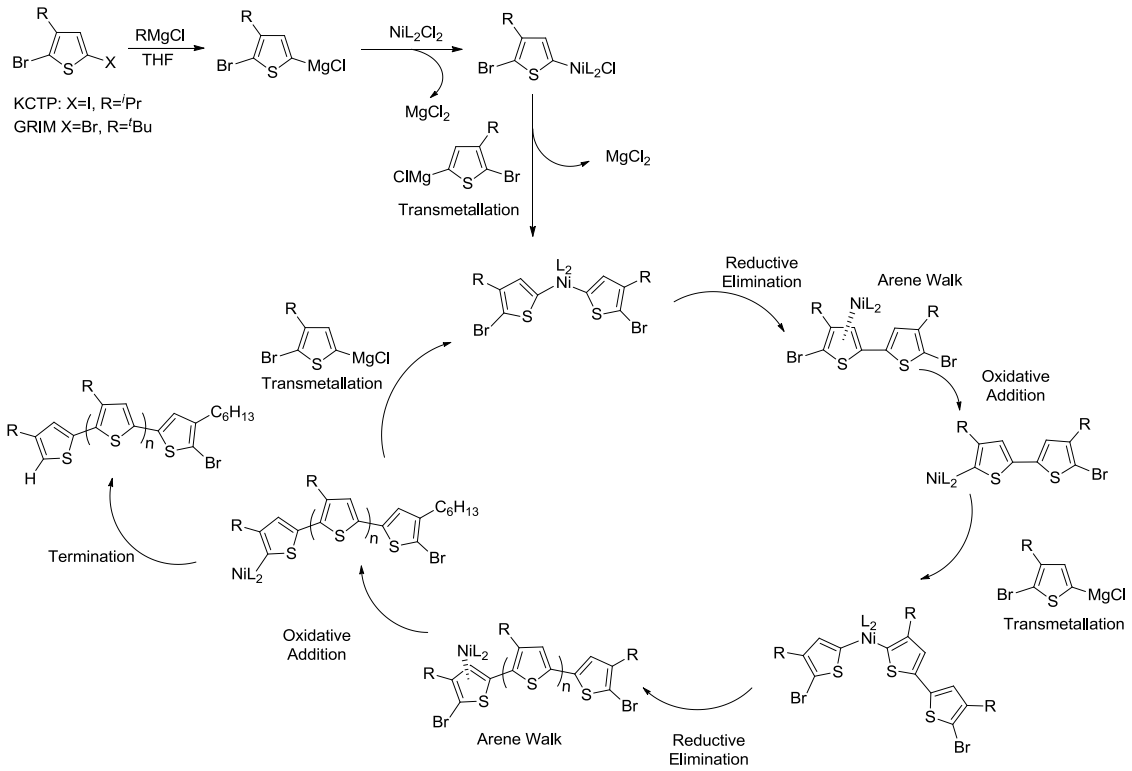

Figure 4.3 Catalytic cycle involved in KCTP and GRIM.

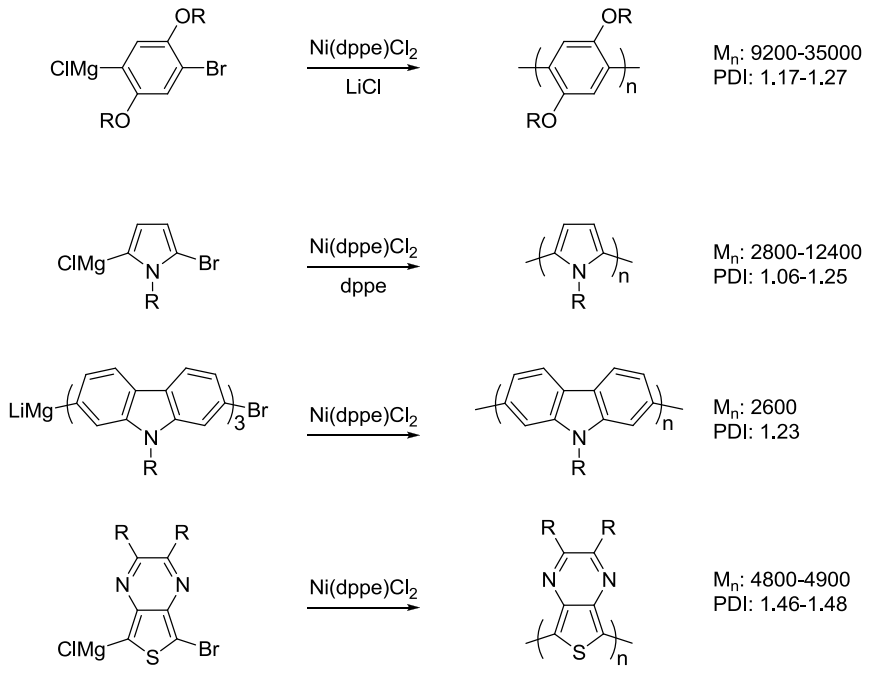

Figure 4.4 Polymerization of other monomer units using Grignard metathesis. Molecular weights and distributions from references 7-10.

4.2 External initiation of KCTP

In order to initiate a KCTP a halide must be reactive towards the Grignard reagent; the initiator need not necessarily be a thiophene; aryl halides also fulfill the requirement, so that external initiation is possible.[11] The Luscombe group, collaborators at University of Washington, developed a protocol for external initiation of KCTP making use of the inexpensive, air stable $Ni(PPh_3)_4$ to oxidatively add to aryl halides.[12] Since triphenylphosphine groups are not good ligands for the transmetallation, a ligand exchange in performed for dppp.[12] The Grignard monomer is added and the KCTP proceeds as usual.

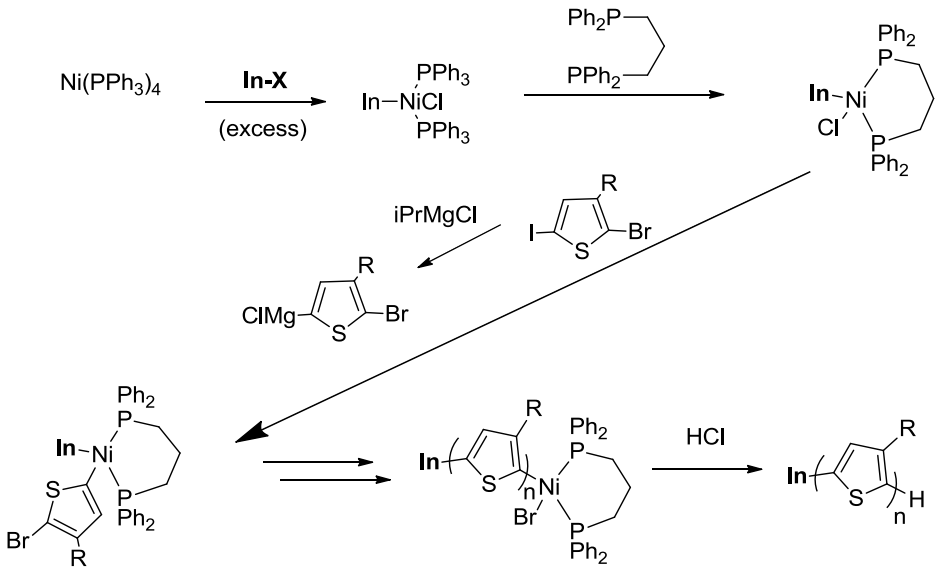

Figure 4.5 External initiation for polymerization of alkylthiophene. Exchange of the triphenylphosphines after oxidative addition for 1,3-bis(diphenylphosphino)propane affords more controlled polymerization.[11]

Oxidative addition of the aryl halide bond of the initiator to the Ni(0) catalyst (or catalyst precursor) is strongly dependent on the position and the type of functionality on the aryl group. The Luscombe group observed that the presence of *para*-substituents on the aryl halide initiator dramatically influenced the percent initiation efficiency of the polymerization: initiation decreases by at least 50% if such a substituent is an electron-withdrawing group and falls to almost 0% when the functionality is electron donating.[13] On the other hand, methyl substitution in the *ortho* position gave initiation percentages and polymer chains similar to that of chlorobenzene (90% initiation, 92% regioregularity, PDI 1.4 as judged by Matrix-Assisted Laser Desorption Ionization Mass Spectrometry (MALDI/MS) and GPC).[11] The effect of other bulkier substituents in that same position had not yet been investigated.

4.3 Design and synthesis of phosphonates and phosphonic acids for external initiation of polymerization of thiophenes

Phosphonic acid anchoring groups were proposed to initiate polymerization of thiophenes from ITO and related oxides. It remained to be determined if phosphonate functionalities would be detrimental to the complexation and polymerization steps. Among the range of substituents in aryl halide initiators that the Luscombe group had examined for external initiation was the diethylphosphonate group (precursor to the phosphonic acid) in *para* position relative to the halide; for this, complete degradation of the Ni catalyst/initiator complex was observed. If solution-phase studies using other phosphonates were successful for externally initiating polymerization, there would be no reason to believe it should not work from a surface-bound modifier as well. Characterization of homogeneous polymerizations would allow full characterization of intermediates and polymers made by standard techniques such as NMR, GPC and MALDI-MS.

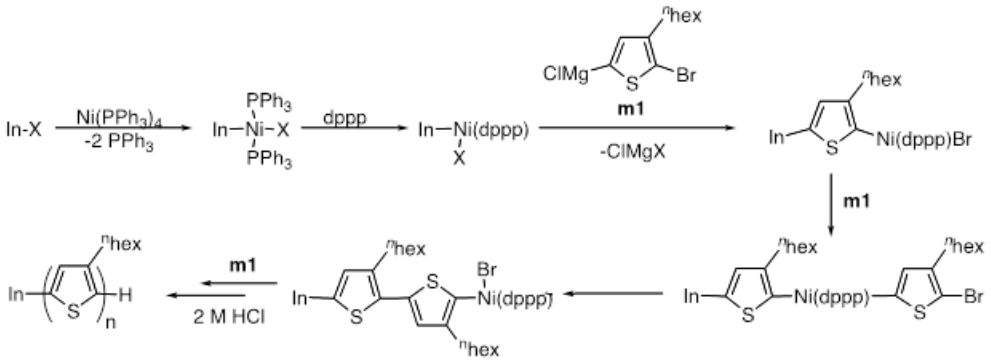

Figure 4.6 Polymerization pathway for phosphonate-terminated initiators.

The author of this dissertation synthesized several phosphonate and phosphonic acid initiators, most of them previously unreported, in order to test the phosphonates as initiators to devise the best aryl groups to try in the phosphonic acid version for surface initiated polymerization from ITO. The Luscombe group used the phosphonates made by

the author to study the electronic vs. steric interactions and their effect on the chain-growth polymerization mechanism.[14] The design and synthesis of the molecules (Figure 4.7) are discussed in this section.

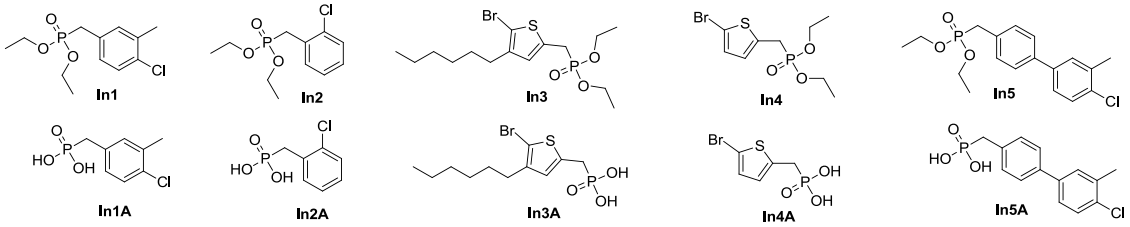

Figure 4.7 Initiators synthesized by the author.

Figure 4.8 shows the synthesis of a phosphonate/phosphonic acid designed with the phosphonate in *para* position to the halogen, and a methyl *ortho* to the halogen to stabilize the complex that would form with the Ni as observed for 2-chlorotoluene, which initiates quantitatively.[12] The first route (A) used reduction of the carboxylic acid via $BH_3 \cdot THF$.[15] While the crude contained the alcohol in high amounts, it also contained deprotonated starting material, and separating them required additional steps from those reported. The final yield was low because of multiple extractions/crystallizations. A second batch of the compound was made through reduction with $LiAlH_3$ instead, and the crude product was taken through the next steps (conversion to the bromide and phosphorylation) and then purified, which resulted in better overall yield and a larger quantity of phosphonate.

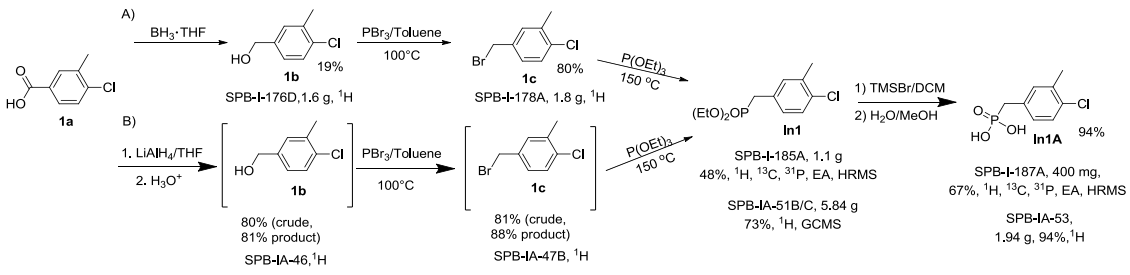

Figure 4.8 Synthesis of diethyl 4-chloro-3-methylbenzylphosphonate In1 and its acid In1A using two different reductions.

Figure 4.9 shows the synthesis of **In2**, with the methylene phosphonate group placed in *ortho* position to the halogen to stabilize the Ni complex.[12] As in the case of **In1** and **In1A**, the Arbuzov reaction and subsequent conversion to the acid gave no problem.

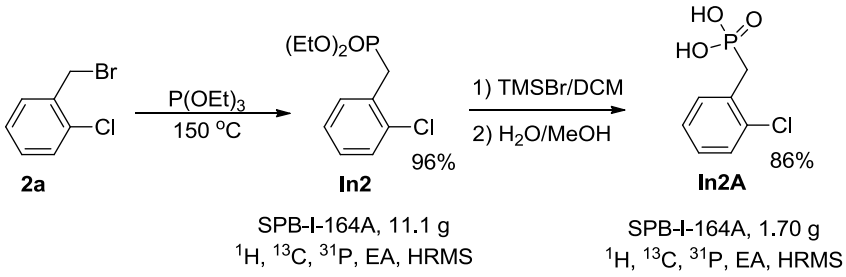

Figure 4.9 Synthesis of diethyl 2-chlorobenzylphosphonate **In2** and its acid **In2A** from the methyl bromide.

Figure 4.10 shows the scheme for synthesis of thiophene-containing phosphonates / phosphonic acids. **In4** and **In4A** are obvious choices since the corresponding thiol and the 2-bromothiophene alone have worked before for this kind of polymerization.[13,16] **In3** and **In3A** are interesting since the chemistry should be the same as with **In4** and **In4A**, but the alkyl chain might change the ordering of a monolayer prepared with **In3A**, perhaps making a smoother "transition" into the P3HT polymer brush. The bromination in the first step was based on work by Mamane, *et al*.[17]

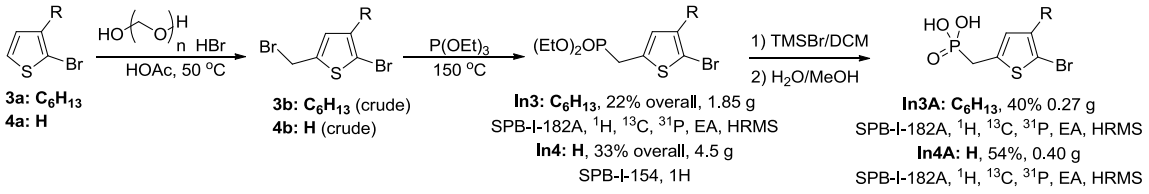

Figure 4.10 Synthesis of diethyl (5-bromo-4-hexylthiophen-2-yl) methylphosphonate **In3**, its acid **In3A**, diethyl (5-bromothiophen-2-yl)methylphosphonate **In4** and its acid **In4A**.

With the intention of attempting thiophene growth further from the ITO, the distance between the initiating group and the phosphonic acid was increased: 4'-chloro-3'-methylbiphenyl-4-methanophosphonic acid **In5A** was made according to Figure 4.11. The phosphonate **In5** was also purified to use as initiator for homogeneous polymerization studies.

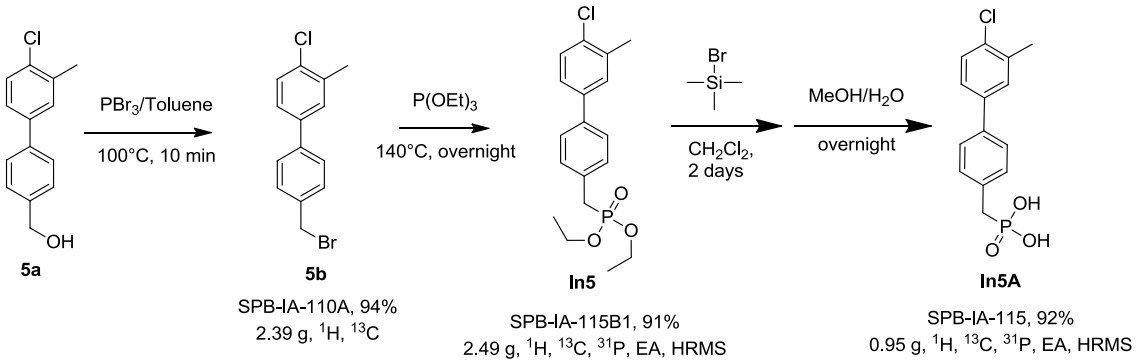

Figure 4.11 Synthesis of 4'-chloro-3'-methylbiphenyl-4-methanophosphonate and its acid from the commercially available hydroxide.

4.4 Synthesis of polymers from the phosphonates

Natalia Doubina from the Luscombe group used the phosphonates as initiators for synthesis of P3HT (adding 30 equivalents of monomer which in theory would result in M = 5.3 kDa) using the scheme from Figure 4.6. The results were analyzed by GPC, ^{1}H and ^{31}P NMR, and MALDI MS (Table 4.1). The latter technique allows the determination of initiation efficiency via comparison of the intensities of large fragments with the molecular weight of the initiating group plus monomer units vs. those fragments that do not contain initiating groups. **In4** did not result in complexation with the Ni, and **In5** was not part of this study. From ^{1}H NMR spectroscopy, regioregularity can be determined give that different couplings result in slightly different chemical shifts.[18]

Table 4.1 Results from polymerization reactions with phosphonates. Data from N. Doubina using the initiators synthesized by the author.[14]

Initiator	End Groups	M_n (Da) (PDI)	% Regioregularity	% Initiation
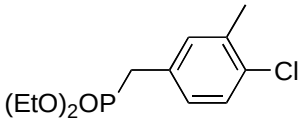 **In1**	Initiator/H (75%) Initiator/^{i}Pr (9%) H/H (13%) Others (3%)	5200 (1.2)	94	84
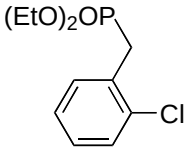 **In2**	Initiator/H (37%) Initiator/^{i}Pr (8%) H/H (47%) Others (8%)	3900 (1.6)	92	45
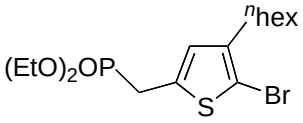 **In3**	Thiophene/H (18%) Thiophene/Br (9%) H/Br (65%) H/H (8%)	2900 (2.6)	89	27

It is clear that **In1** provided good initiation given the molecular weight (close to the expected), its low PDI, high regioregularity, and high initiation percentage. These results indicate predominance of chain-growth polymerization for that initiator compared to the others. The initiator/^{i}Pr groups are likely to arise from a minor mismatch between the relative amounts of **m1** and ^{i}PrMgCl solution because of difficulties in precisely measuring very small volumes of ^{i}PrMgCl solution and its high sensitivity to moisture and air.

DFT calculations comparing the thermodynamics of formation of the Ni-complex with **In1** and **In2** showed that the energetics were within 1 kcal/mol of each other;[14] the lower initiation efficiency of **In2** is, therefore, presumably related to kinetic effects, likely due to the bulky phosphonate group being next to the metal insertion site.

4.5 Modification of ITO with KCTP-initiating phosphonic acids

Deposition of monolayers of these PAs was demonstrated by using conventional room temperature immersion for 2 days (Figure 4.12). The overlayers were analyzed by XPS. Table 4.2 shows that the results were consistent with the molecules being on the surface: similar P/In ratios were determined in most cases (slightly higher for **In4A**), and the heteroatom ratios were close to the expected 1.0. The P/C ratios were always lower than expected, in part because of the phosphorus being further from the surface than the carbon atoms, but also the presence of adventitious contamination was to be expected in this procedure, as reported in Chapter 2 for other benzylphosphonic acids deposited at room temperature.

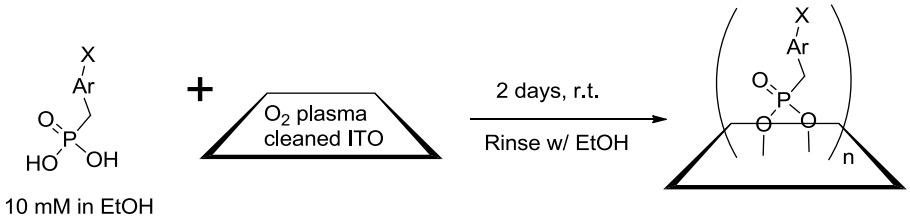

Figure 4.12 Original modification procedure of ITO with phosphonic acids.

Table 4.2 Atomic percentages and atomic ratios for the modified slides determined by XPS. Expected stoichiometric ratios in parenthesis.

Ratio\ Modifier	In1A	In2A	In3A	In4A
P/In	0.063	0.068	0.073	0.093
P/C	0.067 (0.12)	0.090 (0.14)	0.059 (0.091)	0.11 (0.20)
Br/P	-	-	0.91 (1.0)	0.84 (1.0)
S/P	-	-	0.90 (1.0)	1.25 (1.0)
Cl/P	1.33 (1.0)	0.92 (1.0)	-	-

4.6 Attempts at surface-initiated polymerization of P3HT and P3MT from ITO

Surface-initiated (SI) KCTP had already been reported by Kiriy and coworkers on silicon wafers; they embedded a poly(4-bromostyrene) on silicon wafers and glass slides on spin-coated and cured poly(glycidyl methacrylate), locking it into place via UV cross-

linking. They reported 60 nm thick films with roughness of 8 nm from AFM images.[19] A variation of this method was used on silicon wafers and ITO slides where again the macroinitiator was fixed after spin-coating it.[20] While this system resembles what is anticipated as the ideal morphology with columns that can interpenetrate an accepting material, the photovoltaic properties when using PCBM as acceptor and the grafted P3HT as donor were very poor (0.01%) due to the insulating backbone of non-conjugated polymer. Using a 4-bromophenyl-terminated alkylsilane grafted to silica nanoparticles, SI KCTP was carried out to generate P3HT[21] and poly(dialkylfluorene)[22] composites from the nanoparticles, with applications as dispersable donors in bulk heterojunction solar cells. In those cases ligand exchange for dppp and the ethane analogue dppe was used to afford more controlled polymerization.

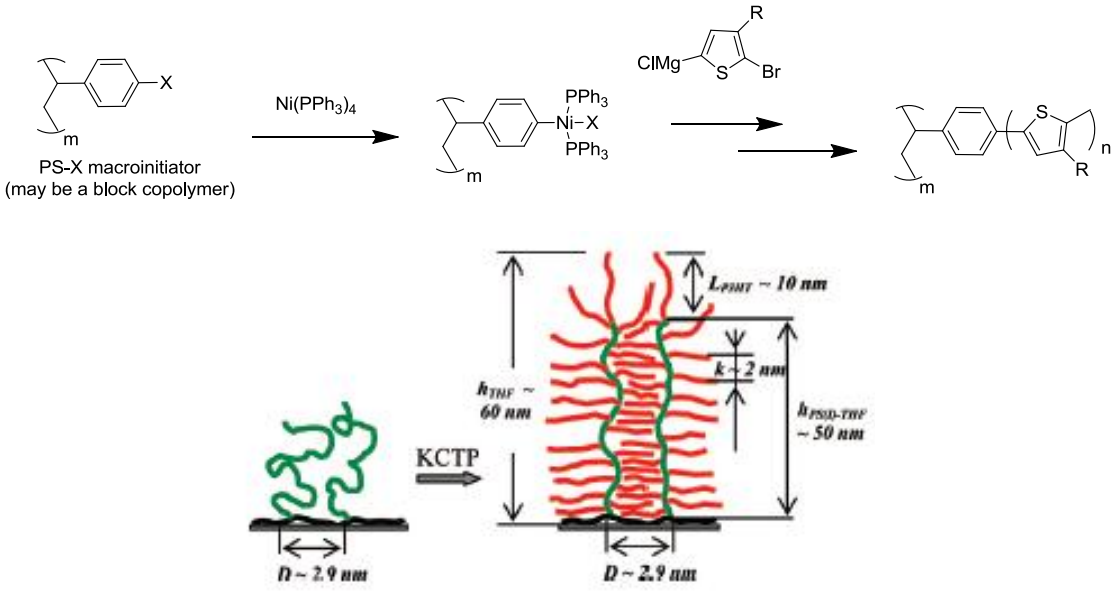

Figure 4.13 SI-KCTP as proposed by Kiriy and coworkers. The green grafts represent the cured macroinitiator, and the red grafts are the grown P3HT chains. Reproduced from Khanduyeva, *et al*. [20]

Locklin and coworkers used monolayers with trichlorosilane, thiol and phosphonic acid anchor groups to grow polymers films from SiO_2 wafers, gold and ITO on glass respectively. Poly(*p*-dialkoxyphenylenes)[23] and poly(3-methylthiophene) films were reported using either ligand exchange from an initial bypyridine ligand or direct

reaction with PPh_3[24] or dppe,[25] the second of which the Luscombe group did not find able to complex except through ligand exchange of triphenylphosphine. On ITO they reported 33 nm thick films which gave λ_{max} = 450 nm and were also characterized by IRRAS.

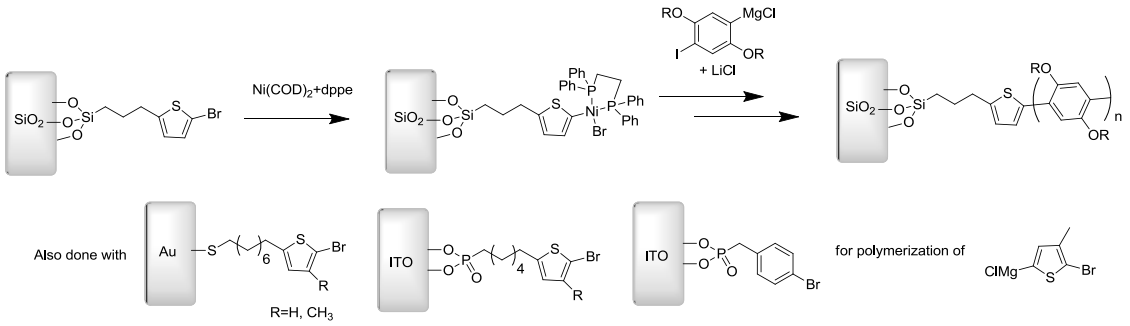

Figure 4.14 Methodology for SI-KCTP according to Locklin, *et al*.

Figure 4.15 shows the scheme followed in the first attempts to graft from ITO by the Luscombe group and the author of this work, in which the annealed phosphonatic acid overlayers were used as initiators for polymerization, using a similar procedure to that for 2-chlorotoluene in solution.[12] Unfortunately, no evidence of polymer formation was found (no change in transparency, no XPS sulfur signals for attempts with the benzylic initiators).

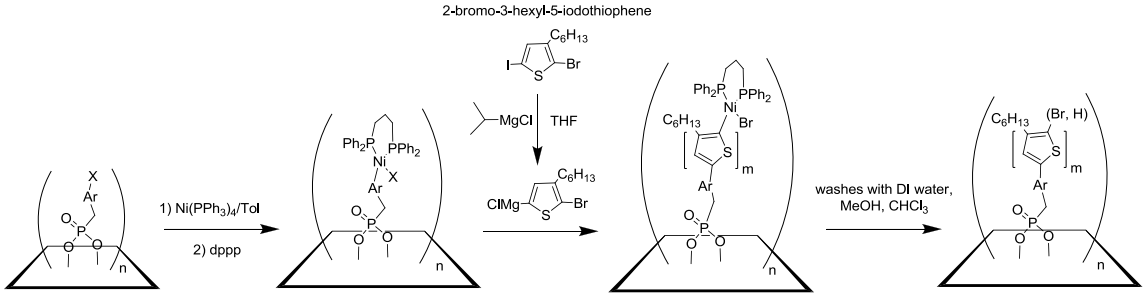

Figure 4.15 Original procedure used in surface initiated polymerization attempts from ITO. Intermediate species extrapolated from homogeneous polymerization NMR characterization.

Parallel to this author attempts, Ms. Doubina in the Luscombe group had promising results with **In1A** when using 2-bromo-3-methyl-5-iodothiophene 3MT (**2** in

Figure 4.16) as monomer using a modified procedure where the oxidative addition involves $Ni(COD)(PPh_3)_2$ (COD=1,5-cyclooctadiene) instead of $Ni(PPh_3)_4$ (Figure 4.16). It was hypothesized that steric hindrance from the alkyl chain in the hexyl monomer was preventing it from reacting with the complexed monolayer, and the methyl group in P3MT did not cause such issue.

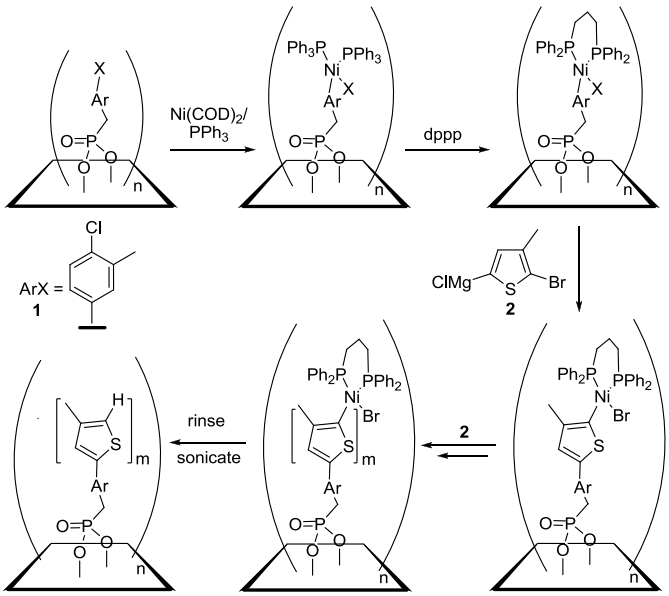

Figure 4.16 Modified procedure for surface initiated polymerization from ITO. The identity of the intermediate species is extrapolated from homogeneous polymerization NMR characterization.

Using this modified scheme, an absorption feature peaking close to 500 nm was observed by UV/Vis, with a correlation between absorbance and polymerization time (Figure 4.17).

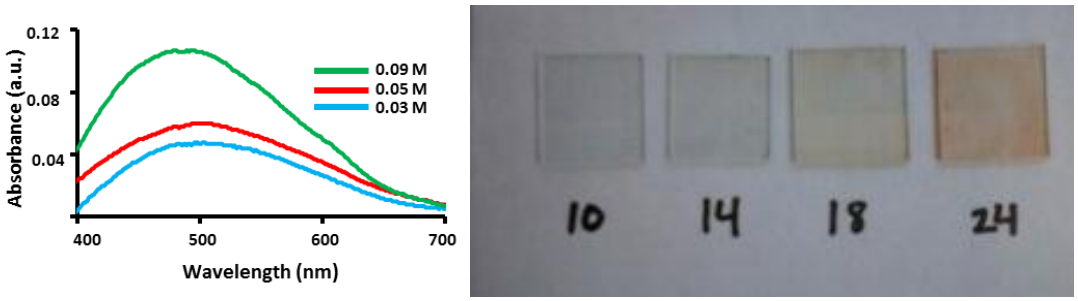

Figure 4.17 UV/Vis and photographs of **In1A**-treated ITO slides subjected to polymerization for increasing amount of hours in 0.09 M monomer solution following scheme in Figure 4.16. Data and figures from N. Doubina.[26]

AFM showed heterogeneous growth of polymer: while thicknesses up to 80 nm could be reached, the root mean square roughness was at its lowest around 20 nm regardless of thickness (it was *ca*. 4 nm for the starting monolayer).

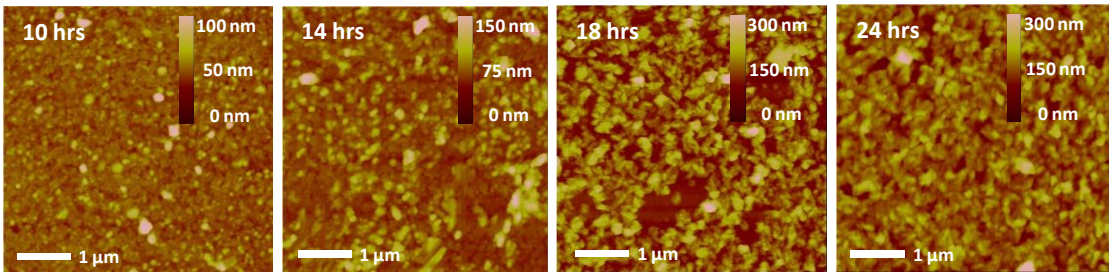

Figure 4.18 AFM micrographs of **In1A**-treated ITO slides (same as those in Figure 4.17). Thickness determined from step height measurements resulted in 18, 47, and 84 nm for 14, 18 and 24 h polymerizations respectively. Images from K. Mazzio (University of Washington).[26]

Figure 4.19 shows some of the most successful surface-polymerization results obtained by the author. Given the possibility of homocoupling reactions of neighboring complexed adducts (Figure 4.20),[25] and a mixed monolayer with an inert benzyl phosphonic acid (BPA) was used to determine if higher quality and longer polymer chains could be grown by separating initiating sites (as attempted on BTO nanoparticles for surface-initiated polymerization in Chapter 3). Most samples were prepared using hydriodic acid (HI) etching[27] and room temperature deposition, following the success in the Luscombe group in generating homogeneous films using that pretreatment.

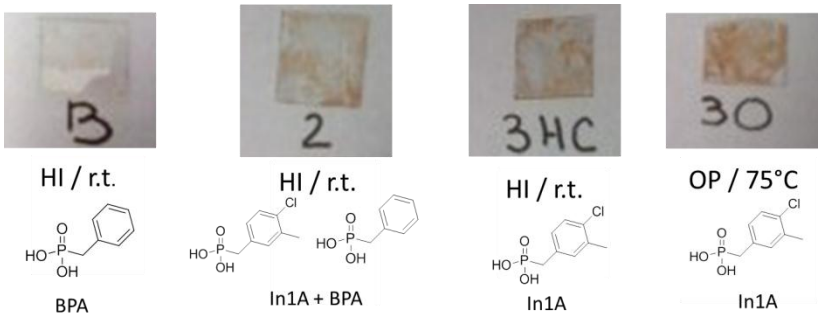

Figure 4.19 Results from 3-day polymerizations using a control (inactive) monolayer of benzylphosphonic acid, a mixed monolayer with active **In1A**, a monolayer made with **In1A** and a monolayer prepared instead with oxygen plasma pretreatment and immersion at 75 °C.

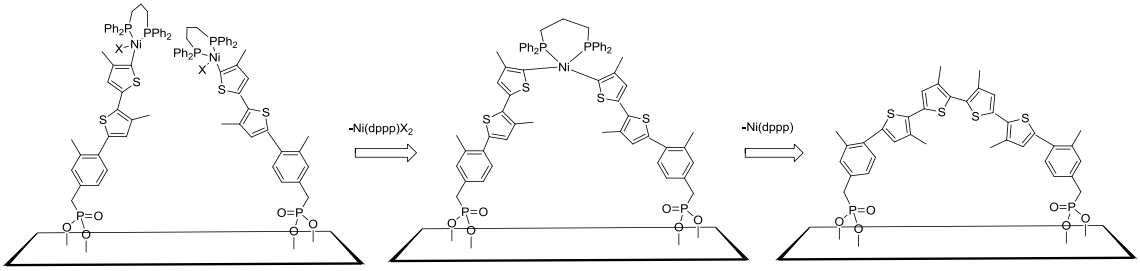

Figure 4.20 Proposed mechanism for early termination due to surface-confined disproportionation.

It was evident that pretreatment with oxygen plasma (OP) and deposition of phosphonic acid at high temperature led to the most film grown, as would also be verified by UV/Vis spectroscopy (Figure 4.21). All films showed stability to degrafting by sticky tape, further verifying the covalent attachment.[25] The mixed monolayer and the pure monolayer deposited at room temperature after HI pretreatment gave similar film color and coverage, and finally the control sample using benzyl phosphonic acid gave no polymer. These results correlate with XPS analysis, where the relative coverage of active phosphonic acid was tracked by the Cl/In ratio. The oxygen plasma pretreated sample gave the highest ratio, followed by the pure monolayer on HI-etched ITO, followed by the mixed monolayer.

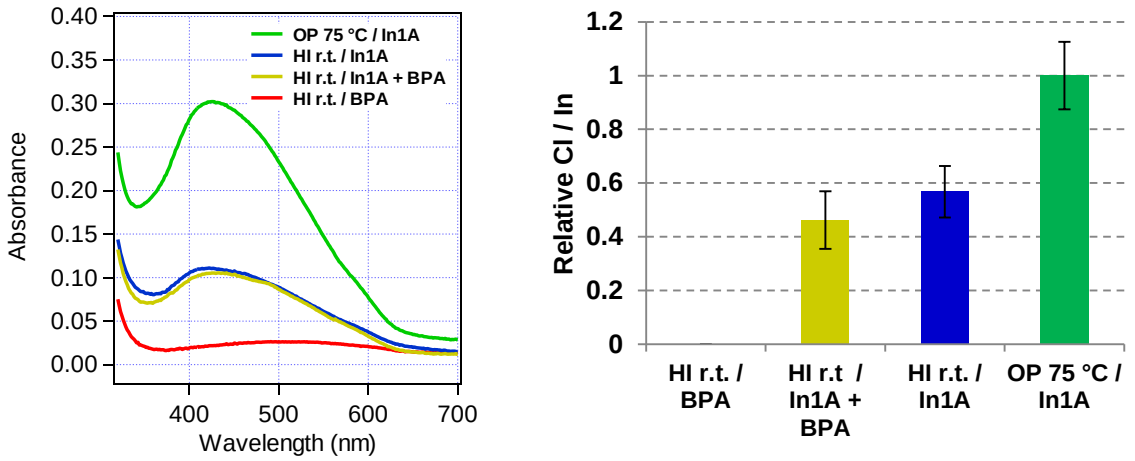

Figure 4.21 Left: UV/Vis spectra of samples from Figure 4.19. Right: XPS Cl / In ratios as a means of determining relative coverage of initiator.

P3MT polymer grafts prepared by Ms. Doubina in the Luscombe group were studied by the Armstrong group at University of Arizona to determine their feasibility as donor materials and hole-selective contacts. C_{60} was vapor-deposited on the grafted films, and devices were characterized under illumination and in the dark.[28] HI-pretreatment resulted in no photovoltaic behavior regardless of whether the P3MT was undoped or electrochemically doped. With OP-pretreatment, there was a small photocurrent under illumination (J_{SC} = 0.83 ± 0.38 $mAcm^{-2}$) with an open circuit voltage of 0.20 ± 0.15 V. The grafts when using oxygen plasma were visibly much thicker by eye than those that were HI-pretreated, and these results seem to verify that pretreatment conditions are very important in such a system and might be affecting not only the thickness of the polymer chains but also the electroactivity of the underlying substrate.[27]

4.7 XPS studies of species involved in surface-initiated KCTP

XPS was used to probe the intermediate species and determine reaction yields on the surface. The next subsections summarize two studies. In the first one, surface pretreatments were compared given the results from the last section, and also experimented multiple routes towards oxidative addition. In a second study, an inert

sample transfer system was used and the focus was to prove that the Ni (II) comes from oxidative addition and not from nickel oxidized by oxygen.

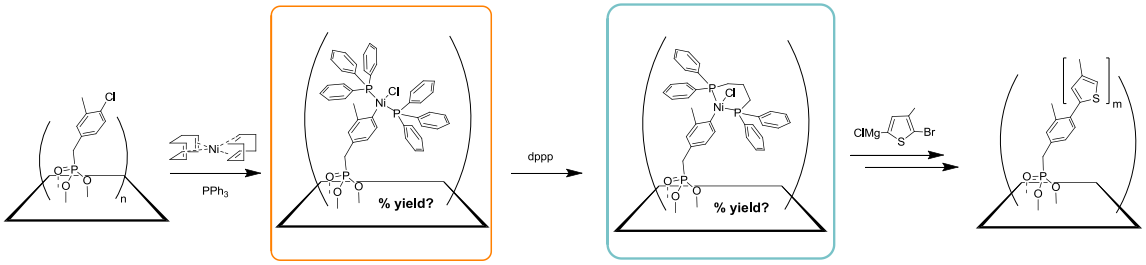

Figure 4.22 Intermediate species under scrutiny.

4.7.1 First study: consideration of multiple routes for oxidative addition

In this study, multiple oxidative addition conditions were attempted and the results analyzed via XPS to determine reaction yields. Replicate samples of a monolayer of **In1A** (ML) were subjected to the following treatments (Figure 4.23): (A) the Luscombe methodology using 4 equivalents of PPh_3 in the presence of $Ni(COD)_2$;[26] (B) the Locklin methodology using 2 equivalents of PPh_3 in the presence of $Ni(COD)_2$: this stoichiometry leaves no free PPh_3 after complexation with ligand exchange wih one of the cyclooctadienes; (C) an alternate approach where the $Ni(COD)_2$ is left to react for an hour, and then 2 equivalents of PPh_3 are added: to determine if $Ni(COD)_2$ by itself can attach to the surface and facilitate oxidative addition; (D) immersion in $Ni(COD)_2$ without phosphine ligands; and (E) direct reaction with Ni(COD)(dppp) (which does not work with the phosphonates).

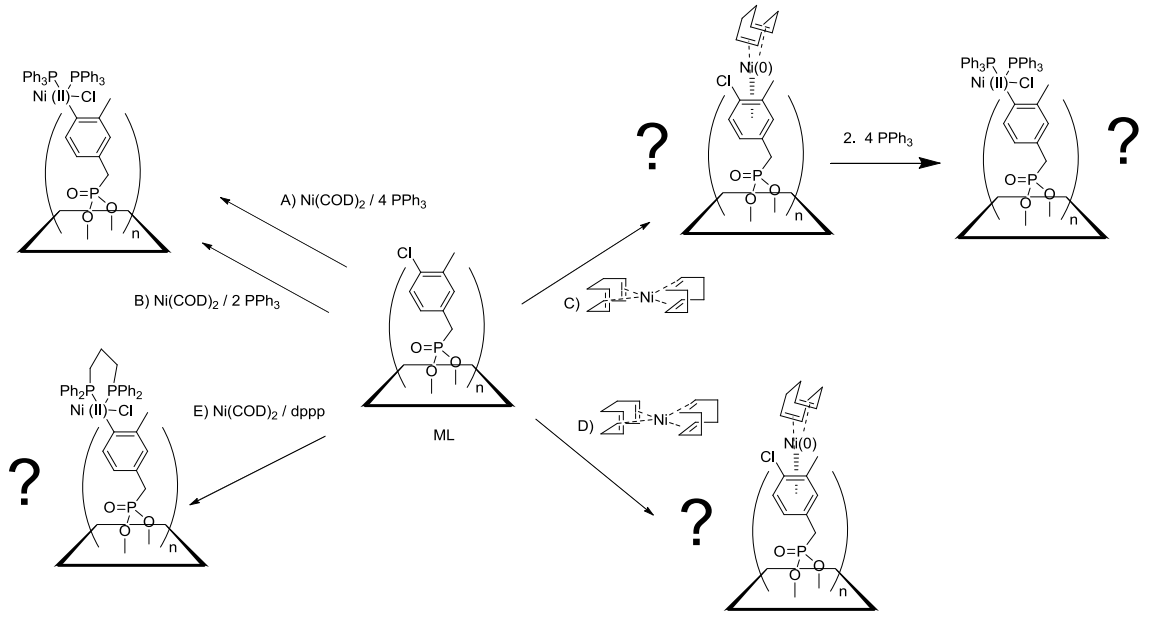

Figure 4.23 Reaction schemes for intermediate species probing. Expected outcomes shown.

For the first batch of experiments, HI etching was used to activate the ITO samples, room temperature deposition of **In1A** was carried out overnight followed by annealing in glovebox at 140 °C before treating for 3 h with the different complexing reagents inside the glovebox. After rinsing the samples with fresh solvent, the samples were sealed and transported to the XPS where they were exposed to air for roughly two a couple of minutes before starting the load-lock pumping. Figure 4.24 summarizes the results. The ML sample shows a Cl/C in agreement with good quality monolayer (stoichiometric Cl/C is 0.125, determined 0.10; the P/Cl was 1.1, close to the expected 1.0). Reaction with $Ni(COD)(PPh_3)_2$ (with excess PPh_3) as in the Luscombe recipe results in very low Ni content (as tracked by Ni/In), a P/Cl no different than that of the starting monolayer, and a carbon content just barely higher than the pure monolayer (as judged by C/In). Using only 2 equivalents of PPh_3 (B) does not give significantly different results. The Ni signal is so weak that quantification via Ni/In is semiquantitative at best. Consideration of the sensitivity factors and attenuation lengths as explained in Section 2.3.1 show that for the same amunt of material, the Ni $2p_{3/2}$ peak should be 8 times more

intense than P 2s and 4 times more intense than Cl 2p; given that the Ni 2p is so weak, while P 2s and Cl 2p are reaily observed for a monolayer, it can be concluded that less than a monolayer of Ni has deposited.

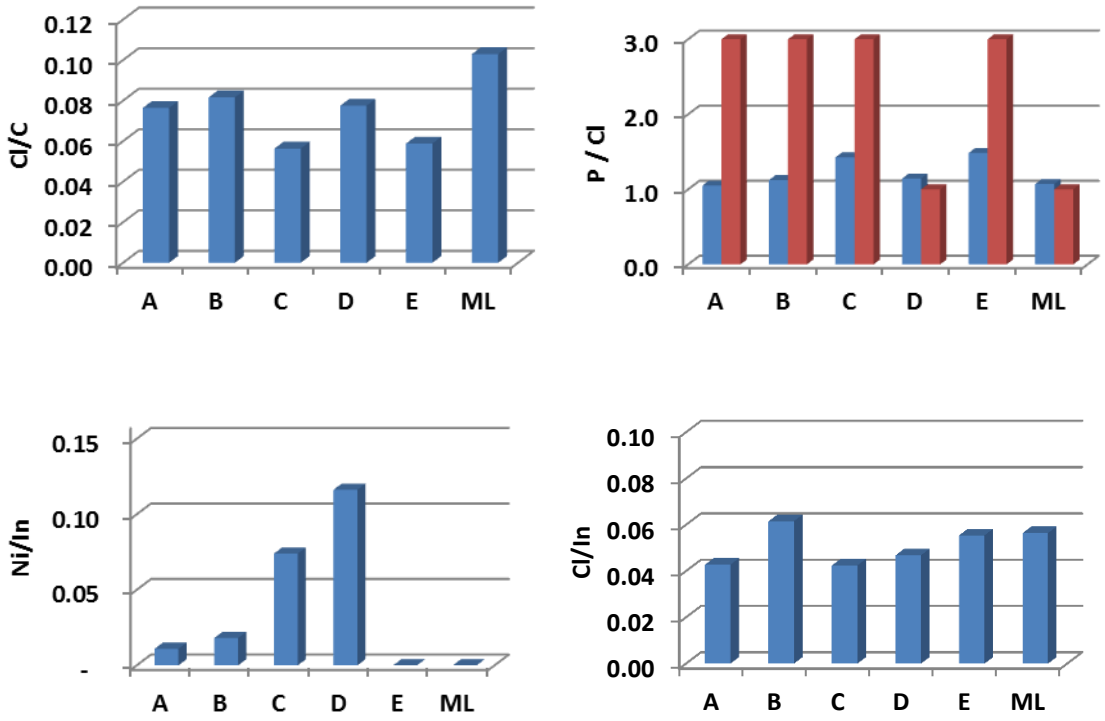

Figure 4.24 XPS ratios for HI-pretreated ITOs after immersion with the complexing agents as in Figure 4.23. Red bars are the expected ratios for 100% reaction yields.

Interestingly, the two-step reaction consisting of treatment first with $Ni(COD)_2$ followed by PPh_3 (reaction C) gives much higher Ni content, as well as increased P/Cl ratio (1.4, expected 3.0); nonetheless, there are two Ni peaks, one associated with Ni(0) and a higher binding energy that agrees with Ni(II) or a satellite from Ni(0);[29] succesful oxidative addition should result only in Ni(II). Hence, it seems that some Ni(0) from $Ni(COD)_2$ strongly physisorbs. Treatment of the ML exclusively with $Ni(COD)_2$ (reaction (D)) shows a Ni(0)/Ni(II) ratio higher than the case for (C). This might suggest some oxidative addition in the presence of PPh_3, but in the case of $Ni(COD)_2$ alone the

Ni(II) is likely only from oxidation by oxygen. Finally, reaction between $Ni(COD)_2$ and 1.5 eq dppp (Scheme E) generates Ni(COD)dppp (as evidenced by the yellow solution), but this gives no distinguishable Ni on the surface, and only a slightly increased P/Cl over that of the pure monolayer, perhaps from physisorption of free dppp. In concluision, the results for HI-pretreated ITOs point to very low oxidative addition yields regardless of protocol used.

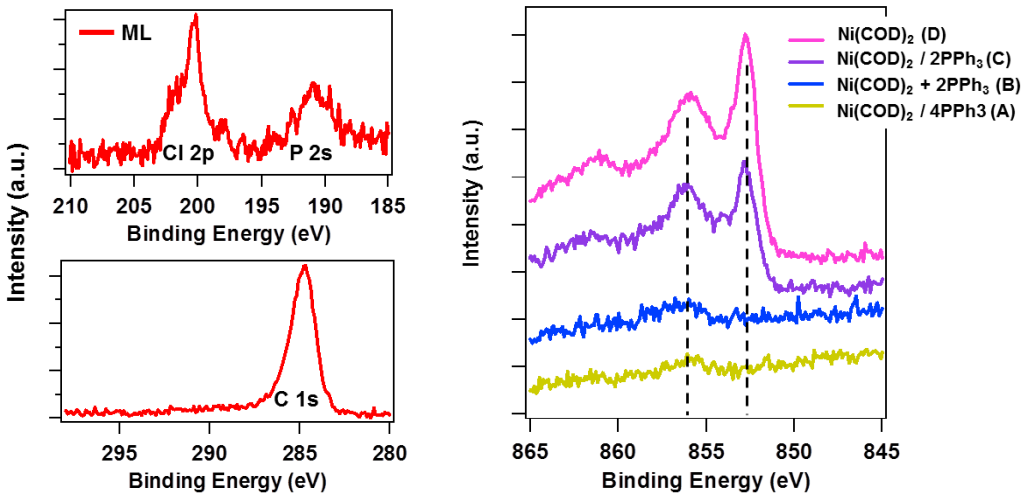

Figure 4.25 High resolution XPS scans for HI-pretreated ML: (a) C 1s, Cl 2p and P 2s; (b) Ni $2p_{3/2}$ spectra offset for clarity: reaction with 4 eq PPh_3 + $Ni(COD)_2$ (A), 2 eq of PPh_3 + $Ni(COD)_2$ (B), $Ni(COD)_2$ followed by addition of PPh_3 (C), and reaction with $Ni(COD)_2$ without phosphine ligands (D).

A second batch of samples was prepared, now using air plasma (AP) pretreatment, and letting **In1A** react for 2 days at room temperature. The graphs in Figure 4.26 summarize the XPS results. The ML sample was slightly better in both quality and coverage than that made with HI pretreatment as judged by Cl/In and Cl/C ratios. Reaction (B) was once again more successful on oxidative addition than (A) based on Ni/In and P/Cl ratios. The C/In ratio also increased, consistent with more organic material present as expected after complexaton. All Ni present agrees with the binding energy expected for Ni(II) (Figure 4.27). From the P/Cl a reaction yield of 25% can be calculated. These are on the order of what Locklin and coworkers observed for other

initiating group on gold (typical yield around 10%) by coupling the oxidative addition product to the Grignard of a ferrocenyl-functionalized thiophene and determining coverage by CV.[25] These are reasonable yields considering the steric hindrance that other free $Ni(COD)(PPh_3)_2$ would have to overcome to oxidatively add to other initiating groups, given the bulky PPh_3 ligands involved on a surface confined reaction. To truly verify air had no significant effect on the species observed, an XPS study of the samples free from any air exposure would need to be done. This is discussed in the next section. Procedures (C), (D) and (E) did not give significantly different results from those observed on HI-pretreated samples.

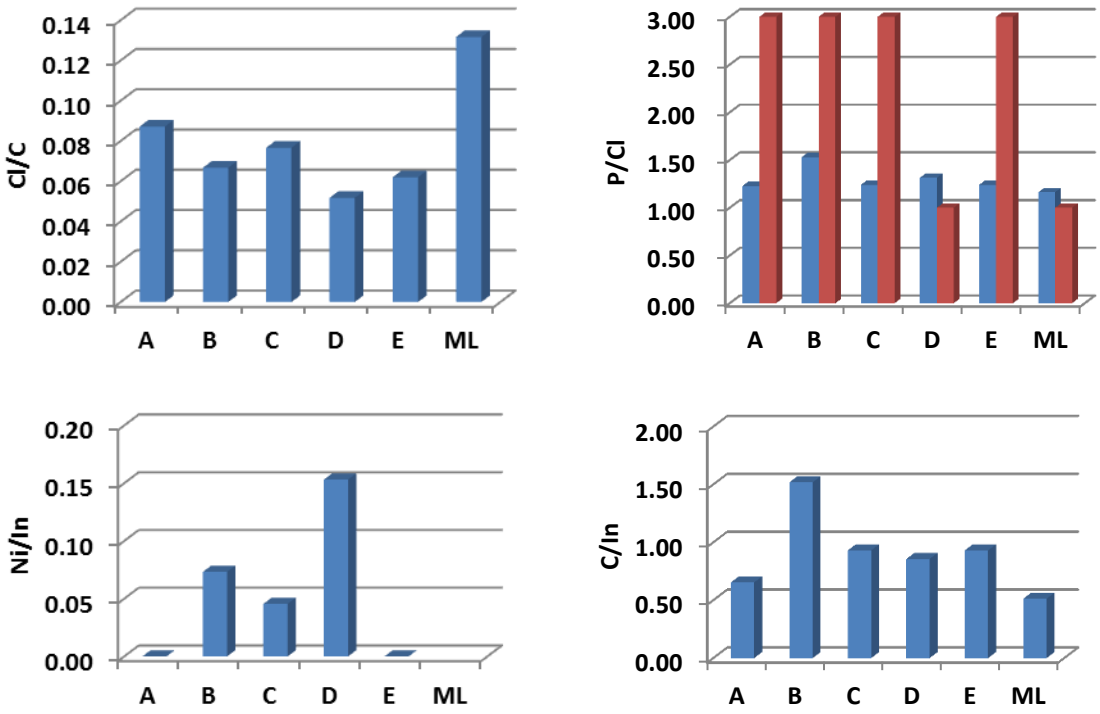

Figure 4.26 XPS ratios for monolayers on AP-pretreated ITOs after immersion with the complexing agents as in Figure 4.23. Red bars are the expected ratios for 100% reaction yields.

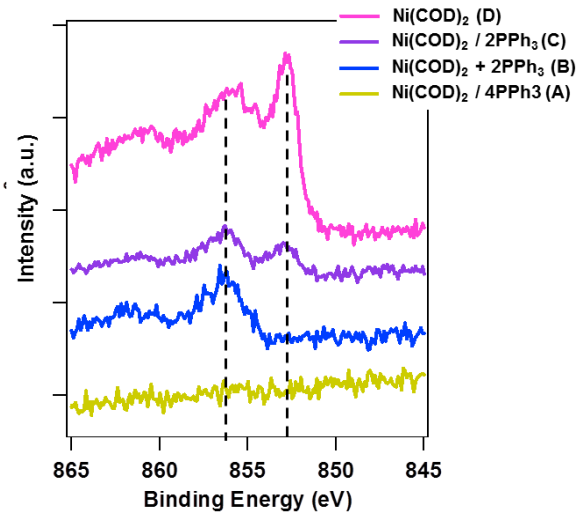

Figure 4.27 Ni 2p high resolution after treatments for oxidative addition on monolayers deposited after air plasma pre-treatment: (A) $Ni(COD)_2$+ 4 eq PPh_3, (B) $Ni(COD)_2$ + 2 eq PPh_3, (C) $Ni(COD)_2$, rinse, then 4 eq PPh_3, and (D) only $Ni(COD)_2$ treatment.

4.7.2 Second study: probing oxidative addition via air-free transfer into the XPS

For the second study, a newly acquired inert sample transporter was employed to transfer samples in and out of the glovebox under N_2 and bring it into the XPS without any exposure to air; the sample transporter has a seal that can hold positive nitrogen pressures (and vacuum down to 1×10^{-7} Torr). Monolayers were prepared at 75 °C on DSC ITO using 10 mM **In1A** for 90 min. Given that only one sample at a time could be analyzed, protocol (B) (treatment with $Ni(COD)_2$+$2PPh_3$) was chosen, since it afforded the best results based on the Ni signals and P/Cl ratios in the first study. High resolution XPS spectra (Figure 4.28) showed that Ni (II) is indeed present while Ni(0) is absent in this methodology. Subsequent treatment with dppp (on a duplicate sample) shows as well presence of only Ni (II), which is also the case for *o*-chlorotoluene treated with $Ni(COD)PPh_3$, a solution initiator typically used as standard for KCTP, which was dropcasted on ITO (red trace). This verifies the results from the first study since in this occasion additional measures were taken to minimize oxidation by O_2.

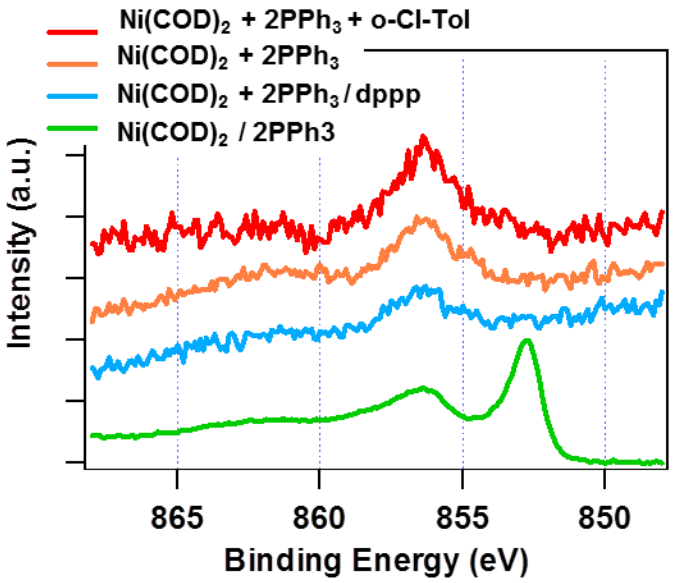

Figure 4.28 Comparison of samples in XPS Ni $2p_{3/2}$ region for air-free transferred samples.

Figure 4.29 shows atomic ratios of interest. Since the Ni 2p peaks were noisy even with many scans taken over various spots, the yield of oxidative addition was once again determined instead from P/Cl, which for both the initial oxidative addition and the ligand exchange gave an increase of ~25% that expected for the pure monolayer. These results confirm that there are still ways to improve upon the quality of polymer films that can be made, but further process development will be needed to find optimal conditions, which may involve not only changing the equivalents of ligands or the order of addition of reagents but changing temperature and time of reactions.

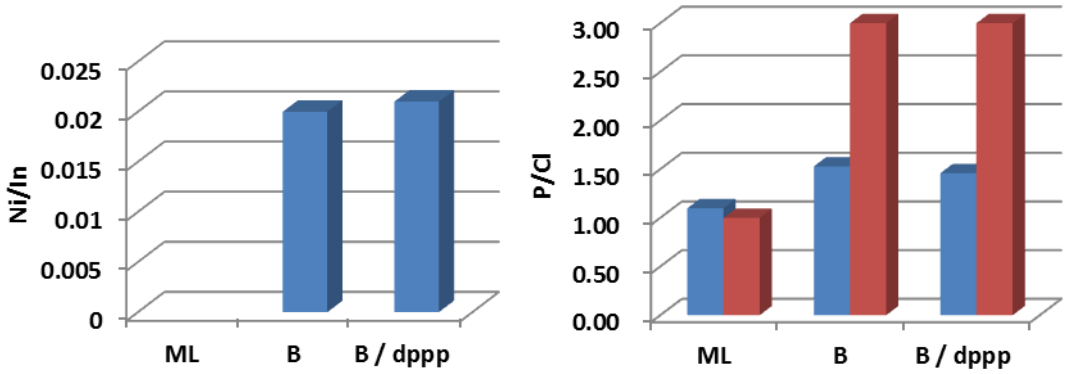

Figure 4.29 XPS ratios for monolayers on DSC cleaned ITOs after treatments with the complexing agents as in Figure 4.21. Red bars are the expected ratios for 100% reaction yields.

4.8 Conclusions

In this chapter the synthesis of new initiators designed for Grignard metathesis polymerizations bearing phosphonate and phophonic acid groups has been presented. Initiation efficiencies for the phosphonates varied depending on the substitution patterns, with **In1** giving the highest efficiency thanks to the methyl group in *ortho* position to the halogen which stabilizes the Ni complex without introducing steric hindrance as the phosphonate group in **In2** likely does. All phosphonic acids can covalently attach to ITO, as demonstrated by XPS.

In terms of surface-initiated KCTP, a correlation was found between initiating phosphonic acid **In1A** coverage on ITO and amount of polymer grown. Mixed monolayers, with dilution of initiator by inert phosphonic acid to attempt reduction of early termination reactions did not result in more polymer being grown, and merely serve to reduce the number of initiating sites per area unit. When precautions are taken to preclude oxygen from coming into contact with the hypothesized oxidative addition complex using **In1A** on plasma treated ITO, XPS showed only Ni(II) species, consistent with oxidative addition. Oxidative addition as probed by (P/Cl XPS ratios) was determined to occur 25-30% of the reactive sites.

Preliminary tests do show P3MT polymer grafts to be electroactive even in undoped form. However, P3MT polymer grafts still need optimization to perform at the efficiencies of spin-coated polythiophenes.

4.9 Experimental

4.9.1 Synthesis

All chemicals were purchased from Aldrich, Alfa-Aesar or TCI and use as received unless otherwise stated. Tetrahydrofuran (THF) and toluene were dried using a solvent drying system from Innovative Technologies. All polymerizations were performed under N_2.

*Synthesis of diethyl 4-chloro-3-methylbenzylphosphonate (**In1**, route (A), see Figure 4.8):* The starting carboxylic acid was reduced to the alcohol by a procedure reported for a similar compound.[15] A mixture of 4-chloro-3-methylbenzoic acid (9.5 g, 55 mmol) in distilled THF (30 mL) was stirred at 0 °C under N_2 atmosphere. A solution of 1 M borane in THF (75 mL, 1.3 eq) was added dropwise via an addition funnel and the mixture stirred for 4.5 h. The excess hydride was quenched by addition of water/THF (1:1) mixture, and basification with potassium carbonate (12 g) and saturated bicarbonate solution followed. After extraction, **1b** was recovered as orange-colored crystals from toluene (19%). Conversion to **1c** was performed by mixing **1b** in dry toluene with phosphorus tribromide under nitrogen at 40 °C, followed by heating to 100 °C for 10 min, then letting cool to room temperature (80% yield). After extraction, conversion to phosphonate proceeded through neat reaction of **1c** with triethyl phosphite at 150 °C under nitrogen (quantitative crude yield). The pure product was obtained as a yellow oil (1.1 g, 48% yield) after purification through silica plug with ethyl acetate as the eluent.

^{1}H NMR (300 MHz, $CDCl_3$) δ 7.21 (d, J = 8.2 Hz, 1H), 7.12 (dd, J = 2.4, 2.2 Hz, 1H), 7.01 (ddd, J = 8.2, 2.4, 2.2, 1H), 3.98 (dq, $J_{H\text{-}P}$ = 8.4 Hz, $J_{H\text{-}H}$ = 7.1 Hz, 4H), 3.03 (d, $J_{H\text{-}P}$ = 21.6 Hz, 2H), 2.30 (s, 3H), 1.21 (t, J = 7.1 Hz, 6H). $^{13}C\{^{1}H\}$ NMR (75 MHz, $CDCl_3$): δ 136.3, 133.2, 132.5, 130.3, 129.3, 128.6, 62.4, 33.2 (d, $J_{C\text{-}P}$ = 138.6 Hz), 20.2, 16.6. $^{31}P\{^{1}H\}$ NMR (162 MHz, $CDCl_3$): δ 26.6. HRMS(EI) Calcd for $C_{12}H_{18}ClO_3P$ (M^+): 276.0682. Found: 276.0686. Anal. Calcd. for $C_{12}H_{18}ClO_3P$: C 52.09, H 6.56, Cl 12.81. Found: C 51.85, H. 6.67, Cl 12.58.

*Synthesis of diethyl 4-chloro-3-methylbenzylphosphonate (**In1**, route (B), Figure 4.8):*

For the conversion of 4-chloro-3-methylbenzoic acid to the alcohol,[52] a solution of 4-chloro-3-methylbenzyl carboxylic acid (10 g, 59 mmol) in dry THF (100 mL) was added dropwise to a cooled suspension (0 °C) of lithium aluminum hydride (2.50 g, 64 mmol) in dry THF (60 mL) and left to warm up overnight. The excess hydride was destroyed by the addition of ethyl acetate (50 mL) followed by dropwise addition of 10% H_2SO_4 (50 mL) and 30% H_2SO_4 (50 mL). Stirring was continued until all solids were dissolved, and washed with water (3×) to isolate the organic compound. After washing the combined organic layers with brine, $MgSO_4$ was used as drying agent and after filtering and evaporating the solvent, a dark red oil was obtained from which yellow crystals precipitated, leaving just a trace of oil (7.41 g, of which 81% is the expected alcohol according to GC-MS, ^{1}H NMR). Conversion to the bromide and phosphonate proceeded in similar fashion to route (A).

*Conversion of **In1** to the acid **In1A***. The phosphonate (2.0 g) was dissolved in anhydrous CH_2Cl_2 (20 mL). Trimethylsilylbromide (3.0 mL, 3.2 eq) was added via syringe, and the mixture allowed to stir overnight. Volatiles were removed under reduced pressure, and the resulting oil dissolved in a 20:1 MeOH:water mixture (20 mL) and allowed to stir over 2 d. The volatiles were again removed under reduced pressure and the product

filtered and washed with water. The resulting material was washed in hot acetonitrile, and after letting stand for 2 d, the product was filtered and washed with cold MeCN and hexane. ^{1}H NMR (300 MHz, DMSO-d_6) δ 7.29 (d, J = 8.1 Hz, 1H), 7.19 (dd, J = 2.3, 2.1 Hz, 1H), 7.06 (ddd, J = 8.1, 2.3, 2.1 Hz, 1H), 2.90 (d, $J_{H\text{-}P}$ = 21.4 Hz, 2H), 2.27 (s, 3H). ^{13}C{^{1}H} NMR (100 MHz, DMSO-d_6): δ 135.4, 134.1, 133.2, 131.6, 129.6, 129.0, 35.3 (d, $J_{C\text{-}P}$= 132 Hz), 20.2. ^{31}P{^{1}H} NMR (162 MHz, DMSO-d_6): δ 21.7. HRMS (EI): Calcd for $C_8H_{10}ClO_3P$ (M^+)220.0056. Found 220.0061. Anal. Calcd for $C_8H_{10}ClO_3P$: C 43.56, H 4.57, Cl 16.07. Found: C 43.62, H 4.53, Cl 15.86.

*Synthesis of diethyl 2-chlorobenzylphosphonate (**In2**, see Figure 4.9).* The solventless reaction of bromide **2a** with triethyl phosphite (21 mL, 3 eq) at 150 °C under nitrogen atmosphere overnight was followed removal of volatiles at 60 °C under reduced pressure which resulted in **In2**, a colorless oil in 96% yield which did not require further purification.[30] ^{1}H NMR (300 MHz, $CDCl_3$) δ 7.42 (m, 1H), 7.35 (m, 1H), 7.24-7.12 (m, 2H), 4.02 (dq, $J_{H\text{-}P}$ = 8.0, $J_{H\text{-}H}$ = 7.1 Hz, 4H), 3.34 (d, $J_{H\text{-}P}$ = 22.0 Hz, 2H), 1.25 (t, J = 7.1 Hz, 6H). ^{13}C NMR (75 MHz, $CDCl_3$): δ 134.4, 131.9, 130.1, 129.8, 128.5, 127.0, 62.4, 30.9 (d, $J_{C\text{-}P}$ = 133 Hz), 16.6. ^{31}P NMR (162 MHz, $CDCl_3$): δ 26.3. HRMS(EI) Calcd for $C_{11}H_{16}ClO_3P$ (M^+): 262.0526; found: 262.0518. Anal. Calcd for $C_{11}H_{16}ClO_3P$: C 50.30, H 6.14, Cl 13.50. Found: C: 50.16 H: 6.41 Cl: 13.23.

*Conversion of **In2** to the acid **In2A***. The phosphonate (2.50 g, 10 mmol) was dissolved in dry DCM (25 mL) and trimethylsilylbromide (4.7 mL, 3.2 eq) was added after purging with N_2. After overnight stirring, the DCM was removed under reduced pressure. A 20:1 mixture of MeOH:water (25 mL) was added and left again to stir overnight. The solid was recrystallized from MeCN/pentane (white crystals, 1.70 g, 86% yield) . ^{1}H NMR (400 MHz, d_6-DMSO): δ 10.7 (br s, 1H), 7.42-7.38 (m, 2H), 7.27-7.18 (m, 2H), 3.07 (d, J = 21.7 Hz, 2H). ^{13}C{^{1}H} NMR (101 MHz, d_6-DMSO): δ 134.0, 132.9, 132.5, 129.8,

128.5, 127.4, 62.2, 33.1 (d, J = 133 Hz). $^{31}P\{^{1}H\}$ NMR (162 MHz, DMSO-d_6): δ 21.0. HRMS (EI) Calcd for $C_7H_8ClO_3P$ (M^+) 205.9900; found: 205.9912. Anal. Calcd for $C_7H_8ClO_3P$: C 40.70, H 3.90, Cl 17.16. Found: C: 40.71, H: 3.87, Cl 16.99.

*Synthesis of diethyl (5-bromo-4-hexylthiophen-2-yl) methyl phosphonate (**In3**) and diethyl (5-bromothiophen-2-yl) methyl phosphonate (**In4**), Figure 4.10).* The procedure was based on previous reports for the synthesis of **In4**.[31,32] **In4** was obtained as light-yellow oil. ^{1}H NMR (400 MHz, $CDCl_3$): δ 6.85 (d, J = 3.7 Hz, 1H), 6.69 (ddt, J = 3.7, 3.7, 0.9 Hz, 1H), 4.05 (dq, J = 7.1, 7.1 Hz, 4H), 3.23 (dd, J_{H-P} = 20.7, J_{H-H} = 0.8 Hz, 2H), 1.26 (t, J = 7.1 Hz, 6H).

Similar conditions were used to obtain **In3**. The crude phosphonate (a dark brown oil, 58% pure product by GC-MS) was subjected to silica column chromatography with 2% ethanol in DCM, followed by a subsequent column with 1:1 hexane:ethyl acetate as the eluent to afford **In3** as deep orange. ^{1}H NMR (300 MHz, $CDCl_3$) δ 6.63 (d, J = 3.6 Hz, 1H), 4.10-3.98 (m, 4H), 3.18 (dd, J_{H-P} = 21.7 Hz, J_{H-H} = 0.8 Hz, 2H), 2.45 (t, J = 7.6 Hz, 2H), 1.55-1.43 (m, 2H), 1.29-1.21 (m, 12H), 0.84 (t, J = 6.4 Hz, 3H). $^{13}C\{^{1}H\}$ NMR (75 MHz, $CDCl_3$): δ 142.2, 132.3, 128.7, 122.4, 62.7, 30.8 (d, J_{C-P} = 150 Hz), 29.6, 29.5, 29.0, 27.7, 22.8, 16.6, 14.3. $^{31}P\{^{1}H\}$ NMR (162 MHz, $CDCl_3$): δ 24.6. HRMS (EI) Calcd for $C_{15}H_{26}BrO_3PS$ (M^+): 396.0524; found: 396.0507. Anal. Calcd. for $C_{15}H_{26}BrO_3PS$: C 45.35, H 6.60, Br 20.11, S 8.07. Found: C 45.52 H 6.77 Br 20.19 S 8.33.

*Conversion of **In3** to **In3A***. Proceeded in similar fashion to the synthesis of **In1A**, starting from **In3** (790 mg, 2.0 mmol) which afforded pink crystals (270 mg, 40% yield) . Two recrystallizations were needed to pass elemental analysis. ^{1}H NMR (400 MHz, DMSO-d_6): δ 6.70 (d, J = 2.7 Hz, 1H), 3.08 (d, J = 20.5 Hz, 2H), 2.42 (t, J = 7.3 Hz, 2H), 1.47 (m, 2H), 1.25 (m, 2H), 0.84 (t, J = 6.8 Hz, 3H). $^{13}C\{^{1}H\}$ NMR (101 MHz, DMSO-d_6): δ

141.7, 136.5, 128.6, 106.1, 31.7, 30.8 (d, *J* = 137 Hz) 29.9, 29.5, 29.0, 22.7, 14.6. $^{31}P\{^{1}H\}$ NMR (162 MHz, DMSO-d_6): δ 19.6. HRMS (EI) Calcd for $C_{11}H_{18}BrO_3PS$ (M^+) 339.9898; found 330.9898. Anal. Calcd. For $C_{11}H_{18}BrO_3PS$: C 38.72, H 5.32, Br 23.42, S 9.40. Found: C 38.51 H 5.21 Br 23.18 S 9.58.

*Conversion of **In4** to **In4A***. Proceeded in similar fashion to the synthesis of **In1A**,starting from **In4** (0.91 g, 2.9 mmol), which afforded pink crystals (0.40 g, 54%). ^{1}H NMR (400 MHz, d_6-DMSO): *δ* 7.00 (d, *J* = 3.7 Hz, 1H), 6.73 (d, *J* = 3.5 Hz, 1H), 3.13 (d, *J* = 20.4 Hz, 2H). $^{13}C\{^{1}H\}$ NMR (101 MHz, d_6-DMSO): *δ* 138.5, 130.4, 128.2, 109.4, 30.7 (d, *J* = 136 Hz). $^{31}P\{^{1}H\}$ NMR (162 MHz, d_6-DMSO): *δ* 19.7. HRMS (EI) Calcd for $C_5H_6BrO_3PS$ (M^+) 255.8959. Found: 255.8951. Anal. Calcd. for $C_5H_6BrO_3PS$: C 23.36, H 2.35. Found: C: 23.61, H: 2.25.

*Synthesis of diethyl 4'-chloro-3'-methylbiphenyl-4-methanophosphonate (**In5**, see Figure 4.11).* The starting alcohol (Aroz Technologies, 1.97 g, 8.5 mmol) was dissolved in dry toluene (~30 mL), heated to 45°C, and then PBr_3 (0.35 eq) was added. The solution was stirred and heated to 100 °C, left to react for 10 min, and then cooled to room temperature. The liquid was decanted and washed with water (2×25 mL) and brine (35 mL). The aqueous layers were back-extracted with ether (2×25 mL), and the organic layer saved, and mixed with the other organic layer. Finally the organic layer was rotavapped to afford yellow crystals of **5b** (2.39g, 94% yield). ^{1}H NMR (400 MHz, $CDCl_3$): δ 7.35-7.54 (m, 7H), 4.54 (s, 2H), 2.44 (s, 3H). ^{13}C NMR$\{^{1}H\}$ (101 MHz, $CDCl_3$): δ 140.3, 138.9, 137.0, 136.4, 133.9, 129.6, 129.5, 129.4, 127.4, 125.7, 33.3, 20.2. Triethylphosphite (4.5 eqs) was added to **5b** (2.30 g), and the mixture heated at 140°C overnight. The unreacted triethylphosphite was removed under vacuum at 110 °C. The resulting phosphonate **In5** (2.49 g, 91% yield) was sufficiently to continue with conversion to **In5A**. The rest of the phosphonate (1.26 g) was further purified by

Kugelrohr distillation at 250 mTorr and 250°C (1.0 g). ^{1}H NMR (400 MHz, $CDCl_3$): δ 7.48 (d, J = 8.0 Hz, 2H) 7.40 (d, J = 2.2 Hz, 1H), 7.36-7.33 (m, 2H), 7.30 (dd, J = 8.3, 1.9 Hz, 2H), 4.03 (dq, J_{HP} = 8.6 Hz, J = 7.1 Hz, 4H), 3.16 (d, J_{HP} = 21.7 Hz, 2H), 2.40 (s, 3H), 1.25 (t, J = 7.1Hz). ^{13}C{^{1}H} NMR (101 MHz, $CDCl_3$): δ 139.2, 138.6, 136.2, 133.5, 130.9, 130.2, 129.4, 129.3, 127.0, 125.5, 61.9, 33.5 (d, J_{C-P} = 138.1 Hz), 20.2, 16.4. ^{31}P{^{1}H} NMR (162 MHz, $CDCl_3$): δ 26.8. HRMS (EI) for $C_{18}H_{22}ClO_3P$ (M^+): Calcd: 352.0995. Found: 352.1006. Anal. Calcd. for $C_{18}H_{22}ClO_3P$: C 61.28, H 6.29, Cl 10.05. Found: C 61.25, H 6.34, Cl 10.12.

*Conversion of **In5** to **In5A***. Phosphonate **In5** (1.23 g, 3 mmol) was dissolved in anhydrous DCM (12 mL). TMSBr (1.5 mL, 3.2 eq) was added via syringe, and the mixture allowed to stir overnight. The volatiles were removed under reduced pressure, and the resulting powder was dissolved in a 20:1 MeOH: water mixture (12 mL) and allowed to stir overnight. Again, volatiles were removed under reduced pressure and the product filtered and washed with water followed by hot MeCN. The material was refridgerated for two days, after which it was washed again with cold acetonitrile and hexane and the crystals of **In5A** dried in Schlenk line (white powder, 0.95 g, 92% yield). ^{1}H NMR (400 MHz, $CDCl_3$): δ 7.63 (br s, 1H) 7.56 (d, J = 8.1 Hz, 2H), 7.49-7.43 (m, 2H), 7.31 (dd, J = 8.1, 2.2 Hz, 2H), 2.98 (d, J_{HP} = 21.5 Hz)), 2.37 (s, 3H). ^{13}C NMR{^{1}H} (101 MHz, $CDCl_3$): δ 139.3, 137.1, 136.3, 134.2, 132.8, 130.8, 129.7, 129.6, 126.7, 126.0, 36.1 (d, J_{CP} = 132.0 Hz), 20.2. ^{31}P{^{1}H} NMR (162 MHz, $CDCl_3$): δ 22.1. HRMS (EI): Calcd for $C_{14}H_{14}ClO_3P$ (M+): 296.0369; found: 296.0363. Anal. Calcd. for $C_{14}H_{14}ClO_3P$: C 56.68, H 4.76 Cl 11.95. Found: C 56.27, H 4.75, Cl 12.09.

4.9.2 Monolayer formation, polymerization protocol and characterization

All ITO films were detergent solvent cleaned as usual, followed by activation with HI 3.7 M/5.5 M, oxygen plasma or air plasma for 3 min as done in Chapter 2.

Monolayers were made using 10 mM solutions at either r.t. for at least overnight or 80 °C for 1 h followed by rinsing with EtOH and sonicating for at least 10 min in triethylamine/EtOH 5%. For Section 4.7 all ITO sample were annealed inside the glovebox (140 °C, 1h) prior to reaction with the nickel species.

General procedure for surface-initiated polymerizations. All glassware was dried in 200 °C oven, the toluene degassed through three cycles of freeze-pump-thaw, and the THF distilled over Na/benzophenone under N_2. Inside the glovebox, master solutions of 4 eq (or 2 eq) of PPh_3 in toluene were prepared, to which 1 eq of $Ni(COD)_2$ was added. The ITO slides were left to react with this solution overnight while stirring, time after which the ITOs were washed with toluene. Then dppp toluene solutions were added and left to react for 3-5h, before washing with toluene and THF.

The Grignard monomer was prepared by doing a 1:1 equivalent reaction between the isopropyl magnesium chloride (2.0 M) and the iodothiophene by adding the Grignard reagent dropwise to stirring iodothiophene at 0 °C over 2 min and left to react for 45 min while warming to r.t. The Grignard monomer was then added and left to react with the ITOs.

UV-vis spectra were collected on Perkin Elmer Lambda 9 Spectrophotometer. XPS for Section 4.5 was done in an ESCA SSX-100 with 20 mA and 10 kV X-rays using the charge neutralizer at 0.5 eV with spot sizes of 800 microns. For Section 4.7.1, the Thermo K-Alpha XPS was used as stated in Chapter 2. For Section 4.7.2, the Kratos Ultra^{DLD} XPS was used as stated in Chapter 2.

4.10 References

(1) Günes, S.; Neugebauer, H.; Sariciftci, N. S. *Chem. Rev.* **2007**, *107*, 1324.

(2) Khanduyeva, N.; Senkovskyy, V.; Beryozkina, T.; Horecha, M.; Stamm, M.; Uhrich, C.; Riede, M.; Leo, K.; Kiriy, A. *J. Am. Chem. Soc.* **2008**, *131*, 153.

(3) McCullough, R. D.; Lowe, R. D.; Jayaraman, M.; Anderson, D. L. *J. Org. Chem.* **1993**, *58*, 904.

(4) Chen, T. A.; Rieke, R. D. *J. Am. Chem. Soc.* **1992**, *114*, 10087.

(5) Yokoyama, A.; Miyakoshi, R.; Yokozawa, T. *Macromolecules* **2004**, *37*, 1169.

(6) Iovu, M. C.; Sheina, E. E.; Gil, R. R.; McCullough, R. D. *Macromolecules* **2005**, *38*, 8649.

(7) Miyakoshi, R.; Shimono, K.; Yokoyama, A.; Yokozawa, T. *J. Am. Chem. Soc.* **2006**, *128*, 16012.

(8) Yokoyama, A.; Kato, A.; Miyakoshi, R.; Yokozawa, T. *Macromolecules* **2008**, *41*, 7271.

(9) Stefan, M. C.; Javier, A. E.; Osaka, I.; McCullough, R. D. *Macromolecules* **2008**, *42*, 30.

(10) Wen, L.; Duck, B. C.; Dastoor, P. C.; Rasmussen, S. C. *Macromolecules* **2008**, *41*, 4576.

(11) Doubina, N.; Stoddard, M.; Bronstein, H. A.; Jen, A. K.-Y.; Luscombe, C. K. *Macromol. Chem. Phys.* **2009**, *210*, 1966.

(12) Bronstein, H. A.; Luscombe, C. K. *J. Am. Chem. Soc.* **2009**, *131*, 12894.

(13) Doubina, N.; Ho, A.; Jen, A. K. Y.; Luscombe, C. K. *Macromolecules* **2009**, *42*, 7670.

(14) Doubina, N.; Paniagua, S. A.; Soldatova, A. V.; Jen, A. K. Y.; Marder, S. R.; Luscombe, C. K. *Macromolecules* **2011**, *44*, 512.

(15) Kelley, J. L.; Linn, J. A.; Selway, J. W. T. *J. Med. Chem.* **1989**, *32*, 1757.

(16) Sontag, S. K.; Marshall, N.; Locklin, J. *Chem. Commun.* **2009**, 3354.

(17) Mamane, V. L.-R., I.; Deveau, S.; Zyss, J.; Riant, O. *Synthesis* **2003**, *3*, 455.

(18) Trznadel, M.; Pron, A.; Zagorska, M.; Chrzaszcz, R.; Pielichowski, J. *Macromolecules* **1998**, *31*, 5051.

(19) Senkovskyy, V.; Khanduyeva, N.; Komber, H.; Oertel, U.; Stamm, M.; Kuckling, D.; Kiriy, A. *J. Am. Chem. Soc.* **2007**, *129*, 6626.

(20) Khanduyeva, N.; Senkovskyy, V.; Beryozkina, T.; Horecha, M.; Stamm, M.; Uhrich, C.; Riede, M.; Leo, K.; Kiriy, A. *J. Am. Chem. Soc.* **2009**, *131*, 153.

(21) Senkovskyy, V.; Tkachov, R.; Beryozkina, T.; Komber, H.; Oertel, U.; Horecha, M.; Bocharova, V.; Stamm, M.; Gevorgyan, S. A.; Krebs, F. C.; Kiriy, A. *J. Am. Chem. Soc.* **2009**, *131*, 16445.

(22) Tkachov, R.; Senkovskyy, V.; Horecha, M.; Oertel, U.; Stamm, M.; Kiriy, A. *Chem. Commun.* **2010**, *46*, 1425.

(23) Marshall, N.; Sontag, S. K.; Locklin, J. *Macromolecules* **2010**, *43*, 2137.

(24) Sontag, S. K.; Marshall, N.; Locklin, J. *Chem. Commun.* **2009**, 3354.

(25) Sontag, S. K.; Sheppard, G. R.; Usselman, N. M.; Marshall, N.; Locklin, J. *Langmuir* **2011**, *27*, 12033.

(26) Doubina, N.; Jenkins, J. L.; Paniagua, S. A.; Mazzio, K. A.; MacDonald, G. A.; Jen, A. K.-Y.; Armstrong, N. R.; Marder, S. R.; K., L. C. *Langmuir* **2012**, *28*, 1900.

(27) Brumbach, M.; Veneman, P. A.; Marrikar, F. S.; Schulmeyer, T.; Simmonds, A.; Xia, W.; Lee, P.; Armstrong, N. R. *Langmuir* **2007**, *23*, 11089.

(28) Jenkins, J. L., Unpublished results, 2011.

(29) Barr, T. L. *J. Phys. Chem.* **1978**, *82*, 1801.

(30) Franke, A.; Frickel, F. F.; Schlecker, R.; Thieme, P. C. *Synthesis* **1979**, 712.

(31) Jiang, X.; Yang, X. C.; Zhao, C. Z.; Jin, K.; Sun, L. C. *J. Phys. Chem. C* **2007**, *111*, 9595.

(32) Mamane, V.; Ledoux-Rak, I.; Deveau, S.; Zyss, J.; Riant, O. *Synthesis* **2003**, 455.

CHAPTER 5 PRODUCTION OF HEAVILY N- AND P-DOPED CVD GRAPHENE WITH SOLUTION- PROCESSED REDOX-ACTIVE METAL-ORGANIC SPECIES

5.1 Modulation of electric and electronic properties of graphene

Graphene exhibits ambipolar field effect with zero band gap, properties not observed for other group 14 elements and even other 2D electron gases (2DEG) such as AlGaN/GaN (Table 5.1). Usually, transport properties are measured in a field-effect transistor configuration,[1] Hall bar,[2] or 4 point probe method (typically van der Pauw arrangement).[3] Measurements in a transistor configuration are usually done as a means to characterize the electrical properties, not to show that graphene is useful as a semiconductor for transistor applications since having a zero band gap in its pristine state makes it behave like a semimetal, with I_{ON}/I_{OFF} ratios typically less than 10.[4] However, there is ongoing research attempting to controllably open a band gap using a variety of approaches summarized in the review article by Cooper, *et al*.[4]

Table 5.1 From Giannazzo, et al.[5] Electronic properties of grapheme compared with those of common bulk semiconductors and with those of the 2DEG at AlGaN/GaN heterointerface.

	Si	Ge	GaAs	4H-SiC	GaN	AlGaN/GaN 2DEG	Graphene
Energy band gap (eV) @ 300 K	1.1	0.67	1.43	3.3	3.4	3.4	~0
Electron effective mass (m^* / m_e)	1.08	0.55	0.067	0.3	0.19	0.19	~0
Electron mobility ($cm^2\ V^{-1}\ s^{-1}$)	1,350	3,900	4,600	800	1,300	1,500–2,000	2×10^5
Carrier concentration (cm^{-3})	1	0.6	2	2	3	3	>5

In its undoped state, the conductivity of graphene is at its minimum. If a band was partially filled, as in the case shown in Figure 5.1a, it is possible to displace the k-value of each electron from its ground state with application of an electric field: the current carrying state illustrated in Figure 5.1b has higher energy than the ground state, given that some electrons have been transferred to orbitals at higher energy in the band;[6] the change in velocity for these electrons is proportional to the current that can flow through the material.

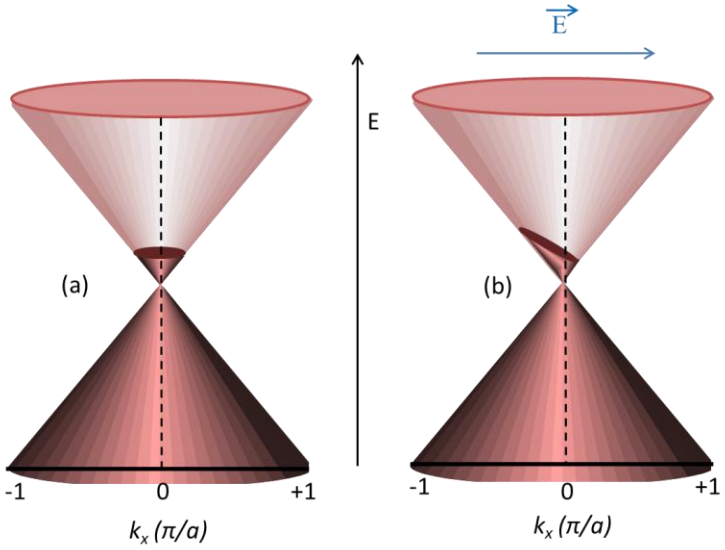

Figure 5.1 Electronic conduction in graphene: (a) conduction band partially filled, (b) electrons are shifted in k-space by application of an electrical field $\vec{E}$.

Figure 5.2 illustrates a side view of a bottom-contact, back-gated 3-probe transistor, where gold contacts were deposited on an insulator (typically SiO_2) that was grown from highly doped Si and CVD graphene is transferred on top (see Section 5.3). The charge carrier density can be increased by applying a gate voltage between the doped silicon substrate and graphene. This gate voltage induces a surface charge density as in Equation 5.1, where $\epsilon_r\epsilon_0$ is the permittivity of the dielectric, t the thickness, and V_G the gate voltage applied. The permittivity and thickness can be accounted for in a capacitance per area C_G.

Equation 5.1 $$n = \frac{\epsilon_r \epsilon_0 V_G}{te} = \frac{C_G V_G}{e}$$

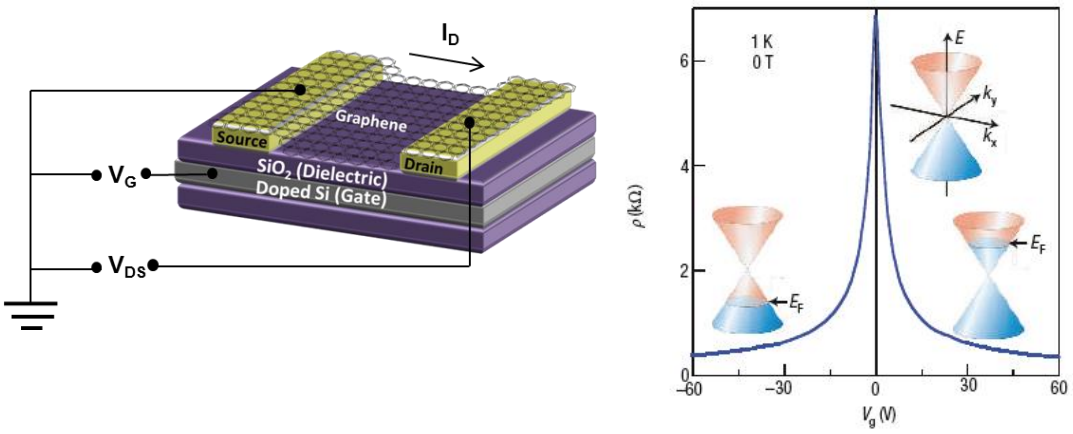

Figure 5.2 Left: Bottom-gate, bottom-contact graphene field effect transistor to electrogate graphene and measure its source/drain current. Right: typical resistivity as function of gate voltage in a GFET. The filling or emptying if the Dirac cones is shown. Reproduced from Geim, *et al*.[7]

Electrogating graphene in this way serves only as a research tool, since an electric field needs to be applied to increase the conductivity of graphene. A practical way to permanently induce charge carriers into graphene is via adsorption of electron- and hole-donating molecules. In this chapter, doping of graphene using submonolayer adsorption of redox-active, solution processable metal-organics is studied and shown to increase its conductivity while maintaining single-layer transparency. This is not only interesting from a purely scientific perspective, but graphene is promising as an alternative to the metal oxide transparent electrodes mentioned earlier in the introduction to this thesis. This potential is briefly discussed in the next section.

5.2 Doping via adsorption

Adsorption of dopants on the surface of graphene is an effective method to tailor its electrical properties,[8] which can be used to increase the number of charge carriers[2] and/or open a band gap.[9,10] The main application envisaged for large area, chemically

vapor deposited (CVD) graphene at present times is as a transparent conductive electrode,[11] where results are already rivaling those of ITO in organic electronic devices.[12,13] Issues to be addressed include better control of contact resistance with metals and semiconductors, for which careful work function tuning is needed, along with sheet resistance reduction.[14] Chemical doping can be used to modulate the work function and decrease the sheet resistance by introduction of charge carriers. There are precedents for deposition of gaseous species leading to n- or p-doping (Figure 5.3)[15]. The changes in conductivity observed are explained by mixing of orbitals with those of graphene and partial charge transfer due to the position of their energy levels relative to the Fermi level of graphene,[16] leading to emptying or filling of the valence or conduction bands respectively. The interaction with the gases is rather weak,[17] and graphene can be dedoped in vacuum with low temperature annealing.[18] Alkali metals, which are not air stable, have been deposited in UHV to n-dope graphene given their low ionization potential, but can damage the graphene,[19] and the resulting metal cations act as charge-scattering centers, significantly reducing the mobility.[20]

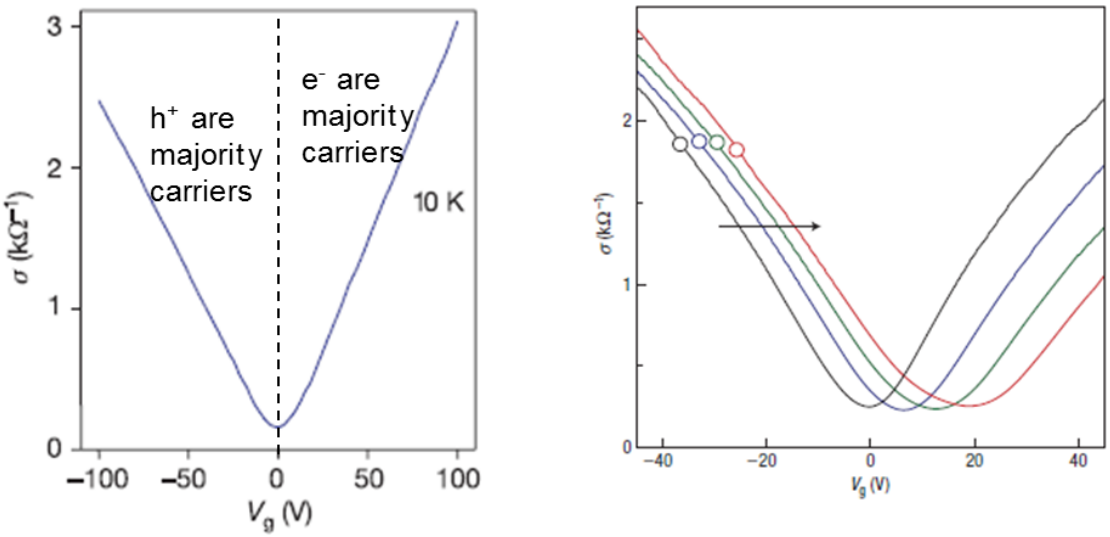

Figure 5.3 Left: conductivity changes in undoped graphene as the gate voltage is varied, and holes or electrons become the majority carriers.[21] Right: GFET-tracking of the doping of exfoliated graphene via increasing exposure to NO_2 gas doping increase from zero to ~1.5×10^{12} holes/cm^2 from the black to the red trace.[18]

Solid state molecular dopants are an interesting alternative since more complex structures can be synthesized than molecular or atomic gases. An ideal n dopant (p-dopant) should a) have a low ionization potential, IP (high electron affinity, EA) so that there is thermodynamic force for charge transfer to occur into (out of) graphene, b) undergo one-electron redox chemistry to ensure full transfer, c) form a large, stable cation (anion) that does not migrate in its environment and does not act as a charge trap, and d) be easy to process and have low cost.[22]

In the case of n-dopants (reducing agents), when the IP is lower than 4.0 eV, reactivity with O_2 is likely to be an issue, limiting its storage and application, as in the case of alkali metals. For p-doping, the most widely used dopant has been 2,3,5,6-tetrafluorocyanoquino-dimethane (F_4-TCNQ), given its large electron affinity (estimated at 5.24 eV[23]), a consequence of the electron withdrawing fluorine atoms and cyano groups present. The hole transfer is accompanied by a significant surface dipole due to the electron cloud rearrangement after the charge transfer.[24] However, F4-TCNQ is very volatile, interdiffuses in organic films,[25,26] and shows low solubility in most solvents, which has limited its application.

The Marder group recently reported that the essentially air-stable dimers formed by several highly organometallic sandwich compounds act effectively as "masked" forms of the highly reducing monomers and can be used for the n-doping of organic materials with EA as small as *ca.* 3.0 eV through either vacuum or solution processing.[22,27] Figure 5.4 shows the possible mechanisms by which a substituted rhodene dimer $\mathbf{1_2}$, used in this chapter, can donate to an electron accepting material. Compounds such as this act as "masked" versions of the corresponding monomers and react to give two electrons to an acceptor, forming two monomer cations; this reaction can proceed by either initial cleavage of the dimer or an electron transfer from the dimer,[28] but regardless of the mechanism, the overall thermodynamics of doping depend on the strength of the dimer's central C–C bond and the IP of the monomer. The central bond of $\mathbf{1_2}$ is estimated from

experiment ($\Delta G_{diss}(\mathbf{1_2})$ < 0.24 eV) and theory to be particularly weak, meaning that, although the solid-state IP of $\mathbf{1_2}$ is estimated to be *ca.* 3.8 eV, it behaves as a significantly stronger donor with the estimated IP of the monomer (2.7 eV) providing a better gauge of its effectiveness as a reductant.[29]

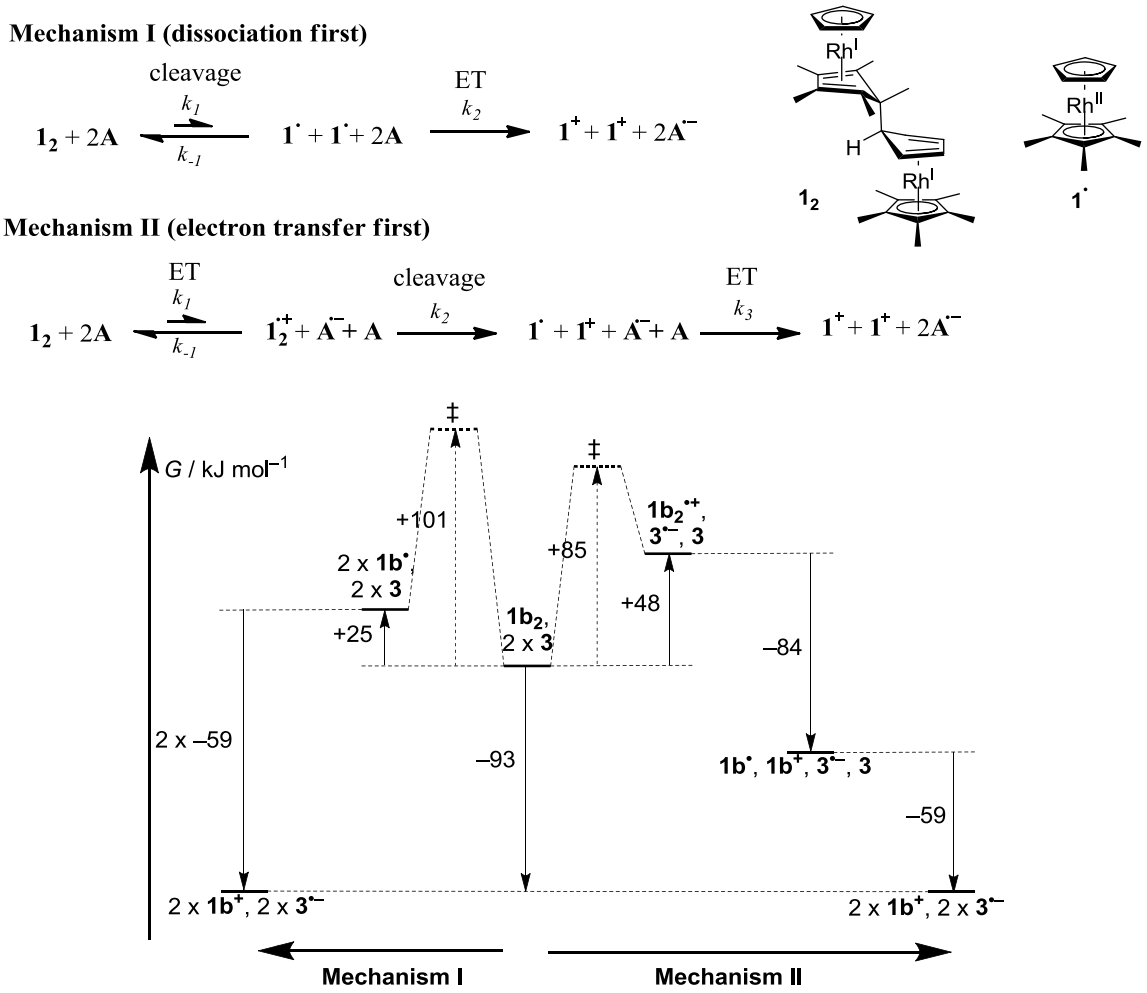

Figure 5.4 Top: two possible mechanisms by which dimer $\mathbf{1_2}$, formed by highly reducing $\mathbf{1}^{\bullet}$, can reduce an acceptor (**A**). Bottom: free-energy diagram for the reaction of $\mathbf{1_2}$ with TIPS-pentacene (labeled here as **3**).

Molybdenum tris-[1,2-bis(trifluoromethyl)ethane-1,2-dithiolene], $Mo(tfd)_3$, which accepts electrons in a simple redox reaction, has been used as a p-dopant for organic hole-transport materials with the advantages of larger size, lower volatility, and higher

electron affinity (5.6 eV) over F_4-TCNQ;[30,31] its solubility can be controlled by the terminal groups on the dithiolenes.

In this chapter, CVD semi-metal graphene is treated using these solution-processable, air-stable molecular dopants for which the mechanism of action has already been studied in traditional organic semiconductors (Figure 5.5).[22,27,28,30,31] The extent to which dopants $\mathbf{1_2}$ and the molybdenum dithiolene derivative **2** react with graphene is determined and the products are found to be consistent with the expected based on previous publications. A multi-technique approach is used to understand the phenomena upon treatment with the metal-organic species, including graphene-field effect transistors to determine doping type and measure neutrality point changes, x-ray photoelectron spectroscopy (XPS) to determine quantity of the molecular species adsorbed and assess changes in the donor/acceptor system, ultraviolet photoelectron spectroscopy (UPS) to track work function (φ) changes and estimate charges transfer per dopant, and Raman spectroscopy as an additional technique to verify doping and the condition of graphene post-treatment, all without exposure to air.

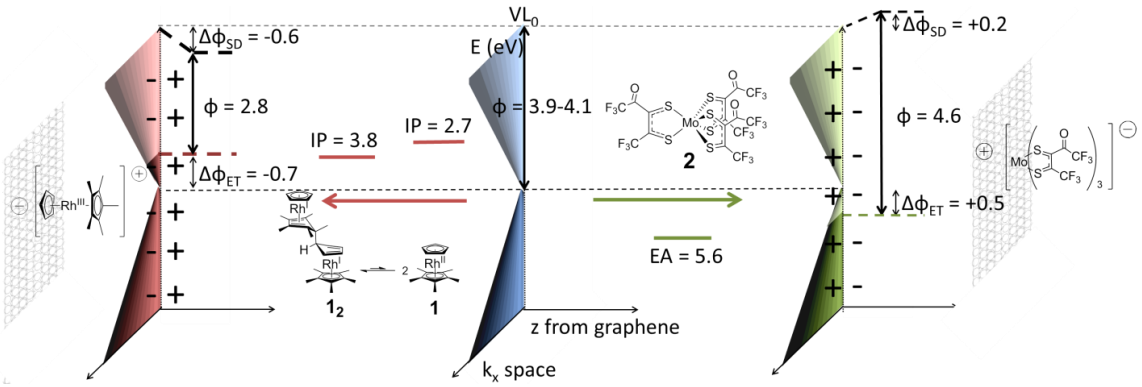

Figure 5.5 Schematic representation of n- and p-doping of graphene by $\mathbf{1_2}$ (in equilibrium with **1**, 10 min dip) and **2** (overnight dip), with associated energy levels. IP, EA and WF (φ) values were estimated from electrochemical and UPS data. The pristine graphene φ depended on the batch (4.1 eV for the sample before n-doping and 3.9 eV before p-doping). After treatment, the φ is affected by electron transfer (ET) between dopant and graphene, shifting the Fermi level (EF) relative to the Dirac point (ED), and the induced

surface dipoles (SD) from the resulting charges, which change the local vacuum level (VL).

5.3 Synthesis of graphene

As Figure 5.6 shows, there is a multitude of approaches for making graphene, and they vary in quality and mass-producibility, and hence the potential applications (Table 5.2). Chemical-vapor deposition (CVD) offers the possibility of producing large area graphene (20"×15" production already demonstrated[32]), using several sources of carbon for the graphene,[33] and the transferability to any substrate of interest.[34] Since CVD graphene was used in the project discussed in this chapter, the methodology is explained below.

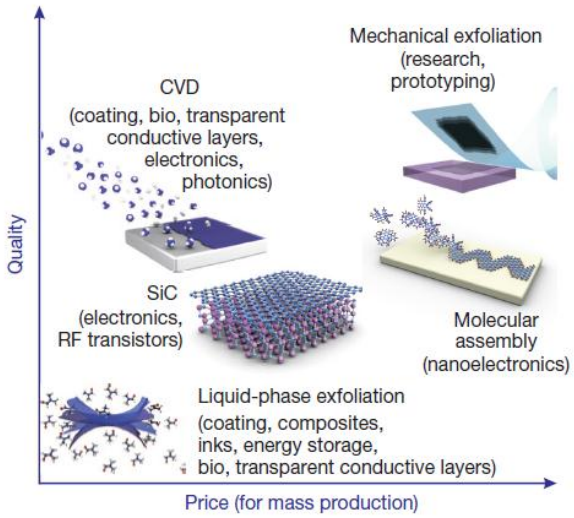

Figure 5.6 Summary of methods for synthesis of graphene plotted as a function of quality and price (for mass production). Reproduced from Novoselov, et al.[14]

Table 5.2 Properties of graphene obtained by different methods.

Method	Crystallite size (μm)	Sample size (mm)	Mobility ($cm^2 V^{-1} s^{-1}$)	Application
Mechanical exfoliation	>1,000	>1	$>2 \times 10^5$	Research
Chemical exfoliation	≤0.1	Infinite	100*	Coatings, paint or ink composites, transparent conductive layers, energy storage, bioapplications
Chemical exfoliation via graphene oxide	~100	Infinite*	1*	Coatings, paint or ink composites, transparent conductive layers, energy storage, bioapplications
CVD	1,000	~1,000	10,000	Photonics, nanoelectronics, transparent conductive layers, sensors, bioapplications
SiC	50	100	10,000	High-frequency transistors and other electronic devices

*for a layer of overlapping flakes

In CVD, the carbon source is usually supplied in gas form and a metal film is used as both catalyst and substrate for the growth. Hossein Sojoudi from the Graham group in Mechanical Engineering at GATECH used this procedure to synthesize single layer graphene that was used by the author in all experiments discussed in this chapter. In his case, copper foil is annealed at 1000 °C in a H_2/Ar atmosphere before introducing methane, the reduction of which is catalyzed on the surface of copper film, followed by dissolution of the carbon into the metal film, which after careful cooling will precipitate multi-domain, single layer graphene over a defined area (1 cm^2 in our case). Figure 5.7 shows a schematic of the process.

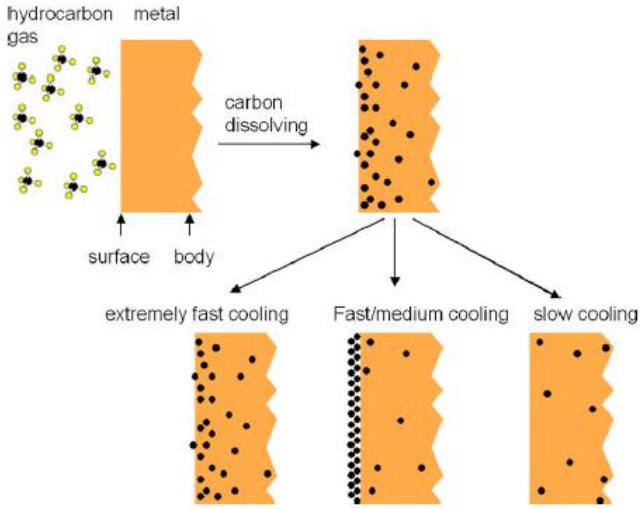

Figure 5.7 Illustration of the CVD growth process via dissolution/precipitation of graphene. Reproduced from Yu, et al.[35]

The graphene then needs to be transferred to the substrate of interest. In order to do this, the graphene is coated with PMMA for support to avoid defects during the manipulation involved in the transfer. Etching of the copper film is done with aqueous $FeCl_3$. The graphene on PMMA is then washed with HCl and water to remove all $FeCl_3$, and floated on water to be fished by the substrate of interest (typically glass or SiO_2). Once in position, a short low temperature anneal is used to remove water at the interface of the graphene and the substrate, followed by another deposition of PMMA to redissolve the prime layer of PMMA for mechanical relaxation of the underlying graphene before PMMA removal with acetone at 50 °C.[34] Figure 5.8 summarizes the transfer steps.

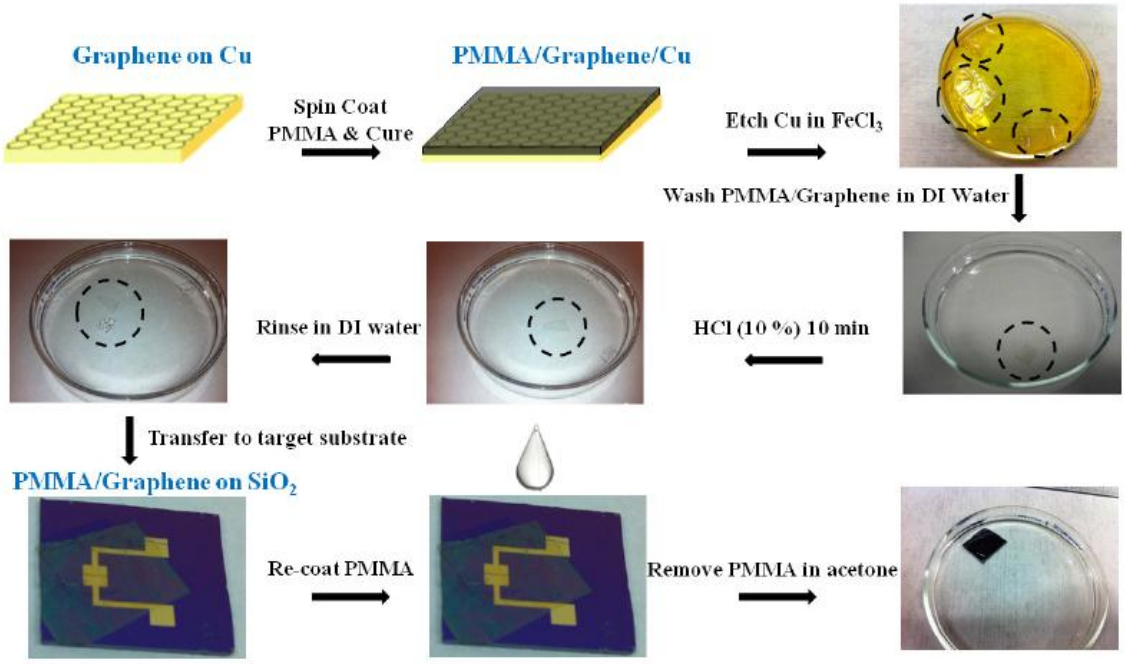

Figure 5.8 Transfer process of CVD graphene onto a patterned SiO_2 substrate. Reproduced from Sojoudi.[36]

Among the characterization techniques, Raman spectroscopy is one of the most popular given its availability and ease of measurement. Its fundamentals and application for analysis of graphene are discussed in the following section.

5.4 Raman spectroscopy for graphene characterization

In the case crystalline solids such as graphene, vibrational modes occur at discrete frequencies and are called phonons. The phonon band structure can be solved in reciprocal space considering vibrations in three-dimensions, and results in eigenvalues corresponding to two out-of-plane vibrations (known as acoustic and optical) and for in-plane vibrations labeled transverse acoustic (TA), transverse optical (TO), longitudinal acoustic (LA) and longitudinal optical (LO), as shown in Figure 5.9. These modes can be excited not only directly through IR excitation, but through inelastic scattering of excited electrons in the conduction band, as done in Raman spectroscopy.

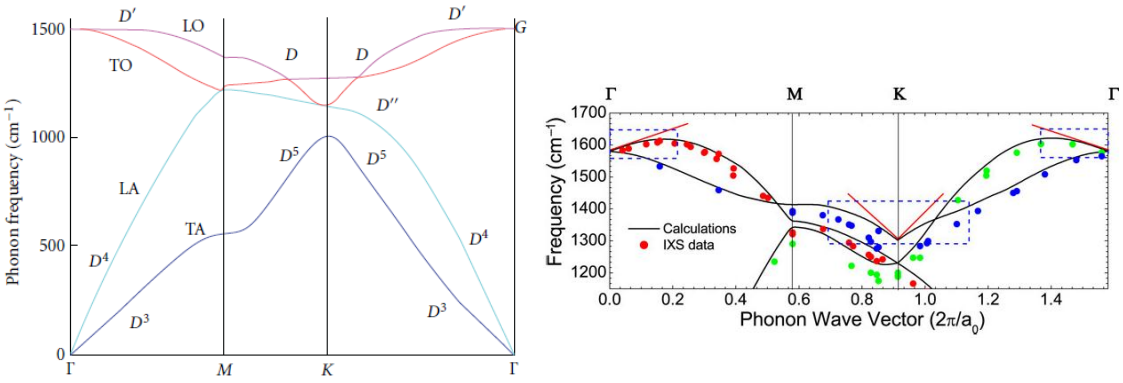

Figure 5.9 Left: theoretical phonon dispersion of graphene, with the special momentum coordinates from Figure 1.49 shown. G and D labels identify peaks associated with the processes in Figure 5.10. Reproduced from Cooper, *et al*.[4] Right: zoom into the 1200-1700 cm^{-1} frequencies: discontinuities (also known as Kohn anomalies) at coordinates K and Γ are marked with red lines and dashed boxes. Reproduced from Ferrari.[37]

Raman is a vibrational spectroscopy that relies on inelastic scattering of monochromatic light (usually a laser in the visible range): the material undergoes an electronic transition (can be to a virtual state), but instead of fluorescing immediately back to the ground state, partial loss of the energy absorbed to vibrational modes occurs. It is also possible that the system will relax but to an excited vibrational state. As Figure 5.10 shows, the graphitic G peak follows the first case mentioned: due to the cone shape of the π/π* bands close to the Dirac points, an electron from the valence band is promoted vertically with a momentum close to the K point, suffers inelastic loss within the conduction band to a lower momentum, and relaxes back to the valence band. The spectrometer detects the loss of energy and plots the intensity versus shift observed.

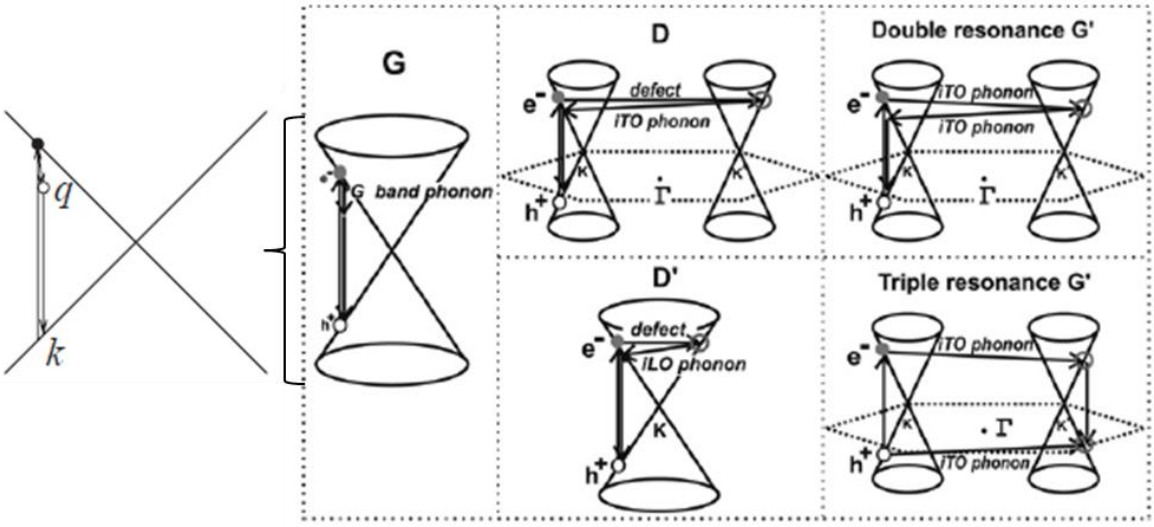

Figure 5.10 Origin of Raman peaks in graphene. The graphitic (G) peak arises from a first-order process involving electronic absorption followed by vibrational scattering to a small momentum, losing a fraction of an eV. The other peaks are second-order in origin from intercone transitions or mediated by in-plane longitudinal optic phonon. The D peaks arise from defect scattering. Reproduced from Malard, *et al*.[38]

Raman spectroscopy is sensitive to defects in graphene; this includes any areas that deviate from the perfect honeycomb hexagonal lattice,[37,39] encompassing point defects, multiple vacancies, carbon adatoms, substitutional impurities, edges, and covalently attached foreign atoms among others. The process that give rise to the defect "D" peak and the smaller "D´" peak are second-order, involving intercone scattering and an in-plane longitudinal optic transition respectively. The G´ peak, most commonly referred to as 2D since it appears at approximately twice the Raman shift that of D, involves energy losses from intercone transverse optical transitions. Figure 5.11 shows an example spectrum from a graphene edge, displaying the transitions shown in Figure 5.10.

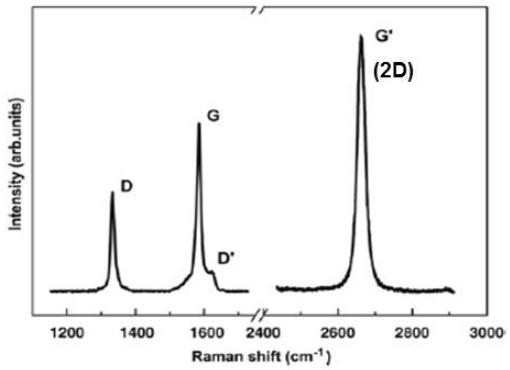

Figure 5.11 Raman spectrum of a graphene edge, showing most of the modes accounted for in Figure 5.10. Reproduced from Malard, *et al*.[38]

Doping changes the energy for the phonon dispersions in graphene: the discontinuities shown in Figure 5.9 change coordinates slightly, which can be probed by Raman.[37] Das and coworkers examined an electrochemically top-gated graphene transistor with in situ Raman, applying a potential to inject charges into the graphene and measuring its Raman peaks. The electron and hole concentrations could be calculated from Equation 5.1 (Section 5.1). Figure 5.12 shows the results from this study. Given the electron-phonon coupling in graphene, the G peak stiffens upon doping, while the 2D peak broadens, resulting in a decrease I_{2D}/I_G. The position of the G peak blue shifts regardless of injected carrier type, while the 2D peak position depends on the doping type as shown in Figure 5.12c. In the next sections, these empirical results are used to semiquantitatively estimate injected charge carriers.

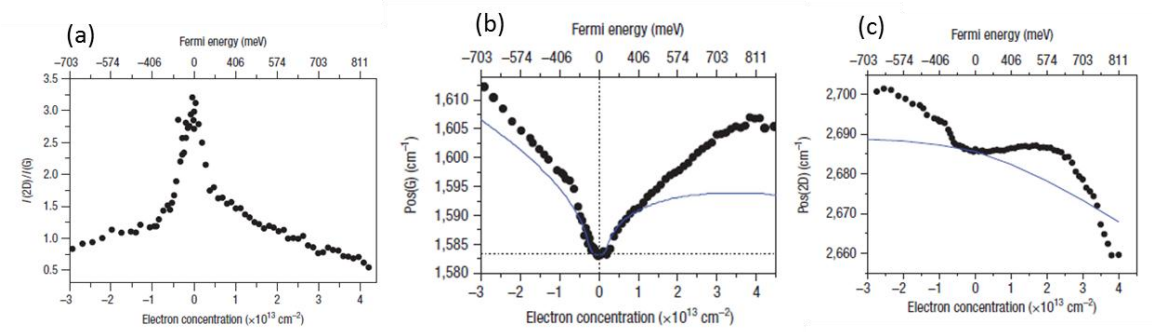

Figure 5.12 Raman peak intensities changes (a) and peak shifts (b, c) for electrogating experiment inside glovebox: experimental (dots) and computer-predicted (solid trace) results are shown.

5.5 n-Doping with rhodocene dimer $\mathbf{1_2}$

Toluene was chosen as solvent for $\mathbf{1_2}$ given the good solubility, ease of purification and non-reactivity towards $\mathbf{1_2}$ and graphene. As explained in detail in the experimental section, all sample modifications and characterizations were done without exposure to air. CVD-grown graphene was transferred onto patterned SiO_2 and annealed inside a glovebox until the neutrality point (V_{NP}) was zero (from hereon referred to as pristine). Samples were then exposed to toluene solutions of dopants for various times, followed by rinsing with additional toluene to remove any weakly physisorbed material.

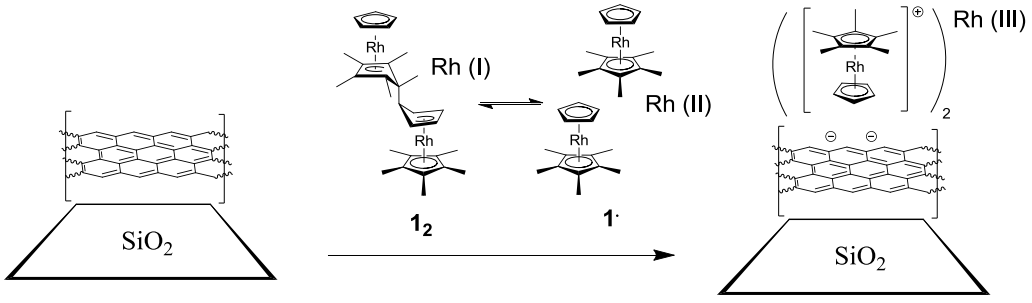

Figure 5.13 Treatment of graphene with rhodocene dimer $\mathbf{1_2}$ and proposed products. Homolysis of the C-C dimer bridge leads to oxidation state change of the metal centers, which will be Rh(II) for rhodocene monomers **1**. Electron transfer can occur from $\mathbf{1_2}$ or $\mathbf{1}^{\cdot}$ into the conduction band of graphene, resulting in transfer of two e- per dimer (one per metal center), leaving a Rh(III) salt on the surface of graphene.

Changes in electrical behaviour were determined by measuring the transfer characteristics of a back-gated / bottom-contact graphene field effect transistor (GFET, Figure 5.2). While this technique does not offer an absolute value of sheet resistance due to the setup contact resistance, it gives relative changes in conductivity and provides insight into the type and extent of doping involved. Figure 5.14 shows the transfer characteristics of a back-gated / bottom-contact graphene field-effect transistor (GFET) before and after successive treatments with $\mathbf{1_2}$. A short immersion time (*ca.* 1 s) in a low concentration solution (0.025 mM) gave a significant shift of the neutrality point to negative voltage (V_{NP} = –66 V), consistent with n-doping. Equation 5.1 was used to estimate the electron density in the conduction band,[40] *n*, from V_{NP} and the capacitance per unit area of the gate dielectric (300 nm SiO_2, C_G = 115 aF μm^{-2}), resulting in a value of $n = 4.7 \times 10^{12}$ e cm^{-2}.

Longer treatments (10 s, 10 min) on the same sample with a 2.5 mM solution gave slight additional increases in conductivity (at V_G = 0 V), but the neutrality point was no longer observable due to the –100 V limit imposed by the dielectric, precluding determination of *n* from Equation 5.1. The increase in conductivity, up to 130% (2.3×) appears to be limited by the on/off ratio of the pristine graphene.

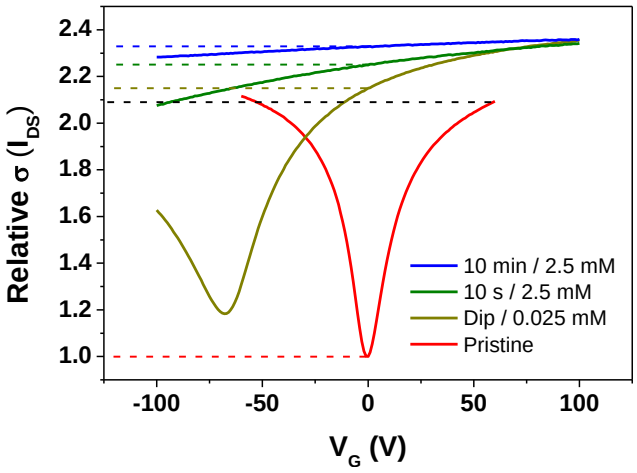

Figure 5.14 GFET transfer characteristic before and after treatment with $\mathbf{1_2}$: pristine (red) quick dip 0.025 mM (yellow), 10 s 2.5 mM (green) and 10 min 2.5 mM (blue).

To determine the extent of adsorption by graphene and identify the species present on the surface, XPS was run using an inert atmosphere accessory to transfer the samples from the glovebox to the spectrometer and vice versa without seeing air. The density of dopant monomers (**1**) that fit in a close-pack arrangement can be estimated to determine an expected $Rh/C_{graphene}$ for a monolayer and compared with the obtained ratio from the XPS Rh/C ratio. Figure 5.15 shows an estimation of molecular footprint considering the van der Waals radius for carbon and crystallographic data from $(RhCp^*Cp)^+PF_6^-$.[41] An average molecular radius of 4.6 Å is obtained (from which the footprint can be calculated to be 66 $Å^2$). Consideration of the (optimal) hexagonal close packing of discs leads to a unit cell that can be viewed as a rhombus (defined by green traces in Figure 5.15); its area is calculated to be 73 $Å^2$. By comparison with graphene, for which the unit cell encompassing 2 carbons is 5.24 $Å^2$ (2.62 $Å^2$ / C), it is estimated that 3.6 molecules of **1** fit on top of 100 carbon atoms in single layer graphene; since each monomer **1** has one Rh atom, then $\frac{\mathrm{Rh}}{\mathrm{C_{graphene}}} = 0.036$. Hence, a monolayer of such cations would lead to *ca.* 1 Rh atom per 28 graphene carbons. Note that the Rh/C XPS ratio needs to be corrected to separate contribution from graphene's carbon signal and that of the dopant.

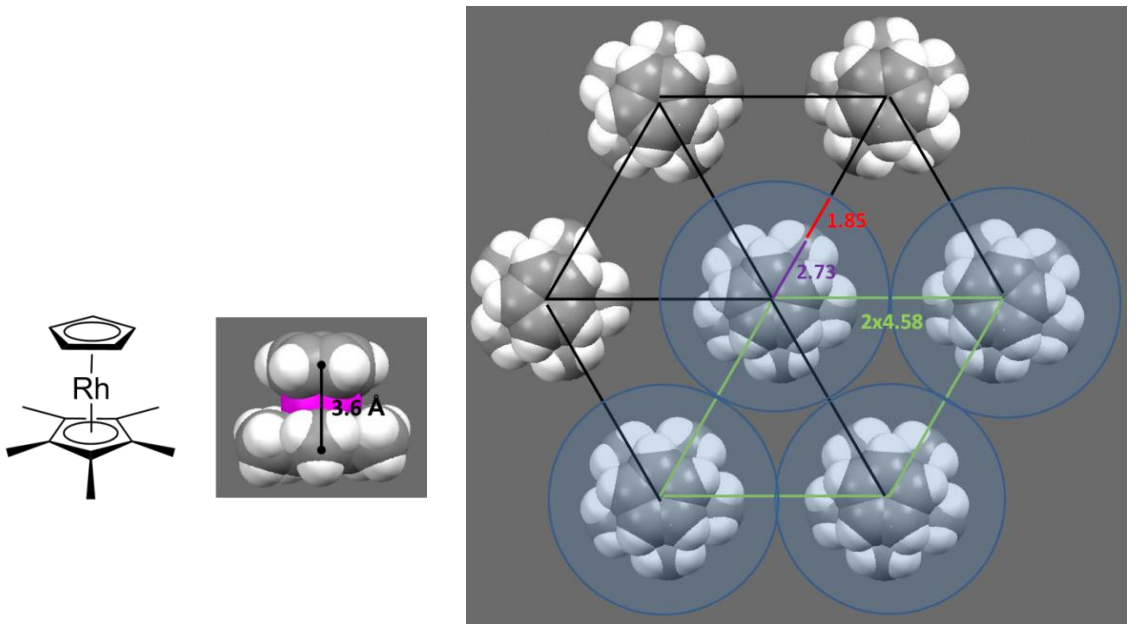

(a) (b) (c)

Figure 5.15 (a) Chemical structure and (b) space-filling model of **1** (monomer of $\mathbf{1}_2$). Molecular height estimated from crystallography of (RhCp*Cp)+PF_6^-,[41] from Cp* centroid to Cp centroid. (c) Top view of a close packed model for monolayer of RhCp*Cp treating the molecules as circular discs. Cp* centroid to C from methyl group (the atom furthest from the Cp* plane) is 2.73 Å. A van der Waals radius of non-bonded C of 1.85 Å was considered.[42] The sum of the disc areas inside the rhombus defined by green lines is 91% that of the rhombus.

The C/Rh ratio from XPS corrected for the C from the dopant itself (which has a ratio of $\frac{C_{dopant}}{Rh} = 15$) can be used to estimate the experimental $Rh/C_{graphene}$ as follows.

Equation 5.2
$$\frac{C}{Rh} = \frac{C_{dopant}}{Rh} + \frac{C_{graphene}}{Rh} = 15 + \frac{C_{graphene}}{Rh}$$

Solving for $\frac{C_{graphene}}{Rh}$ and inverting gives Equation 5.3:

Equation 5.3
$$\frac{Rh}{C_{graphene}} = \left(\frac{C}{Rh} - 15\right)^{-1}$$

The theoretical monolayer coverage of **1** on single layer graphene can now be compared with the experimental data from XPS, as summarized on Table 5.3 and discussed below.

Table 5.3 Summary of GFET, XPS and UPS characterization after treatments with dopant $\mathbf{1}_2$. Error bars are 1σ.

Result after treatment with $\mathbf{1}_2$/**1**	1 s in 0.025 mM	10 s in 2.5 mM	10 min in 2.5 mM
% Close-packed ML (XPS)	2.9 ± 0.3	25 ± 1	75 ± 2
$\varphi_{treated} - \varphi_{pristine}$ (eV) (UPS SEE)	-0.26 ± 0.09	-0.67 ± 0.10	-1.28 ± 0.10
E_D-E_F /eV (UPS VB)	-0.20 ± 0.05	-0.50 ± 0.05	-0.70 ± 0.05
n calculated from E_D-E_F (cm^{-2})	(4 ± 1) x 10^{12}	(2.6 ± 0.4) x 10^{13}	(5.2 ± 0.5) x 10^{13}
Electrons transferred per adsorbed dopant (UPS+XPS)	1.1 ± 0.4	0.75 ± 0.10	0.49 ± 0.05
$[Rh^{III}]/([Rh^{I}]+[Rh^{III}])$ (XPS)	1.0	0.81 ± 0.01	0.71 ± 0.01

Figure 5.16a shows the (small) Rh $3d_{5/2}$ and $3d_{3/2}$ core ionizations observed after the short treatment with dilute solution, with a binding energy for the Rh $3d_{5/2}$ peak of 310.8 eV. Data for the sample dipped in dilute solution suggests *ca.* 3% of a monolayer, whereas that for samples exposed to 2.5 mM suggest 23% and 75% of a monolayer for 10 s and 10 min immersions respectively.

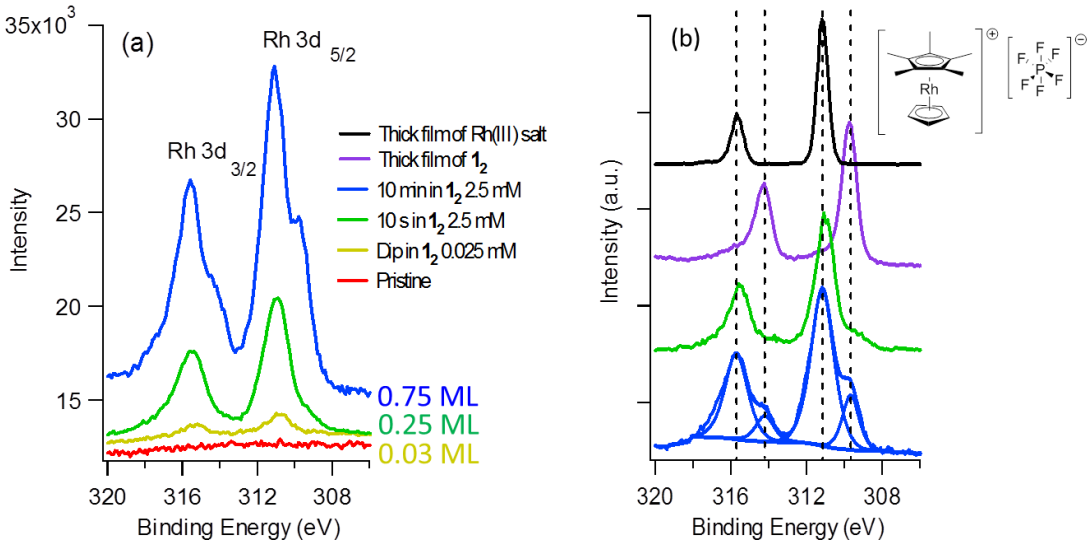

Figure 5.16 XPS spectra for pristine and $\mathbf{1}_2$-treated graphene. (a) Rh 3d XPS regions, (b) comparison with thick films of $\mathbf{1}_2$ and $\mathbf{1}^+PF_6^-$. Peak fits are shown for graphene treated with for 10 min. Traces offset vertically for clarity in (b).

Further treatment with the dopant, now at 2.5 mM concentration for 10 s (followed by washes) gives a slight increase in conductivity and a higher coverage of the dopant on the surface (25% of the theoretical close packed monolayer) as determined from XPS, with a slight shift of the Rh $3d_{5/2}$ position to 311.0 eV and a small shoulder at lower binding energy (Figure 5.16a) with an area of 23% that of the high binding energy component. The oxidation state of the Rh in the $\mathbf{1_2}$ dimer is formally Rh(I), whereas the monomer is a Rh(II) compound, and the monomeric cation formed when the dimer is oxidized is a Rh(III) species (Figure 5.13). Comparison of the Rh signals observed on the treated graphene with that of dropcast films (on SiO_2) of a salt of the Rh(III) cation, $(Rh^{III}Cp^*Cp)^+PF_6^-$, and $\mathbf{1_2}$ (Figure 5.16b) strongly suggest the Rh is predominantly present as Rh(III), consistent with the expected product doping, with a residual amount of Rh(I) attributable to unreacted dimer (19% of total Rh). 10 min treatment gives a coverage of 75% that of the close packed monolayer, with the low binding energy component for Rh 3d assigned to Rh(I) (from $\mathbf{1_2}$), having 40% of the Rh(III) peak area. Hence, for the short treatments most of the deposited species appears to be the monomer after electron transfer to graphene, consistent with the picture in Figure 5.13. With increased time and extent of doping the dimer becomes less reactive towards the substrate, presumably due to the changes in band filling and surface dipole as well as the electrostatic effect of other $\mathbf{1}^+$ cations already present at the surface, but strongly physisorbs. These treatments do not change appreciatively the transparency of graphene in the visible region, as shown in Figure 5.17.

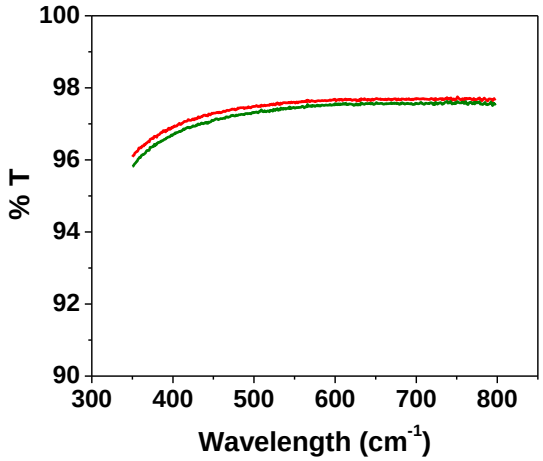

Figure 5.17 UV/Vis spectroscopy for graphene on glass before (red) and after treatment (green) with $\mathbf{1_2}$ 2.5 mM for 10 s.

A control experiment with $Rh^{III}Cp^*CpPF_6$ salt was carried out consisting of deposition on pristine graphene to check if it changed the neutrality point. Neither dipping nor drop-casting changed the neutrality point significantly, as shown in Figure 5.18. Dipping the samples in pure toluene did not give any appreciable change in neutrality point either.

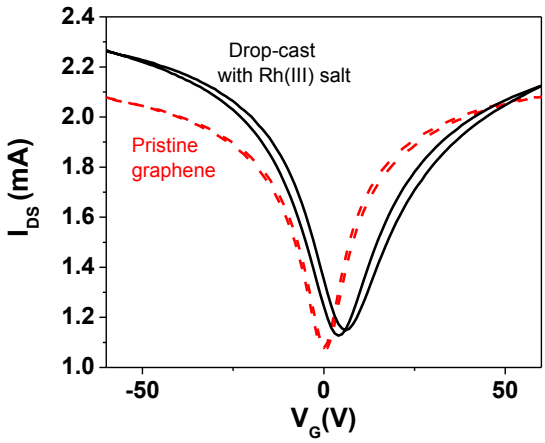

Figure 5.18 Transfer characteristics of graphene before and after dropcasting $Rh^{III}Cp^*CpPF_6$.

UV photoelectron spectroscopy (UPS) was used to probe the electronic structure changes. The valence band region is examined first (Figure 5.19), and looks as expected

for the undoped sample (in red): there is emission all the way to zero binding energy (the Fermi level). Upon short n-doping, the conduction band will start filling, and hence the Fermi level (E_F) will move closer to the vacuum level, while the Dirac point (E_D) stays constant relative to vacuum; the yellow trace shows different emission than the undoped sample (red trace). The changes in emission are more clear with further doping; the green trace, acquired after 10 s treatment, clearly shows a decrease in emission as the binding energy approaches 0.5 eV, to rise again and then extinguish abruptly as the binding goes to zero. A larger shift is observed after 10 min treatment, with a minimum of emission at 0.7 eV binding energy. The π/π* band structure changes upon successive doping are shown to the right: the conduction band fills with higher doping concentration / immersion time, reducing the work function.

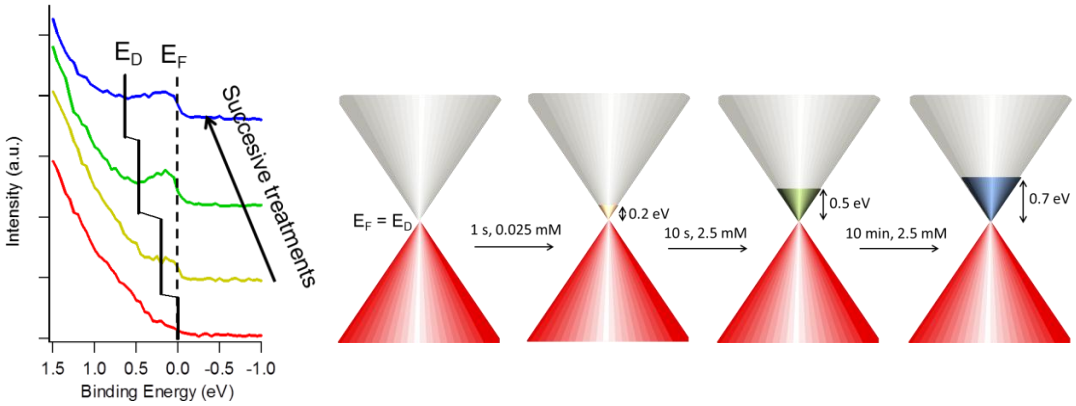

Figure 5.19 Left: valence band region for graphene and after successive treatments. Right: filling of the conduction band of graphene as observed by UPS (and XPS) for successive treatments with **1**$_2$.

Given the shift of the Fermi level relative to the vacuum level from the conduction band filling, it is expected that the core level energies will change by the same amount. The XPS binding energies of the Si 2p and O 1s core ionizations (Figure 5.20) do track linearly the change observed for the UPS valence band. Since the whole system is grounded through graphene, if affects the substrate peaks. The graphene C 1s peak should experience the same increase in BE, but since the dopant also contains a

significant amount of carbon (at a different BE), the appearance of a new component leading to broadening is observed in addition to the shift, especially at high coverages. Table 5.4 summarizes the XPS findings.

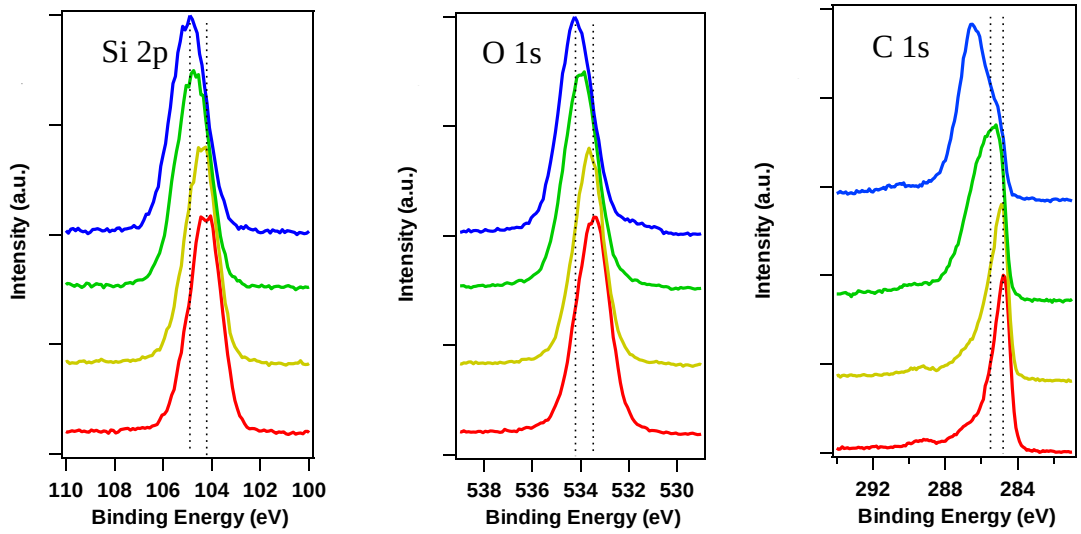

Figure 5.20 XPS high resolution spectra for pristine graphene (red) and after quick dip in 0.025 mM n-dopant solution (yellow), 10 s in 2.5 mM (green) and 10 min in 2.5 mM (blue). Plots offset vertically for clarity.

Table 5.4 Binding energies (in eV) of main peaks in graphene treated with n-dopant $\mathbf{1_2}$.

Treatment	C 1*s*	Rh^{III} $3d_{5/2}$	Rh^{III} $3d_{5/2}$	Si 2*p*	O 1*s*
Pristine	284.8	-	-	104.2	533.4
Quick dip 0.025 (mM)	285	310.8	-	104.4	533.6
10 s, 2.5 (mM)	285.4	311.0	309.4	104.7	533.8
10 min 2.5 (mM)	286.5	311.2	309.7	104.9	534.1

The contribution to the WF change from filling of the conduction band, $\Delta\phi_{ET} = E_D - E_F$, was used to determine the number of charge carriers introduced, *n*, according to Equation 5.4. This equation is derived from consideration of the band structure of graphene near the K point (where it shows linear dispersion $E_{\pm}(k) \approx \hbar v_F|k - K|$ as mentioned in section 1.9.1.[21,43] The results are shown in Figure 5.21 and compared with XPS estimates, which assume formation of each $\mathbf{1}^+$ cation is accompanied by transfer of one electron to graphene. In general, the UPS and XPS estimates are in good agreement.

Moreover, the value of *n* estimated from Equation 5.4 for the short immersion in dilute solution,[27] (4 ±1) × 10^{12} cm^{-2}, agrees well with that obtained from GFET data via Equation 5.1 (4.7 × 10^{12} cm^{-2}).

Equation 5.4

$$n = \frac{1}{p}\left(\frac{\Delta f_{ET}}{\hbar n_F}\right)^2$$

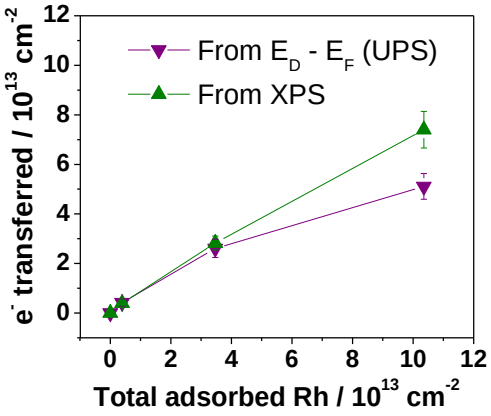

Figure 5.21 Electrons transferred into graphene, calculated from the VB region in UPS or the XPS-determined Rh(III)/Rh_{total} as a function of total Rh adsorbed (determined from XPS).

The secondary electron edge (SEE) from the UP spectrum was used to determine the WF (φ = 21.22 eV – E_{SEE}, Figure 5.22); the results are summarized on the right hand side, as a function of adsorbed Rh^{III} (from XPS). The pristine sample used for n-doping had a WF of 4.10±0.08 eV. The WF decreases slightly (–0.26 eV) with the quick exposure to dilute solution, with the slight dip in the emission at a BE = 0.2 eV mentioned previously, which is attributed to the Dirac point shift from E_F (still aligned with the spectrometer, at BE = 0) due to filling of the graphene conduction band by electron transfer from $\mathbf{1_2}$. 10 s treatment with the 2.5 mM solution leads to a further decrease in WF (–0.66 eV relative to pristine) with the clearly observable Dirac point at BE = 0.5 eV. A 10 min treatment with the concentrated solution gave an additional decrease of -1.29 eV to render a WF of 2.81±0.06 eV, with E_D – E_F = 0.7 eV. To the best

of the author's knowledge, this is the largest decrease in WF reported for graphene using adsorbed molecular dopants (see Table 5.5 for comparison to some other graphene surface treatments).

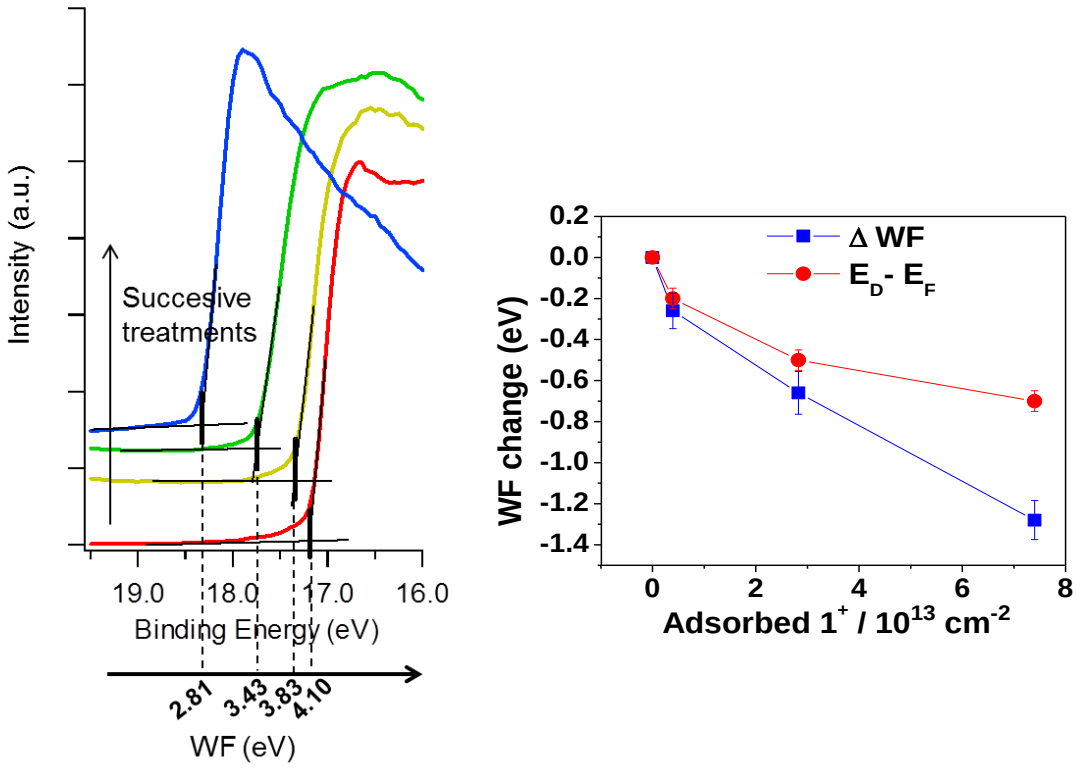

Figure 5.22 Left: the UPS secondary electron edge was used to determine the work function for graphene before and after successive treatments. Right: Electronic structure changes as probed by UPS. Total work function change observed (ΔWF, in blue) and shift of the Dirac point relative to the Fermi level (red).

Table 5.5 Comparison of the effects of various modifiers on the electronic properties of graphene.[a]

Graphene	Modifier	$\Delta\phi$ / eV[b]	$\Delta\phi_{CT}$ / eV[b]	n / cm^{-2}	Ref
CVD	Silane SAM under graphene	-0.3	–	2×10^{12} (e)[c]	1
CVD	Spin-coated MeO-DMBI	-0.7	–	1.9×10^{13} (e)[d]	44
CVD	Soaking in Cs_2CO_3	-0.85	~0.0[d]	–	45
rGO-CNT	Spin-coated Cs_2CO_3/250 °C	-1.7	–	–	46
Epitaxial	1 ML of Rb or Cs	–	-1.0	–	19
CVD	PEIE (polymer)	-0.8[e]	–	–	47
CVD	Submonolayer from $\mathbf{1_2}$	-1.3	-0.7	$2\text{-}5\times10^{13}$(e) [b,d]	This work

[a]Note that the mechanism by which the electronic changes are induced is not necessarily clear in every case, and that the work function differences for all CVD-graphene except Ref 1 and this work are determined relative to air-exposed graphene, which is generally found to be p-doped, while epitaxial

graphene in its initial state is usually n-doped. Note also that the shift of WF due to (de)population of the graphene bands is described here in terms of charge transfer (CT) rather than ET, where CT is a more general term encompassing both integral electron transfer to / from the graphene and partial charge transfer (for example, such as that found in weak CT complexes). [b]From photoemission measurements. [c]From GFET measurements. [d]From Raman shifts. [e]From Kelvin probe in air.

The difference observed between the two traces in Figure 5.22 (right) can be attributed to the surface dipole resulting from the formation of a layer of $\mathbf{1}^+$ cations on top of a negatively charged graphene sheet, which will contribute $\Delta\phi_{SD}$ to the total WF change, as shown in Equation 5.5, where $q(z)$ and $\varepsilon_r(z)$ describe the variation in charge density and effective dielectric constant along the direction normal to the surface.

Equation 5.5 $$\Delta\varphi = \Delta\varphi_{ET} + \Delta\varphi_{SD} = \hbar v_F \sqrt{n\pi} + \frac{n}{\varepsilon_0}\int_0^z \frac{q(z)}{\varepsilon_r(z)}dz$$

Without a detailed knowledge of $q(z)$ and $\varepsilon_r(z)$, the integral cannot be evaluated, but the model is broadly consistent with the data under certain assumptions, as discussed below. Qualitatively, the increasing importance of $\Delta\phi_{SD}$ relative to $\Delta\phi_{ET}$ is consistent with their predicted respective n and $n^{1/2}$ dependencies. For the quick-dip sample the WF change is almost entirely due to $\Delta\phi_{ET}$ ($E_D - E_F$), whereas in the most heavily doped case the two contributions are of comparable magnitude, as shown schematically in Figure 5.23.

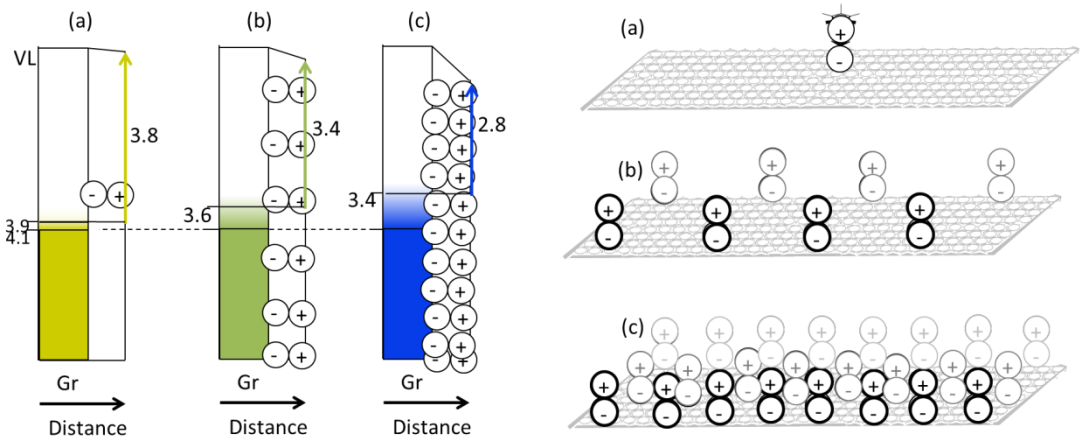

Figure 5.23 Representation in real space of the contributions to the work function (band filling and surface dipoles) after successive treatments with $\mathbf{1}_2$. The charges generated are represented as point charges. (a) Quick dip, (b) 10 s in 0.025 mM, (c) 10 min in 0.025 mM.

To test Equation 5.5, the scenario shown in Figure 5.24 is considered, where point charges have been assumed with the negative charge at the graphene plane separated from the positive charge residing on the Rh atom at 2 vdW radii[42] apart + half the molecular length. Considering an average $\epsilon_r = 10$, the estimated surface dipole from Equation 5.5 reproduces fairly well the observed surface dipole for a given *n* (see Table 5.6).

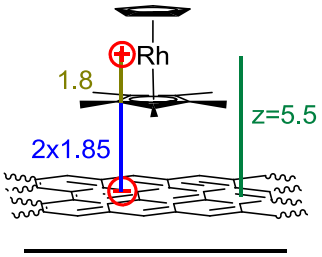

Figure 5.24 Schematic representation of surface dipole from electron transfer by **1**.

Table 5.6 Estimation of surface dipole $\Delta\varphi_{SD}$ after treatment with n-dopant. Electron transfer contribution to work function change ($\Delta\varphi_{ET}$), from which *n* was determined, is shown as well.

Treatment	Observed Δf_{ET} (eV)	n from Δf_{ET} / 10^{13}	Inferred $\Delta\varphi_{SD}$ (eV)	μ_{SD} =q×z (C*m)	Estimated $\Delta\varphi_{SD}$ (eV)
Quick dip	-0.20 ± 0.05	0.4	-0.06 ± 0.10	1.3×10^{-28}	-0.04
10 s 2.5 mM	-0.50 ± 0.05	2.6	-0.17 ± 0.12	5.4×10^{-29}	-0.26
10 min 2.5 mM	-0.71 ± 0.05	5.2	-0.59 ± 0.11	1.0×10^{-28}	-0.51

Raman spectra were also acquired without exposure to air[48] (Figure 5.25 and 5.26) and compared with data acquired *in situ* with heavy electrical doping (overviewed in Section 5.4).[43,49] The significant decrease in the intensity ratio of the 2D and G peaks (Figure 5.25), the increase of the G peak position, and the decrease in 2D peak position observed after treatment with $\mathbf{1_2}$ (Figure 5.26) are all consistent with strong n-doping. By comparing the G peak shift with experimental plots from Das and Pisana,[43,49] the charge-carrier concentration, *n*, was estimated as ~ 5×10^{12} cm^{-2} for the quick dip in dilute solution (in accordance with our GFET data), and > 2×10^{13} cm^{-2} for successive treatments, again in agreement with the values inferred from photoemission spectroscopy. The values of *n* for the more heavily doped samples are comparable to, or exceed, those reported for other molecular n-dopants (Table 5.5).

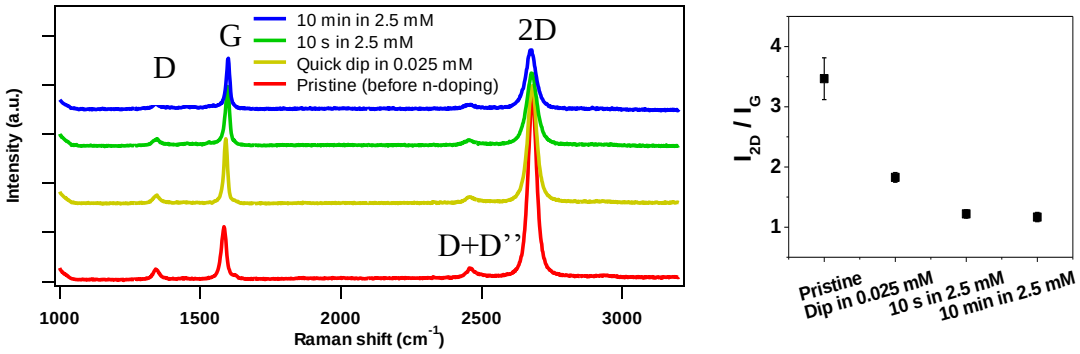

Figure 5.25 Left: Raman spectra for graphene before and after successive n-doping treatments. Plots offset vertically for clarity. Right: ratio of intensities of 2D peak to G peak. Data acquired by Siyuan Zhang.

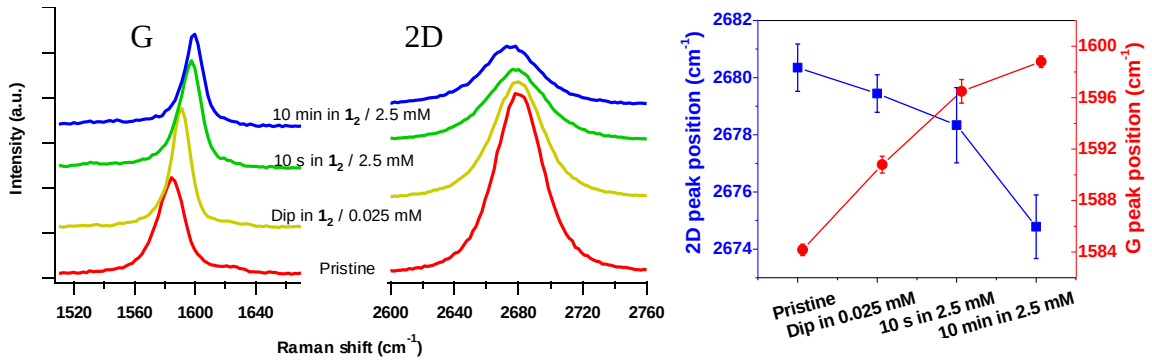

Figure 5.26 Left: Zoom into G and 2D Raman peaks of graphene before and after successive 1_2 treatments. Right: summary of results. Data acquired by Siyuan Zhang.

A summary of the XPS/UPS findings after 10 min treatment of graphene with **1_2** is shown in Figure 5.37.

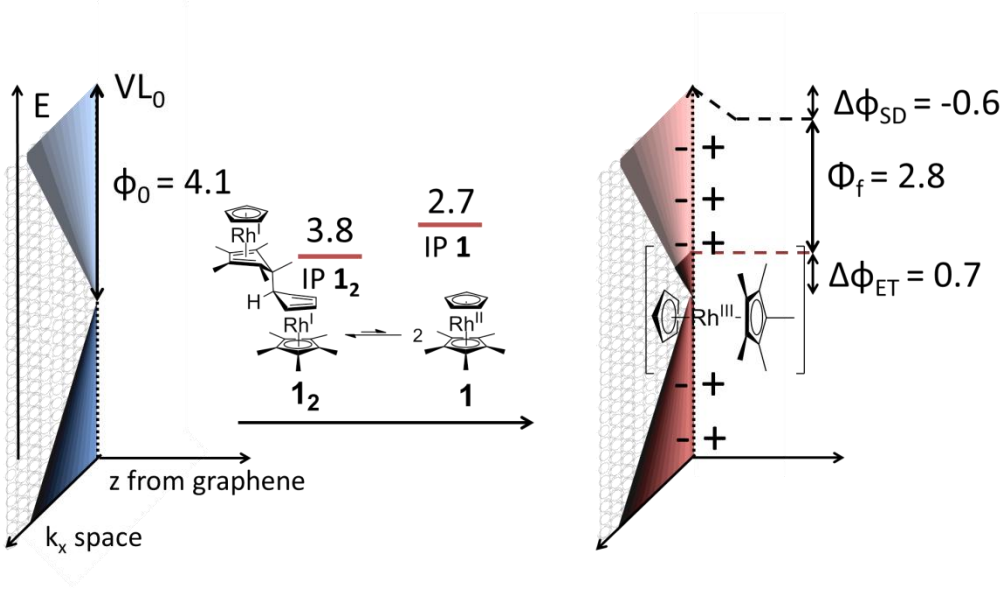

Figure 5.27 Summary of electronic structure changes from treatment of graphene with **1_2** for 10 min. Transfer of electrons filled the conduction band, and generation of charges spawn a significant surface dipole.

5.6 p-Doping with molybdenum dithiolene derivative 2

A similar study was performed using p-dopant **2**. Figure 5.28 shows the GFET results after successive treatments of graphene with **2**. As with the n-dopant, the increase

in conductivity seems to be limited by the intrinsic on/off ratio of the pristine graphene, as further treatments with more concentrated solutions and for more extended periods of time give an increase in conductivity of 120% (2.2×), not much more beyond the original 80% increase after the quick dips. From the observed V_{NP} after two quick dips in 0.05 mM solution, a hole density of 4.3×10^{12} cm^{-2} is calculated according to Equation 5.1. Additional immersion times and higher concentrations give neutrality points outside the measureable range.

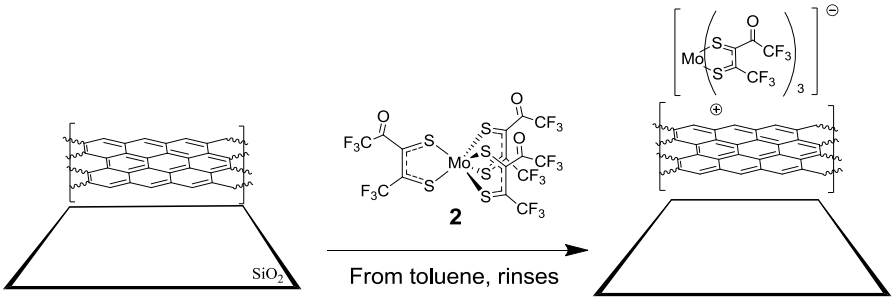

Figure 5.28 Proposed redox reaction between **2** and graphene.

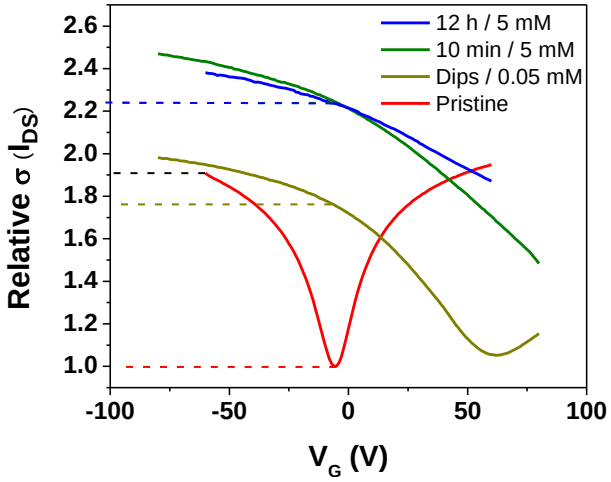

Figure 5.29 GFET transfer characteristics before and after treatment with **2**. Initial on/off ratio (black dash) and relative increases in current at V_G~0 are shown (V_{DS} = 0.1 V).

A similar approach to that used in Section 5.5 to calculate coverages was used for the p-dopant, but in this case given the molecule's geometry, it was considered as a triangle, with alternated close-packing (Figure 5.30). The area of each triangle comes to 81 Å^2. Knowing the F/C ratio for the dopant is 18/15, the $F_{dopant}/C_{graphene}$ can be estimated from Equation 5.6 (derived in the same way as Equation 5.2), and finally determine the dopant coverage by accounting for the 18 fluorine atoms per dopant as in Equation 5.7. For the graphene sample used here, the C content for the pristine sample was 30% higher than the usual single layer graphene, so the C area was corrected to account for that excess of carbon in the coverage determination.

Equation 5.6
$$\frac{F}{C_{graphene}} = \left(\frac{C}{F} - \frac{15}{18}\right)^{-1}$$

Equation 5.7
$$\frac{C_{Dopant}}{C_{graphene}} = \left(\frac{F}{C_{graphene}}\right)/18$$

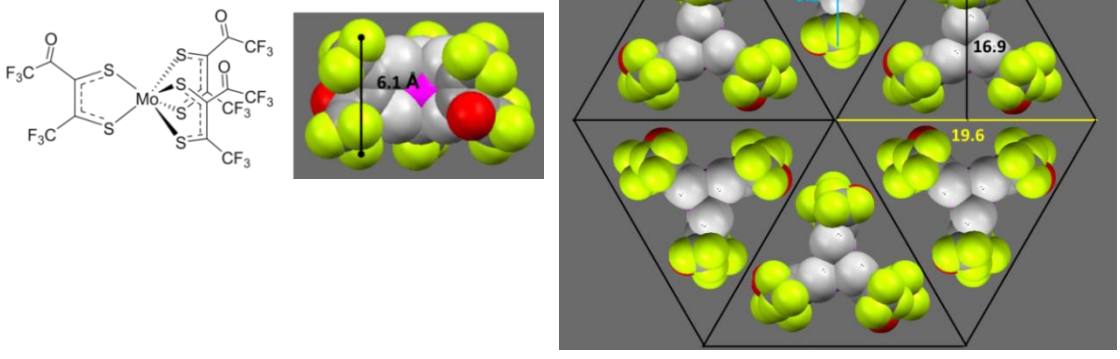

(a) (b) (c)

Figure 5.30 (a) Chemical structure and (b) space-filling model of **2**. Molecular height estimated from crystallography defining planes from the F atoms at the edges of the molecule. (c) Top view of a close packed model for monolayer of **2** treating the molecules as triangles. Molecular lengths are estimated from planes using the outermost F atoms, which give 11.9 Å on the x axis (white) and 9.2 in the y axis (light blue). A closest separation of the van der Waals radius of non-bonded F of 1.35 Å was considered

($2\times R_{vdW}$ = 2.7 Å in red).[42] This defines triangles of 19.6 Å of base and 16.9 Å height, for an effective footprint of 166 $Å^2$.

Table 5.7 Summary of GFET, XPS and UPS characterization after treatments with dopant **2**.

Result after treatment with **2**	1 s in 0.05 mM	10 min in 5 mM	12 h in 5 mM
% Close-packed ML (XPS)	6 ± 2	26 ± 1	54 ± 5
$\varphi_{treated} - \varphi_{pristine}$ /eV (UPS SEE)	0.23 ± 0.12	0.48 ± 0.13	0.71 ± 0.07
E_D-E_F /eV (from C1s)	0.20 ± 0.10	0.40 ± 0.10	0.50 ± 0.10
n calculated from E_D-E_F / cm^{-2}	$(4 \pm 2) \times 10^{12}$	$(1.7 \pm 0.4) \times 10^{13}$	$(2.6 \pm 0.5) \times 10^{13}$
h^+ transferred per adsorbed dopant (XPS)	1.1 ± 0.6	1.0 ± 0.3	0.8 ± 0.2

XPS reveals increasing surface concentrations of F, Mo, and S as treatment time increases (Figure 5.31). From the XPS F/C ratios the dopant's surface concentrations are estimated to be 6%, 26% and 54% after quick dips in dilute toluene solution, 10 min and overnight immersion in 5 mM respectively. Figure 5.31c follows the evolution of the C 1s signal, where the appearance of a C-F component from the dopant around 293 eV is noticeable after 10 min and is much better observed after overnight treatment. Removing electrons from the valence band through p-doping will shift the main graphene C1s peak to lower binding energies since the Fermi level is being lowered relative to the Dirac point.[50] Given the contribution from the dopant to the main C 1s peak is negligible, the induced hole density was calculated from the difference in binding energies with respect to that of pristine graphene, and the results are shown in conjunction with the UPS data in Table 5.7.

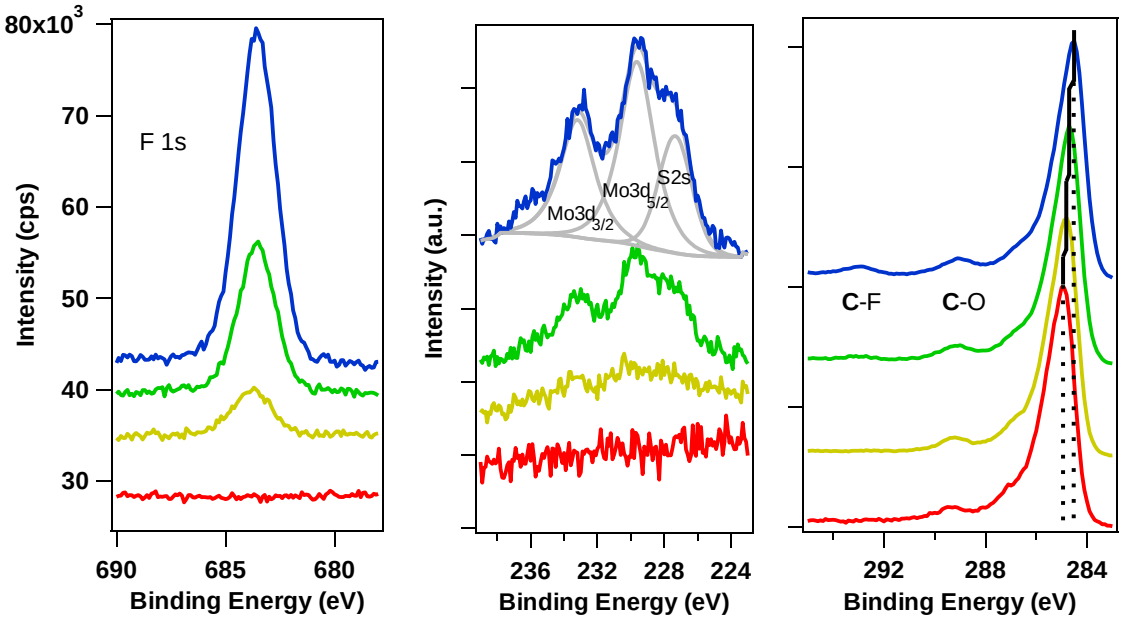

Figure 5.31 XPS comparison of pristine graphene (red) and after treatments with **2** (quick dips in 0.05 mM-yellow, 10 min in 5 mM-green, overnight in 5 mM-blue): (a) F 1s, b) Mo 3d / S 2s region, c) C 1s region, with BE shift tracked for the main graphene peak, and C-F appearance after overnight treatment; the sample treated overnight has been fitted to show both atom types are present.

Table 5.8 Binding energies (in eV) of main peaks in graphene treated with p-dopant **2**.

Treatment	C 1s	F 1s	Mo $3d_{5/2}$	Si 2p	O 1s
Pristine	285.0	-	-	104.3	533.5
Quick dips 0.05 mM	284.8	688.7	-	104.1	533.3
10 min, 5 mM	284.6	688.6	229.7	103.9	533.1
Overnight 5 mM	284.5	688.5	229.6	103.8	533.0

Figure 5.32 shows representative UPS secondary electron edges (SEE) and valence band maxima for pristine graphene and after successive treatments with the p-dopant. An increase in the work function is determined as the SEE shifts to lower binding energies. In contrast to n-doped samples, the Dirac point is not observed below the Fermi level. While from UPS it cannot be ascertained that the Dirac point is above the Fermi level, the C 1s binding energy shift shown in Figure 5.31 is consistent with that shift, and is proof of transfer p-doping.

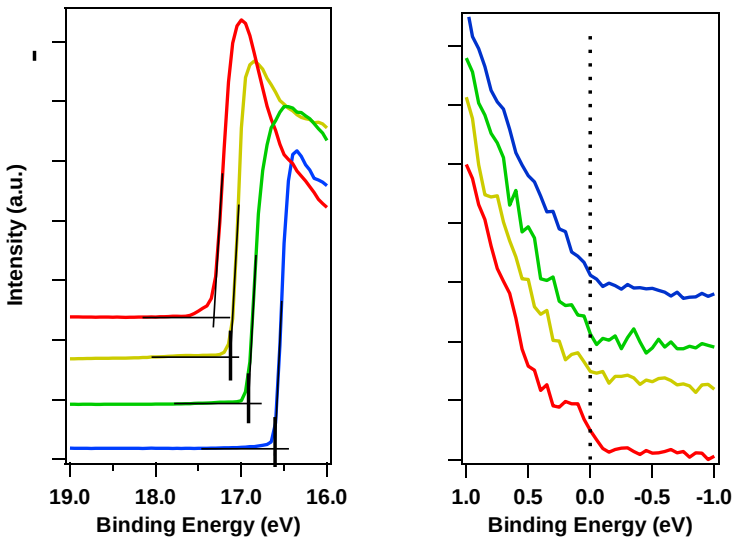

Figure 5.32 UPS secondary electron edge and valence band maximum region for pristine graphene –red, after treatments with **2** (quick dips in 0.05 mM-yellow, 10 min in 5 mM-green, overnight in 5 mM-blue). Traces offset vertically for clarity in all graphs.

Figure 5.33a shows the extent of electron transfer from graphene to the dopant; depleting the population of the valence band in graphene (introduction of holes) does not account for all the observed changes in work function. Equation 5.5 once again explains the differences (see next paragraph), where the surface dipole from the charges generated increases linearly with hole transfer. The plot in Figure 5.33b shows that as the adsorbed dopant coverage increases, hole transfer becomes more difficult, and as Figure 5.33a makes clear, for each charge transferred, the surface dipole increases concomitantly.

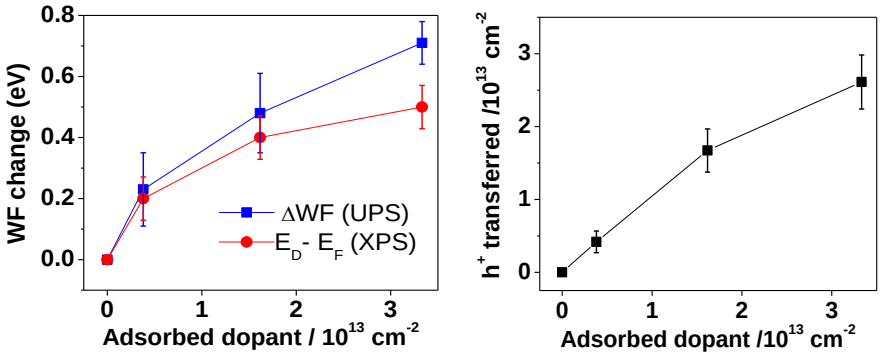

(a) (b)

Figure 5.33 (a) Work function change and shift of the Dirac point (with respect to Fermi level) with increasing deposited dopant 2. (b) XPS-estimated density of holes transferred as a function of deposited dopant **2**.

In Figure 5.34 point charges are assumed with the positive charge at the graphene plane separated from the negative charge residing in the middle of the molecule, at vdW distance $(C_{vdW} + F_{vdW})$[42] from each other. Considering an average $\epsilon_r = 15$, the estimated surface dipole from Equation 5.5 reproduces fairly well the observed surface dipole for a given *n*. Table 5.9 summarizes the observations and inferred results.

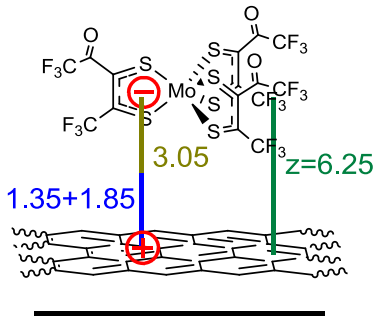

Figure 5.34 Schematic representation of surface dipole from hole transfer from **2**.

Table 5.9 Estimation of surface dipole (SD) after treatment with p-dopant. The contribution of electron transfer from graphene to dopant to the WF shift, from which *n* was determined, is shown as well.

Treatment	Observed $\Delta\varphi_{ET}$ (eV)	n from Df_{ET} / 10^{13}	Inferred $\Delta\varphi_{SD}$ (eV)	μ_{SD} =q×z (C*m)	Estimated $\Delta\varphi_{SD}$ (eV)
Quick dips 0.05 mM	0.2 ± 0.1	0.4	0.03 ± 0.14	$9.5x10^{-29}$	0.03
10 min 5 mM	0.4 ± 0.1	1.7	0.08 ± 0.15	$6.4x10^{-29}$	0.13
Overnight 5 mM	0.5 ± 0.1	2.6	0.21 ± 0.10	$1.1x10^{-28}$	0.20

Figure 5.35 summarizes the Raman observations under inert atmosphere. A comparison of these results with those of Das and coworkers acquired *in situ* with heavy electrical doping allows again to assess doping extent.[49] After treatments with the concentrated solution of the p-dopant, a significant decrease in the ratio of intensities of the 2D peak over the G peak is observed, consistent with strong doping. The 2D peak position suffers a shift to higher wavenumbers when using the concentrated solutions, in agreement with p-doping specifically. Finally, hole concentration is suggested to be on the order of 10^{13} cm^{-2} for the 10 min and overnight treatments, based on the G peak position,[49] again in in accordance with the inferred values from photoemission spectroscopy.

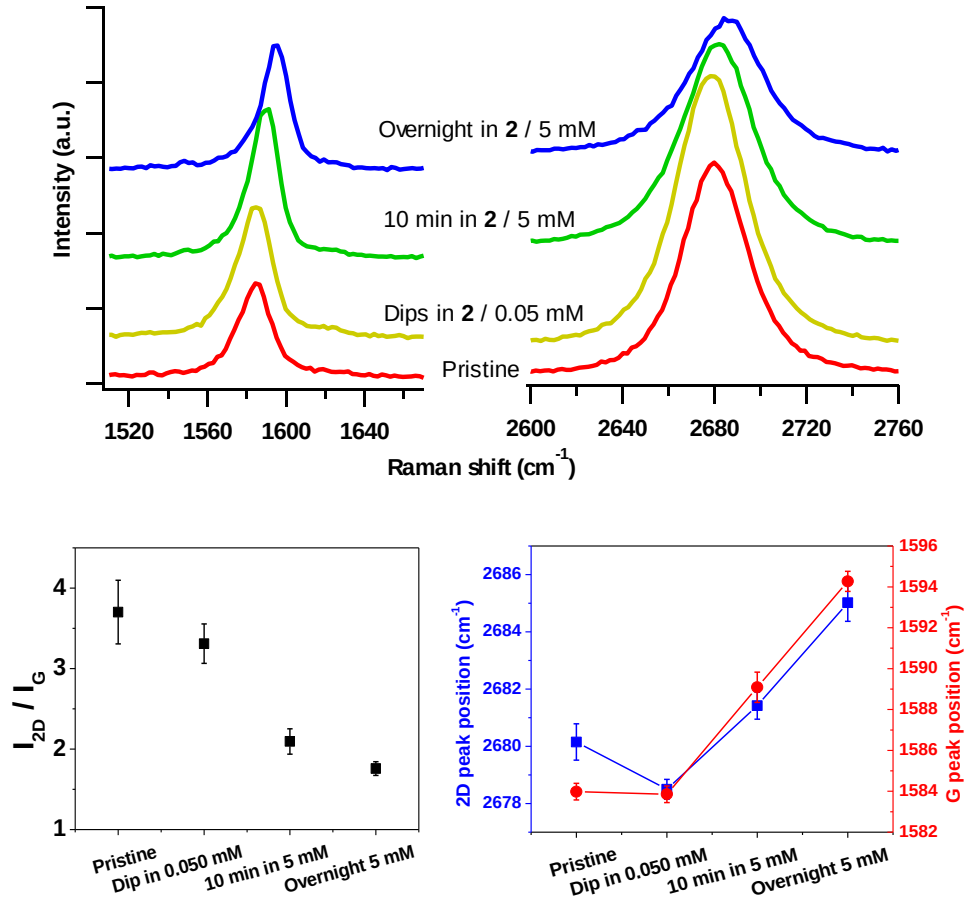

Figure 5.35 Zoom into the G and 2D Raman peaks for graphene before and after successive p-doping treatments, I_{2D}/I_G and 2D/G peak positions. Plots offset vertically for clarity. Data acquired by Siyuan Zhang.

Table 5.10 compares the results from the p-doping with 2 with state-of-the-art reports from literature using different approaches to p-doping. It can be concluded that without much process optimization, compound **2** results in significant doping, but needs to be left reacting overnight, which was not the case for $\mathbf{1}_2$. Preliminary tests with high temperature deposition (vial placed on hotplate set to 100 °C) sped up the uptake of **2**, giving work function changes in 10 min similar to those of overnight treatment at room temperature. The transparency of the graphene is barely affected after treatment (Figure

5.38). A summary of the findings after overnight treatment of graphene with **2** is shown in Figure 5.37.

Table 5.10 Comparison of the effects of various modifiers on the electronic properties of graphene.[a]

Graphene	Modifier	$\Delta\phi$ / eV[b]	$\Delta\phi_{CT}$ / eV[b]	n / cm^{-2}	Ref
CVD	Spin-coated $(CF_3SO_2)_2NH$	–	+0.7[d]	1×10^{14} (h)[d]	51
Epitaxial	Thin film MoO_3	+1.4	+0.7	1×10^{13} (h)[b]	50
Epitaxial	Thin film F_4-TCNQ	+1.0	+0.4	Dedoped[e]	52
Epitaxial	~ 1 ML of F_4-TCNQ	+1.3	+0.5	–	24
CVD	7 ML TCNQ/O_2	–	–	~10^{13} (h)[c]	53
CVD	Au NPs from $AuCl_3$	+0.5[f]	–		54
CVD	Treatment with HNO_3	+0.13[g]	–	~5×10^{12}	32
CVD	Submonolayer from **2**	+0.7	+0.5	1-3×10^{13}(h)[b,c]	This work

[a]Note that the mechanism by which the electronic changes are induced is not necessarily clear in every case. Note also that the shift of WF due to (de)population of the graphene bands are described here in terms of charge transfer (CT) rather than ET, where CT is a more general term encompassing both integral electron transfer to / from the graphene and partial charge transfer (for example, such as that found in weak CT complexes). [b]From photoemission measurements. [c]From Raman shifts. [d]From Hall measurements. [e]n-doping of 1×10^{13}cm^{-2} was reduced to 1.5×10^{11}cm^{-2}. [f]From scanning Kelvin probe in air. [g]GFET data for the as-transferred graphene showed p-doping corresponding to E_D-E_F~0.27 eV, or 4.3x10^{12} cm^{-2}. Treatment with HNO_3 increases the doping further to 0.4 eV, which implies a total n=9.4×10^{12} holes cm^{-2}.

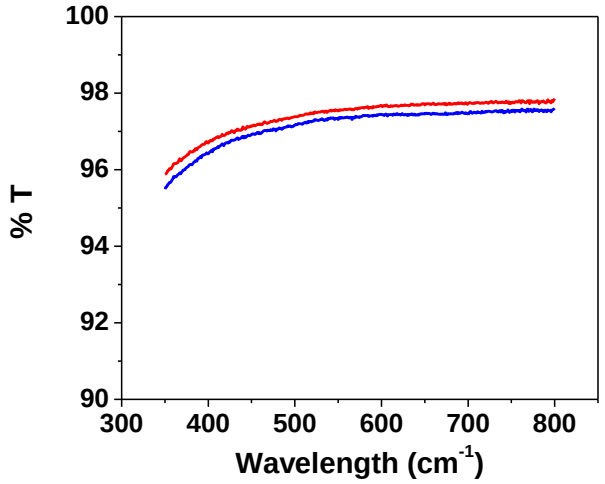

Figure 5.36 UV/Vis spectra for pristine graphene (red) on glass and after 10 min treatment in **2** at 100 °C (blue). This abbreviated procedure gives similar WF changes and coverage as overnight treatment at r.t. according to photoemission spectroscopies.

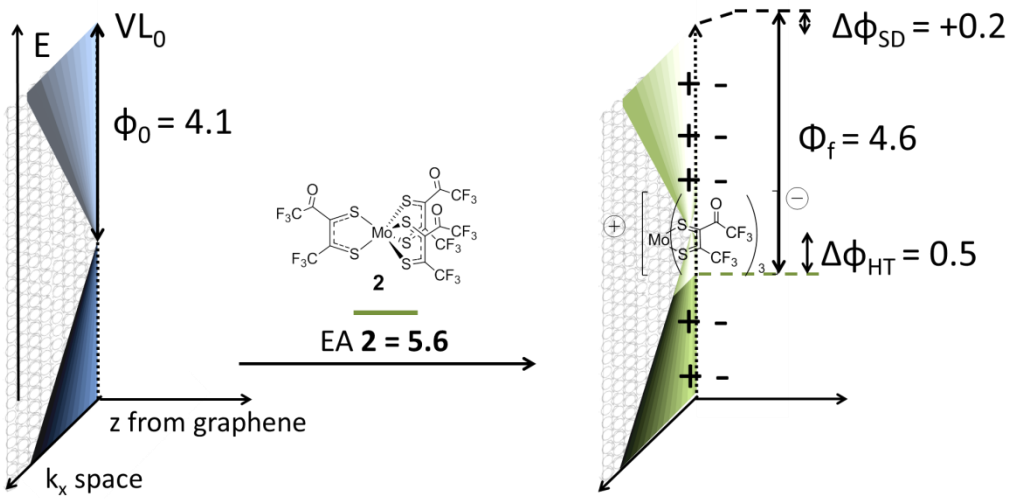

Figure 5.37 Summary of electronic structure changes for graphene after overnight treatment with **2**. Transfer of holes deplete the valence band, and generation of charges spawn a surface dipole.

5.7 Conclusions

Controllable n- and p-doping of graphene using solutions of redox-active metal-organic dopants has been demonstrated. Large carrier densities can be achieved and the work function can be tuned over a range of 1.8 eV, depending on the nature of the dopant, its concentration, and the exposure time. The WF shift is due to a combination of changes in population of the graphene band structure through electron transfer to or from graphene, and the surface dipole created by the charges generated. Resistivity is decreased due to the partial filling or emptying of graphene's bands, and the low on/off ratio is to be blamed for not being able to achieve more significant changes in resistivity, which can be traces back to the various scattering processes that limit conductivity in graphene. These dopants can potentially be applied to modulate the electronic properties of graphene for use as transparent conductive electrode in a variety of electronic devices (LEDs, OFETs, organic photovoltaics, etc) where WF tuning and high conductivity are

required. Thermal stability can be important for applications such as these. Preliminary experiments indicate that 10 min annealing at 150 °C does not lead to a significant change in the GFET behavior or XPS signals of a sample of $\mathbf{1_2}$-doped graphene.

5.8 Experimental

5.8.1 Synthesis of dopants and ionization potentials

The synthesis of $\mathbf{1_2}$, Rh(Cp*Cp)PF_6 and **2** are reported elsewhere.[28,55,56] The ionization potential of **1** was estimated through electrochemistry. The electrochemical potential of the $\mathbf{1}^+/\mathbf{1}$ couple is –2.06 V vs. ferrocenium/ferrocene in THF/0.1 M nBu_4PF_6.[28] A solid-state IP of 3.3 V has been measured using UPS for decamethylcobaltocene[57] which is oxidized at –1.86 V in the same solvent.[22] Assuming similar solid-state polarization effects and solution solvation effects for these two systems, one would then estimate an IP of ca. 3.1 eV for **1**. A somewhat lower estimate of 2.7 eV would be obtained based on the IP of 4.8 eV reported for a bis(biphenyl) derivative of ferrocene (for which the oxidation potential is 0.00 V).[29] The IP of the unmethylated rhodocene dimer (irreversible oxidation potential E_{ox} = –0.75 V at 50 mV s^{-1}) has been measured as ca. 4.0 eV; the IP of $\mathbf{1_2}$ (E_{ox} = -0.95 V) is therefore likely to be ca. 3.8 eV.

5.8.2 Sample preparation and characterization

Graphene was grown on 25 μm Cu foils (Alfa Aesar, item No. 14482) using a low pressure chemical vapor deposition technique. The Cu substrates were heated up to 1000 °C in a low pressure Ar/H_2 (100/20 sccm) environment and were annealed for 30 min to increase the Cu grain size and remove any oxygen. In a typical growth step, CH_4 (35 sccm) was introduced for 15 min, and the sample was cooled to room temperature rapidly maintaining the same gas flow. The graphene samples were transferred onto bare SiO_2

substrate or prefabricated GFET devices with care taken to minimize the introduction of defects during the transfer process. During the transfer process, the Cu was etched in iron (III) chloride (30%) overnight and graphene samples were treated with hydrochloric acid (10%) for 10 min, followed by washing in deionized water to remove contaminants on the graphene film.[1] For GFET fabrication, the source and drain contacts (gold 50 nm/ chromium 2 nm thick) were defined using conventional photolithography and lift-off processes on a highly p-doped Si substrate with a 300 nm thick SiO_2 layer to create back-gated field effect transistor structures. The resulted channel size was 10 μm × 2 mm. GFET devices were measured using a probe station equipped with a HP 4156 semiconductor parameter analyzer under a nitrogen atmosphere.

Toluene was purified in a MBRAUN solvent purification system with moisture absorbing filters, and additionally dried over CaH_2 or sodium/benzophenone, distilled and subjected to three freeze-pump-thaw cycles. Dissolution of the compounds, treatment of the graphene samples and GFET measurements were carried out inside a Unilab MBRAUN glovebox (< 0.1 ppm of water, < 5 ppm oxygen. Samples were typically annealed in the glovebox at 200 °C for a few minutes to removed physisorbed species until the neutrality point was zero. Glassware was heated in an oven at 140 °C for at least 30 min and brought into the glovebox while hot. After treatment of the graphene films in vials or bottles, samples were rinsed in fresh toluene 3-times with shaking to remove physisorbed materials, and dried out with N_2 from a rubber bulb. The GFET with the pristine graphene in Figure 5.31 had an I_{DS} at minimum σ of 1.3 mA, and output characteristics were linear before and after doping for all samples.

Transfers from the glovebox into the photoelectron spectrometer were done under N_2 atmosphere using a Kratos air-sensitive transporter 39-322 that couples into the transfer chamber of our Kratos Axis Ultra^{DLD} XPS/UPS system under positive N_2 pressure. All samples were in electronic equilibrium with the spectrometer via a metallic clip on the graphene and characterizations were performed at normal take-off angle. XPS

using monochromatic Al Kα line was run at a base pressure of 10^{-9} Torr with the Fermi level calibrated using atomically clean silver. Spot size was *ca.* 700 μm. Survey XPS scans were run at 160 eV pass energy and high resolution scans typically at 20 eV pass energy and 100 meV steps, while UPS was acquired at 5 eV pass energy and 0.05 eV step size with the aperture and iris set to 55 μm . Calibration of spectra of thick $\mathbf{1_2}$ (which needed charge neutralization) was done with the Si 2p peak set to BE = 104.9 eV, same as that of the treated graphene (10 min) on silica. XPS peak fits were done with Vision Processing Software 2.2.8 using mixed Gaussian/Lorentzian distributions to minimize *chi* squared.

UV/Visible spectroscopy was acquired in an Agilent Cary 5000 UV/Vis spectrometer for 0.5 cm radius spots (under air). Glass was used as the sample and reference to calibrate the 100%T, and 0%T was calibrated by blocking the sample light path. CVD graphene was transferred to the same type of glass slides and annealed in the glovebox at 200°C before treatment.

Raman spectroscopy was acquired in a Renishaw InVia microscope spectrometer with laser excitation at 532 nm and collection in backscattering configuration with a laser power below 0.5 mW to avoid laser-induced heating of the samples. A 50× objective lens was used to focus the laser on the graphene samples during the Raman measurements. For all of the Raman measurements, the samples were placed in N_2-filled glovebox inside a sealed microscope stage (Linkam TS 1500) to avoid air exposure during transfer and measurements.[48] The stage was mounted onto an X-Y-Z micropositioning stage to control focusing and the measurement position. A quartz window was used to allow optical access to the sample during the measurements. All Raman peaks were fitted with Gauss-Lorentzian line shapes to determine the peak position, linewidth, and intensity of the 2D and G Raman peaks.

5.9 References

(1) Baltazar, J.; Sojoudi, H.; Paniagua, S. A.; Kowalik, J.; Marder, S. R.; Tolbert, L. M.; Graham, S.; Henderson, C. L. *J. Phys. Chem. C* **2012**, *116*, 19095.

(2) Novoselov, K. S.; Geim, A. K.; Morozov, S. V.; Jiang, D.; Zhang, Y.; Dubonos, S. V.; Grigorieva, I. V.; Firsov, A. A. *Science* **2004**, *306*, 666.

(3) Venugopal, A.; Chan, J.; Li, X.; Magnuson, C. W.; Kirk, W. P.; Colombo, L.; Ruoff, R. S.; Vogel, E. M. *J. Appl. Phys.* **2011**, *109*, 104511.

(4) Cooper, D. R.; D'Anjou, B.; Ghattamaneni, N.; Harack, B.; Hilke, M.; Horth, A.; Majlis, N.; Massicotte, M.; Vandsburger, L.; Whiteway, E.; Yu, V. *ISRN Condens. Matter Phys.* **2012**, *2012*, 56.

(5) Giannazzo, F.; Raineri, V.; Rimini, E. In *Scanning Probe Miscroscopy in Nanoscience and Nanotechnology*; Springer: Berlin, 2011; Vol. 2.

(6) Cox, P. A. *The electronic structure and chemistry of solids*; Oxford University Press: Oxford, 1987.

(7) Geim, A. K.; Novoselov, K. S. *Nat. Mater.* **2007**, *6*, 183.

(8) Liu, H.; Liu, Y.; Zhu, D. *J. Mater. Chem.* **2011**, *21*, 3335.

(9) Ohta, T.; Bostwick, A.; Seyller, T.; Horn, K.; Rotenberg, E. *Science* **2006**, *313*, 951.

(10) Park, J.; Jo, S. B.; Yu, Y.-J.; Kim, Y.; Yang, J. W.; Lee, W. H.; Kim, H. H.; Hong, B. H.; Kim, P.; Cho, K.; Kim, K. S. *Adv. Mater.* **2012**, *24*, 407.

(11) Gunho, J.; Minhyeok, C.; Sangchul, L.; Woojin, P.; Yung Ho, K.; Takhee, L. *Nanotechnology* **2012**, *23*, 112001.

(12) Wang, Y.; Chen, X.; Zhong, Y.; Zhu, F.; Loh, K. P. *Appl. Phys. Lett.* **2009**, *95*, 063302.

(13) Han, T.-H.; Lee, Y.; Choi, M.-R.; Woo, S.-H.; Bae, S.-H.; Hong, B. H.; Ahn, J.-H.; Lee, T.-W. *Nature Photon.* **2012**, *6*, 105.

(14) Novoselov, K. S.; Falko, V. I.; Colombo, L.; Gellert, P. R.; Schwab, M. G.; Kim, K. *Nature* **2012**, *490*, 192.

(15) Hugo, E. R.; Prasoon, J.; Awnish, K. G.; Humberto, R. G.; Milton, W. C.; Srinivas, A. T.; Peter, C. E. *Nanotechnology* **2009**, *20*, 245501.

(16) Leenaerts, O.; Partoens, B.; Peeters, F. M. *Microelectron. J.* **2009**, *40*, 860.

(17) Yong-Hui, Z.; Ya-Bin, C.; Kai-Ge, Z.; Cai-Hong, L.; Jing, Z.; Hao-Li, Z.; Yong, P. *Nanotechnology* **2009**, *20*, 185504.

(18) Schedin, F.; Geim, A. K.; Morozov, S. V.; Hill, E. W.; Blake, P.; Katsnelson, M. I.; Novoselov, K. S. *Nature Mater.* **2007**, *6*, 652.

(19) Watcharinyanon, S.; Virojanadara, C.; Johansson, L. I. *Surf. Sci.* **2011**, *605*, 1918.

(20) Chen, J. H.; Jang, C.; Adam, S.; Fuhrer, M. S.; Williams, E. D.; Ishigami, M. *Nat Phys* **2008**, *4*, 377.

(21) Novoselov, K. S.; Geim, A. K.; Morozov, S. V.; Jiang, D.; Katsnelson, M. I.; Grigorieva, I. V.; Dubonos, S. V.; Firsov, A. A. *Nature* **2005**, *438*, 197.

(22) Guo, S.; Kim, S. B.; Mohapatra, S. K.; Qi, Y.; Sajoto, T.; Kahn, A.; Marder, S. R.; Barlow, S. *Adv. Mater.* **2012**, *24*, 699.

(23) Gao, W.; Kahn, A. *J. Appl. Phys.* **2003**, *94*, 359.

(24) Chen, W.; Chen, S.; Qi, D. C.; Gao, X. Y.; Wee, A. T. S. *J. Am. Chem. Soc.* **2007**, *129*, 10418.

(25) Drechsel, J.; Pfeiffer, M.; Zhou, X.; Nollau, A.; Leo, K. *Synth. Met.* **2002**, *127*, 201.

(26) Duhm, S.; Salzmann, I.; Broker, B.; Glowatzki, H.; Johnson, R. L.; Koch, N. *Appl. Phys. Lett.* **2009**, *95*, 093305.

(27) Qi, Y.; Mohapatra, S. K.; Kim, S. B.; Barlow, S.; Marder, S. R.; Kahn, A. *Appl. Phys. Lett.* **2012**, *100*, 083305.

(28) Guo, S.; Mohapatra, S. K.; Romanov, A.; Timofeeva, T. V.; Hardcastle, K. I.; Yesudas, K.; Risko, C.; Brédas, J.-L.; Marder, S. R.; Barlow, S. *Chem. Eur. J.* **2012**, *18*, 14760.

(29) D'Andrade, B. W.; Datta, S.; Forrest, S. R.; Djurovich, P.; Polikarpov, E.; Thompson, M. E. *Org. Electron.* **2005**, *6*, 11.

(30) Qi, Y.; Sajoto, T.; Barlow, S.; Kim, E.-G.; Brédas, J.-L.; Marder, S. R.; Kahn, A. *J. Am. Chem. Soc.* **2009**, *131*, 12530.

(31) Qi, Y.; Sajoto, T.; Kröger, M.; Kandabarow, A. M.; Park, W.; Barlow, S.; Kim, E.-G.; Wielunski, L.; Feldman, L. C.; Bartynski, R. A.; Brédas, J.-L.; Marder, S. R.; Kahn, A. *Chem. Mater.* **2009**, *22*, 524.

(32) Bae, S.; Kim, H.; Lee, Y.; Xu, X.; Park, J.-S.; Zheng, Y.; Balakrishnan, J.; Lei, T.; Ri Kim, H.; Song, Y. I.; Kim, Y.-J.; Kim, K. S.; Ozyilmaz, B.; Ahn, J.-H.; Hong, B. H.; Iijima, S. *Nature Nanotech.* **2010**, *5*, 574.

(33) Ruan, G.; Sun, Z.; Peng, Z.; Tour, J. M. *ACS Nano* **2011**, *5*, 7601.

(34) Li, X.; Zhu, Y.; Cai, W.; Borysiak, M.; Han, B.; Chen, D.; Piner, R. D.; Colombo, L.; Ruoff, R. S. *Nano Lett.* **2009**, *9*, 4359.

(35) Yu, Q.; Lian, J.; Siriponglert, S.; Li, H.; Chen, Y. P.; Pei, S.-S. *Appl. Phys. Lett.* **2008**, *93*, 113103.

(36) Sojoudi, H., Ph.D. Thesis, Georgia Institutute of Technology, 2012.

(37) Ferrari, A. C. *Solid State Commun.* **2007**, *143*, 47.

(38) Malard, L. M.; Pimenta, M. A.; Dresselhaus, G.; Dresselhaus, M. S. *Physics Reports* **2009**, *473*, 51.

(39) Banhart, F.; Kotakoski, J.; Krasheninnikov, A. V. *ACS Nano* **2010**, *5*, 26.

(40) Zhang, Y.; Tan, Y.-W.; Stormer, H. L.; Kim, P. *Nature* **2005**, *438*, 201.

(41) Mohapatra, S. K.; Romanov, A.; Angles, G.; Timofeeva, T. V.; Barlow, S.; Marder, S. R. *J. Organomet. Chem.* **2012**, *706–707*, 140.

(42) Housecroft, C. E.; Sharpe, A. G. *Inorganic Chemistry*; 3rd ed.; Pearson / Prentice Hall: Essex, UK, 2008.

(43) Pisana, S.; Lazzeri, M.; Casiraghi, C.; Novoselov, K. S.; Geim, A. K.; Ferrari, A. C.; Mauri, F. *Nature Mater.* **2007**, *6*, 198.

(44) Wei, P.; Liu, N.; Lee, H. R.; Adijanto, E.; Ci, L.; Naab, B. D.; Zhong, J. Q.; Park, J.; Chen, W.; Cui, Y.; Bao, Z. *Nano Lett.* **2013**.

(45) Kwon, K. C.; Choi, K. S.; Kim, B. J.; Lee, J.-L.; Kim, S. Y. *J. Phys. Chem. C* **2012**, *116*, 26586.

(46) Huang, J.-H.; Fang, J.-H.; Liu, C.-C.; Chu, C.-W. *ACS Nano* **2011**, *5*, 6262.

(47) Zhou, Y.; Shim, J. W.; Fuentes-Hernandez, C.; Sharma, A.; Knauer, K. A.; Giordano, A. J.; Marder, S. R.; Kippelen, B. *PCCP* **2012**, *14*, 12014.

(48) Sojoudi, H.; Baltazar, J.; Henderson, C.; Graham, S. *J. Vac. Sci. Technol., B* **2012**, *30*, 041213.

(49) Das, A.; Pisana, S.; Chakraborty, B.; Piscanec, S.; Saha, S. K.; Waghmare, U. V.; Novoselov, K. S.; Krishnamurthy, H. R.; Geim, A. K.; Ferrari, A. C.; Sood, A. K. *Nature Nanotech.* **2008**, *3*, 210.

(50) Chen, Z.; Santoso, I.; Wang, R.; Xie, L. F.; Mao, H. Y.; Huang, H.; Wang, Y. Z.; Gao, X. Y.; Chen, Z. K.; Ma, D.; Wee, A. T. S.; Chen, W. *Appl. Phys. Lett.* **2010**, *96*, 213104.

(51) Tongay, S.; Berke, K.; Lemaitre, M.; Nasrollahi, Z.; Tanner, D. B.; Hebard, A. F.; Appleton, B. R. *Nanotechnology* **2011**, *22*, 425701.

(52) Coletti, C.; Riedl, C.; Lee, D. S.; Krauss, B.; Patthey, L.; von Klitzing, K.; Smet, J. H.; Starke, U. *Phys. Rev. B* **2010**, *81*, 235401.

(53) Qi, Y.; Mazur, U.; Hipps, K. W. *R. Soc. Chem. Adv.* **2012**, *2*, 10579.

(54) Shi, Y.; Kim, K. K.; Reina, A.; Hofmann, M.; Li, L.-J.; Kong, J. *ACS Nano* **2010**, *4*, 2689.

(55) Moseley, K.; Kang, J. W.; Maitlis, P. M. *J. Chem. Soc. A* **1970**, *0*, 2875.

(56) Paniagua, S. A.; Baltazar, J.; Sojoudi, H.; Mohapatra, S. K.; Zhang, S.; Henderson, C.; Graham, S.; Barlow, S.; Marder, S. R. *Mater. Horiz.* **2013**, *In press*.

(57) Chan, C. K.; Zhao, W.; Barlow, S.; Marder, S.; Kahn, A. *Org. Electron.* **2008**, *9*, 575.

CHAPTER 6 CONCLUSIONS AND OUTLOOK

This thesis has presented the use of surface modifiers to tune the electronic properties of non-metallic transparent electrodes such as ITO, NiO_x, and graphene, as well as grow polymers from ITO electrodes and $BaTiO_3$ nanoparticles which can have applications in conductive and capacitive devices. It has been the author's intension to show that several types of surface engineering can be performed, which include tailoring the electronic properties (Chapters 2 and 5) as well as performing chemistry off surfaces (Chapters 3 and 4). All these interfacial systems have been rigorously characterized as required to make assertions on the species present from a qualitative and quantitative perspective. Phosphonic acids were used in Chapter 2, 3 and 4 for these purposes and the plausible applications are manifold; as shown in Figure 6.1, which is not limited to the specific systems probed in this thesis.

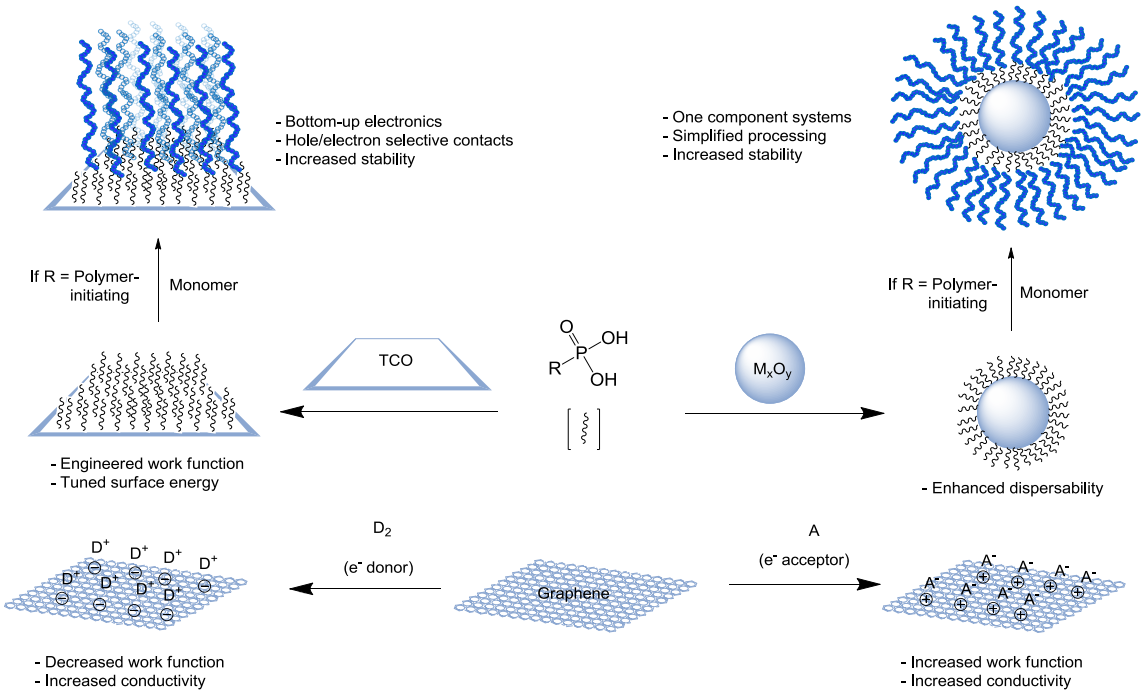

Figure 6.1 Surface engineering of metal oxide flat surfaces, nanoparticles and graphene for electronic/wetting properties tuning and surface-initiated polymerization.

Chemisorption such as that discussed in Chapter 2 can have great impact on the work function of a substrate, and as previously explored, also greatly affect the surface energies.[1] Incomplete monolayers could be used to fine-tune these properties to match the needs for a specific system. Nanoparticle-containing systems can immensely benefit from the enhanced dispersability afforded by surface modification,[2] and, as Chapter 3 proved, phosphonic acid anchored initiators are compatible with ATRP chemistry such that polymeric matrices can be grown from the modified oxides in simple manner, which will also facilitate the processing of such materials. This concept of bottom-up electronics, where the materials are produced through in-situ generation was also explored in Chapter 4, where conjugated polymers were synthesized with the use of carefully designed phosphonates and phosphonic acids. Such approach can potentially lead to more stable devices. While phosphonic acids cannot anchor to graphene, the latest material to emerge as a potential replacement to ITO, redox active materials can be used to tailor its electronic properties and likely even its surface energy, something that could be explored in the future.

There was a need for a comprehensive study of the effect of immersion time, concentration, and plasma *vs.* no plasma treatment of the substrate on the quality and coverage of phosphonic acid overlayers on TCOs given the increasing use of phosphonic acid modification in the last few years. Knowledge of the range in electronic structure changes that a single phosphonic acid can impart as the coverage increases was also lacking. Chapter 2 gave a review on kinetics of chemisorption of phosphonic acids on metal oxides and presented a study using XPS to follow the chemisorption kinetics for deposition of pentafluorobenzylphosphonic acid (PFBPA) which has found application as a modifier for TCOs in OPVs and OLEDs. Of the concentrations probed, 10 mM gave the highest observed rate constant at room temperature and was chosen as the concentration for a second series of experiments that probed as well the quality of the

overlayers achieved (by means of the F/C XPS ratios) and the electronic structure changes. It was clear that room-temperature deposition saturated at submonolayer coverage, regardless of whether plasma activation was employed or not. 75 °C deposition with plasma pretreatment afforded high quality monolayers within 10 min, while detergent-solvent cleaning (DSC) alone results on a surface where adventitious carbon must be replaced by the modifier, delaying the formation of a full monolayer, for which a day of immersion in needed. No significant differences were observed in binding modes after long immersion times when using plasma *vs.* no plasma and for high/low temperature depositions.

In all these cases there is subtle balance between intrinsic surface dipole of ITO and that imparted by the phosphonate coating, and for DSC-only ITO, for coverages between *ca.* 25% and 65% a linear behavior in surface dipole changes is observed as expected from the simple Helmholtz equation. Submonolayer coverages could be used to fine-tune the work function of the metal oxide in a continuous fashion.

It might be of interest to thoroughly study the effect of the medium acidity on phosphonic depositions: given that is seems higher acidity has a detrimental effect on adsorption rates, a non-nucleophilic buffer system could keep a relatively neutral pH so that less material is needed to achieve a monolayer in a reasonable amount of time. Using buffered solutions might also make it feasible to better modify other metal oxides, such as ZnO, that can be etched at low pHs. Similar phosphonic acids were shown to form high quality monolayers on ITO and NiO_x using high-temperature depositions.

From a fundamental science perspective, these studies contribute to building a molecular picture of the assembly of phosphonic acid monolayers on ITO, which should not be assumed to occur in an analogous fashion to that of thiols on gold given the different chemistries involved. The recent progress in surface-sensitive techniques is allowing the surface science community to learn more about the monolayers of interest for organic electronics, where orientation and order of monolayers can now be predicted

through computational studies and compared with experimental results from IRRAS and NEXAFS.[3,4]

While ITO is currently the transparent electrode of choice for commercial applications, other transparent conductive oxides containing lower quantities of the expensive indium have been proposed to replace it. Significantly, phosphonic acid modifiers have proven to be attachable to most metal oxides.[5] The author of this thesis collaborated with the Graham group in the development of spray coating as a means to chemisorb PFBPA to various TCOs. When performed at high temperature, this appears to be a quicker alternative than immersion to deposit full monolayers on ITO, taking a couple of minutes, as opposed to at least 10 min. In both cases, sonication for 10 min in diluted triethylamine was used to ensure removal of multilayers (which are especially obvious in the case of spray coating), and it would be of interest to verify if spray coating the diluted base can also remove multilayers in a matter of seconds. This might be of industrial importance for high-throughput modification of TCOs.

Chapter 3 showed the protocol development for surface-initiated polymerization of styrene from phosphonic acid-modified $BaTiO_3$ nanoparticles via ARGET ATRP, which required very small amount of copper catalyst compared to the traditional ATRP and less stringent oxygen-removal requirements. The critical factor that separates little growth of polystyrene (PS) from significant growth was the removal of the solvent so that the concentration of all reagents increased. Reaction time and temperature can control the amount of polymer grown. The protocol developed affords spin or blade-castable composites that can be processed much more rapidly than composites obtained through the traditional scheme of ball-milling for 12 days. Control experiments proved that surface-initiated polymerization proceeds only with the use of catalyst, reducing agent, and the right initiator on the surface of the nanoparticles.

The grafted-nanoparticles made were used to build hybrid capacitors with and without mixing with free polystyrene as dielectric. In both cases the permittivity

increased considerably for high nanoparticle loadings as expected relative to the pure polymer, but the breakdown strength decreased significantly, which can be attributed to porosity of the polystyrene component. Hence, the same protocol developed for surface-initiated polymerization was used to grow polymethylmethacrylate instead; this afforded devices which had similar breakdown strengths to the pure polymer with increased dielectric constant, resulting in higher maximum energy densities. Further studies on the relation between polymer weight and distribution, as well as volume fraction on the resulting film morphology and device behavior, might lead to optimized systems. Other non-conjugated polymers or block copolymers incorporating polarizable groups, such as polyacrylonitrile, could be grown as well, and other perovskite nanoparticles could be considered as substrates for the surface-initiated polymerization. The polymers could also be grown directly off one of the electrodes, for example, exploiting the affinity of phosphonic acid groups for the native oxide found on aluminum.

One way to increase the permittivity of these composites is to introduce a ferroelectric polymer such as polyvinylidene fluoride (pVDF) into the mixture. While this has been done for Viton using surface modification and blending,[2,6,7] it would be most interesting to do this through chemical attachment to reduce particle-particle contact. Figure 6.2 shows a scheme for coupling pVDF to PS (which can already be attached to $BaTiO_3$) through click chemistry. While the conversion of the halide-terminated PS worked (as shown by proton NMR spectroscopy),[8] it has not been possible to determine if in fact the pVDF has a terminal alcohol moiety as the supplier claims, or if the propargylation is successful (no terminal groups are observed by proton NMR or MALDI MS). Perhaps using a ^{13}C-labeled version of the propargyl will make it easy to identify on the polymer after work-up.

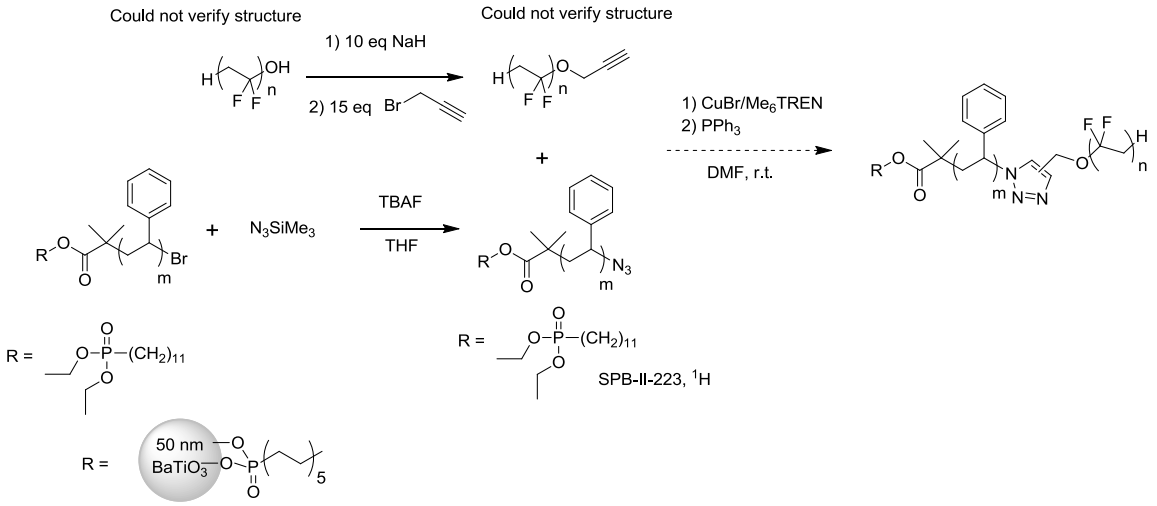

Figure 6.2 Coupling polystyrene to poly(vinylidene difluoride) through click chemistry.

In Chapter 4, three thrusts of monolayer science were explored: design and synthesis of modifiers, characterization of monolayers, and study of the applications for these. New molecules were designed and synthesized bearing groups for initiation of Grignard metathesis reactions. The Luscombe group determined initiation efficiencies and molecular weights for four of the phosphonate initiators made for Kumada Catalyst-Transfer Polymerization (KCTP). 4-Chloro-3-methylbenzyl phosphonate **In1** afforded results similar to those of the analogous 2-chlorotoluene[9] (which has the same substitution pattern but no phosphonate), with high yield (90%), high initiation percentage (84%), high regioregularity (94%) and low polydispersity (1.2). **In2** and **In3** did not perform as well based upon these parameters, and the thiophene-based **In4** did not form the oxidative addition product, which the analogue without the phosphonate does form.[10]

Monolayers of the phosphonic acid analogues of these initiators were proven to chemisorb on ITO, and many attempts varying polymerization conditions were done, mostly focusing on **In1A**, 4-chloro-3-methylbenzyl phosphonic acid, given the success of its phosphonate precursor. While films of poly(3-methylthiophene) (P3MT) were grown,

the quality and reproducibility is still far from what is needed to use it as a donor material in OPVs. The characterization of intermediate species presented towards the end of the chapter shed some light into how to optimize the protocol given that surface-confined reactions seem to not work as well as those in solution. If not used as donors in OPVs, grown P3MT films could be used as hole-transport layers for applications in which transparency in the IR is needed, where PEDOT:PSS, the typical hole-selective contact briefly discussed in Chapter 2, starts absorbing. Once optimization of film quality is achieved, it might be of interest to explore chemical doping and determine if the covalent attachment of the grafted film imparts different optical, electrical, or mechanical properties than a spin-coated film, as well as increased stability. The Locklin group recently published the first device results using P3MT grafts grown in similar fashion from ITO as hole transport layers.[11] Grafts of thicknesses ~3 to ~20 nm performed close to PEDOT:PSS in P3HT/PCBM: up to 2.5% efficiency compared to 3.0% when using PEDOT:PSS instead (1.1% when using no hole-selective contact) after electrochemical doping to make the P3MT film more conductive, and the films were sufficiently robust that the substrate could be reused to make fresh solar cells after removal of previous active material. These are promising results that encourage further work to be done.

On the other hand, graphene has emerged with the potential to be a disruptive technology in organic electronics given its remarkable electrical conductivity, transparency, and flexibility. This atomically-thin film has shown various unique properties, which may lead to applications in several fields beyond transparent electrodes.[12] In Chapter 5, a study on the doping of chemical-vapor deposited (CVD) single-layer graphene was presented were metal-organic, redox active species are deposited from solution to change the electronic structure and concomitantly its electrical conductivity. XPS and UPS suggest that the species on the surface are the same as those observed in experiments in solution of these dopants when doping traditional organic semiconductors.[13-15] Raman and electrical measurements from field-effect transistor

geometry verified the p- and n-doping of graphene, with doubles the conductivity in just a few seconds of immersion in dilute solutions of the dopants.

Comparison of the efficiency of a simple OPV or OLED when using the doped graphene *vs.* that of undoped graphene should exemplify the benefits of such treatment, particularly with an increase in short-circuit current. Deposition of multiple graphene layers should lead to reduction in sheet resistance with concomitant increase in current, and might allow the device behavior to be comparable with that obtained when using ITO. While the proof-of-concept for graphene as a transparent electrode has been shown,[16] it remains to be seen if it really amounts to be commercializable and ubiquitous as projected by some.[12]

Other future work on doping of graphene might involve using alternate n-dopants previously published[17] and recently made in the Marder group such as those shown in Figure 6.3. These have the potential of raising the Fermi level of graphene higher than what could be achieved with $(RhCpCp^*)_2$ in Chapter 5 due to the lower ionization potentials of the corresponding monomers. However, the dissociation energies needed to generate monomers are larger than in the case of $(RhCpCp^*)_2$, which means that the differences in overall reducing power between these dopants may not be as large as suggested by the monomer redox potentials. Moreover, these stronger bonds might result in too low monomer concentration for doping to occur through the dissociative mechanism, although the reaction can still proceed, at least for lower extents of doping / higher work function graphene, by the alternative "ET-first" mechanism.[13] Since drying of a solution during spin coating results in large concentrations, perhaps this methodology can succeed at placing sufficient monomer on graphene to dope graphene appreciably in a reasonable time scale. It might even be possible to use graphene as a doping test bed for a series of dopants where their reducing power of a solid acceptor can be compared with each other under a given set of conditions.

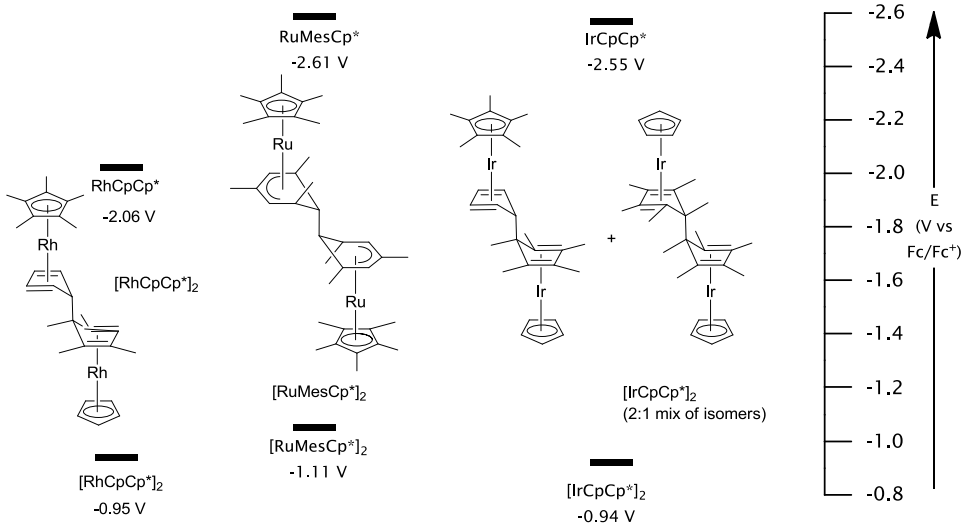

Figure 6.3 Ionization potentials relative to ferrocene for the n-dopant used in Chapter 5 $(RhCpCp^*)_2$, a ruthenium dimer and a mixture of iridocene dimers.

It is interesting that $Mo(tfd\text{-}COCF_3)_3$, the p-dopant in Chapter 5, was slow in appreciatively increasing the work function of graphene, needing overnight exposure to introduce less holes into graphene while the n-dopant needed only 10 min to introduce even more electrons. Perhaps changing solvent can result in faster doping. Some early experiments with a dopant where the $-COCF_3$ functionalities are replaced for –COOMe (methyl ester) moieties also gave low coverages; hence, this might be an intrinsic problem of the $Mo(tfd)_3$ core, perhaps related to poor wetting of the graphene by the oleophobic $–CF_3$ groups. Preliminary experiments on p-doping with $Mo(tfd\text{-}COCF_3)_3$ at 100 °C for 10 min afforded similar coverages and electronic structure changes as those observed after overnight immersion. This is something that might be explored further, since it would be of interest to develop a faster method for p-doping. Stronger oxidants such as the commercially available "magic blue" and its derivatives[18] might be worthy trying as well to determine if they give can p-dope further or faster than $Mo(tfd\text{-}COCF_3)_3$.

Finally, other two-dimensional crystals that could benefit from doping studies such as those presented in Chapter 5 include MoS_2,[19] which displays a band gap even in single layer and thus is finding use in field-effect transistors where on/off ratios as high

as 1×10^8 have been reported with mobilities of ~200 $cm^2V^{-1}s^{-1}$.[20] It would be interesting to see the effect that dopants used in Chapter 5 have on the electronic structure (intrinsically p-doped) and mobility of such devices.

In conclusion, this thesis has consisted of a number of studies of surface modification relevant to organic capacitive and conductive devices. This is already a diverse and growing area which is expected to grow more so in the coming years, and it is the author's intension that the systematic investigations presented here can serve as a guideline in future research and development of new systems.

6.1 References

(1) Paniagua, S. A.; Hotchkiss, P. J.; Jones, S. C.; Marrikar, F. S.; Mudalige, A.; Pemberton, J. E.; Marder, S. R.; Armstrong, N. R. *J. Phys. Chem. C.* **2008**, *112*, 7809.

(2) Kim, P.; Jones, S. C.; Hotchkiss, P. J.; Haddock, J. N.; Kippelen, B.; Marder, S. R.; Perry, J. W. *Adv. Mater.* **2007**, *19*, 1001.

(3) Gliboff, M.; Sang, L.; Knesting, K. M.; Schalnat, M. C.; Mudalige, A.; Ratcliff, E. L.; Li, H.; Sigdel, A. K.; Giordano, A. J.; Berry, J. J.; Nordlund, D.; Seidler, G. T.; Brédas, J.-L.; Marder, S. R.; Pemberton, J. E.; Ginger, D. S. *Langmuir* **2013**, *29*, 2166.

(4) Gliboff, M.; Li, H.; Knesting, K. M.; Giordano, A. J.; Nordlund, D.; Seidler, G. T.; Brédas, J.-L.; Marder, S. R.; Ginger, D. S. *J. Phys. Chem. C* **2013**.

(5) Hotchkiss, P. J., Ph.D. Thesis, Georgia Institute of Technology, 2008.

(6) Kim, P.; Doss, N. M.; Tillotson, J. P.; Hotchkiss, P. J.; Pan, M.-J.; Marder, S. R.; Li, J.; Calame, J. P.; Perry, J. W. *ACS Nano* **2009**, *3*, 2581.

(7) Yang, K.; Huang, X.; Huang, Y.; Xie, L.; Jiang, P. *Chem. Mater.* **2013**.

(8) Matyjaszewski, K.; Nakagawa, Y.; Gaynor, S. G. *Macromol. Rapid Commun.* **1997**, *18*, 1057.

(9) Bronstein, H. A.; Luscombe, C. K. *J. Am. Chem. Soc.* **2009**, *131*, 12894.

(10) Doubina, N.; Ho, A.; Jen, A. K. Y.; Luscombe, C. K. *Macromolecules* **2009**, *42*, 7670.

(11) Yang, L.; Sontag, S. K.; LaJoie, T. W.; Li, W.; Huddleston, N. E.; Locklin, J.; You, W. *ACS Appl. Mater. Interfaces* **2012**, *4*, 5069.

(12) Novoselov, K. S.; Falko, V. I.; Colombo, L.; Gellert, P. R.; Schwab, M. G.; Kim, K. *Nature* **2012**, *490*, 192.

(13) Guo, S.; Mohapatra, S. K.; Romanov, A.; Timofeeva, T. V.; Hardcastle, K. I.; Yesudas, K.; Risko, C.; Brédas, J.-L.; Marder, S. R.; Barlow, S. *Chem. Eur. J.* **2012**, *18*, 14760.

(14) Guo, S.; Kim, S. B.; Mohapatra, S. K.; Qi, Y.; Sajoto, T.; Kahn, A.; Marder, S. R.; Barlow, S. *Adv. Mater.* **2012**, *24*, 699.

(15) Qi, Y.; Sajoto, T.; Kröger, M.; Kandabarow, A. M.; Park, W.; Barlow, S.; Kim, E.-G.; Wielunski, L.; Feldman, L. C.; Bartynski, R. A.; Brédas, J.-L.; Marder, S. R.; Kahn, A. *Chem. Mater.* **2009**, *22*, 524.

(16) Bae, S.; Kim, H.; Lee, Y.; Xu, X.; Park, J.-S.; Zheng, Y.; Balakrishnan, J.; Lei, T.; Ri Kim, H.; Song, Y. I.; Kim, Y.-J.; Kim, K. S.; Ozyilmaz, B.; Ahn, J.-H.; Hong, B. H.; Iijima, S. *Nature Nanotech.* **2010**, *5*, 574.

(17) Moseley, K.; Kang, J. W.; Maitlis, P. M. *J. Chem. Soc. A* **1970**, *0*, 2875.

(18) Connelly, N. G.; Geiger, W. E. *Chem. Rev.* **1996**, *96*, 877.

(19) Wang, Q. H.; Kalantar-Zadeh, K.; Kis, A.; Coleman, J. N.; Strano, M. S. *Nature Nanotech.* **2012**, *7*, 699.

(20) Radisavljevic, B.; Radenovic, A.; Brivio, J.; Giacometti, V.; Kis, A. *Nature Nanotech.* **2011**, *6*, 147.